UNIVERSITÄTSmedizin. MAINZ

Max Planck Graduate Center
mit der Johannes Gutenberg-Universität

Evaluation of Mesoporous Silica Nanoparticles for Head and Neck Cancer Therapy

Dissertation

for attaining the academic degree of

Doctor rerum naturalium (Dr.rer.nat.)

in accordance with regulations of the **Max Planck Graduate Center**
of the departments
08 – Physics, Mathematics, and Computer Science,
09 – Chemistry, Pharmaceutical Sciences, Geography, and Geosciences,
10 – Biology, and the University Medicine
of the Johannes Gutenberg University

submitted by

Anna Elisabeth Katharina Watermann

from Göttingen

August 2019

I. Declaration

I hereby declare that I wrote the dissertation submitted without any unauthorized external assistance and used only sources acknowledged in the work. All textual passages which are appropriated verbatim or para-phrased from published and unpublished texts as well as all information obtained from oral sources are duly indicated and listed in accordance with bibliographical rules.

In carrying out this research, I complied with the rules of standard scientific practice as formulated in the statutes of Johannes Gutenberg-University Mainz to insure standard scientific practice.

Here I declare that the scientific thesis I am now handing in has not yet been published at any other German University, or any university abroad, or any comparable institution, with the aim of attaining a scientific degree.

Here I also declare that I have not yet finished any other doctoral PhD or any similar graduation program in any of the subjects represented by the MPGC-JGU without success.

_____ _____

Place, Date Signature

In loving memory of my father and grandfather

II. Zusammenfassung

Jedes Jahr erhalten etwa 500 000 Deutsche die Diagnose Krebs und die Anzahl der Krebspatienten wird laut Prognosen in den nächsten Jahren steigen. Die therapeutischen Möglichkeiten sind abhängig von der Krebsart und der Konstitution des Patienten/ der Patientin wie auch die Überlebenschancen. Falls möglich, wird der Tumor chirurgisch entfernt, bestrahlt und/ oder mit Chemotherapie behandelt. Jedoch sind insbesondere die Entfernung und Bestrahlung nicht für alle malignen Tumore möglich, besonders Metastasen stellen eine Herausforderung dar. Außerdem führen Bestrahlung und Chemotherapie häufig zu Nebenwirkungen, die die Therapieoptionen weiter einschränken können. Durch eine gezieltere Verabreichung des Wirkstoffs können unerwünschte Arzneimittelwirkungen abgemildert und eine Erhöhung der Dosis am Tumor erreicht werden. Dafür eignen sich Wirkstofftransportsysteme wie mesoporöse Silikananopartikel (MSN), die in dieser Arbeit als Transporter evaluiert wurden. Die hier verwendeten MSN bestanden aus einem dendritischen Siliciumoxidgeflecht mit integriertem Fluoreszenzfarbstoff. In die daraus resultierenden Poren konnten verschiedene Wirkstoffe eingebracht werden und diese wurden anschließend mit einem pH- und Redox-sensitiven Verschlusssystem ausgestattet, das aus Ferrocen und β-Cyclodextrin bestand. Dann wurden die Biokompatibilität sowie die zelluläre Aufnahme anhand von Zellkulturversuchen und die *in vivo* Biodistribution mit dem HET-CAM Model untersucht. Insgesamt war die Biokompatibilität sehr hoch und eine zeitabhängige zelluläre Aufnahme in Endosomen und Lysosomen wurde festgestellt. *In vivo* wurden die MSN hauptsächlich in der Leber und den Nieren detektiert, gleichzeitig auch wenige MSN in einem Tumor, der in die CAM eingewachsen war. Weiterhin konnte die zelluläre Aufnahme durch die Konjugation eines *Epidermal Growth Factor Receptor* (*EGFR*)-Antikörpers an den unbeladenen Wirkstofftransporter beschleunigt werden. Als Zweites wurden die Wirkstoffbeladung und -freisetzung untersucht, indem das Chemotherapeutikum Doxorubicin, das über toxische und fluoreszierende Eigenschaften verfügt, in die MSN inkorporiert wurde. Es konnte eine effiziente Beladung durchgeführt und eine retardierte Freisetzung in zwei Krebszelllinien beobachtet werden. Als besonders herausfordernd stellte sich die Beladung der MSN mit *siRNA* und die Freisetzung dieser dar, da eine Wirkung der siRNA nicht festgestellt werden konnte. Die Porengröße der MSN wurde vergrößert und verschiedene Beladungsprotokolle wurden verwendet, jedoch ohne eine Wirkung der *siRNA* nachweisen zu können. Schließlich wurden die mit *siRNA* beladenen MSN mit einem lipidbasierten Transfektionsreagenz verschlossen, was zu einer starken Erhöhung der zellulären Nanopartikelaufnahme führte, nicht jedoch zu einer Wirkung der *siRNA* auf die mRNA- und

Proteinexpression. Dies konnte auch nicht durch die Konjugation eines *EGFR*-Antikörpers an *siRNA*-beladene und mit Ferrocen und β-Cyclodextrin verschlossene MSN erreicht werden.

Insgesamt zeigten die MSN mit dem primär verwendeten Verschlusssystem vielversprechende Eigenschaften bezüglich Biokompatibilität und Wirkstofftransport von Doxorubicin, jedoch konnte ein effizienter *siRNA*-Transport nicht umgesetzt werden. Somit stellen große und geladene Moleküle eine Herausforderung für den Wirkstofftransport mittels MSN dar. Gleichwohl sind MSN als Wirkstofftransportsystem niedermolekularer Wirkstoffe hervorragend für eine zielgerichtete Therapie von Kopf- und Halsplattenepithelkarzinomen geeignet.

III. Abstract

More than half a million Germans are newly diagnosed with cancer every year, and prognosis revealed increasing numbers in the future. The therapeutic options are dependent on the cancer type and the patients' overall health condition; the same applies to survival rates. If possible, solid tumors are surgically removed, irradiated, or treated with chemotherapy. However, not all malignant tumors – especially metastases – can be reached with irradiation or surgical intervention and side-effects often limit the therapeutic intervention. Targeted therapy can reduce side-effects and increase the dose at the tumor site. This can be achieved by drug delivery vehicles such as mesoporous silica nanoparticles (MSNs) that were evaluated as drug nanocarrier in this work. MSNs consist of a dendritic silica network that generates pores that can be loaded with different drugs and should be sealed. First, MSNs were equipped with a pH- and redox-sensitive gatekeeper system consisting of ferrocene and β-cyclodextrin. The biocompatibility, cellular uptake, and biodistribution of the sealed MSNs were analyzed *in vitro* in several cancer cell lines and *in vivo* using the CAM assay, respectively. The overall biocompatibility was remarkably good; the MSNs were taken up time-dependently by cancer cells and localized in the endolysosomal system. The MSNs were found mainly in the liver and kidneys of chicken embryos but also in the tumor which grew within the CAM. The addition of an epidermal growth factor receptor (EGFR)-antibody to the MSNs accelerated nanoparticle uptake. Second, the drug loading and release were examined with the chemotherapeutic drug doxorubicin because of its toxic and fluorescent characteristics. Efficient drug loading was achieved, and a retarded release of doxorubicin was observed in two cancer cell lines. Third, siRNA loading and release were studied which was highly challenging. The MSN pore size had to be adjusted, and different loading protocols were tested without success. Eventually, siRNA was loaded to the MSNs and a lipid-based transfection agent was added to seal the pores. Although MSN uptake increased tremendously, no siRNA release could be detected by determining mRNA and protein expression, respectively. When an EGFR-antibody was added to the siRNA-loaded MSNs, also no siRNA efficacy was noticed.

Overall, the MSN-based drug delivery system showed promising characteristics regarding biocompatibility and transport of the small molecule drug doxorubicin, but efficient siRNA transport was not achieved. Thus, the transport of large and charged molecules by MSNs is challenging. Nevertheless, MSNs are suited as drug delivery vehicles for small molecule drugs in head and neck cancer therapy.

IV. Table of contents

V. List of abbreviations

°C	degree Celsius
A	Ampere
APS	ammonium peroxide sulfate
ATP	adenosine triphosphate
β-CD	methyl-β-cyclodextrin
BSA	bovine serum albumin
CAM	chorioallantoic membrane
CI	confidence interval
cm^2	square centimeter
cm^3	cubic centimeter
CTAB	cetyltrimethylammonium bromide
Cy5	Cyanine5
ddH_2O	double-distilled water
DMEM/F12	Dulbecco's modified Eagle's medium: Nutrient mixture F12
DMSO	dimethyl sulfoxide
DOPE	dioleoyl-phosphatidylethanolamine
Dox	doxorubicin hydrochloride
ECM	extracellular matrix
EDTA	ethylene diamine tetraacetic acid
EEA1	early endosome antigen 1
eGFP	enhanced green fluorescent protein
EGF(R)	epidermal growth factor (receptor)
Ep-CAM	epithelial cell adhesion molecule
EPR	enhanced permeability and retention
ER	endoplasmic reticulum
FCS	newborn calf serum
FDA	US Food and Drug Administration
FVD	fixable viability dye
g	gravitation force
GA	Golgi apparatus
GRAS	generally recognized as safe
h	hour(s)
hnRNP K	heterogeneous nuclear ribonucleoprotein K
H_2O	purified water
IC_{50}	half maximal inhibitory concentration
IgG2a	immunoglobulin G 2a

K	Kelvin
Lamp-1	lysosome-associated-membrane protein 1
LE	loading efficiency
M	mol per liter
mAb	monoclonal antibody
MFI	mean fluorescence intensity
mg	milligram
mL	milliliter
mM	millimol per liter
mm	millimeter
min	minute(s)
MPS	mononuclear phagocytic system
MRI	magnetic resonance imaging
mRNA	messenger ribonucleic acid
MSN	mesoporous silica nanoparticle
MTT	3-(4,5-dimethylthiazol-2-yl)-2,5-diphenyltetrazolium bromide
µL	microliter
µM	micromol per liter
µm	micrometer
NEAA	non-essential amino acids
NH_2-β-CD	3A-Amino-3A-deoxy-(2AS,3AS)-β-cyclodextrin
nm	nanometer
nsRNA	non-sense ribonucleic acid
PBS	Dulbecco's phosphate buffered saline
PDI	polydispersity index
PEG	poly(ethylene glycol)
PEI	poly(ethyleneimine)
PFA	para formaldehyde
PLGA	poly(lactic-co-glycolic acid)
qPCR	quantitative real-time polymerase chain reaction
RGD	arginine-glycine-aspartic acid
RISC	RNA-induced silencing complex
ROS	reactive oxygen species
rpm	rotations per minute
RT	room temperature
S.D.	standard deviation
SDS	sodium dodecyl sulfate
SDS-PAGE	SDS-polyacrylamide gel electrophoresis

$Si(OH)_4$	orthosilicic acid
SiO_2-NP	silica nanoparticle
siRNA	short-interference ribonucleic acid
SPION	superparamagnetic iron oxide nanoparticles
TBST	Tris-buffered saline with Tween® 20 (for immunofluorescence)
TBS-T_{20}	Tris-buffered saline with Tween® 20 (for immunoblot analysis)
T/E	trypsin- EDTA solution
TEM	transmission electron microscopy
TEMED	tetramethylethylenediamine
TEOS	tetraethyl orthosilicate
U	unit
V	Volt
VEGF	vascular endothelial growth factor

VI. List of Figures

VII. List of Tables

1 Introduction

This chapter gives an overview of the current state of research on drug delivery systems for cancer therapy with a focus on mesoporous silica nanoparticles (MSNs), siRNA delivery with MSNs and active targeting of MSNs. Some parts and three figures (Figures 5, 6, and 8) of this introductory chapter were adopted from the review “Mesoporous silica nanoparticles as drug delivery vehicles in cancer” written by me and Juergen Brieger and published in *Nanomaterials* 2017, 7, 189 under a Creative Commons Attribution (CC BY) license [1]. These parts were indicated according to the standard bibliographic rules.

1.1 General introduction

Every year more than 500 000 people are newly diagnosed with malignant neoplasms in Germany, and because of an aging demographic, the number of cancer patients will increase in the following years [2]. The treatment of cancer is highly dependent on the kind of malignancy, for example, some solid tumors can be surgically removed, others are irradiated, and in most cases, chemotherapeutics are administered, too. Still, therapy of tumors at anatomical critical sites is challenging. For example, the surgical removal of head and neck squamous cell carcinoma (HNSCC) would often greatly constrain the patient’s quality of life and therefore, radio- and chemotherapy are mainly applied. However, the unfavorable effects of those therapies include resistances, metastasis and second primary tumors. Furthermore, adverse effects diminish the patient’s quality of life and provoke numerous adjuvant drugs to be taken that themselves induce side-effects. Some of the most severe chemotherapeutic side-effects are neuropathy, neutropenia, nephrotoxicity, and cardiotoxicity, but also milder side-effects such as hair loss and nausea greatly affect the patient. For that reason, new therapeutic strategies are needed that specifically target the malignant tumors and spare healthy tissues as good as possible. On one side, the advantages of specific gene expression regulation by RNA interference can be exploited as a new therapeutic option in cancer therapy and will be described in 1.2. On the other side, nanoparticles (NPs) and especially MSNs will be thoroughly introduced and characterized in 1.3. Also, the model drug doxorubicin (Dox) (1.4) and the chorioallantoic membrane model (1.5) as *in vivo* model will be briefly described.

1.2 RNA interference

The phenomenon of post-translational silencing of gene expression after the introduction of double-stranded RNA (dsRNA) was first identified in *Caenorhabditis elegans* by Fire et al. in 1998 and termed RNA interference (RNAi) [3]. RNAi can reduce gene expression with high efficiency [4], and therefore was extensively studied and improved during the last 15 years [5]. Since Elbashir et al. found that 21-nucleotide siRNA duplexes specifically suppress genes in mammalian cells [4], the tool of RNAi is broadly being used to study gene function in mammalian cells and is being exploited to develop new cancer therapies. Along these lines, a multitude of siRNAs targeting abundant proteins became commercially available.

1.2.1 The mechanism of RNA interference

The multistep process of RNAi is depicted in Figure 1 and occurs in the cytoplasm. First, dsRNA is cleaved into siRNA segments of about 20 nucleotides (approx. 7.5 nm long and 2 nm in diameter) by the enzyme Dicer (not shown here) [6]. Second, the siRNA is incorporated into an enzyme called RNA-inducing silencing complex (RISC). After ATP-dependent activation of RISC, one strand of the siRNA remains in the RISC which exploits this strand to bind to single-stranded mRNA molecules with a complementary sequence. Finally, this target mRNA is cleaved by the RISC's nuclease activity at a single site in 21 or 22 nucleotides-long siRNAs – the cleaving site of the target mRNA is 11 or 12 nucleotides downstream of the first nucleotide that is complementary to the siRNA – resulting in mRNA degradation followed by a reduction in gene expression [7]. The siRNA sequence must be carefully designed to minimize off-target effects, and to optimize the degradation of the target mRNA. Also, a mix of several siRNAs targeting one gene can be applied to enhance gene suppression. Since siRNAs can be designed with high specificity, they became interesting as a new therapeutic tool for cancer therapy, e.g. to circumvent chemoresistance [8].

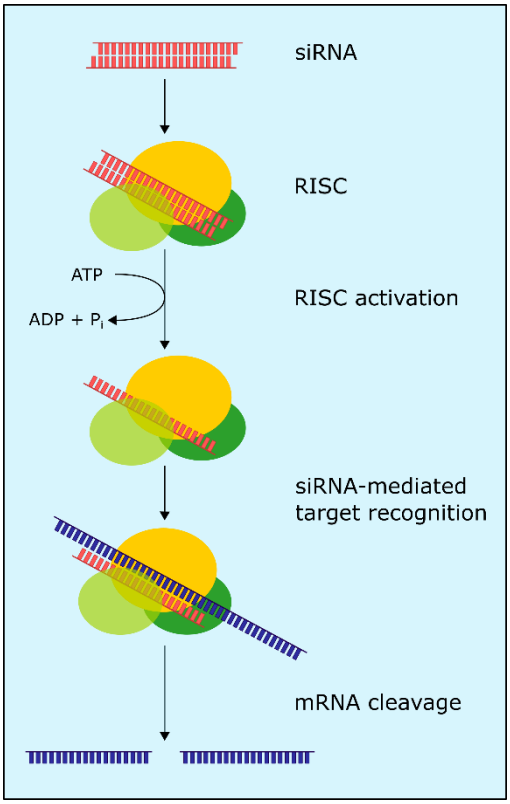

Figure 1: The mechanism of RNA interference technology used for gene silencing
Double-stranded 21-23 nucleotide segments (siRNA) are incorporated into the RNA-inducing silencing complex (RISC). This enzyme is ATP-dependently activated and unwinds the siRNA duplex. Next, the single-stranded antisense strand guides the RISC to the target mRNA which has a complementary composition. Finally, the target mRNA is cleaved by the RISC, thus the target gene expression is reduced. Graphic adapted from [9] and [10].

1.2.2 Application of RNA interference in therapy

The application of siRNA in a physiological environment faces several hurdles: siRNAs are degraded by endogenous nucleases in plasma and tissues and are rapidly cleared by the mononuclear phagocytic system (MPS) or renal filtration, respectively [5]. Moreover, siRNAs are negatively charged, thus they are not able to penetrate the cellular membrane directly. For this reason, siRNAs can be taken up only by endocytosis or pinocytosis. Yet, this also causes the necessity of endosomal escape before degradation in the endolysosomal system. Different approaches were utilized to stabilize the siRNA and to circumvent these hurdles: siRNAs were chemically modified, conjugated to biomolecules or incorporated into organic and inorganic NPs, respectively [5,11]. Recently, chemical modifications of siRNA and siRNA conjugation to biomolecules were extensively reviewed by Chernikov et al. [11]. For example, methylation of the 2'-OH of the ribose entity enhances nuclease resistance *in vitro* and *in vivo* [12,13] while consecutive 2'O-methyl groups inhibit RNAi [14]. Moreover, ribose 2'F analogs

can increase the nuclease resistance, too, while only a slight decrease in RNAi was observed [15,16]. These and other modifications increase the *in vivo* stability of the siRNA but do not enable cellular penetration. For this reason, siRNA was conjugated to various biomolecules such as antibodies [17], aptamers [18], peptides [19], folate [20], and carbohydrates [21] as ligands for membrane receptors, or molecules that facilitate membrane penetration by natural mechanisms, e.g. cholesterol [22]. Also, siRNA was modified with neutral phosphotriester groups in the siRNA's phosphate backbone that enabled membrane penetration. Afterward, cytoplasmic thioesterases restored the native siRNA form, and RNAi was induced [23]. In most cases, cleavable linkers were applied so that RISC formation was not obstructed by the biomolecules. These linkers can contain pH- or photosensitive bonds [24,25], or consist of disulfide bonds that are cleaved in the cytoplasm by glutathione, respectively [26,27]. Yet, the application of siRNA bioconjugates in the clinic is still limited due to low bioavailability, inconvenient pharmacokinetics, and high production costs [11]. So far, only one siRNA-based drug was approved by the FDA and the EMA, namely Patisiran [28]. The drug was developed by Alnylam Pharmaceuticals and is used for the treatment of hereditary transthyretin polyneuropathy [29]. It significantly reduces the symptoms of the disease compared to placebo, but it also exhibits proinflammatory side-effects caused by the cationic lipid that complexes the siRNA. For that reason, Patisiran must be combined with antihistamines, corticosteroids, and acetaminophen [30]. Several siRNA-based cancer therapeutics were and are evaluated in clinical trials [31] but were not approved yet. Another possibility to deliver siRNAs to the target tissue is to use NPs as delivery vehicles. This approach is consequential because of "the enhanced permeability and retention (EPR) effect of solid tumors: Due to a leaky vasculature and the lack of lymphatic drainage small structures such as NPs can accumulate in the tumor [32]." [1] For example, several organic siRNA drug delivery systems for cancer therapy were already tested in clinical trials: TKM-080301 is a stable nucleic acid lipid particle formulation with siRNA that targets polo-like kinase 1, a cell proliferation promoting protein. The siRNA is incorporated into the aqueous core of a liposome consisting of cationic lipids (1,2-dilinoleyloxy-N,N-dimethyl-3-aminopropane), release promoting lipids (1,2-distear-oyl-sn-glycero-3-phosphocholine), and cholesterol for stabilization. The surface was modified with polyethylene glycosylated lipids which facilitate crossing barriers and stabilizes the formulation, too [33]. In a first phase I/II clinical trial (NCT02191878) of TKM-080301, the drug was generally well-tolerated and showed preliminary antitumor efficacy [34,35]. Moreover, the pharmacodynamics and antitumor activity were analyzed in a subsequent trial (NCT01262235) [36]. Half of the patients (4/8) who received at least two treatment cycles (0.6 or 0.75 mg/ kg/ week TKM-080301) exhibited an improvement of the stable disease, but seri-

ous adverse effects were musculoskeletal pain, ECG T-wave inversion and infusion reaction [37]. Still, the drug was generally well tolerated for up to 18 cycles, and in patients with refractory adrenocortical cancer, the siRNA showed antitumor activity. The siRNA formulation siG12D-LODER (by Silenseed Ltd) is also already evaluated in clinical trials for pancreatic cancer treatment. The target of the siRNA is G12D-mutated KRAS, and the siRNA is transported by a biodegradable poly lactic-co-glycolic acid (PLGA) matrix which has a small cylindrical rod shape. This local drug eluter (LODER, 0.8 mm x 5.5 mm ± 1 mm) enables sustained siRNA release directly into the tumor tissue. In a phase I/IIa clinical trial (NCT01188785) the safety, tolerability and antitumor effects of siG12D-LODER were studied in non-operable Locally Advanced Pancreatic Cancer (LAPC) patients [38]. Different doses of siG12D-LODER were administered directly in the tumor tissue by a standard endoscope ultrasound biopsy procedure, and the patients were also treated with concomitant chemotherapy such as Gemcitabine or FOLFIRINOX (Leucovorin, Fluorouracil, Irinotecan, Oxaliplatin). The drug siG12D-LODER was regarded as safe and well-tolerated. Two patients even demonstrated partial response, and most patients had stable disease [39]. In a current phase II study (NCT01676259), 2.8 mg (eight 0.35 mg siG12D-LODERs) are administered in a 12-week cycle to patients combined with chemotherapy (Gemcitabine + nab-Paclitaxel) and the progression-free survival will be evaluated compared to chemotherapy alone [40]. Still, siG12D-LODER must be directly administered to the tumor and therefore is not suited for the treatment of metastasis. The drug Atu027 was developed to reduce tumor growth and metastatic spreading. This synthetically synthesized siRNA targets protein kinase N3 (PKN3), which is part of the phosphoinositide 3-kinase signaling cascade in highly vascularized tissue. A reduction of PKN3 stabilizes vessel integrity, amends inflammation in the tumor environment, and decreases metastasis [41]. The siRNA-lipoplex Atu027 consists of PKN3 targeting siRNA, the cationic lipid AtuFECT01 to complex the siRNA, a neutral helper lipid and a PEGylated lipid to protect from clearance by the immune system [42]. In a phase I clinical trial, Atu027 was examined in patients with advanced refractory solid tumors to determine safety, tolerability, pharmacokinetics, pharmacodynamics and anticancer activity (NCT00938574) [43]. Overall, Atu027 was well-tolerated and stabilized the disease in circa half of the treated patients and even reduced metastatic lesions in some patients. For that reason, a phase I/II clinical trial was initiated (NCT01808638) in patients with advanced or metastatic pancreatic carcinoma. In this trial, Atu027 was administered together with gemcitabine which exhibited good tolerability. Patients who received higher doses of Atu027 exhibited a longer progression-free survival and overall survival [33]. Although the described siRNA delivery systems showed promising results in the performed clinical trials, the applied

lipids and polymers might still exhibit toxicity and immune response in higher concentrations. Therefore, the use of inorganic materials such as silica to deliver siRNA is widely studied [44] and will be described in the following paragraphs.

1.3 MSNs as drug delivery vehicles

“Research in nanomedicine prospered over the last decades and yielded several prerequisites for drug delivery systems. NPs should have a high loading capacity and the cargo should be protected until it reaches the side of action. Moreover, NPs should be taken up predominantly and efficiently by cancer cells and evade the MPS. Once drug carriers are incorporated by the cells, endosomal escape and drug release are crucial. Good tumor accumulation and deep tumor penetration are also favorable. Importantly, NPs need good biocompatibility which is dependent on the used material but also influenced by degradation and excretion.

Over the past decades a plethora of different NPs for drug delivery, organic and inorganic, were developed. Organic NPs are represented for example by liposomes, polymer micelles, dendrimers, and PLGA-based NPs. In fact, some liposomal formulations are already approved by the US Food and Drug Administration (FDA), e.g. liposomal Dox (Doxil®/Caelyx™) for treatment of Kaposi’s sarcoma, ovarian cancer and multiple myeloma [45]. Yet, the advantage of liposomes compared to the free drug is mostly limited to a longer half-life and reduced toxicity [46]. Furthermore, several polymeric and micelle based vehicles for cancer therapy were or are in clinical trials, respectively, among others as described above (1.2.2) [45].

Drug delivery systems can also be based on inorganic materials, e.g. gold NPs, metal oxide such as iron oxide particles, carbon nanotubes, quantum dots and MSNs [47–51]. Particularly, iron oxide NPs are already approved for glioblastoma therapy in Europe and as contrast enhancers for magnetic resonance imaging [45]. So far, no clinical trials were performed with MSNs but an early phase I study (NCT02106598) is conducted with targeted silica NPs [SiO_2-NPs] for image-guided operative sentinel lymph node mapping [52]. However, MSNs exhibit several superior features in comparison to other inorganic NPs: MSNs possess a unique structure with a tunable pore and particle size, resulting in a high specific surface area which can be easily functionalized, and most importantly are highly biocompatible. Silica is classified as “generally recognized as safe” (GRAS) by the FDA and is used in cosmetics and as a food additive [53]. The MSNs’ porous structure allows a high drug loading capacity and a

time-dependent drug release, but the cargo can also be absorbed to the particle's surface. The pores are usually sealed by a gatekeeper system which is often also used for additional functionalization and improvement of pharmacodynamical characteristics." [1] Overall, SiO_2-NPs were increasingly studied from the beginning of the 21st century and most studies on SiO_2-NPs and MSNs were published in the last two years.

1.3.1 MSN synthesis and characterization

"First, MSN synthesis will be discussed briefly with regard to NP diameter and pore size. Then, the influence of the characteristics is described regarding drug delivery vehicles.

1.3.1.1 MSN synthesis

Several different approaches are used for MSN synthesis resulting in a variety of engineered particle and pore sizes. For instance, MSNs are synthesized based on a modified Stöber synthesis, using e.g. tetraethyl orthosilicate (TEOS) as the precursor for silica condensation and different additives as templates such as surfactants like cetyltrimethylammonium bromide (CTAB), polymers, micelle forming agents or other dopants [54,55]. In brief, surfactants are stirred in a mixture of water and alcohol under basic conditions and TEOS or other silicates are added under agitation. Concentrations and compositions of silica sources, template-agents and stirring conditions determine particle size, pore size, and shape. When the surfactant concentration is above the critical micelle concentration, CTAB self-aggregates into micelles and the silica precursor condensates at the surface. A silica structure is formed around the surface of the micelles. Then, the surfactants have to be completely removed to obtain biocompatible [MSNs] which are usually further modified [56]." [1] An exemplary transmission electron microscopy (TEM) image is shown in Figure 2 which depicts the dendritic silica network that generates the porous structure of MSNs.

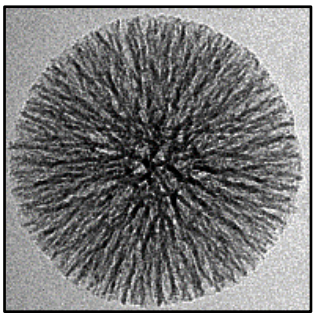

Figure 2: Representative TEM image of a mesoporous silica nanoparticle
The spherical NP consists of a dendritic silica network that generates a porous structure. Here, cetyltrimethylammonium chloride (CTAC) was used as a surfactant and TEOS as a silica source. Image provided by [redacted].

"Another approach was first introduced by Zhao et al. who used triblock copolymers as templating agents for well-ordered hexagonal mesoporous silica structures with up to 30 nm pores [57]. The common pore size of MSNs ranges between 2 and 5 nm but larger pore sizes of 23 nm can be generated e.g. by adding swelling agents such as trimethyl benzene [58]. Also, hollow-structured MSNs were examined as drug carriers by Wu et al. who employed a stability difference-based selective bond breakage strategy. In brief, this strategy relies on the fact that a Si-C bond is weaker than a Si-O bond and can be degraded by hydrothermal treatment. By applying different temperatures, pore sizes were increased gradually up to 24 nm [59]. A greater variation can be found in the particle diameter which is also dependent on surface modifications. While some [SiO_2-NPs] are 100- 120 nm in diameter others are larger than 200 nm, yet pore sizes are similar (2.5 nm or 3.0 nm, respectively) [60–62]. However, the denoted particle diameter is also dependent on surface modifications such as coatings and the suspension medium. A more detailed description of MSN synthesis strategies can be found here [56].

1.3.1.2 Influence of MSN characteristics on biological systems

The influence of NP characteristics including size, shape, surface area and chemistry on biological systems play an important role for efficient drug delivery and was extensively reviewed by A. Albanese, P.S. Tang, and W.C.W. Chan [63]. MSNs exhibit a high specific surface area of up to 1000 m^2/ g which is decreased by surface modifications such as amination or coating [64,65]. Accordingly, large-pore NPs (10 nm) exhibit a smaller specific surface area [66]. Yet, a large surface area increases loading efficiency for small molecule drugs and siRNA. For example, a nearly 1000 fold higher amount of Dox could be loaded in MSNs compared to the FDA-approved liposomal formulation Doxil® [67]. MSNs uniformity is important for quality

assurance and can be determined by dynamic light scattering [DLS]. Analyzing the Brownian motion reveals the polydispersity index (PDI) as an indication for the colloidal dispersion size range and a low PDI is favorable [68]. Also, particle shape and size are analyzed with TEM.

The NP characteristics such as shape, size and charge have an influence on particle uptake. Cellular entry is also dependent on the applied targeting strategy. In general, several possible endocytic pathways for cellular NP uptake were proposed [as shown in Figure 3], namely caveolae or clathrin-dependent endocytosis, caveolae or clathrin-independent endocytosis and micropinocytosis [69]. The most prominent cellular entry strategy is [clathrin-dependent] receptor-mediated endocytosis of targeted NPs. After the MSNs' ligands bound the corresponding receptors on the cellular membrane, the endocytic process is initiated and particles are incorporated in endosomes [70]. Yet, untargeted MSNs can also interact with the plasma membrane through their surface modifications by non-specific binding forces, and then are endocytosed or penetrate the cellular membrane [71]." [1]

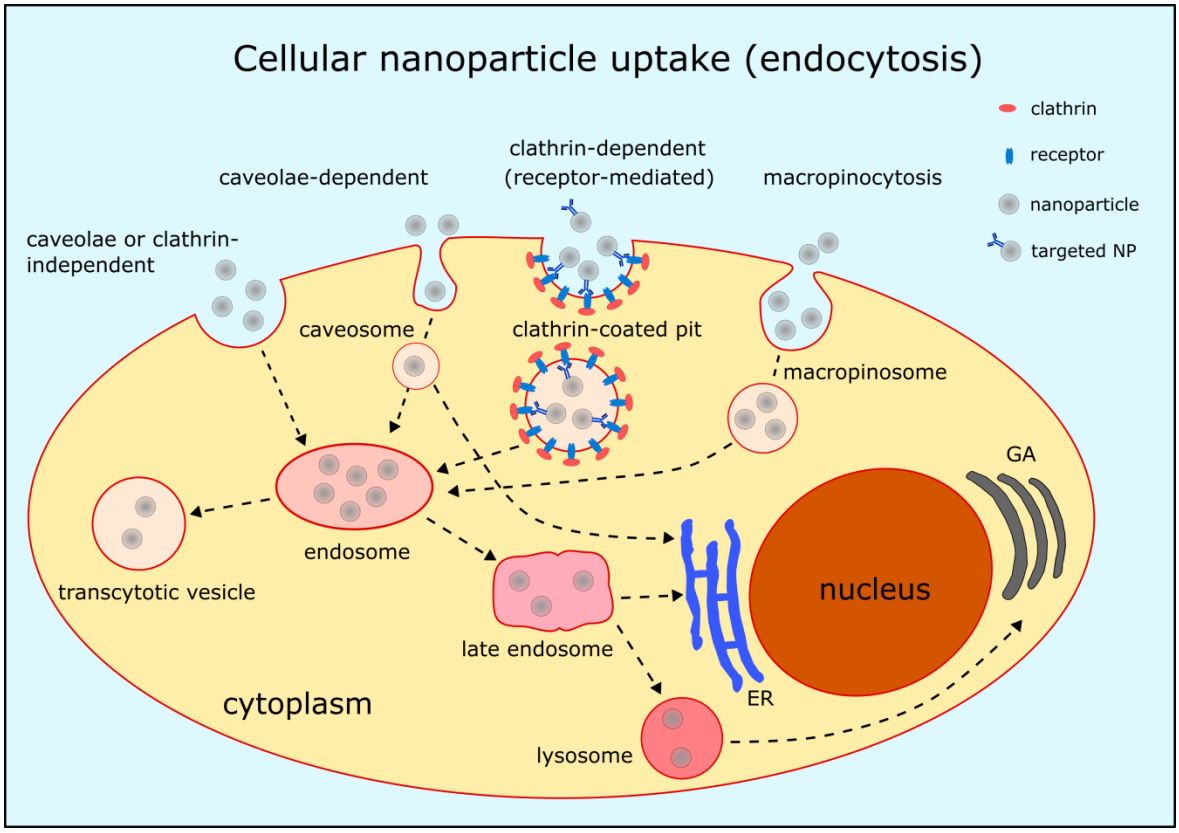

Figure 3: A simplified illustration of the cellular nanoparticle uptake in nonphagocytic cells

The NPs are taken up via different routes of endocytosis and are trafficked through the cell. Here, macropinocytosis is presented as only one route through macropinosomes which form after incorporation of NPs by invagination of the cellular membrane. A similar mechanism is caveolae-dependent endocytosis of NPs. The small membrane invaginations contain caveolins and can incorporate small NPs which are then trafficked further to endosomes and sometimes to the endoplasmic reticulum (ER). The most prominent NP uptake route is clathrin-dependent endocytosis, also called receptor-mediated endocytosis. NPs with targeting ligands bind to the extracellular receptors and are taken up by clathrin-coated pits. In the next step, the vesicles are processed to endosomes and further to late endosomes, and NP degradation is mediated by lysosomes. Moreover, the lysosomes are processed to the Golgi apparatus (GA). However, NPs can also be transported through the cell by transcytotic vesicles. Graphic adapted from E. Fröhlich [69].

“Regarding the NP shape, the best cellular uptake was achieved by rods, followed by spheres, cylinders, and cubes when particles were larger than 100 nm [63,72]. Yet, spherical MSNs of 50 nm showed notable better incorporation by HeLa cells than 110, 170 or 280 nm particles, respectively [73]. The membrane-wrapping process and ligand-receptor interactions influence the uptake efficiency of different particle sizes. A smaller NP of 50 nm [can] induce membrane-wrapping by binding a sufficient number of receptors. While larger NPs interact with a higher number of receptors and the uptake is limited by the receptors’ redistribution on the cellular membrane through diffusion to compensate for local receptor shortage [63,71].

Since endosomes exhibit an acidic pH and pH decreases along the endocytic pathway from late endosomes to lysosomes [74], this acidic environment is used for a controlled release strategy, which is reviewed later. The surface charge also influences NP uptake. Positively charged particles have been found to be taken up faster than neutral or negatively charged particles by human cancer cells [70]. The cellular membrane has a slightly negative charge and favors the binding of positively charged NPs by electrostatic interaction. Yet, in a physiological environment, NPs are coated by a protein corona consisting of serum proteins, opsonins, and ions which changes the *in vitro* determined parameters such as size and charge and thereby also influences cellular uptake and toxicity [71]. The absorbed proteins facilitate clearance by the MPS and agglomeration, but this can be prevented by coating the NPs with poly(ethylene glycol) (PEG) resulting also in longer blood-circulation times [58,75]. So, MSN size and shape have a great influence on the NPs' *in vitro* and *in vivo* behavior. Yet, surface modifications have an even greater impact on the drug delivery vehicle's properties and will be discussed next.

1.3.2 Modifications to control cellular uptake, drug release and endosomal escape

MSN surface modifications are necessary for several purposes: targeting moieties are supposed to direct the drug carrier to the desired destination, different capping systems ensure controlled drug release at the site of action and endosomal escape is not only crucial for efficacy but can also be influenced by certain alterations. The […] [MSNs] can be modified with various functional molecules [inside the pores and on the surface]. These alterations will be discussed in the following sections.

1.3.2.1 Passive and active targeting of MSNs

Scientists imagine a site-directed cancer therapy to lower toxic side-effects, enhance efficacy and reduce required drug doses. In general, three different strategies are exploited for this purpose, namely passive targeting, active targeting, and magnetic-field directed targeting." [1] Next, passive and active targeting will be introduced in detail.

1.3.2.1.1 Passive targeting

"As mentioned above, NPs accumulate favorably in solid tumor tissue due to the EPR effect, which is considered as passive targeting [(see Figure 4)]. Generally, tumors exceeding about one cubic millimeter in size require oxygen and nutrient supply to proliferate further [76]. Therefore, they rapidly form a highly abnormal vasculature by angiogenesis. The blood ves-

sels are lined by a single, thin layer of flattened endothelial cells, the basement membranes have fenestrations varying in size, and little or no pericytes cover the vessels [77]. Hence, macromolecules larger than 40 kDa, which is the threshold of renal clearance, can leave the blood vessels and accumulate in the adjacent tumor tissue but not in normal tissue. Also, solid tumors commonly lack effective lymphatic drainage, so accumulated macromolecules or NPs remain longer in the tumor tissue without being cleared by the immune system [78]. To achieve efficient passive targeting, so far the focus laid on prolonging circulation time which is dependent on renal clearance and MPS escape. Phagocytic cells such as monocytes and macrophages are mainly located in the liver, spleen, bone marrow and lymph nodes [79]. Hence, NPs also tend to accumulate in these organs." [1]

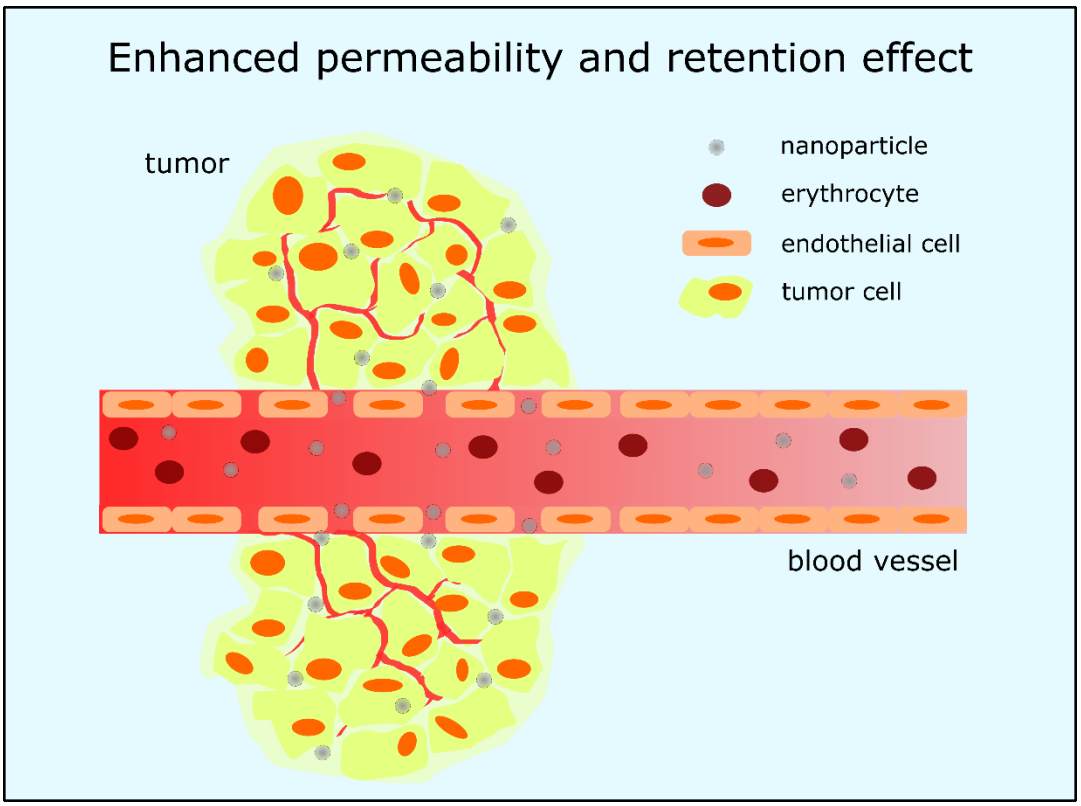

Figure 4: The enhanced permeability and retention effect of solid tumors
The fenestrations in the endothelial layer allow NPs to leave the bloodstream and to accumulate in vascularized tumors. Also, the lymphatic drainage is reduced in the tumor environment thus, NPs are not cleared by the immune system.

"For efficient passive targeting several NP characteristics [must] be considered such as particle size, morphology and surface modifications. To avoid renal clearance, particles have to be at least 10 nm in diameter and a size of 100- 200 nm seems to be optimal to also evade the MPS [80]. Besides, the NP shape also plays a role in passive targeting based on the EPR

effect and was examined by Huang et al. *in vivo*. Using short-rod and long-rod MSNs the main accumulation was found in the liver, spleen, and lung, which is no surprise considering the high blood flow rate of these organs. Yet, short-rod MSNs tended to preferably accumulate in the liver with a fast clearance rate while long-rod MSNs were distributed in the spleen with relatively slow clearance [81]. However, this study was performed without tumors and therefore no passive targeting was shown. Lu and colleagues could demonstrate enhanced tumor accumulation of MSNs in comparison to normal tissue *in vivo* while MSNs also exhibited good biocompatibility [82].

Surface modifications also have a major influence on NP tumor accumulation. As mentioned above, PEG is used to minimize opsonization and thereby evade the MPS. However, it has been implicated that PEGylation reduces cellular NP uptake in cancer cells but also in macrophages [75,83,84]. Nevertheless, Zhu and colleagues reported improved uptake of PEGylated hollow MSNs in comparison to naked particles in cervical cancer cells and mouse embryonic fibroblasts [85]. Another considerable aspect with regard to passive targeting is the elevated interstitial fluid pressure in solid tumors which can be 10 to 40 fold higher compared to normal tissue [86]. This can create pressure gradients and heterogeneous flow in the interstitium which influences the distribution of NPs and can lead to reduced particle concentrations in the tumor. Nonetheless, larger tumors and metastases often have necrotic tissue or highly hypovascular areas in the center because angiogenesis was slower than tumor growth. For this reason, NPs can barely reach these regions by passive targeting.

Moreover, based on the data collected and analyzed by Wilhelm and colleagues [77] only 0.4 % ± 0.2 % of the administered untargeted MSN dose (7 data sets) could be found in the tumor tissue. However, 0.8 % ± 0.5 % of injected targeted MSNs (6 data sets) were found in tumors supporting the advantage of active targeting which will be discussed in the following paragraphs.

1.3.2.1.2 Active targeting

In order to enhance drug delivery with nanocarriers and drug efficacy, active targeting is conducted to membrane receptors predominantly expressed in tumors, in vascular structures or in the nuclear membrane. In the case of leukemic diseases, NP targeting is inevitable because the EPR effect does not apply. So, different targeting moieties can be added to the MSNs' surface such as small molecules, short peptides, aptamers, and whole antibodies or antibody fragments. Usually, the MSNs are then taken up by receptor-mediated endocytosis. An overview of the described targeting ligands is given in Figure 5.

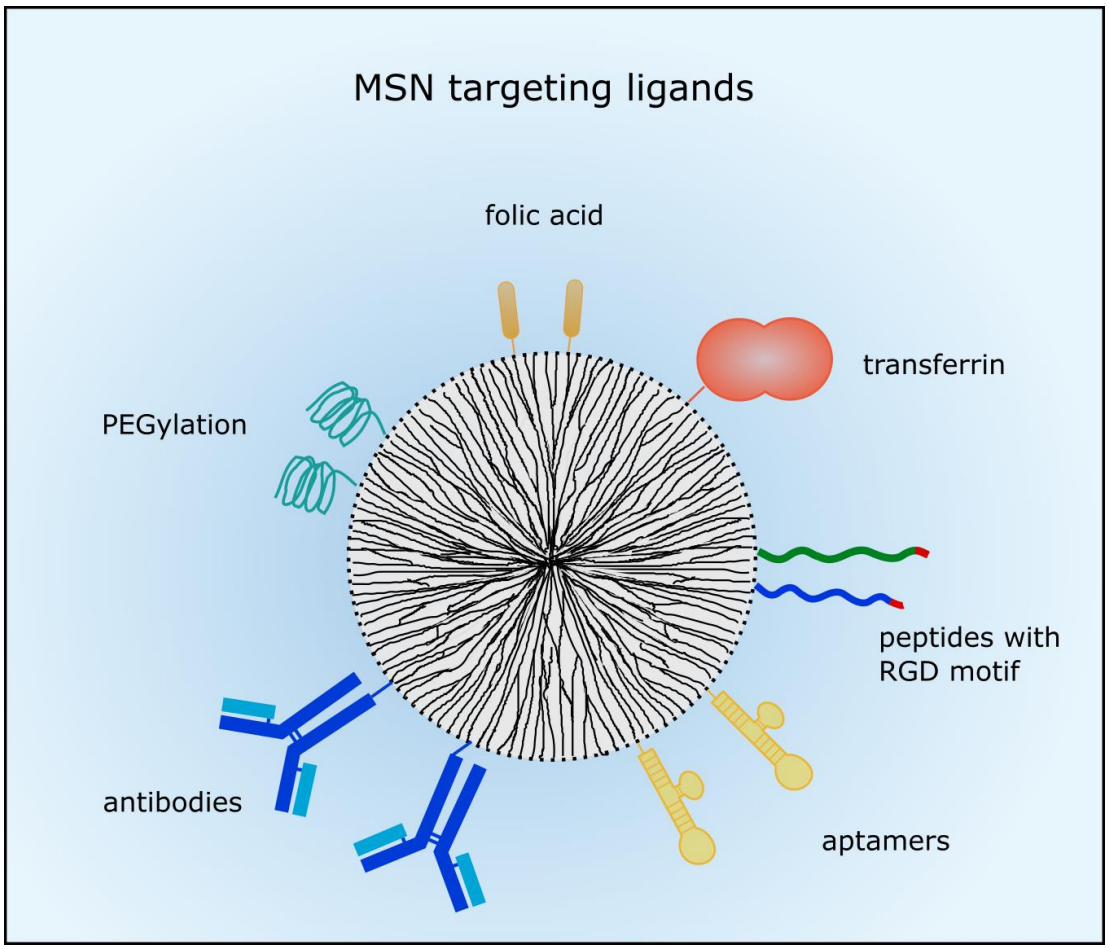

Figure 5: Ligands for active tumor targeting

MSNs can be coated with PEG to prolong the circulation time. Small molecules such as folic acid are often used for active targeting. Different peptides with the RGD motif or proteins such as transferrin were also employed for tumor targeting. Moreover, aptamers or antibodies are utilized to target membrane-receptors which are commonly overexpressed in cancer cells. Adopted from [1].

A prominently used tumor cell target is the folate receptor which is overexpressed in many tumors in comparison to healthy tissue [87]. Qi et al. targeted laryngeal carcinoma with folic acid-modified MSNs. They successfully delivered commonly used chemotherapeutic drugs (paclitaxel, cisplatin, 5-fluorouracil) and siRNA targeting ABCG2, a drug efflux pump involved in multidrug-resistance, to CD133+ positive laryngeal cancer cells *in vitro* and *in vivo* [88]. Before, the group showed a greater reduction in laryngeal tumor size in a mouse model by using cisplatin-loaded and folate-conjugated MSNs compared to untargeted MSNs [61]. Zhang and colleagues also utilized folate as targeting ligand on MSNs to improve the radio-enhancer effect of valproic acid in glioblastoma cells [89]. Moreover, PEG-conjugated folate was applied by Cheng et al. as targeting ligand on pH-sensitive polydopamine coated MSNs *in vitro* and *in vivo*. Dox delivery via folate-targeted MSNs had improved efficacy compared to

the free drug and untargeted MSNs with Dox in a xenograft tumor model. Also, distinctly higher tumor accumulation of folate-targeted MSNs in comparison to untargeted NPs was observed [90].

Using another concept, the glycoprotein transferrin was applied as targeting-ligand and redox-responsive gatekeeper by Chen et al. who could show the same toxicity of the free drug Dox and Dox in transferrin-targeted-MSNs in hepatocellular carcinoma cells [91]. Furthermore, Chen and colleagues exploited the fucose-binding lectin UEA1 for colorectal adenocarcinoma, adenoma, and polyposis coli targeting and detection. Fluorescently labeled and UEA1 carrying MSNs were successfully tested in a mouse colon cancer model as a contrast agent to visualize malignant lesions in the colon [92].

Not only proteins can be utilized for targeting but also short peptides. For instance, Sweeney and co-workers attached a bladder-cancer specific peptide named Cyc6 to Gd_2O_3-MSNs and thereby improved the detection of tumor boundaries in magnetic resonance imaging (MRI) scans in a mouse bladder cancer model [93]. The arginine-glycine-aspartic acid (RGD) motif is a prominent peptide sequence targeting integrin αvβ3 which is overexpressed in certain tumors [94,95]. Therefore, peptides including the RGD motif have been used for targeting MSNs to tumors *in vivo* by Pan et al. who showed good tumor accumulation and efficacy of Dox-loaded MSNs. Even better tumor accumulation and reduction in tumor size were found when the cell-penetrating and nuclear-targeting peptide TAT was also coupled to the MSNs besides RGD. In addition, bare MSN accumulation in the liver and spleen was distinctly greater than RGD/TAT-MSN accumulation in those organs while untargeted MSNs were found only in small concentrations in the tumor tissue [96]. A similar approach was conducted by Ashley and colleagues who used the peptide SP-94 and a nuclear localization signal (NLS) for cancer cell and nuclear targeting, respectively. The MSNs were loaded with siRNA and different chemotherapeutic drugs, and were then coated with a lipid bilayer which conveyed the targeting moieties, a fusogenic peptide for endosomal escape and PEG. Dox-loaded and targeted MSNs significantly decreased cellular viability of hepatocellular carcinoma cells in comparison to hepatocytes which were barely affected [67].

Apart from small molecules and peptides, aptamers can be used for tumor cell targeting. Aptamers are synthetic single-stranded DNA or RNA oligonucleotides that show high affinity and specificity toward different targets. They are polyanionic and larger than small peptides but smaller than antibodies [97]. An aptamer binding to epithelial cell adhesion molecule (EpCAM) was employed by Babaei and colleagues for hepatocellular carcinoma targeting *in vitro*

and *in vivo*. They encapsulated 5-Fluorouracil in MSNs with citrate-modified gold NPs as gatekeepers which were PEGylated and conjugated with the EpCAM aptamer. Targeted NPs showed a greater reduction of cellular viability than untargeted NPs. Moreover, *in vivo,* the system was tested as a theranostic device, and profoundly better tumor accumulation was observed after Rhodamine-6G-loaded MSN injection in *in vivo* imaging [98]. Another receptor for aptamer targeting is nucleolin which is expressed on cancer cells. Tang et al. developed a photoresponsive drug delivery system based on graphene oxide wrapped MSNs for light-mediated drug release and a conjugated nucleolin-targeting aptamer. However, *in vitro,* no difference between targeted and untargeted Dox-loaded MSNs on the cellular viability of breast cancer cells was recognized [99].

Finally, whole antibodies or antibody fragments are used for tumor targeting of drug delivery vehicles. For instance, antibodies already approved for cancer therapy are utilized for this purpose including cetuximab (targeting […] [epidermal growth factor (EGF)] receptor), trastuzumab (targeting HER2/neu receptor), and bevacizumab (targeting […] [vascular endothelial growth factor (VEGF)] receptor) or related antibodies with similar targets. The group of Jeffery Brinker developed a drug nanocarrier named “protocell” which consists of an MSN core for drug loading and a lipid bilayer as gatekeeper and platform for surface modifications. They availed an epidermal growth factor receptor (EGFR)-antibody for targeting leukemic cells efficiently *in vitro* and *in vivo* [100].” [1] The EGFR belongs to the family of ErbB/HER protein kinases which are transmembrane growth factor receptors consisting of a glycosylated extracellular domain for ligand binding (e.g. EGF), a single transmembrane region, and a cytoplasmic domain with kinase activity. In the case of ligand binding, the EGFR dimerizes, and autophosphorylation initiates a signaling cascade that stimulates e.g. cell proliferation and inhibits apoptosis in normal and malignant tissues. For that reason, the EGFR has been linked with cancer development and progression [101]. In about 70-90% of HNSCC, the EGFR expression is upregulated, and therefore the EGFR became a target in HNSCC therapy [102,103]. In the past years, several EGFR inhibitors were approved for cancer therapy. On the one side, several tyrosine kinase inhibitors were approved which are small molecule drugs that inhibit the cytoplasmic kinase activity of the EGFR. On the other side, biologicals were developed. The most prominent biological is Cetuximab (Erbitux®, Merck KGaA), a chimeric monoclonal IgG1 antibody that binds the extracellular domain of EGFR with high affinity and thereby inhibits the receptor function [104]. Another EGFR targeting antibody is Panitumumab (Vectibix®, Amgen) which is a fully human monoclonal IgG2a antibody. So,

EGFR targeting antibodies can execute dual functions – as targeting moiety and inhibitors – and therefore are valuable tools for drug delivery systems.

“Moreover, Zhou and colleagues conjugated Rituximab to MSNs and evaluated the drug delivery vehicle *in vitro* and *in vivo* [105]. Rituximab is a chimeric monoclonal antibody targeting the CD20 antigen on B cells and is approved amongst others for B-cell non-Hodgkin lymphoma therapy [106]. In a murine xenograft lymphoma model, a pronounced effect on tumor volume reduction was observed for Rituximab-targeted Dox-loaded MSNs, while the mice constitution remained better in comparison to mice treated with free Dox [105]. Furthermore, for tumor vasculature targeting, the anti-CD105 antibody (TRC105) has been employed by Chen et al. in a murine breast cancer model. Tumor uptake of antibody-conjugated MSNs was significantly larger compared to untargeted NPs but still, liver accumulation 24 hours after injection was witnessed [107]. The same group also used a TRC105 antibody fragment (Fab) to target dual-labeled MSNs for *in vivo* targeted positron emission tomography (PET) imaging/ near-infrared fluorescent dye (NIRF) imaging of the tumor vasculature in a mouse model [108].

In conclusion, several strategies are available for NP targeting and some have already been employed successfully in murine models. However, high accumulation in organs such as liver, spleen, lungs, and kidneys still raises a problem for application in cancer therapy and regulatory approval.

1.3.2.2 Systems for controlled drug release

A plethora of different approaches have been used to control MSN drug release and are reviewed in detail by Mekaru, Lu and Tamanoi [109]. The various gatekeeper systems are categorized by internal and external stimuli responses and an overview of the here described examples is shown in Figure 6. Internal stimuli include decreasing pH, reducing environment and enzymes. As mentioned before, NPs are often engulfed via endocytosis, so a system responding to low pH is frequently applied using different concepts. Besides, the tumor microenvironment exhibits a low pH due to hypoxia [110] and therefore, drug release can be facilitated at the target site. Examples for low pH activated capping systems include pH-sensitive nanovalves such as pseudorotaxane encircled by β-cyclodextrin (β-CD) [111], tannic acid [112], polymer and lipid coatings as applied by Popat et al. and Durfee et al., respectively [100,113]. Another pH-sensitive system consisted of a block copolymer containing positively charged artificial amino acids and oleic acid blocks, which acted simultaneously as capping and endosomal release agents [66]. Upon protonation, the pore blocking agents

were removed or degraded and the cargo could be released. Furthermore, J. Liu et al. developed a cascade pH-responsive system using the weak acidic pH of the tumor microenvironment and the acidic endolysosomal pH. First, β-CD was conjugated to hollow MSNs with a boronic-acid-catechol ester bond for sealing the pores which was degraded in the endosomes or lysosomes at pH 4.5 to 6.5. Second, PEG was grafted to adamantine via a weak pH-sensitive benzoic-imine bond which was degraded at pH 6.8 and PEGylated adamantine reacted with the sealed NPs via host-guest interactions. Therefore, PEG was released in the tumor microenvironment facilitating NP uptake and more efficient drug delivery [114]. Another dual-responsive drug carrier was developed by X. Liu and co-workers who induced drug release at high temperature and low pH. The polymer poly[(N-isopropylacrylamide)-co-(methacrylic acid)] was grafted onto MSNs to seal the pores and control the diffusion of the cargo in and out of the pore channels depending on temperature and pH [61].

MSN drug release can also be modulated by a redox-sensitive system. As intracellular glutathione concentration can be up to 10 mM, disulfide bonds linking the capping system to the MSNs are reduced upon entering the cytoplasm and cargo can be released [115]. For example, Kim et al. used β-cyclodextrin directly linked to the MSNs with a disulfide bond to seal the pores and efficient Dox toxicity in lung adenocarcinoma cells was shown [116]. Also, polymers cross-linked by cystamine were utilized to close the MSNs' pores and the polymeric network was degraded in a reducing environment [117]. Besides, Wu et al. sealed their hollow structured MSNs with poly-(β-amino-esters) via a disulfide-linker which was also reduced intracellularly [59]. Furthermore, a redox- and pH-sensitive dual response system was developed by Y. Li and colleagues who utilized ammonium salt to seal the MSNs' pores. The ammonium salt was connected via an amide and a disulfide linker to the MSNs. Hence, the disulfide bond was reduced glutathione-dependently and the amide bond was degraded at low pH upon cellular uptake [118].

Using a biomolecule activated system, Mondragón et al. encapsulated camptothecin in MSNs with a protease cleavable ε-poly-ı-lysine, and in human cervix epithelial carcinoma cells viability was reduced after camptothecin-loaded NP incubation [119]. The same group also [utilized] […] several hydrolyzed starch products as saccharides for enzyme-responsive drug release [120].

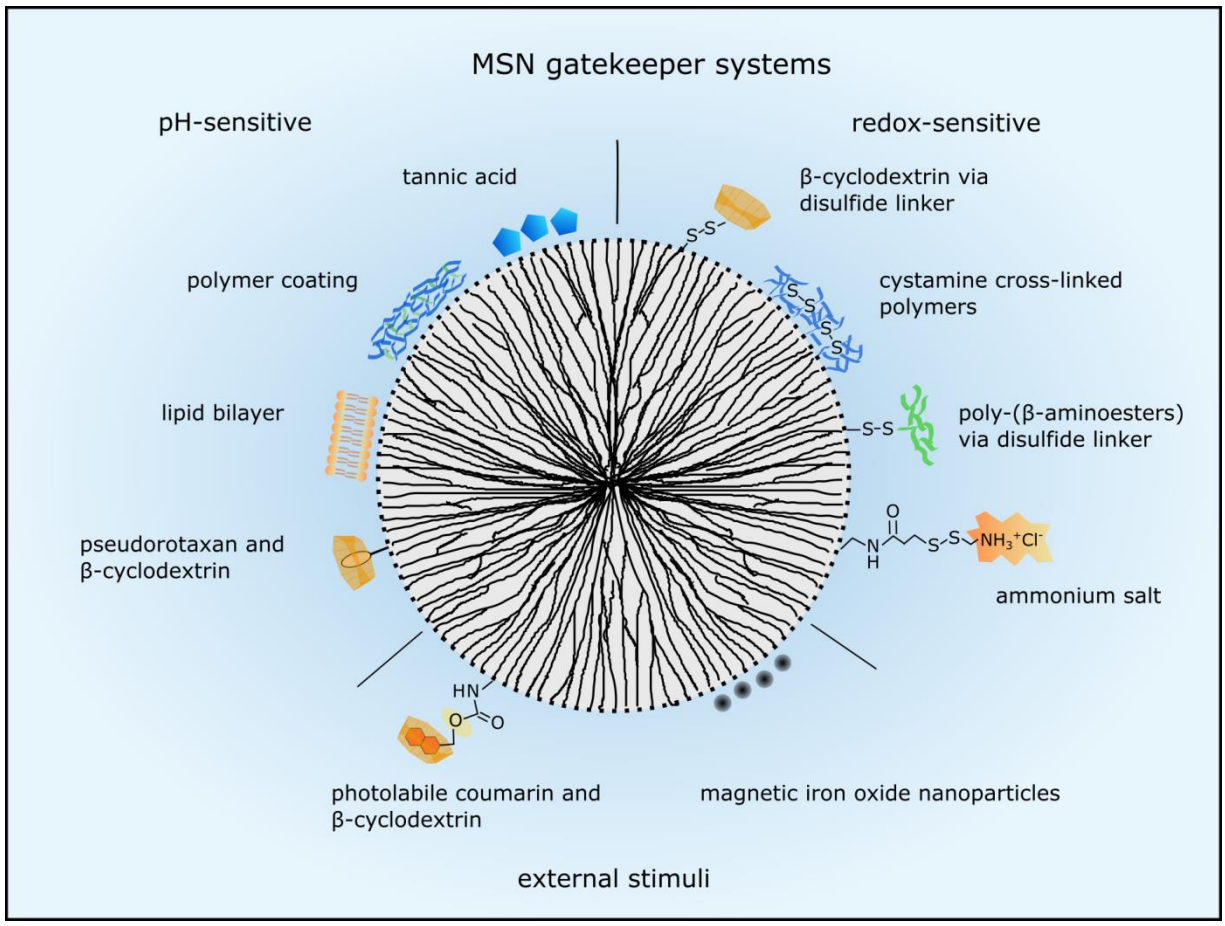

Figure 6: Mesoporous silica nanoparticle gatekeeper systems to control drug release
Drug release can be regulated by internal stimuli such as pH decrease or reduction by glutathione or by external stimuli. PH-sensitive systems respond to acidic pH in the tumor microenvironment and in the endolysosomal system. Several examples are presented here such as pseudorotaxan encircled by β-cyclodextrin, tannic acid, polymer and lipid coatings. Several capping structures are linked to the MSNs via disulfide bonds which are reduced by glutathione intracellularly. Then the pore blocking agents such as β-cyclodextrin, cystamine, poly-(β-aminoesters) and ammonium salt are released, and the drugs can escape the NP. External stimuli such as light and magnetism are utilized to control drug release, too. Photolabile coumarin encircled by β-cyclodextrin is cleaved from the MSNs by light or a magnetic field stimulates iron oxide NPs to release the encapsulated drugs. Adopted from [1].

Apart from internal stimuli also external stimuli such as light or magnetic fields are utilized to control gatekeepers. These systems can generate more precise and local drug release, hence reducing toxicity towards normal cells. With regard to light-activated drug release, the best wavelengths for adequate tissue penetration are within the biological spectra, typically 800-1100 nm [109]. In an *in vitro* model, Guardado-Alvarez et al. used two-photon excitation at 800 nm to cleave the NPs' cap which consisted of photolabile coumarin-molecules bound to the NP surface and non-covalently conjugated β-cyclodextrin molecules [121]. Moreover,

Croissant and colleagues also used two-photon light to control drug release via a photo-transducer from mesoporous silica nanoimpellers in human cancer cells [122]. However, tissue penetration of light is still limited, so using a magnetic field for external stimulated cargo release is more advantageous even though a magnetic component is necessary. Therefore, a magnetic iron oxide core is coated with mesoporous silica or MSNs are capped with iron oxide NPs [123,124]. The iron oxide core has superparamagnetic properties and can be heated up by an oscillating magnetic field which in turn can be used to open a nanovalve and for example release Dox [124]. Several superparamagnetic iron oxide NPs (SPION) are already FDA-approved imaging agents (Endorem®/ umirem®) and iron oxide NPs (Nanotherm®) are also approved in the European Union for glioblastoma therapy [45].” [1]

In this work, a combination of a pH-sensitive and redox-sensitive gatekeeper system for pore sealing was developed and applied. The amino-functionalized MSNs were conjugated to ferrocenecarboxaldehyde (ferrocene) via a pH-labile imine bond at pH 7.6 and methyl-β-cyclodextrin (β-CD) or amino-functionalized β-cyclodextrin (NH_2-β-CD) was added to encircle the ferrocene stalk and seal the pore as illustrated in Figure 7. The cyclic oligosaccharide β-CD consists of seven glucopyranosyl units linked by α-(1,4) bonds and has a hydrophobic center that can interact with other hydrophobic molecules, and β-CD can also increase the solubility of hydrophobic drugs in aqueous solutions [125]. The β-CD has a cylindrical shape: The dimensions are 0.79 ± 0.01 nm from top to bottom, 0.60- 0.65 nm internal diameter, and 1.54 ± 0.04 nm external diameter, respectively [126]. So, the organic moiety of ferrocene interacts with β-CD by hydrophobic-hydrophobic interaction and several ferrocene/ β-CD moieties seal one pore. Upon cellular entry of the MSNs, the iron can be oxidized ($Fe^{2+} \rightarrow Fe^{3+}$) by intracellular oxidizing agent e.g. reactive oxygen species (ROS), so the hydrophobic (NH_2)-β-CD interaction is diminished and (NH_2)-β-CD leaves the ferrocene stalk [127]. Furthermore, upon protonation, the imine bond is cleaved in an acidic environment ($pH \leq 5.2$) and thereby the pore is opened and the cargo can be released [128].

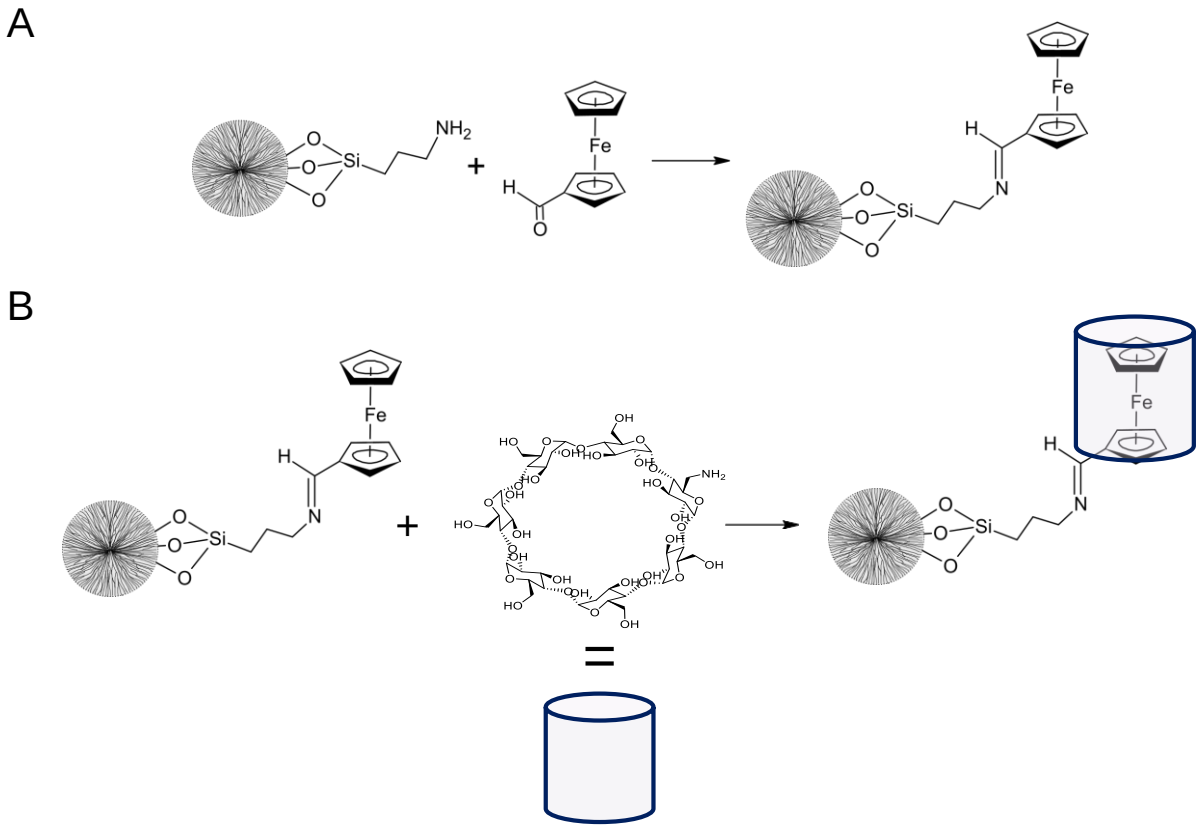

Figure 7: Mesoporous silica nanoparticle conjugation with the gatekeeper system applied in this project

(A) Ferrocenecarboxaldehyde is conjugated to the amino-functionalized MSNs by an imine bond. The imine bond is labile in an acidic environment. (B) The hydrophobic core of NH_2-β-CD interacts hydrophobically with the organic moieties of the ferrocene and thereby the pores are sealed. The NH_2-β-CD can be further modified at the amino group e.g. the addition of a linker is possible to conjugate a targeting antibody.

1.3.2.3 Endosomal escape of MSNs and their cargo

“Once MSNs entered the cancer cells by endocytosis, an endosomal escape of the NPs or the delivered drug is mandatory for efficacy. The endosomal pH ranges from 6.0-6.5, but along the endocytic pathway acidity increases and late endosomes and lysosomes exhibit a pH from 4.5 to 5.5 [74]. Thus, the MSNs’ cargo could be degraded or inactivated by lysosomal enzymes. To avoid this, several concepts are applied to enable drug release in the cell, based on different theories (Figure 8). For example, endosomal escape can be achieved by the so-called ‘proton sponge effect’, which relies on an increase of proton concentration during hydrolysis. This leads to an increase in membrane potential and an influx of counter-ions resulting in osmotic swelling and bursting of the endosome [129]. Hence, the cargo is released to the cytosol and can take full effect. For instance, the MSN system utilized by Wu et al. released siRNA and Dox into the cytoplasm after the coating with poly-(β-aminoesters)

induced endosome bursting [59]. In the same way, cationic polyethyleneimine (PEI) coating can trigger the proton sponge effect which was applied by Finlay and colleagues to deliver TWIST1 siRNA to xenograft tumors and reduce tumor burden [130].

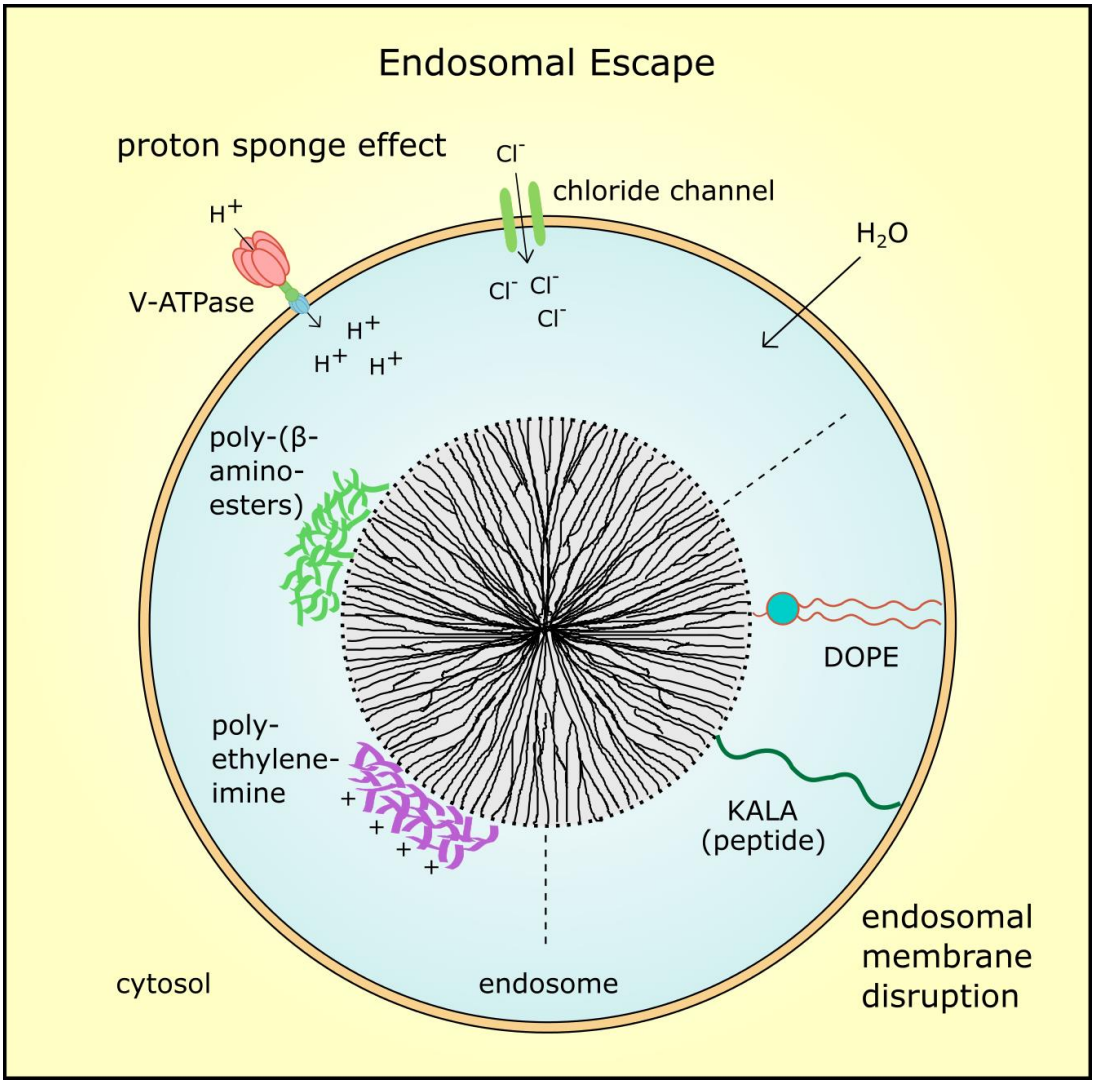

Figure 8: Endosomal escape mechanisms

After MSNs were taken up by endocytosis, an endosomal escape is mandatory for drug efficacy. Coating with cationic polymers such as polyethyleneimine or poly-(β-aminoesters) induces the proton sponge effect. The proton concentration increases during hydrolysis which leads to an increase in membrane potential and influx of counter-ions such as chloride ions. Finally, osmotic swelling by water inflow bursts the endosome, and the MSNs with its cargo are delivered into the cytosol. Also, fusogenic peptides such as KALA or zwitterionic co-lipids such as dioleoyl-phosphatidylethanolamine (DOPE) can destabilize the endosomal membrane resulting in MSN release. Adopted from [1].

Other methods use fusion lipids, cationic polymers or peptides to destabilize the endosomal membrane by proton absorption and acidification [131]. One example is the zwitterionic co-

lipid dioleoylphosphatidylethanolamine (DOPE) which was also utilized in combination with a polymer to coat MSNs and improve drug release [132,133]. Moreover, Ashely et al. employed a fusogenic peptide to enhance the endosomal escape of protocells in hepatocellular carcinoma [67]. Fusogenic peptides referred to as KALA were conjugated to PEI-coated MSNs by X. Li and colleagues and were used to deliver VEGF targeting siRNA in a xenograft tumor model. The siRNA-loaded MSNs with KALA peptides inhibited tumor proliferation significantly compared to control particles without siRNA or control siRNA, respectively [134]. However, many so far developed MSN systems relied on the proton sponge effect for endosomal escape. Aside from endocytosis, other mechanisms for NP uptake are possible, thus endosomal escape is not always necessary for drug efficacy.

Overall, surface modifications play an important role for efficient drug transport via MSNs, MSN targeting, and drug release. However, the ‘perfect’ system does not exist and is unlikely to be invented due to the heterogeneity of cancer.

1.3.3 Biocompatibility of MSNs

A major advantage of MSNs is their high biocompatibility *in vivo*. Several studies examined biodistribution, toxicity, and excretion of MSNs. The FDA classified silica as ‘Generally Recognized as Safe’ and silica is used as a food additive and in cosmetics [53]. In general, silica particles are degraded into water-soluble orthosilicic acid ($Si(OH)_4$) which is also absorbed by humans to form silica as a trace element [135]. Many *in vitro* studies showed no toxicity for up to 100 µg mL^{-1} MSNs in cell culture [90,100,105,135]. Sometimes even higher concentrations were tested without significant toxicity [91,136]. It is generally recognized that crystalline [SiO_2-NPs] can cause reactive oxygen species (ROS) formation which compromises cellular viability [137]. Yet, MSNs seem to induce ROS formation only in high concentrations. For example, MSN concentrations of 1 mg mL^{-1} and higher exhibited ROS in colon carcinoma cells while 200 µg mL^{-1} did not induce ROS [138]. Furthermore, a relatively small MSN concentration did not promote ROS formation in hepatocellular carcinoma cells [139]. Elle and colleagues covalently coated MSNs with antioxidants to reduce ROS formation and rutin decreased ROS formation dose-dependently in a keratinocyte cell line and dose-independently in colon carcinoma cells [62]. However, ROS formation after MSN application has been rarely examined due to the overall good biocompatibility.

One of the first *in vivo* studies was conducted by Park and colleagues who examined biodistribution of silica for four weeks. A relatively low dose of 20 mg kg^{-1} MSNs (126 nm diameter)

was administered intravenously into mice and the bodyweight increased in the same manner as in the control group. The NPs predominantly accumulated in [mononuclear phagocytic system] (MPS)-related organs such as the liver and spleen. Yet, after one week, MSNs were mostly cleared from the analyzed organs (liver, spleen, heart, kidney, brain, and lung) and almost completely vanished after four weeks. Moreover, the histopathological analysis indicated no significant toxicity compared to controls, even though apparently macrophages in the liver (Kupffer cells) were swollen one day after MSN injection. The authors assumed that MSNs were degraded and then excreted via the kidneys [135]. Furthermore, Q. He and coworkers thoroughly studied NP excretion and biodistribution *in vivo*. On that account, MSNs and PEGylated MSNs of several sizes (80 nm, 120 nm, 200 nm, and 360 nm) were analyzed. Fluorescently labeled MSNs were evaluated in different organs with fluorescence intensity measurements of homogenized samples at several time points after injection of 20 mg kg^{-1} NPs. Most NPs accumulated in the spleen and liver, 30 minutes after injection also in the lungs, and low accumulation was detected in the heart and kidneys. PEGylation reduced the accumulation of larger particles in the lung and overall in the spleen 30 minutes after injection. However, after one month, smaller particles were only observed in the liver and spleen in low concentrations while 200 nm particles were also detected in even lower concentrations in the heart, lung, and kidneys. Regarding 360 nm MSNs, the lowest concentrations were found after one month, whereas PEGylated MSNs were still visible in all examined organs. Besides, the NP concentration of larger particles in the liver and spleen decreased over time. Blood clearance of MSNs was slower for PEGylated particles, and after eight hours, particles were barely detectable, yet the smallest MSNs had the longest blood circulation time. With regard to excretion, MSNs and PEGylated MSNs were mainly already excreted after 30 minutes and smaller particles mostly within five days. However, after one month, larger particles were still detectable in urine. Histopathological evaluation showed no significant tissue toxicity and [no] inflammation one month after injection for all particle sizes compared to controls [140]. In a study conducted by the group of F. Tamanoi biodistribution, biocompatibility, and drug-delivery efficiency of MSNs were analyzed in a xenograft tumor model. First, they determined a maximally tolerated dose of 50 mg kg^{-1} spherical MSNs (100- 130 nm) after intravenous injection and monitoring for ten days. Then, MSNs were administered intraperitoneally with the same concentration in 18 doses over two months for long-term toxicity profiling. No unusual responses or behaviors compared to controls were observed and all measured hematologic factors were within normal ranges, proposing that the treatment did not induce an inflammatory response. However, all experiments were conducted in nude mice which lacked a thymus and therefore a possible T-cell response. Good biocompatibility could

also be […] [because] more than 90 % of the administered silicon concentration was excreted via feces and urine within four days. Moreover, in a xenograft breast cancer tumor model MSNs were mainly found in tumor, lung, and kidneys 24 hours after tail-vein injection, while 48 hours after injection the spleen exhibited increased silicon concentration. Targeting with folic acid increased the tumor accumulation of NPs. Furthermore, camptothecin-loaded MSNs reduced tumor size faster and greater after in total 18 intraperitoneal injections over nine weeks. Also, hematology profiling suggested reduced toxicity of camptothecin-loaded MSNs compared to the free drug [82]. In a more recent study, J. Liu et al. evaluated 120 nm hollow MSNs with a pH-dependent gatekeeper system in a xenograft hepatocellular carcinoma model. The untargeted but PEGylated MSNs were loaded with Dox and inhibited tumor proliferation over a time period of 21 days. At the same time, the mice's weight increased while mice treated with the free drug lost weight. The same tendency was observed in survival analysis where mice treated with free Dox all died shortly after the treatment stopped. However, half of the mice treated with PEGylated MSNs survived more than one month after the last injection until the end of the experiment. In a biodistribution study after a single injection, most of the particles accumulated in liver, spleen, and lung whereas PEGylated MSNs exhibited less accumulation. During the first week after injection, naked particle concentrations increased in the liver and spleen while PEGylated MSNs also increased in lung tissue. Only low concentrations of nanocarriers were detected in heart and kidney tissues. Yet after one month, MSN concentrations were decreased as expected [114]. Zhou and colleagues utilized a relatively high concentration of 100 mg kg^{-1} Rituximab-conjugated MSNs for toxicity and distribution analysis *in vivo*. After seven MSN doses during three weeks, the bodyweight increased correspondingly to control mice and histological analysis indicated no significant pathological lesions or damages in the major organs. Still, experiments were conducted in immunodeficient nude mice and therefore a lack of pathological damages is not surprising [105].

In brief, MSNs exhibited remarkable good biocompatibility in many *in vivo* studies so far while tested particle concentrations increased over time. Still, the accumulation of NPs in MPS-related organs presents a challenge but this seemed to have no major impact on the animals' constitution and inflammatory responses remained mild. However, most studies were performed in immunodeficient mice decreasing the chances for a severe immune response. So, more studies in rodents with an intact immune system are necessary to fully evaluate the toxic profile of MSNs before clinical trials. Nevertheless, the first early phase I clinical trial involving targeted SiO_2-NPs for image-guided operative sentinel lymph node mapping is realized

[52]. In conclusion, MSNs are promising drug delivery vehicles for cancer therapy from a biocompatibility perspective.” [1]

1.4 The chemotherapeutic drug doxorubicin

The antibiotic doxorubicin (Dox) is one commonly used chemotherapeutic drug for the treatment of various metastatic solid tumors often in combination with other cytostatic drugs. Dox is an anthracycline, a 14-hydroxylated form of daunorubicin, and intercalates with the DNA. Thereby the DNA is irreversibly damaged, and topoisomerase IIb (TopoIIb) is inhibited. Normally, the enzyme TopoIIb prepares the DNA for transcription by unwinding supercoils in the DNA. Therefore, DNA and RNA synthesis are inhibited, DNA repair mechanisms are induced, and apoptotic and necrotic cell deaths occur [141,142]. Moreover, Dox also increases ceramide levels which can lead to growth arrest, apoptosis, or senescence, respectively. Dox can be oxidized to a semiquinone radical by NAD(P)H-oxidoreductases. The semiquinone radicals react with oxygen thus, ROS are formed and cause DNA damage, but also induce cardiotoxicity [142]. For that reason, the therapeutic application of Dox is limited, and targeted therapy is favorable. For example, a PEGylated liposomal formulation of Dox (Doxil®) enhances blood circulation time, tumor accumulation, reduces adverse effects, and has an increased efficacy compared to Dox [46,143]. Moreover, Dox is frequently used as a model drug to evaluate drug delivery systems because the toxicity of Dox can be exploited in cell culture experiments to study drug release. Also, Dox is soluble in water, has a red color, and exhibits fluorescence. The fluorescence (λ_{ex}= 480 nm, λ_{em}= 560-590 nm) enables the quantification of small Dox concentration and quantification of the loading efficiency. The red color gives a visual proof if drug loading was successful and the fluorescence can be exploited *in vitro* with different techniques such as flow cytometry and confocal laser scanning microscopy (CLSM). Moreover, effective doses of Dox usually are below 0.5 µM dependent on the used cell line [142]. So, results can be obtained dose-dependently in short time e.g. by measuring the metabolic activity of cells or determining the number of dead cells by DNA staining with subsequent flow cytometry analysis. The DNA damage repair upon Dox treatment can already be detected after two hours incubation with staining of γH2AX foci (own observation). Because of these characteristics, Dox is often exploited as a model drug for new drug delivery systems.

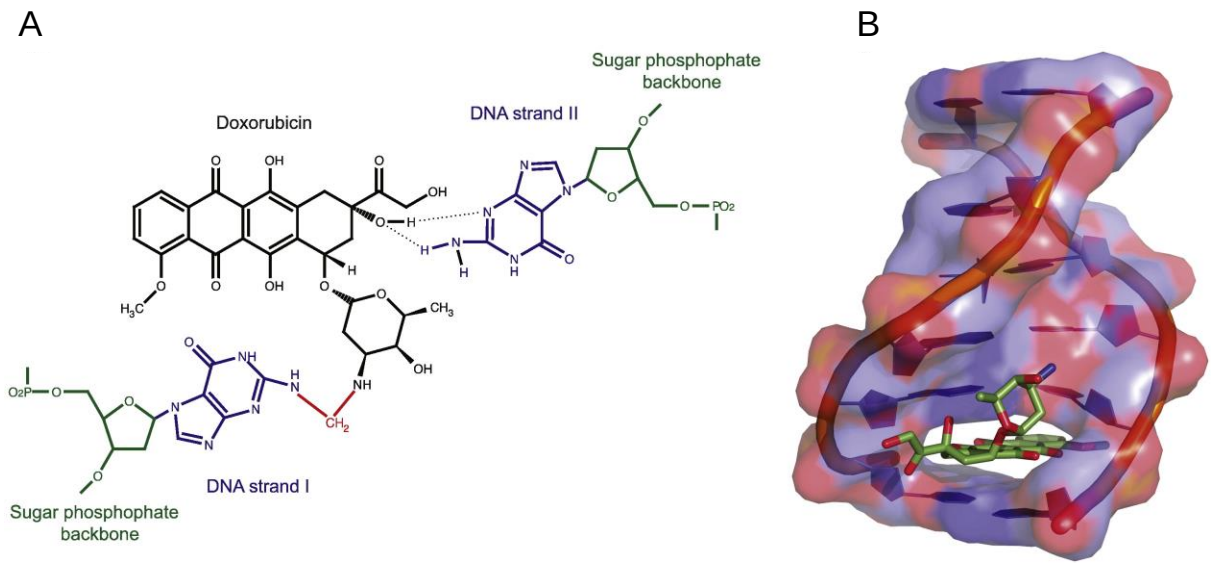

Figure 9: Doxorubicin intercalates with the DNA

(A) Mediated by formaldehyde a covalent bond between Dox with guanine is formed (shown in red). Also, hydrogen bonds occur with the guanine on the opposing DNA strand [144]. (B) When Dox intercalates with the DNA, Dox parts the flanking base pairs with the sugar moiety sitting in the minor groove. Adopted from [142] with permission under CC BY NC SA license.

1.4.1 γH2AX as marker for DNA damage

After DNA damage by e.g. Dox, several mechanisms in the cell are induced to repair the DNA damage or, in case of severe DNA damage, induce apoptosis. Normally, the DNA is wrapped around histone complexes and forms nucleosomes to pack the whole DNA in the nucleus. The histone complex consists of two copies each of histone proteins H2A, H2B, H3 and H4 [145]. Besides forming nucleosomes, these histone variants have specialized biological functions, e.g. the histone H2A variant H2AX plays a role in maintaining genomic stability [146]. Upon DNA damage, a highly conserved serine residue located 4 amino acids from the COOH terminus (Ser139) is rapidly phosphorylated [147]. This phosphorylation of H2AX is mediated by a rapid kinase-based signaling pathway upon DNA double-strand breaks. The main mediators in this pathway are the Phosphatidylinositol-3 kinase-like family of kinases (PIKK) and among these ataxia telangiectasia mutated (ATM), ATM- and Rad3-related (ATR), ATM-related kinase (ATX) and DNA dependent protein kinase (DNA-PK) were identified as signal transducer after DNA damage to generate phosphorylated H2AX (γH2AX) foci [148]. Next, γH2AX foci recruit repair/ signaling proteins to the DNA damage site. The γH2AX foci can be detected by immunofluorescence staining and are utilized to evaluate DNA damage *in vitro*.

1.5 The chorioallantoic membrane model as *in vivo* model

Chicken embryos and especially the chorioallantoic membrane (CAM) are exploited as *in vivo* models to examine angiogenesis, tumor growth and metastasis, wound healing, tissue grafts, drug delivery and toxicology [149]. In comparison to other *in vivo* models (rodents, guinea pigs, hamster, sheep, etc.), cultivation of chick embryos is simple and cheap, and importantly, no approval by an ethics committee is necessary as long as experiments are terminated before incubation day 14 (until then no experience of pain [150]) or before hatching. The exact incubation times are dependent on the local regulations. The embryonic development lasts 21 days after the start of incubation at 37.5 °C. After incubation for about three and a half days, the allantois of the chicken embryo appears as an evagination from the ventral wall of the endodermal hindgut. The allantois pushes out of the embryonic body into the extraembryonic coelom and its proximal part (allantoic stalk) lies in parallel and caudal to the yolk sac while the distal portion enlarges when it grows clear of the embryo (allantoic vesicle). The allantoic vesicle rapidly grows from days 4-10 of incubation, and meanwhile the mesodermal layer of the allantois and the chorion fuse to form the CAM. In between the chorionic epithelium, a large blood capillary network is established which is connected to the embryonic circulation. The surface of the vascular network increases tremendously within eight days to fulfill its respiratory function by exchanging oxygen and carbon dioxide. Also, the CAM acts as a reservoir for waste products such as urea and urea acid and mobilizes calcium from the shell for bone mineralization. In general, the CAM model offers an immunodeficient environment, however, a nonspecific inflammatory reaction can occur after 15 days incubation. Another limitation is the low number of analytic tools that are compatible with chicken embryonic tissue such as antibodies, cytokines, and primers.

As mentioned above, the CAM model allows a toxicological evaluation of new drugs or drug delivery systems such as MSNs. Tumors can be grown on the CAM to study tumor vascularization and metastasis. Moreover, the biodistribution of fluorescently labeled NPs or other reagents can be analyzed by fluorescence microscopy. So, the CAM is a valued *in vivo* model.

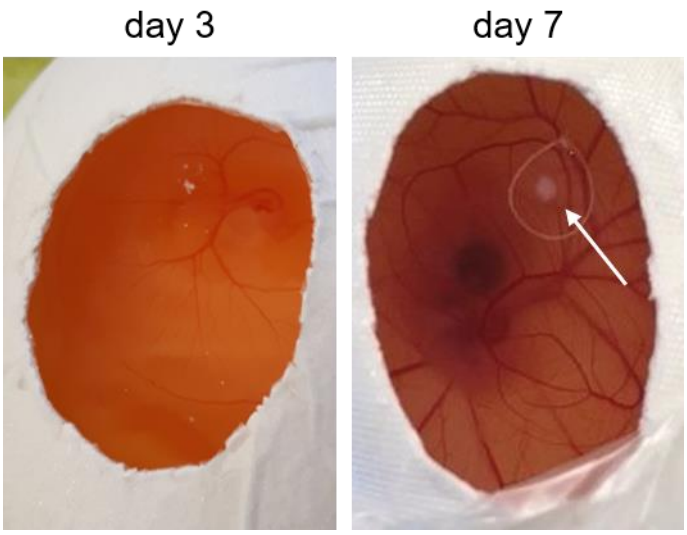

Figure 10: The chorioallantoic membrane on incubation days 3 and 7

Only a few blood vessels exist after opening the fertilized egg on day 3. The vascular network already extended greatly until day 7 when a tumor was placed on the CAM (marked with an arrow) and a thin thread circled the tumor area. The embryo can be seen in the middle.

2 Aims of study

In this work, MSNs were evaluated as drug delivery vehicles to improve HNSCC therapy. For this reason, the MSNs were examined step by step *in vitro* and *in vivo.* First, the MSNs were characterized, and NPs with different sizes and pore sizes were investigated. Second, the MSNs were sealed by a gatekeeper system, and the biocompatibility *in vitro* and *in vivo*, the cellular uptake *in vitro,* and the *in vivo* biodistribution were examined. Third, the drug loading and release were studied with the model drug Dox *in vitro*. Fourth, siRNA loading and release were tested and optimized *in vitro*. Fifth, an EGFR-targeting antibody was conjugated to the MSNs for active targeting, and the influence on cellular uptake was evaluated *in vitro*. Finally, EGFR-targeted and siRNA-carrying MSNs were analyzed *in vitro*.

3 Materials and Methods

3.1 Materials

All used devices, consumables, reagents, kits and software are listed below.

3.1.1 Devices

Table 1: Devices

Device	Manufacturer
Autoklav tuttnauer Systec 5050 ELV	Tuttauer, Breda (Netherlands)
Bank top centrifuge: Fisherbrand Mini-Centrifuge	 Fisher Scientific GmbH, Schwerte
Biofreezer: HERAfreeze™	Kendro Laboratory Products, Hanau
Biometra® Minigel-Twin	Biometra GmbH, Göttingen
Biometra® Standard Power Pack P 25	Biometra GmbH, Göttingen
Biometra® Tpersonal 48 Thermocycler	Biometra GmbH, Göttingen
BLAUBRAND®-counting chamber (Neubauer)	BRAND GmbH + Co KG, Wertheim
Blotter: Trans-Blot® Turbo™ Transfer System	 Bio-Rad Laboratories GmbH, Munich
Centrifuges: Biofuge fresco Multifuge 1L-R Universal 16 R	 Heraeus, Kendro Laboratory Products, Hanau Heraeus, Kendro Laboratory Products, Hanau Hettich Zentrifugen, Tuttlingen
CoolCell® Cell Freezing Container	CryoShop, Munich
Confocal Laser Scanning Microscope: TCS SP-8	 Leica Microsystems, Wetzlar
Darkreader™ 195 M Transilluminator	Clare Chemical Research, Inc., Dolores, CO (USA)
Dishwasher: Spülmaschine Professional G7883CD	 Miele, Gütersloh
Drying oven: Heraeus Function line	Kendro Laboratory Products GmbH, Langenselbold
Flow cytometer: LSR II	 BD Bioscience, Heidelberg
Fluorescence microscope: Eclipse TE2000-U	 Nikon GmbH, Düsseldorf
Fluoroskan Ascent™ Mircoplate Fluorometer	Thermo Fisher Scientific GmbH, Waltham, MA (USA)
Freezers: Liebherr GP 1466 Premium Bosch Economic computer control	 Liebherr Holding GmbH, Biberach Robert Bosch Hausgeräte GmbH, Munich
Fridges: Bosch cooler Liebherr Profi Line	 Robert Bosch Hausgeräte GmbH, Munich Liebherr Holding GmbH, Biberach
ChemiDoc™ MP Imaging System	Bio-Rad Laboratories GmbH, Munich

Gel chamber (PAGE): Minigel-Twin G42	 Biometra GmbH, Göttingen
HIDEX Sense beta plus	HIDEX, Turku (Finland)
Incubators: Cell culture: Heracell 150i CO_2 Incubators Fertilized chicken eggs: Brutmaschine Typ 3000 Digital	 Thermo Fisher Scientific, Waltham, MA (USA) Brutmaschinen-Janeschitz GmbH, Hammelburg
Light microscope: invers TMS (5x/10x/20x/40x) Leitz 307-148.002	 Nikon GmbH, Düsseldorf Leitz Messtechnik GmbH, Wetzlar
Liquid nitrogen tank CRYO-400	Chart Ind., Burnsville (USA)
Luminoskan Ascent	Thermo Fisher Scientific, Waltham, MA (USA)
Magnetic stirrer: IKA MAG® REO	 IKA® -Werke GmbH & CO. KG, Staufen
Multipette® plus	Eppendorf AG, Hamburg
Multichannel pipette: Finnpipette® 50-300µL	 Thermo Fisher Scientific, Waltham, MA (USA)
Multiskan Ascent Microplate Reader	Thermo Fisher Scientific, Waltham, MA (USA)
Nano Drop 2000 Spectrophotometer	Thermo Fisher Scientific, Waltham, MA (USA)
pH-Meter: Hydrus 300	 Fisher Scientific UK Ltd, Loughborough (England)
Pipetts: 1000 µL, 100 µL, 10 µL, 2.5 µL Transferpette® S: 1000 µL, 200 µL, 20 µL	 Eppendorf AG, Hamburg BRAND GmbH + Co KG, Wertheim
Pipettus® Pipetboy	Hirschmann Laborgeräte, Eberstadt Integra Biosciences GmbH, Biebertal
Rotary Microtome Leica RM2165	Leica Biosystems
Safety cabinet: Herasafe Safety cabinets	 Heraeus, Kendro Laboratory Products, Hanau
Scales: Kern Waage ABT 120-5DM Kern PCB 8000-1 prescision scale Kern PCB 250-3	 Kern & Sohn GmbH, Balingen-Frommern
Scotsman® AF80 Ice Flaker	Hubbard Systems, Ipswich (UK)
Shaker: Rocky® 3D Tilt Shaker WS10	 Edmund Bühler GmbH, Bodelshausen
Smartphone Camera: Samsung Galaxy A3 2016	Samsung Electronics, Seoul (South Korea)
Ultrasonic homogenizer: Sonoplus mini20/HD 2070	 BANDELIN electronic GmbH & Co. KG, Berlin
Ultrasonic bath: EMAG Ultraschallreiniger Emmi-40 HC	 EMAG AG, Moerfelden-Walldorf
StepOnePlus™ Real-Time PCR System	Life Technologies GmbH, Darmstadt
Thermomixer comfort	Eppendorf AG, Hamburg
Tissue embedding center Leica EG1140H	Leica Biosystems, Nussloch
Vortex: Top-Mix 11118 Fisherbrand®	 Fisher Scientific GmbH, Schwerte

VV3 Vortex Mixer CLASSIC	VWR International, Radnor (USA) VELP® Scientifica, Usmate (Italy)
Water bath (shaking): GFL® 1083	 GFL Gesellschaft für Labortechnik mbH, Burgwedel

3.1.2 Consumables

Table 2: Consumables

Consumable	Manufacturer
5 mL Polystyrene round-bottom tube FALCON®	Corning Inc., Corning, NY (USA)
µ-slide 8 well, IbiTreat	ibidi GmbH, Munich
Advanced TC Dish, sterile, 60 x 15 mm	Greiner Bio-One GmbH, Frickenhausen
BD Falcon™ cell scraper	BD Bioscience, Bedford (England)
Blotting Paper MN440B	Macherey-Nagel GmbH & Co. KG, Düren
Cell culture flasks, PS, red filter screw cap, clear, CELLSTAR® TC 50 mL, 25 cm^2 250 mL, 75 cm^2 550 mL, 175 cm^2	Greiner Bio-One GmbH, Frickenhausen
Cell culture plates: cell culture microplate, 96-well, PS, F-bottom, µClear®, black/ clear, CELLSTAR® cell culture multiwell plate, 12 well, PS, clear CELLSTAR® Nunc™ Multidish 6 Nuclon™ Delta SI	 Greiner Bio-One GmbH, Frickenhausen Thermo Fisher Scientific, Waltham, MA (USA)
Centrifuge tubes: Safe-lock tubes: 0.5 mL, 1.5 mL, 2.0 mL Falcon CELLSTAR® 15 mL, 50 mL	 Eppendorf AG, Hamburg Greiner Bio-One GmbH, Frickenhausen
Cover glass #1 9 mm x 9 mm	Electron Microscopy Sciences, Hatfield, PA (USA)
Cryotube Cryo. S™	Greiner Bio-One GmbH, Frickenhausen
Disposable weighing dishes	neoLab Migge Laborbedarf-Vertriebs GmbH, Heidelberg
Gloves: Sempercare® premium Sempercare® nitrile skin[2] ABENA classic, Nitrile, powder-free	 Semperit Technische Produkte Gesellschaft mbH., Wien (Austria) Abena GmbH, Aabenraa (Denmark)
Immobilon®-P Transfer Membranes, Pore size 0.45 µm	Merck-Millipore Ltd., Tullagreen (Ireland)
Leukofix®, 2.5 cm x 9.8 m (micropore bandage)	BSNmedical GmbH, Hamburg
Microplate 96 well, PS, U-Bottom, clear	Greiner Bio-One GmbH, Frickenhausen
MicroAmp™ Optical Adhesive Film	Life Technologies, Carlsbad, CA (USA)
Needles: BD Microlance™ 3 Nr. 2, 0.8 x 40 mm, 21 G x 1 ½”	 BD Bioscience, Bedford (England)

Disposable hypodermic needle, 0.45 x 25 mm, 26 G x 1” Gr.18	B.Braun, Melsungen
Parafilm „M“™ Laboratory Film	Pechiney, Chicago (USA)
PCR-Plates: Micro-Amp® Fast Optical 96-Well Reaction Plate	 Life Technologies, Carlsbad, CA (USA)
Petri dishes: CELLSTAR® Cell Culture Dishes (94 mm), Cellview cell culture dish, PS, 35/10 mm, vents, Advanced TC	Greiner Bio-One GmbH, Frickenhausen
Pipettes: CELLSTAR® 2 mL, 5 mL, 10 mL, 25 mL	 Greiner Bio-One GmbH, Frickenhausen
Pipette tips: 10 µL, 20 µL, 200 µL, 1000 µL Finntip® 5- 300 µL MµltiFlex Round Tips 1- 200 µL	 Kisker Biotech GmbH & Co. KG, Steinfurt Thermo Fisher Scientific, Waltham, MA (USA) Sorenson™ BioScience, Inc., Salt Lake City, UT (USA)
Pipette tips with filter: 10 µL/ super slim ART® 100 E Molecular Bio Products 100 µL barrier TipOne 101-1000 µL filter tips	 Nerbe plus GmbH, Winsen (Luhe) Fisher Scientific GmbH, Schwerte Starlab, Ahrensburg
Pipette tips for Multipette®: Combitips advanced 0.5 mL, 5 mL	 Eppendorf AG, Hamburg
Quali-PCR-Tube-Strips 0.2 mL	Kisker Biotech GmbH & Co. KG, Steinfurt
Sterile filter Millex (0.22 µm)	Millipore Corporation, Billerica, MA (USA)
Syringe: BD Discardit™ II Syringe 5 mL, 10 mL	 BD Bioscience, Bedford (England)
Thermo Scientific PageRuler Prestained Protein Ladder	Thermo Scientific, Rockford, IL (USA)
Western Lightning® Plus ECL	PerkinElmer, Waltham, MA (USA)
White tissue embedding cassettes	Kartell Labware, Noviglio (Italy)
Zeba™ Spin Desalting Columns, 7K MWCO, 0.5 mL	Thermo Scientific, Rockford, IL (USA)

3.1.3 Reagents and solutions

Table 3: Reagents for experiments

Reagent	Manufacturer
0.9 % Sodium chloride	Fresenius Kabi, Bad Homburg
3A-Amino-3A-deoxy-(2AS,3AS)-β-cyclodextrin	TCI Deutschland GmbH, Eschborn
Bovine serum albumin Fraction V (BSA)	PanReac AppliChem, Darmstadt
BupH™ Phosphate Buffered Saline Packs	Thermo Fisher Scientific, Waltham, MA (USA)
cOmplete™ Protease inhibitor Cocktail	Hoffmann- La Roche AG, Basel (Switzerland)
DPEC-treated water	Carl Roth, Karlsruhe
Dimethylsulfoxide (DMSO)	Carl Roth, Karlsruhe
Doxorubicin*HCl (Dox)	Sigma-Aldrich, St. Louis, MO (USA)
Ethanol	PanReac AppliChem, Darmstadt
Ethylenediaminetetraacetic acid (EDTA)	Carl Roth, Karlsruhe
Ferrocenecarboxaldehyde	Sigma-Aldrich, St. Louis, MO (USA)
Glycine	Carl Roth, Karlsruhe
Isopropanol	Aug. Hedinger GmbH & Co. KG, Stuttgart
Lipofectamine™ RNAiMAX transfection reagent (Lipo)	Invitrogen™, Thermo Fisher Scientific, Waltham, MA (USA)
Matrigel® Basement Membrane Matrix, Phenol Red-free	Corning Inc. Corning, NY (USA)
Methanol	Honeywell Riedel- de Haën®, Seelze
Methyl-β-cyclodextrin	Sigma-Aldrich, St. Louis, MO (USA)
Para formaldehyde (PFA)	Carl Roth, Karlsruhe
PEG_{12}-SPDP crosslinker	Thermo Scientific, Rockford, IL (USA)
PhosSTOP™	Hoffmann- La Roche AG, Basel (Switzerland)
Roti®-Plast (Paraffin)	Carl Roth, Karlsruhe
Sodium chloride	Carl Roth, Karlsruhe
Sodiumdodecyl sulfate (SDS), ultrapure	Carl Roth, Karlsruhe
TaqMan™ Universal PCR Master Mix	Thermo Scientific, Rockford, IL (USA)
Terralin® liquid	Schülke & Mayr GmbH, Norderstedt
Thermo Scientific PageRuler Prestained Protein Ladder	Thermo Scientific, Rockford, IL (USA)
Traut's reagent (2-Iminothiolane*HCl)	Thermo Scientific, Rockford, IL (USA)
Tris(hydroxymethyl)aminomethane (Tris)	Carl Roth, Karlsruhe
TritonX100	Sigma-Aldrich, St. Louis, MO (USA)
Trypan blue solution (0.4 %)	Sigma-Aldrich, St. Louis, MO (USA)
Tween20	Carl Roth, Karlsruhe
Type F Immersion Liquid $n_e^{23} = 1.5180$	Leica Microsystems, Wetzlar
Vectashield® Antifade Mounting Medium	Vector Laboratories, Burlingame, CA (USA)
Vectashield® Hardset™ Antifade Mounting Medium with DAPI	Vector Laboratories, Burlingame, CA (USA)
White leghorn eggs (fertilized)	LSL, Dieburg
Xylene	PanReac AppliChem, Darmstadt

Table 4: Cell culture reagents

Reagent	Manufacturer
Accutase®	Sigma-Aldrich, St. Louis, MO (USA)
Bovine Calf Serum (FCS)	VWR Seradigm, Radnor, PA (USA)
Dulbecco's Modified Eagle's Medium (DMEM)-Nutrient Mixture F12 (Ham) medium (DMEM/F12)	Gibco™ by Thermo Fisher Scientific, Waltham, MA (USA)
DMEM High Glucose	Gibco™ by Thermo Fisher Scientific, Waltham, MA (USA)
DMEM/F12 without phenol red	Gibco™ by Thermo Fisher Scientific, Waltham, MA (USA)
Dulbecco's phosphate-buffered saline (PBS)	Sigma-Aldrich, St. Louis, MO (USA)
Non-Essential Amino Acids (100x) (NEAA)	Gibco™ by Thermo Fisher Scientific, Waltham, MA (USA)
10 000 units Penicillin/ 10 mg Streptomycin per mL (Pen/Strep)	Sigma-Aldrich, St. Louis, MO (USA)
Trypsin/ EDTA (T/E)	Sigma-Aldrich, St. Louis, MO (USA)

Table 5: Cell culture media

DMEM/HamF12 + 5 %FCS + 2 % Pen/Strep		**DMEM/HamF12 + 10 % FCS + 1 % NEAA + 2 % Pen/Strep**		**DMEM High Glucose + 10 % FCS + 2 % Pen/Strep**	
DMEM/HamF12	500 mL	DMEM/HamF12	500 mL	DMEM High Glucose	500 mL
FCS	25 mL	FCS	50 mL	FCS	50 mL
Pen/Strep	10 mL	NEAA (100x)	5.5 mL	Pen/Strep	10 mL
		Pen/Strep	10 mL		

Table 6: Fluorescent dyes

Dye	Excitation	Emission	Manufacturer
alamarBlue™ Cell Viability Reagent	530- 560 nm	590 nm	Invitrogen™ by Thermo Fisher Scientific, Waltham, MA (USA)
AlexaFluor® 555-Phalloidin	555 nm	565 nm	Invitrogen™ by Thermo Fisher Scientific, Waltham, MA (USA)
4',6-diamidino-2-phenylindole dihydrochloride (DAPI)	360 nm	460 nm	Invitrogen™ by Thermo Fisher Scientific, Waltham, MA (USA)
eBioscience™ Fixable Viability Dye eFlour™ 506	405 nm	506 nm	Invitrogen™ by Thermo Fisher Scientific, Waltham, MA (USA)
eBioscience™ Fixable Viability Dye eFlour™ 780	633 nm	780 nm	Invitrogen™ by Thermo Fisher Scientific, Waltham, MA (USA)
Fluorescein	490 nm	525 nm	-
Sulfo-Cyanine5 *N*-hydroxysuccinimide ester	649 nm	666 nm	Lumiprobe GmbH, Hanover

Table 7: Solutions for (immuno)fluorescence staining

PBS + 0.3% TritonX100		**5%BSA in PBS + 0.3%TritonX100**		**0.5%BSA in PBS + 0.3% TritonX100**	
PBS	500 mL	Albumin Fraction V	2.5 g	5% BSA in PBS + 0.3% TritonX100	5 mL
TritonX100	1.5 mL	PBS + 0.3% TritonX100	Ad 50 mL	PBS + 0.3% TritonX100	45 mL
10x Tris-buffered saline (TBS) pH 7.6		**5% Tween20**		**TBST 400 mM NaCl**	
Tris	302.85 g	Tween20	25 mL	10x TBS	200 mL
NaCl	430.50 g	H_2O	475 mL	5% Tween® 20	20 mL
H_2O	Ad 5 L			NaCl	29.56 g
Adjust pH to 7.60 with concentrated hydrochloric acid				H_2O	Ad 2 L

Table 8: Antibodies

Antibody	**Species**	**Manufacturer**
Anti-β-Actin monoclonal antibody, clone AC-15	Mouse, IgG1	Sigma-Aldrich, St. Louis, MO (USA)
Anti-phospho-Histone H2A.X (Ser139), clone JBW301	mouse IgG1	EMD Millipore Cooperation, Temecula, CA (USA)
Anti-EEA1 C45B10 mAb	rabbit	Cell Signaling Technology, Inc., Danvers, MA (USA)
Anti-EGFR monoclonal antibody (199.12)	mouse/ IgG2a	Thermo Fisher Scientific, Rockford, IL (USA)
Anti-EGF Receptor (D38B1) XP® mAb	rabbit	Cell Signaling Technology, Inc., Danvers, MA (USA)
Anti-LAMP1 (D2D11) XP® mAb	rabbit	Cell Signaling Technology, Inc., Danvers, MA (USA)
IgG2a isotype control antibody	mouse	Thermo Fisher Scientific, Rockford, IL (USA)
Anti-mouse IgG, HRP-linked antibody	horse	Cell Signaling Technology, Inc., Danvers, MA (USA)
Anti-rabbit IgG, HRP-linked antibody	goat	Cell Signaling Technology, Inc., Danvers, MA (USA)
Goat anti-mouse AlexaFlour®488 antibody (H+L)	goat	Molecular Probes by Thermo Fisher Scientific, Waltham, MA (USA)
Goat anti-rabbit AlexaFlour®488 antibody (H+L)	goat	Molecular Probes by Thermo Fisher Scientific, Waltham, MA (USA)

Table 9: Solutions for antibody conjugation

PBS (pH 7.2)		Coupling buffer		pH-Adjusted coupling buffer	
BupH™ Phosphate Buffered Saline Packs	2	EDTA	1.4612 g	Coupling buffer	50 mL
Water for injection	1000 mL	PBS (pH 7.2)	Ad 500 mL	pH adjusted to 8.0 with 1 M NaOH, sterile filtration	
sterile filtration		pH adjusted with 1 M NaOH to 7.2, sterile filtration			

Table 10: siRNAs used for experiments

siRNA	Catalogue #	Sequence (5' → 3')	Manufacturer
Silencer® GFP (eGFP) siRNA	AM4626	Unknown	Ambion®; Thermo Fisher Scientific, Waltham, MA (USA)
Silencer® FAM™ GAPDH siRNA	AM4650	Unknown	Ambion®; Thermo Fisher Scientific, Waltham, MA (USA)
Silencer® Select siRNA hnRNP K	S6739	GAGCUUCGAUCAAAAAUUGAtt	Ambion®; Thermo Fisher Scientific, Waltham, MA (USA)
Silencer® Select Negative Control siRNA #2	4390846	Unknown	Ambion®; Thermo Fisher Scientific, Waltham, MA (USA)

Table 11: Primer for real-time polymerase chain reaction (qPCR)

Primer target	Context Sequence	Dye	Manufacturer
eGFP	AACCGCATCGAGCTGAAGGGCATCG	FAM-NFQ	Applied Biosystems by Thermo Fisher Scientific, Waltham, MA (USA)
GAPDH	GACTCATGACCACAGTCCATGCCAT	FAM-NFQ	Applied Biosystems by Thermo Fisher Scientific, Waltham, MA (USA)
hnRNP K	GACGAGGCGGCCGGGGTGGTAGCAG	FAM-NFQ	Applied Biosystems by Thermo Fisher Scientific, Waltham, MA (USA)
RPLPO (large ribosomal protein)	Unknown	VIC-TAMARA	Applied Biosystems by Thermo Fisher Scientific, Waltham, MA (USA)

Table 12: Buffers and solutions for protein expression analysis

Lysis buffer		**5x Electrophoresis (EPho) buffer**		**Transfer buffer**	
SDS	69 mM	Tris	250 mM	Tris	25 mM
2 M Tris/HCl pH 6.8-7.5	50 mM	Glycine	1.9 M	Glycine	150 mM
Glycerol	1.6 M	Solved in desalted H_2O		Methanol	10 % (V/V)
Solved in desalted H_2O		**1x Electrophoresis buffer**		SDS	0.037 %
cOmplete™	1 tablet/ 40 mL	5x EPho buffer	100 mL	Solved in desalted H_2O	
PhosSTOP™	1 tablet/ 10 mL	10 % SDS	5 mL		
		Desalted H_2O	Ad 500 mL		
10x Tris Buffered Saline (pH 7.6)		**1x TBS-T_{20}**		**25 mM Glycine, pH 2.0**	
Tris	200 mM	10x TBS	100 mL	Glycine	25 mM
NaCl	1.37 M	Tween20	0.01 %	Solved in desalted H_2O, pH adjusted with conc. HCl	
Solved in desalted H_2O, pH adjusted with HCl		Desalted H_2O	Ad 1000 mL	**1 % SDS in desalted H_2O**	
				SDS	35 mM

Table 13: Kits used in experiments

Kit	**Manufacturer**
innuPrep RNA isolation	Analytik Jena AG, Jena
DC™ Protein Assay	Bio-Rad Laboratories GmbH, Munich
TaqMan™ Universal PCR Master Mix	Thermo Fisher Scientific, Waltham, MA (USA)
TGX Stain-Free™ Fast Cast™ Acrylamide Solutions	Bio-Rad Laboratories GmbH, Munich
Western Lightning™ Plus Enhanced Chemi-luminescence Substrate for Western Blotting	PerkinElmer, Waltham, MA (USA)

3.1.4 Software

Table 14: Software for experimental analysis, literature management and graphic design

Software	Manufacturer
ACD/ChemSketch (Freeware) 2018.2.1	Advanced Chemistry Development, Inc, Toronto (Canada)
Ascent Software 2.6	Thermo Electron Corporation, Dreieich
BD FACS Diva Software	BD Bioscience, Heidelberg
Cytobank.org	Cytobank, Inc., Santa Clara, CA (USA)
Fiji (Image J)	https://imagej.net/Fiji Open-Source [151]
GraphPad Prism 5 (Version 5.04)	GraphPad Software, Inc., La Jolla, CA (USA)
ImageLab	Bio-Rad Laboratories GmbH, Munich
Inkscape	Free Software Foundation, Inc., Boston, MA (USA)
Mendeley	Elsevier, Amsterdam (Netherlands)
Microsoft Office 2010, Office 365	Microsoft Corporation, Redmond, WA (USA)

3.2 Methods

3.2.1 Cell culture

The cells and used solutions for cell culture were always handled with care in a safety cabinet and kept sterile. The cell culture media were prepared according to Table 5 and stored at 4 °C.

3.2.1.1 Cell lines

The used cell lines are summarized in Table 15. All cell lines were regularly tested for mycoplasma contamination and only used when no contamination was detected.

Table 15: Cell lines used in this work

Cell line	Origin	Cell culture medium	Passaging ratio	Source
Cal-33	Tongue squamous cell carcinoma [152]	DMEM/F12 + 10 % FCS + 2 % Pen/Strep	1:3	*Deutsche Sammlung von Mikroorganismen und Zellkulturen*
HNSCCUM-02T	base of tongue squamous cell carcinoma [153]	DMEM/F12 + 5 % FCS + 2 % Pen/Strep	1:5	University medical center Mainz, Johannes Gutenberg-University, Mainz, Germany
HuH7	Hepatocellular carcinoma[154]	DMEM/F12 + 5 % FCS + 2 % Pen/Strep	1:4	RIKEN BioResource Center
HuH7-GFP	Hepatocellular carcinoma with stable eGFP expression [155]	DMEM/F12 + 5 % FCS + 2 % Pen/Strep	1:4	Institute of Pharmaceutical Biology, Goethe-University, Frankfurt/Main
NIH-3T3	Mouse embryonic fibroblasts[156]	DMEM High Glucose + 10 % FCS + 2 % Pen/Strep	1:3	ATCC
RPMI2650	nasal septum squamous cell carcinoma (pleural effusion) [157]	DMEM/F12 + 10 % FCS + 1 % NEAA + 2 % Pen/Strep	1:10 every two weeks	*Deutsche Sammlung von Mikroorganismen und Zellkulturen*

3.2.1.2 Passaging of cells

The cells were passaged regularly, usually twice per week, except RMPI2650 cells (see Table 15). For passaging of cells, the medium was discarded, the cells were washed twice carefully with PBS, an appropriate amount of Trypsin/EDTA in PBS (T/E) or Accutase® (for RPMI2650) was added and the cells were incubated at 37 °C until the cells detached. The reaction was stopped by adding the cell line's medium (preheated to 37 °C) and the cells were suspended with a pipette. Then, the cells were centrifuged (1500 rpm, 5 min, 20 °C, Multifuge 1L-R), the supernatant was discarded, and the cell pellet was suspended in fresh medium. Finally, the cells were transferred in the above-mentioned ratios to cell culture flasks (see Table 15) and the medium was added as needed. The cells were incubated in an incubator at 37 °C and 5 % (V/V) CO_2.

3.2.1.3 Counting of cells

Different numbers of cells were needed for different experiments. Therefore, the cells were counted before seeding with the following protocol: A 20 µL aliquot of suspended cells was diluted with 20 µL 0.4 % Trypan blue solution to distinguish between living (clear) and dead (blue) cells and transferred to a counting chamber (BLAUBRAND® counting chamber). The cells were counted manually under a microscope with 100-fold magnification, usually, at least 100 cells or four squares were counted, respectively. The number of cells in solution was determined by Equation 1:

Equation 1

$$\#\,\text{cells} = \frac{\text{counted cells}}{\#\,\text{counted squares}} \times 2\,(\text{dilution factor}) \times 10\,000\,(\text{chamber factor}) \times \text{mL of total cell suspension}$$

The cells were centrifuged (1500 rpm, 5 min, 20 °C, Multifuge 1L-R) and suspended at 1 000 000 cells per mL and diluted with the respective medium as needed.

3.2.1.4 Freezing and storage of cells

The cells were removed from cell culture flasks as mentioned above (3.2.1.2). In the next step, the pelleted cells were suspended at about 1 000 000 cells per mL in 10 % DMSO in FCS and an aliquot of 1 mL was added to a cryotube. The cryotubes were first frozen in a freezing box (-1 °C per min) for 48 hours in a -80 °C freezer, then transferred and stored in liquid nitrogen (-196 °C).

3.2.1.5 Taking cells into culture

The cells' respective medium was preheated to 37 °C and 10 mL were added to a centrifugation tube. The cells were thawed by holding the cryotube in a water bath (37 °C) until almost the whole suspension was thawed. Then, a few drops of medium were added to the cells and the cells were transferred to the centrifugation tube containing the medium. The cells were centrifuged (1 500 rpm, 5 min, 20 °C, Multifuge 1L-R) and the pellet was suspended in medium. The cells were seeded in a cell culture flask and incubated in the incubator at 37 °C and 5 % (V/V) CO_2.

3.2.1.6 Preparation of 3D-cell cultures as tumor models

The 3D-cell cultures were prepared with the technical assistance of [redacted], and the cell lines HuH7 or HuH7-GFP were used for the preparation of 3D-cultures as tumor models. 5 000 000 cells were needed for one tumor model. First, the cells were transferred to a 1.5 mL centrifuge tube and generated a cellular pellet by centrifugation (1 400 rpm, 10 min, 20 °C, Hettich Universal 16R). Second, the supernatants were carefully removed, the cells were quickly suspended in 25 µL Matrigel® Basement Membrane Matrix and pipetted into 6-well plates. After 30 minutes incubation in the incubator (37 °C, 5 % (V/V) CO_2), the tumor model stiffed, medium was added to the wells and the 3D-cultures were incubated overnight.

3.2.1.7 RNA interference

Transfection of cells with Lipofectamine™ RNAiMAX was performed as control experiments. The amount of siRNA and Lipofectamine™ RNAiMAX reagent used was dependent on the cell line and the transfected number of cells as presented in Table 16.

First, plain DMEM/HamF12 (without FCS and without Pen/Strep) was pipetted into a centrifuge tube, then the respective siRNA or nsRNA was added, the solution was vortexed and briefly spun down. The Lipofectamine™ RNAiMAX reagent was added and the tube was vortexed and spun down again. Controls containing no RNA, but Lipofectamine™ RNAiMAX reagent or just DMEM/HamF12 medium were prepared dependent on the experiment, respectively. The transfection formulations were incubated at room temperature (RT) for at least 20 minutes or until the cells were prepared. The preparation and counting of cells was conducted based on the standard protocol (3.2.1.2, 3.2.1.3), but cells were suspended and seeded in DMEM/HamF12 + 5 % FCS (HNSCCUM-02T, HuH7-GFP) or DMEM/HamF12 + 10 % FCS + 1 % NEAA (RPMI2650). The transfection formulation was pipetted in the middle of the well and the cells were added. After all samples were prepared, the plate was briefly

swayed and incubated in an incubator for 24 hours. Then, the medium was removed, the cells were washed once with PBS and the normal cell culture medium was added at a sufficient volume. The cells were further incubated dependent on the performed experiment. Finally, cells were prepared for RNA isolation or stained and fixed for flow cytometry analysis.

Table 16: RNA interference sample preparation

Cell line	# cells seeded	V (DMEM/HamF12)	n (siRNA/ nsRNA)	V (Lipofectamine™ RNAiMAX)
HNSCCUM-02T	200 000 cells in 6-well plate	500 µL	15 pmol Silencer® Select siRNA hnRNP K	2.4 µL
HNSCCUM-02T	200 000 cells in 6-well plate	500 µL	100 pmol Silencer® FAM™ GAPDH siRNA	4 µL
HNSCCUM-02T	200 000 cells in 6-well plate	500 µL	100 pmol Silencer® Select Negative Control siRNA #2	4 µL
RPMI2650	400 000 cells in 6-well plate	500 µL	37.5 pmol Silencer® Select siRNA hnRNP K	6 µL
RPMI2650	400 000 cells in 6-well plate	500 µL	100 pmol Silencer® FAM™ GAPDH siRNA	4 µL
RPMI2650	400 000 cells in 6-well plate	500 µL	100 pmol Silencer® Select Negative Control siRNA #2	4 µL
HuH7-GFP	100 000 cells in 12-well plate	250 µL	25 pmol Silencer® GFP (eGFP) siRNA	2 µL
HuH7-GFP	200 000 cells in 6-well plate	500 µL	50 pmol Silencer® GFP (eGFP) siRNA	4 µL

3.2.2 MSN preparation

3.2.2.1 MSN synthesis and characterization

All used NPs were synthesized and characterized by [redacted]. The MSNs were stored in ethanol at 4 °C and sonicated and vortexed before removing aliquots. The provided MSN dispersions are listed in Table 17 and characterized in chapter 4.1. All MSNs (except SK-214) were labeled with the fluorescence dye Cyanine5 (Cy5, excitation maximum 649 nm, emission maximum 666 nm).

Table 17: Used MSN dispersions

Mesoporous silica nanoparticles	Stock concentration
AS-21-OT+12	4.5 mg/ mL
SK-214	2.23 mg/ mL
SK-267 SK2	2.2 mg/ mL 6.2 mg/ mL
SK-267 2 G	3.8 mg/ mL
Sk-267-SK4	13.2 mg/ mL 5.0 mg/ mL
SK-268 SK3	4.1 mg/ mL
SK-268 3 C	1.4 mg/ mL
SK-275 SK1	6.5 mg/ mL

3.2.2.1.1 MSN synthesis, amino functionalization and characterization

The MSN synthesis was conducted as described in [158] and different stirrers and stirring rates were employed to generate different particle and pore sizes. Tetraethyl orthosilicate was used as silica source and cetyltrimethylammonium chloride (CTAC) was used as surfactant. Also, the fluorescent dye Cyanine 5 was encapsulated during the MSN synthesis and amino functionalization was performed with (3-aminopropyl)-trimethoxysilane (APTMS). The MSNs were stored in ethanol under light protection at 4 °C until further usage and sonicated and vortexed before aliquots were removed.

The MSNs were characterized by TEM, dynamic light scattering, thermogravimetric analysis and nitrogen sorption measurements as described in [158].

3.2.2.2 Nanoparticle capping

The required mass of MSNs was added to PBS and centrifuged (10 000 g, 5 min, RT). Subsequently, the supernatants were carefully removed, and the NPs were washed with PBS by sonicating and vortexing, followed by centrifugation (10 000 g, 5 min, RT). The supernatants were again carefully removed, an appropriate amount of PBS was added to the MSNs and the NPs were sonicated and vortexed until in dispersion. For sealing 0.44 µg ferrocenecarboxaldehyde (ferrocene) and 2.74 µg methyl-β-cyclodextrin (β-CD) or 3A-Amino-3A-deoxy-(2AS,3AS)-β-cyclodextrin (NH_2-β-CD) per µg MSN were added, respectively, vortexed and incubated for six hours at 4 °C. The sealed MSNs are termed “Cy5-MSNs”. Then, the Cy5-MSNs were washed by centrifugation (10 000 G, 5 min, RT), the supernatants were carefully

removed, and the pellet was dispersed in PBS by sonication and vortexing. This washing step was repeated once and finally, the Cy5-MSNs were dispersed in PBS at 1 mg/ mL by sonication and vortexing.

3.2.2.3 Preparation of doxorubicin-loaded nanoparticles

The steps of the Dox loading protocol are presented in Figure 11. First, the MSNs (SK-267) were washed with double-distilled water (ddH_2O) and centrifuged (10 000 g, 5 min, RT). The supernatants were carefully removed and 5 nmol (2 mg/ mL = 3.45 mM Dox stock solution) or 2.15 nmol (5 mg/ mL= 8.6 mM Dox stock solution) Dox per µg MSN in ddH_2O were added for Dox-loaded MSN (Dox-MSNs) and ddH_2O was added for control MSNs. The particles were shortly sonicated and vortexed until dispersed, and incubated overnight at 4 °C. For sealing, 0.44 µg ferrocene and 2.74 µg NH_2-β-CD per µg MSN were added, vortexed and incubated for six hours at 4 °C. The samples were centrifuged, and the supernatants were collected for determining the drug loading efficiency. The NP pellets were dispersed in ddH_2O by sonication and centrifuged again. Washing was repeated at least five times and all supernatants were collected. Finally, Dox-MSNs and Cy5-MSNs were dispersed in PBS at 1 mg/ mL. The Dox-MSNs and Cy5-MSNs were used for experiments within two days.

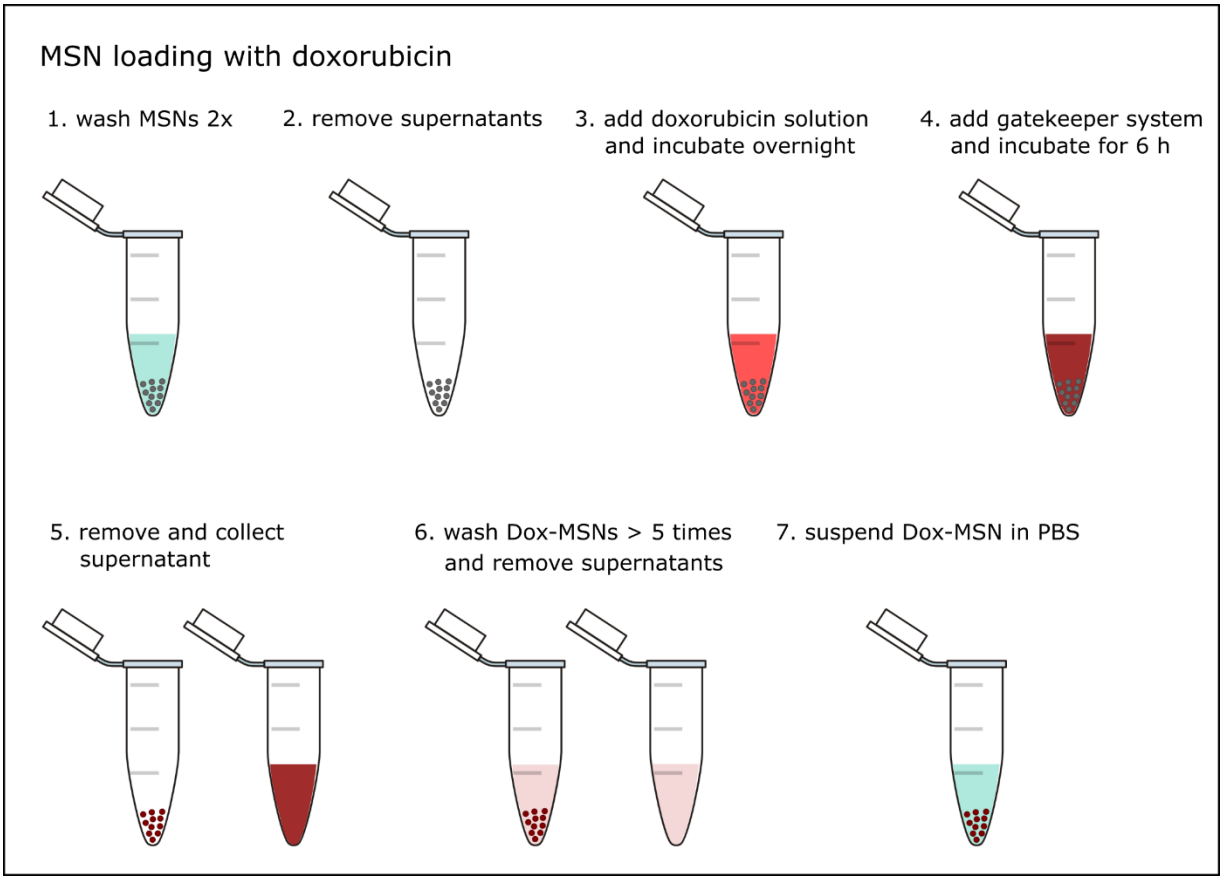

Figure 11: Loading of mesoporous silica nanoparticles with doxorubicin

The MSNs were washed twice, the supernatants were removed, and the Dox solution was added overnight. The next day, the gatekeeper (ferrocene and NH_2-β-CD) were added and the NPs were incubated for 6 hours. The Dox-MSNs were washed, and the supernatants were collected for analysis of the loading efficiency. Finally, Dox-MSNs were dispersed in PBS and used in experiments.

3.2.2.3.1 Analysis of doxorubicin loading efficiency

A standard curve of Dox in ddH_2O was generated and was only used when $R^2 \geq 0.98$. Supernatants were diluted 1:100 or 1:10 or used undiluted, respectively. The absorption at 488 nm and the fluorescence (excitation: 485/10 nm, emission: 560/40 nm) were measured with HIDEX Sense beta plus microplate reader and the amount of Dox left in supernatants was calculated after subtracting the control supernatants. The loading efficiency (LE) was determined by Equation 2:

Equation 2

$$\mathrm{LE}\ (\%) = \ 100\,\% - \frac{\sum \mathrm{Dox\ in\ supernatants}}{\mathrm{total\ Dox\ used\ in\ loading}}$$

3.2.2.3.2 Doxorubicin release in different media

The preparation of 200 µg Dox-MSNs (SK-267 SK2, 5 mg/ mL, 2.15 nmol Dox per µg MSNs) was performed as described above and the loading efficiency was determined. Unloaded MSNs were prepared the same way as the controls. Then, 10 µg/ mL Dox-MSNs and Cy5-MSNs were incubated in different media for 24 and 96 hours in an incubator (37 °C, 5 % CO_2 (V/V)) in duplicates, namely PBS, sterile DPEC-treated water (DPEC-H_2O), DMEM without phenol red and DMEM without phenol red with 5 % FCS and 2 % Pen/Strep. The centrifuge tubes were left open for the first hour to allow the media the reaction with the gaseous environment to imitate cell culture conditions as good as possible. After incubation, the samples were centrifuged (10 000 g, 5 min, 20 °C) and the supernatants were transferred to fresh 1.5 mL centrifuge tubes. A fluorescence standard curve of Dox was generated in each medium from 0.2 µM to 5 µM Dox (linear fluorescence range) in triplicates. The standard curve was used to calculate the Dox concentration in the supernatants when $R^2 \geq 0.97$. The supernatants and the standard curve samples were measured in triplicates with HIDEX Sense beta plus microplate reader (excitation: 485/ 10 nm, emission: 560/ 40 nm). Next, the Dox concentration was determined by the standard curves and the mean of the two samples per time point was normalized to the used Dox concentration (13.1 µM, 14.8 µM, and 13.4 µM). The experiment was performed three times.

3.2.2.4 siRNA loading to MSNs

During the project, different protocols for siRNA loading were tested and applied. These protocols are described in the following paragraphs.

3.2.2.4.1 Loading of eGFP-siRNA and capping with ferrocene/ β-cyclodextrin (I)

First, three aliquots of 80 µg MSNs (SK-267) were washed twice with DPEC-H_2O and dispersed in 60 µL DPEC-H_2O. In the next step, 400 pmol (8 µL of 50 µM stock solution) eGFP-targeting siRNA or nsRNA were added, vortexed and incubated overnight at 4 °C, respectively. One aliquot was incubated with DPEC-H_2O (control). The next day, 0.44 µg ferrocene and 2.74 µg NH_2-β-CD per µg MSN were added to each aliquot for six hours. The eGFP-siRNA-MSNs, nsRNA-MSNs and Cy5-MSNs were washed twice with DPEC-H_2O and were dispersed in DPEC-H_2O at 1 mg/ mL and stored at 4 °C until use.

3.2.2.4.2 Loading of FAM™-siRNA and hnRNP K siRNA and capping with ferrocene/ β-cyclodextrin (II)

Three aliquots of 600 µg MSNs (SK-275) were washed twice with PBS and dispersed in 500 µL PBS. Then, 0.44 µg ferrocene per µg MSN were added for six hours. The NPs were centrifuged (10 000 g, 5 min, RT), the supernatants were removed, and the MSNs were dispersed in 100 µL PBS. Subsequently, 1.5 pmol per µg MSN Silencer® FAM™ GAPDH siRNA (FAM™-siRNA), Silencer® Select siRNA hnRNP K (hnRNP K-siRNA) or Silencer® Select Negative Control siRNA #2 (nsRNA) were added, respectively, briefly vortexed and incubated overnight at 4 °C. The next day, 2.74 µg NH_2-β-CD per µg MSN were added to each aliquot for five hours. The FAM™-siRNA-MSNs, hnRNP K-siRNA-MSNs, and nsRNA-MSNs were washed twice with PBS and were dispersed in PBS at 1 mg/ mL.

3.2.2.4.3 Testing of siRNA loading to MSNs and capping with ferrocene/ β-cyclodextrin

The MSNs SK-275 SK1 were used to test whether ferrocene conjugation before siRNA addition affects the siRNA loading. For that reason, four aliquots of 500 µg MSNs (SK-275 SK1) were washed twice with PBS and dispersed in 400 µL PBS by sonication and vortexing. Then, different amounts of ferrocene were added according to Table 18 and NPs were incubated for five hours at 4 °C. The MSN formulations were centrifuged (10 000 g, 5 min, RT), the supernatants removed, and PBS was added for washing. Next, the MSNs were dispersed in 100 µL PBS by sonication and vortexing and 500 pmol FAM™-siRNA were added according to Table 18. The samples were briefly vortexed and incubated overnight at 4 °C. The next day, 2.72 µg NH_2-β-CD were added, and the MSNs were incubated for five hours at 4 °C. Finally, the NP formulations were washed twice with PBS and were dispersed in PBS. To evaluate the success of siRNA loading, the MSNs were centrifuged (10 000 g, 5 min, RT) and the pellets were examined with Darkreader™ 195 M Transilluminator and a picture was taken with a smartphone camera.

Table 18: Different formulations for testing siRNA loading and release

Label	Ferrocenecarboxaldehyde (µg/ mL)	Silencer® FAM™ GAPDH siRNA (pmol)
A	0	500
B	54.1	500
C	89.6	500
Control	133.2	0

3.2.2.4.4 Sealing with Lipofectamine™ RNAiMAX: Test of different protocols

Furthermore, different incubation protocols were tested for MSN sealing with Lipofectamine™ RNAiMAX after siRNA loading. First, six aliquots of 200 µg MSNs (SK-275 SK1) were transferred to 1.5 mL centrifuge tubes and washed twice with PBS. The supernatants were removed after centrifugation (10 000 g, 5 min, RT) and the MSNs were dispersed in 100 µL PBS. 200 pmol FAM™-siRNA or nsRNA were added according to Table 19 and the NPs were vortexed and incubated at 4 °C overnight. Then, the samples were centrifuged (10 000 g, 5 min, RT), the supernatants were collected for further analysis and the FAM™-siRNA-MSNs or nsRNA-MSNs were dispersed in the stated amount of PBS (see Table 19) by sonication and vortexing, respectively. Subsequently, Lipofectamine™ RNAiMAX was added and samples were incubated as indicated. The NP formulations were centrifuged, washed with PBS, and dispersed in 200 µL PBS. After centrifugation, the NP pellets were analyzed with Darkreader™ 195 M Transilluminator and a picture was taken with a smartphone camera.

Table 19: Different protocols for testing MSN sealing with Lipofectamine™ RNAiMAX

Label	RNA	Incubation parameters	V (PBS)	V (Lipofectamine™ RNAiMAX)
A1	Silencer® FAM™ GAPDH siRNA	1 h (RT)	140 µL	60 µL
B1	Silencer® FAM™ GAPDH siRNA	1 h (RT)	120 µL	80 µL
A3	Silencer® FAM™ GAPDH siRNA	3 h (4 °C)	140 µL	60µL
B3	Silencer® FAM™ GAPDH siRNA	3 h (4 °C)	120 µL	80 µL
ACo	Silencer® Select Negative Control siRNA #2	1 h (RT)	140 µL	60 µL
BCo	Silencer® Select Negative Control siRNA #2	3 h (4 °C)	120 µL	80 µL

3.2.2.4.5 Sealing of siRNA-MSNs with Lipofectamine™ RNAiMAX

The required mass of MSNs (SK-275 SK1) was transferred to 1.5 mL centrifuge tubes, washed twice with an appropriate volume of PBS and dispersed in PBS. Next, 1 pmol FAM™-siRNA, eGFP-siRNA or nsRNA per µg MSN was added, respectively, and incubated overnight at 4 °C. The samples were centrifuged, the supernatants were removed, and the siRNA-loaded NPs were dispersed in PBS and Lipofectamine™ RNAiMAX according to Table 20. After three hours incubation at 4 °C, the sealed MSNs were centrifuged again, the supernatants were removed, and the NPs were dispersed in PBS at 1 mg/ mL.

Table 20: Sealing of siRNA-loaded MSNs with Lipofectamine™ RNAiMAX

Experiment	siRNA	m (MSNs)	V (PBS)	V (Lipofectamine™ RNAiMAX)
10 µg/ mL MSNs, eGFP expression	Silencer® GFP (eGFP) siRNA	50 µg	40 µL	10 µL
25 µg/ mL MSNs, eGFP expression	Silencer® GFP (eGFP) siRNA	150 µg	100 µL	15 µL
10 and 25 µg/ mL MSNs, eGFP mRNA expression	Silencer® GFP (eGFP) siRNA	150 µg	100 µL	15 µL
10 µg/ mL, uptake comparison	Silencer® FAM™ GAPDH siRNA	150 µg	100 µL	15 µL

3.2.2.5 Antibody coupling to nanoparticles

For active targeting, two different antibodies, namely an EGFR-antibody (0.2 mg/ mL) and an IgG2a-control antibody (1 mg/ mL), were coupled to capped MSN based on protocols provided by Thermo Fisher Scientific. The required solutions are stated in Table 9. First, 500 µg MSNs (SK-275 SK1) were sealed according to the standard protocol (3.2.2.2) with ferrocene and NH_2-β-CD, but PBS (pH 7.2) was used for washing. The PEG_{12}-N-succinimidyl-3-(2-pyridyldithiol) propionate (SPDP) crosslinker (Figure 12) required available amino groups on one reagent, provided by NH_2-β-CD of Cy5-MSNs and sulfhydryl groups on the second reagent (antibodies).

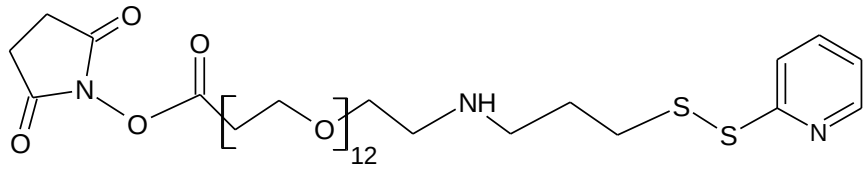

Figure 12: PEG_{12}-SPDP crosslinker

Molecular weight: 912.07 g/mol, spacer arm length: 51.1 Å. The PEG_{12}-SPDP crosslinker contains an amine-reactive group, namely the N-hydroxysuccinimide ester (NHS) (on the left) and a sulfhydryl-reactive portion, namely a 2-pyridyldithio group (on the right). Both reactive groups react best at pH 7- 8.

The antibodies (20 µg) were first incubated with 0.266 nmol Traut's reagent (dihydrothiophen-2(3H)-imine hydrochloride) in pH-adjusted coupling buffer (pH 8.0) for one hour at RT to enhance the number of sulfhydryl groups ($(SH)_x$-antibodies) (see Figure 13).

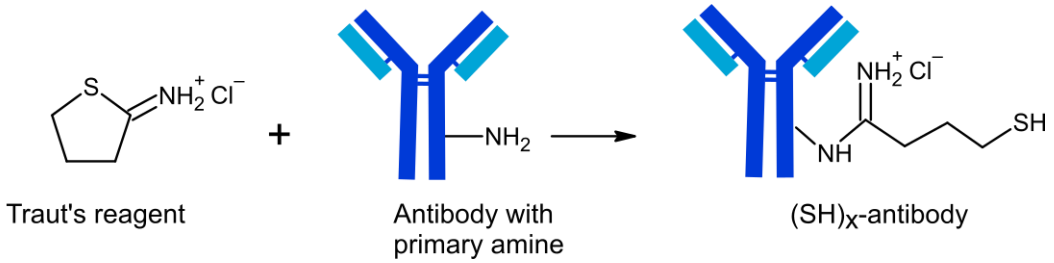

Figure 13: Sulfhydration of antibodies with Traut's reagent (dihydrothiophen-2(3H)-imine hydrochloride)

Traut's reagent reacts with primary amines of antibodies to an amidine compound with a sulfhydryl group.

In the next step, Zeba™ Spin Desalting Columns (7K MW cut-off) were equilibrated with coupling buffer according to the supplier's instructions for buffer exchange. Then, the $(SH)_x$-antibodies were slowly pipetted onto the columns to remove excess Traut's reagent and the flow-through contained the $(SH)_x$-antibodies which were adjusted to 150 µL with coupling buffer. The Cy5-MSNs were suspended in coupling buffer at 1 mg/ mL and incubated with 1 mM PEG_{12}-SPDP crosslinker (10 mM stock solution in DMSO) for 30 minutes at RT as shown in Figure 14. In the next step, the NPs were centrifuged (10 000 g, 5 min, RT) to remove excess linker and the pellet was suspended in 350 µL coupling buffer by sonication and vortexing. The $(SH)_x$-antibodies were added to the linker-modified MSNs and incubated overnight (18 hours) in a Thermomixer comfort with 500 rpm at 22 °C. The next day, the EGFR-MSNs and IgG2a-MSNs were centrifuged (10 000 g, 5 min, RT), the supernatants were removed, and the NPs were washed twice with 500 µL PBS (pH 7.2). Finally, EGFR-MSNs and IgG2a-MSNs were dispersed at 1 mg/ mL.

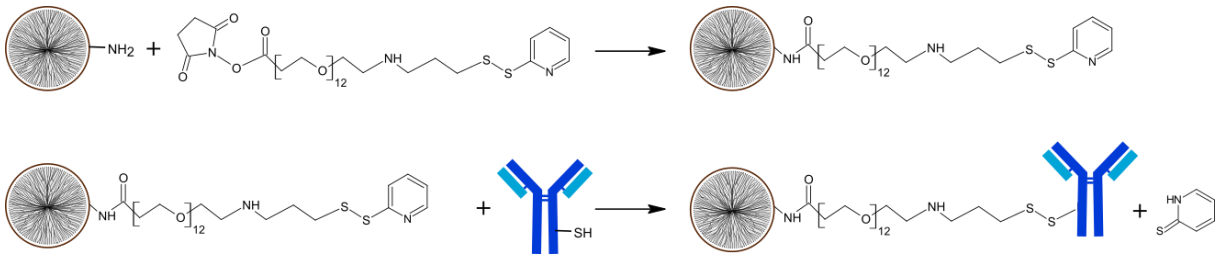

Figure 14: Antibody conjugation to nanoparticles

First, PEG_{12}-SPDP crosslinker was conjugated to MSN sealed with ferrocene and NH_2-β-CD. The reactive NHS ester facilitated the reaction of the carboxy group with the amino group of the NH_2-β-CD to a stable amide bond. Second, $(SH)_x$-antibodies were added to the linker-modified MSNs and incubated overnight. The 2-pyridyldithio group enabled conjugation of the $(SH)_x$-antibodies by a disulfide bond. The reaction byproduct pyridine-2-thione was removed by centrifugation and PBS washing.

3.2.2.5.1 Analysis of antibody coupling efficiency

A fluorophore-labeled anti-mouse antibody was used to estimate the amount of antibody which was successfully coupled to MSNs as presented in Figure 15. First, 250 µL EGFR-MSNs, IgG2a-MSNs and Cy5-MSNs were transferred to centrifuge tubes and from these aliquots, 100 µL were pipetted into a 96-well microplate black with clear bottom in duplicate. The NPs were measured at Fluoroskan Ascent Microplate Reader with 485/ 538 and 590/ 638 filter pairs as reference. Then, the NPs were pipetted back into their respective centrifuge tubes and two 100 µL aliquots were transferred to new centrifuge tubes. 500 µL of goat anti-mouse AlexaFluor® 488 antibody (H+L) (AF488) in PBS (pH 7.2) (1:250, 8 ng/ µL) were added to each tube and incubated for one hour in a Thermomixer comfort with 300 rpm at 22 °C.

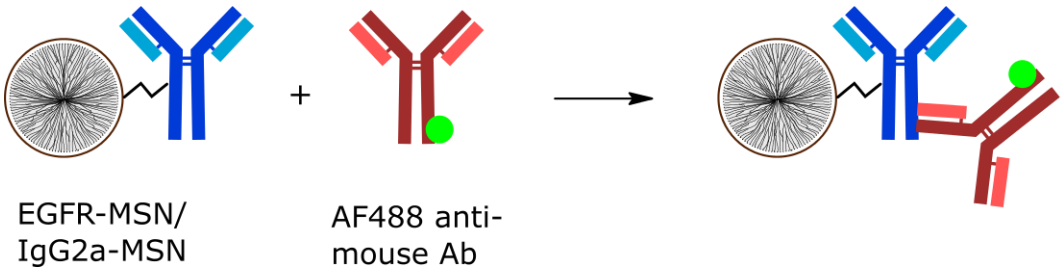

Figure 15: Analysis of antibody-coupling efficiency

EGFR-MSNs, IgG2a-MSNs, and Cy5-MSNs were incubated with goat anti-mouse AlexaFluor® 488 antibody (AF488 anti-mouse Ab). After washing, the AF488 fluorescence was measured and the coupling efficiency was determined.

Next, the samples were centrifuged (10 000 g, 5 min, RT) and the supernatants were collected. The NPs were dispersed in PBS (pH 7.2) by sonication and vortexing, centrifuged

(10 000 g, 5 min, RT), and the supernatants were collected. This washing step was repeated once and finally, the EGFR-MSNs, IgG2a-MSNs, and Cy5-MSNs were dispersed in 100 µL PBS (pH 7.2). A standard curve ranging from 0.0 to 8.0 ng/ µL AF488 was generated using triplicates for each concentration. The NP samples were added to the 96-well microplate black with a clear bottom to the same wells as before and the supernatants were added in triplicates or duplicates (100 µL per well). The fluorescence of the standard curve and the samples was measured at Fluoroskan Ascent Microplate Reader (485/ 538 and 590/ 638 filter pairs) and the analysis was conducted with Microsoft Excel. First, the mean blank value was subtracted from each value and a linear standard curve cutting 0 was generated to determine the slope m. The standard curve was only used if $R^2 \geq 0.99$. As shown in Equation 3, the difference between the fluorescence of AF488 before [$\mathrm{Flu(AF488)_0}$] and after the incubation [$\mathrm{Flu(AF488)_{1h}}$] was calculated and used to determine the mass of secondary antibody per sample [$\mathrm{m(AF488)_S}$] by taking the sample's volume ($\mathrm{V_S}$) into account. The $\mathrm{m(AF488)_S}$ was divided by the fluorescence measured with the 590/ 638 filter pair representing the amount of Cy5-MSNs [$\mathrm{Flu(Cy5)_{1h}}$] to identify the Coupling Factor (CF) as depicted in Equation 4. Finally, the mean for each group was determined and all mean CFs were normalized to the mean CF of control MSNs (Cy5-MSNs). The mean values (blank-subtracted) of the supernatants were utilized to calculate $\mathrm{m(AF488)_S}$ in the supernatants according to Equation 3 and the total mass of AF488 in the sample and the supernatants was compared to the applied AF488 mass evaluating the success of the antibody coupling analysis. The average AF488 recovery rates were 59 ± 4 %, 62 ± 3 % and 69 ± 2 %, respectively.

Equation 3

$$\mathrm{m(AF488)_S} = \frac{\mathrm{Flu(AF488)_{1h}} - \mathrm{Flu(AF488)_0}}{m} \times \mathrm{V_S}$$

Equation 4

$$\mathrm{CF} = \frac{\mathrm{m(AF488)_S}}{\mathrm{Flu(Cy5)_{1h}}}$$

3.2.3 Toxicity analysis (alamarBlue™ assay)

In general, the toxicity was determined by means of a reduction in metabolic activity with the alamarBlue™ assay. Alamar Blue, also called resazurin (7-Hydroxy-3*H*-phenoxazin-3-one-10-oxide), is a weak fluorescent blue dye that is reduced to highly fluorescent pink resorufin (7-Hydroxy-3*H*-phenoxazin-3-one) by the metabolic product nicotinamide adenine dinucleotide ($NADH/H^+$) as shown in Figure 16 and thereby reflects the number of viable cells [159].

For the standard protocol, at least triplicates were used per treatment or control solution, respectively. A dead control was prepared by treating cells with cold Terralin® for ten minutes. The treatment solutions and Terralin® were replaced by 10 % alamarBlue™ in cell culture medium at stated time points. The fluorescence was measured with Fluoroskan Ascent Microplate Reader (538/ 600 nm filter pair) before and after three hours incubation in the incubator. The difference between both measurements was normalized to the mean PBS control generating the relative metabolic activity (in %).

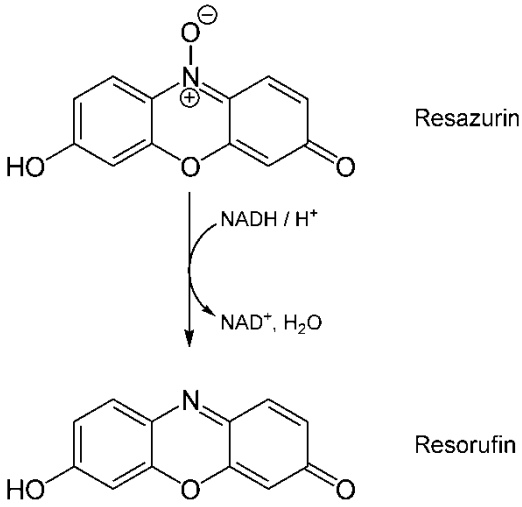

Figure 16: Reduction of resazurin by NADH/H⁺ to resorufin as indicator of metabolic activity

Graphic by Yikrazuul, Own Work, Public domain https://commons.wikimedia.org/w/index.php?curid=2774179, [Accessed: 26-June-2019].

3.2.3.1 IC50 of doxorubicin in HNSCCUM-02T and RPMI2650

The Dox concentration of half-maximal reduction in metabolic activity (IC50) was determined in HNSCCUM-02T and RPMI2650 cells after 24 and 48 hours incubation.

The HNSCCUM-02T (5 000 cells per well) and RPMI2650 (20 000 cells per well) cells were seeded in 96-well cell culture microplates (black with clear bottom) and let adhere overnight. The Dox stock solution (2 mg/ mL, 3.45 mM) was diluted in PBS to working solutions of different concentrations (2 µM, 5 µM, 10 µM, 20 µM, 50 µM, 100 µM, 200 µM, 500 µM Dox in PBS). Then, the working solutions were diluted in the respective cell culture medium to final Dox concentrations (0.1 µM, 0.25 µM, 0.5 µM, 1 µM, 2.5 µM, 5 µM, 10 µM, 25 µM) and the cells were treated in triplicates for 24 and 48 hours. PBS was used as control. The alamarBlue® assay was conducted according to the standard protocol (3.2.3).

The analysis of IC50 was performed with GraphPad Prism via a non-linear fit regression [log c(Dox) vs. normalized response (variable slope)].

3.2.3.2 Biocompatibility examination of unloaded nanoparticles

The cells were seeded in a 96-well cell culture microplate (black with clear bottom) at 5 000 cells per well (HNSCCUM-02T, NIH-3T3), 10 000 cells per well (HuH7) or 20 000 cells per well (Cal-33, RPMI2650) and let adhere for two days. The stock dispersions SK-214 (HNSCCUM-02T, Cal-33, RPMI2650), SK-268 3C (NIH-3T3) or SK-267 2G (HuH7) of capped MSNs (1 mg/ mL, 3.2.2.2) were pre-diluted in PBS and then diluted in the respective cell culture medium to 5, 10, 25, 50 or 100 µg/ mL Cy5-MSNs. The cells were treated with these dispersions for 24 hours and PBS was used as control. Finally, the alamarBlue® assay was performed according to the standard protocol (3.2.3).

3.2.3.3 Doxorubicin-loaded nanoparticles

Different cell lines were incubated with free Dox, Dox-MSNs and Cy5-MSNs, respectively, and the influence of FCS on Dox release was studied, too. The Dox-MSNs were prepared as described in 3.2.2.3 with 5 nmol Dox per µg MSN for the Dox release evaluation, and with 2.15 nmol per µg MSN for examining the influence of FCS on Dox release.

The cells were seeded in a 96-well cell culture microplate (black with clear bottom) at 5 000 cells (HNSCCUM-02T) or 20 000 cells (RPMI2650) per well and let adhere for two days. In the next step, the cells were treated with PBS as control, 1 and 2 µM free Dox, 10 µg/ mL Dox-MSNs, or Cy5-MSNs, respectively, in cell culture medium for 24 and 96 hours. The alamarBlue™ assay was performed and cells were incubated further for 72 hours in cell culture medium without treatment solutions, respectively, and metabolic activity was measured again with the alamarBlue™ assay.

Furthermore, the influence of FCS on Dox and Dox-MSNs' toxicity was examined in HNSCCUM-02T cells. The cancer cells were seeded at 10 000 cells per well in a 96-well cell culture microplate (black with clear bottom) and let adhere overnight. The treatment solutions were prepared in DMEM/F12 + 5 % FCS + 2 % Pen/Strep or DMEM/F12, respectively, and cells were treated for 24 and 96 hours with 2 µM free Dox, 10 µg/ mL Dox-MSNs, or 10 µg/ mL Cy5-MSNs while PBS was applied as control. The alamarBlue™ assay was performed and the cells were incubated further for 72 hours in cell culture medium without treatment solutions, respectively, and metabolic activity was measured with the alamarBlue™ as-

say again. The experiment was repeated three times with the Dox-MSNs and Cy5-MSNs prepared for studying Dox release in different media (3.2.2.3.2).

3.2.4 Flow cytometry

Flow cytometry allows analyzing high amounts of cells in a short time and the principle is shown in Figure 17. In brief, single cells flow through a cuvette flow cell and bypass different lasers which are detected at certain angles. The forward scatter (FSC) is detected in a 180° angle and provides information about the cell's size while the sideward scatter (SCC) is detected at a 90° angle and characterizes the cells' granularity. Furthermore, fluorescent dyes can be identified simultaneously by different lasers and distinctive filters even enhance the number of dyes which can be detected in one measurement. The viable and dead cells can be distinguished by incubating the cells with a fluorescent dye which only penetrates cells with a damaged cellular membrane, e.g. eBioscience™ Fixable Viability Dye eFlour™ 780 (FVD780). Also, fluorescently labeled NPs can be detected when associated with a cell. However, it is not possible to differentiate between the NPs inside the cells and attached to the cells.

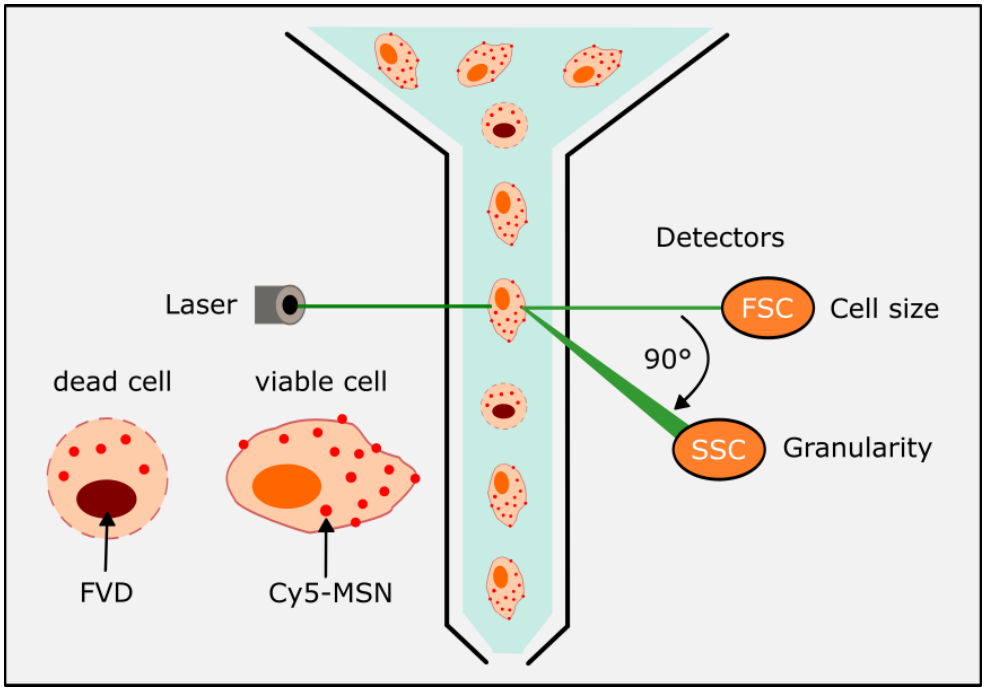

Figure 17: Flow cytometry analysis of nanoparticle treated cells

The cells flow through a cuvette flow cell separately and are excited by different lasers. The forward scatter (FSC) correlates to the cell's size and the sideward scatter (SSC) which is detected at a 90° angle, correlates to the cells' granularity. By using different laser lines and different filter sets, a high number of different fluorescent dyes can be recorded simultaneously. Before analysis, the cells were incubated with a fixable viability dye (FVD) to distinguish viable and dead cells. The dye accumulates only in cells with a permeable membrane and stains the DNA in the nucleus; hence only dead cells are fluorescently labeled. The MSNs were labeled with the fluorescent dye Cy5 and could be detected with a 635 nm laser line, too.

3.2.4.1 General protocol for sample preparation for flow cytometry analysis

The used cell line, cell number and treatment characteristics (NP or drug concentrations, incubation time) are specified in the following chapters. A general protocol was used to obtain samples for flow cytometry analysis. First, supernatants were collected to centrifuge tubes and stored on ice, cells were washed with PBS which was added to the respective centrifuge tube, and cells were detached with Accutase®. After visible detachment of the cells, the samples were thoroughly dispersed by pipetting and transferred to the respective supernatants. Then, the samples were centrifuged (350 g, 5 min, 4 °C) and the supernatants were discarded. The cell pellets were dispersed in PBS and transferred into a 96-well plate with a round bottom. Next, the plate was centrifuged (350 g, 5 min, 4 °C), the supernatants were carefully removed with a multichannel pipette, and the cellular pellets were dispersed in 20 µL of FVD780 (if not stated otherwise) in PBS (1:200). The samples were stained for 30 minutes at 4 °C, then PBS was added, and the samples were centrifuged (350 g, 5 min, 4 °C) again. In

the next step, the supernatants were carefully removed, the cellular pellet was dispersed in 1 % PFA in PBS, and incubated for 30 minutes at RT under light protection. After centrifugation (350 g, 5 min, 4 °C), the samples were washed twice with PBS and stored in PBS at 4 °C until flow cytometry analysis.

3.2.4.2 Nanoparticle uptake

For NP uptake analysis, the MSNs (SK-268 SK3) were sealed overnight in accordance with 3.2.2.2 but with two different gatekeeper solutions: 0.34 mg/ mL ferrocene with 2 mg/ mL methyl-β-cyclodextrin in PBS (Cap 1) and 0.34 mg/ mL ferrocene with 2 mg/ mL 3A-Amino-3A-deoxy-(2AS,3AS)-β-cyclodextrin:methyl-β-cyclodextrin 1:5 in PBS (Cap 2). In total 106.5 µg ferrocene were used for 1 mg MSNs.

3.2.4.2.1 Sample preparation

The HNSCCUM-02T cells were seeded at 100 000 cells per well in 12-well plates and let adhere overnight. Then, HNSCCUM-02T cells were incubated without MSNs (PBS), 10 µg/ mL Cap 1 sealed, or Cap 2 sealed Cy5-MSNs for 24 and 48 hours in triplicates, respectively. The samples were prepared following the general protocol (3.2.4.1). Yet, dead cells were stained with eBioscience™ Fixable Viability Dye eFlour™ 506 (FVD506).

3.2.4.2.2 Flow cytometry analysis

The samples were transferred to 5 mL polystyrene round-bottom tubes and at least 10 000 events were analyzed with LSR II flow cytometer at a high flow rate. The settings are presented in Table 21.

Table 21: Flow cytometer settings for nanoparticle uptake analysis

	Channel	Laser (nm)	Voltage
Size	FSC	488	160
Granularity	SCC	488	231
FVD506	AmCyan	405	357
Cy5-MSNs	APC	635	736

The gating and analysis were performed with cytobank.org. First, the whole cell population was gated in a dot plot (Figure 18A) to remove debris and then single cells were identified by gating the cell population in a dot plot by size (Figure 18B). Next, a histogram of the single cells in the AmCyan channel was used to distinguish between viable (unstained) and dead (stained) cells as shown in Figure 18C. The amount of Cy5-MSNs taken up by or attached to the cells was determined by the mean fluorescence intensity of a histogram of viable cells in the APC channel. The means for each treatment and time point were calculated in each ex-

periment and used to obtain the means and standard deviations for each treatment and time point. The experiment was repeated three times.

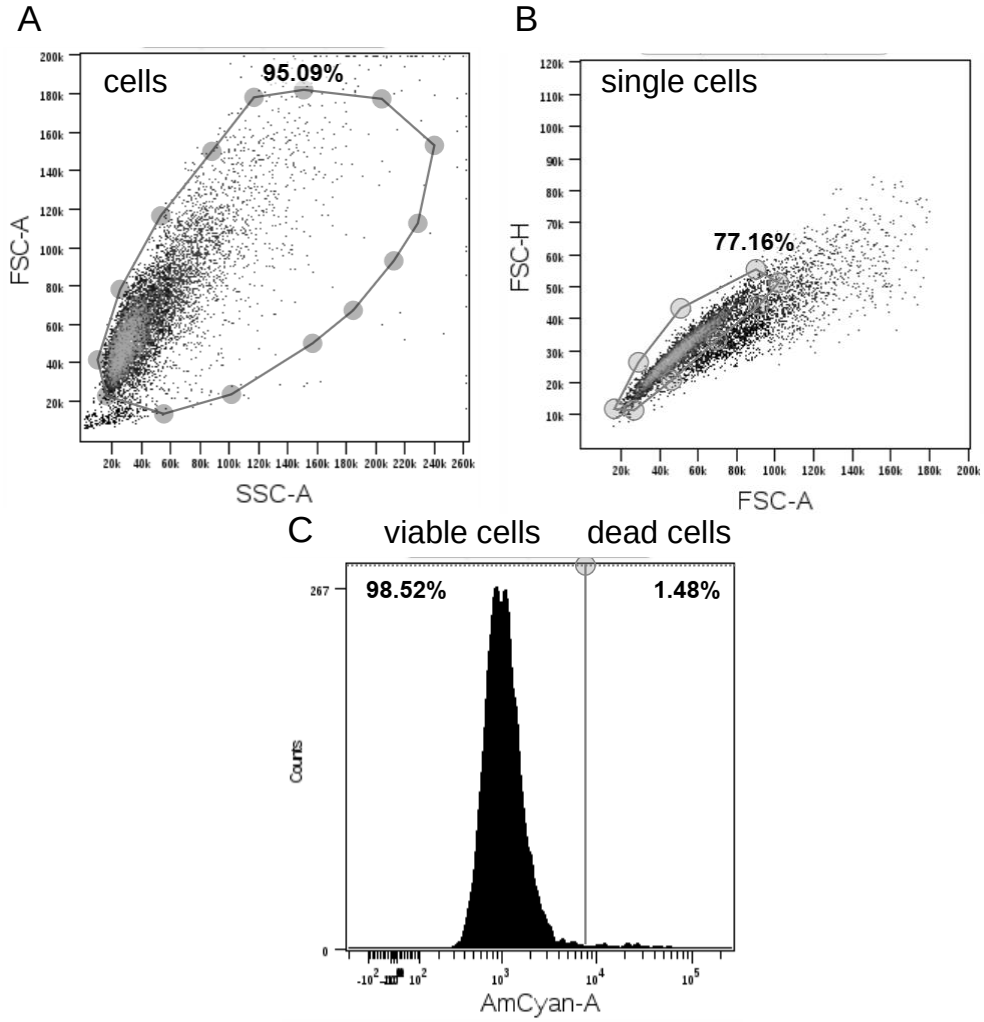

Figure 18: Representative gating of Cap1-sealed MSNs (24 hours) to analyze MSN uptake.

(A) Cells were determined by gating SSC-A vs FSC-A channels in a dot plot. (B) Single cells were identified in the cell population by gating FSC-A vs FSC-H channels in a dot plot. (C) A histogram of single cells was generated in the AmCyan-A channel (FVD506) to separate viable and dead cells. Graphics were obtained from community.cytobank.org.

3.2.4.3 Comparison of MSN uptake after different MSN sealing

The uptake of MSNs sealed with ferrocene and NH_2-β-CD (3.2.2.2) and MSNs encapsulated with Lipofectamine™ RNAiMAX (3.2.2.4.5) was compared in HNSCCUM-02T cells after 24 and 96 hours incubation, respectively.

3.2.4.3.1 Sample preparation

The HNSCCUM-02T cells were seeded at 50 000 cells per well in 12-well cell culture plates and let adhere overnight. The Cy5-MSNs were prepared according to the standard protocol and sealed with ferrocene and NH_2-β-CD (3.2.2.2). Lipo-FAM™-siRNA-MSNs and Lipo-MSNs were prepared according to 3.2.2.4.5. Subsequently, the cells were treated with 10 µg/ mL Cy5-MSNs; Lipo-FAM™-siRNA-MSNs, Cy5-MSNs, or 10 µL PBS in triplicates, respectively. After 24 and 96 hours incubation, samples were prepared for flow cytometry analysis according to the general protocol (3.2.4.1).

3.2.4.3.2 Flow cytometry analysis

The samples were transferred to 5 mL polystyrene round-bottom tubes and at least 10 000 events were analyzed with LSR II flow cytometer at a high flow rate. The settings are shown in Table 22.

Table 22: Flow cytometer settings for uptake comparison of Cy5-MSNs, Lipo-FAM-siRNA-MSNs and Lipo-MSNs

	Channel	Laser (nm)	Voltage
Size	FSC	488	280
Granularity	SCC	488	240
FAM	GFP	488	400
FVD780	APC-Cy7	635	500
Cy5-MSN	APC	635	550

The gating and analysis were performed with cytobank.org. First, the whole cell population was gated in a dot plot (Figure 19A) to remove debris, and then single cells were identified by gating the cell population in a dot plot by size (Figure 19B). Next, a histogram of the single cells in the APC-Cy7 channel was used to distinguish between viable (unstained) and dead (stained) cells as depicted in Figure 19C. The mean fluorescence intensity of Cy5 and fluorescein (FAM) was determined for viable cells only.

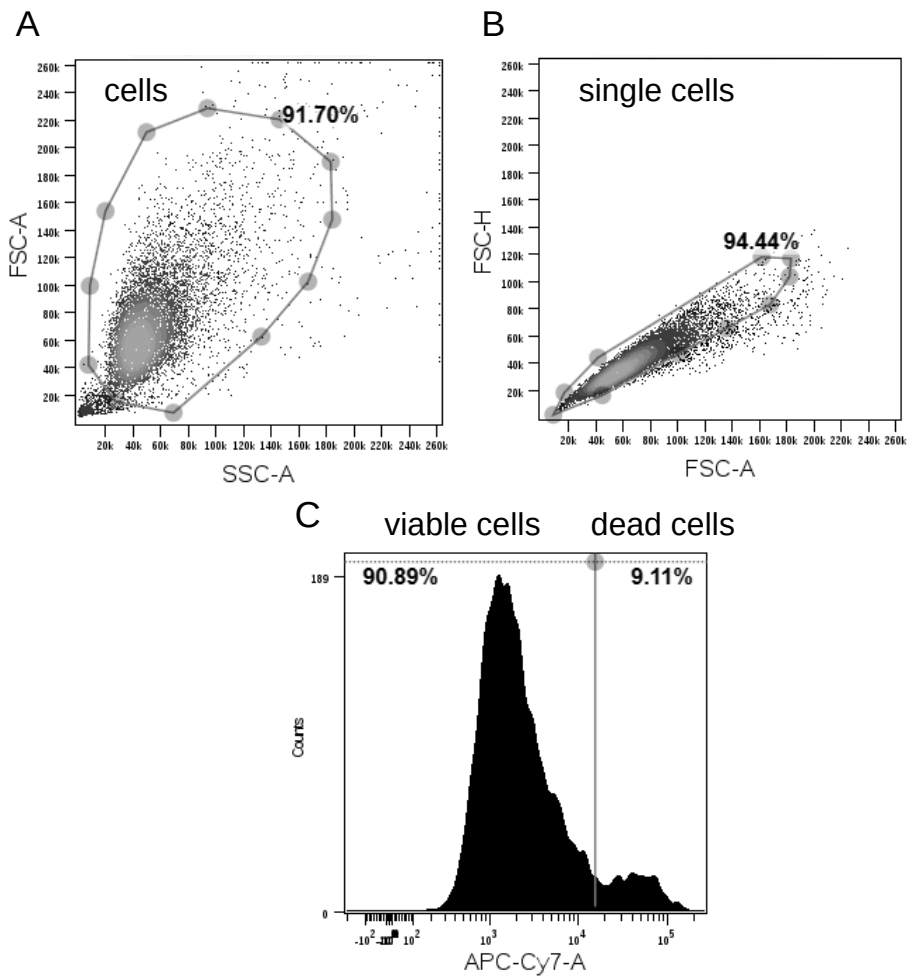

Figure 19: Representative gating of Lipo-FAM™-siRNA-MSNs after 24 hours incubation
(A) The cell population was identified by a dot plot of SCC-A vs FSC-A. (B) Then, the cells were gated in a dot plot with FSC-A vs. FSC-H to determine single cells. (C) The single cells were separated in a histogram of the APC-Cy7-A channel (FVD780) into viable and dead cells. The population of viable cells was used for further analysis.

3.2.4.4 Release of doxorubicin from Dox-MSNs

The uptake of Dox-MSNs and the Dox release was studied in HNSCCUM-02T cells.

3.2.4.4.1 Sample preparation

The HNSCCUM-02T cells were seeded at 50 000 cells per well in 12-well cell culture plates and incubated for two days. The Dox-MSN were prepared according to the standard protocol (3.2.2.3) by loading 2.15 nmol Dox per µg MSNs in ddH_2O. The loading efficiency ranged from 6 % to 31 % Dox (w/w) corresponding to 0.42 ± 0.22 nmol Dox per µg MSNs. The cells were treated for two hours and 24 hours with 1 µM free Dox, 10 µg/ mL Dox-MSNs (corresponded to 4.2 ± 2.2 µM Dox), or Cy5-MSNs, respectively, while PBS was used as control.

Then, the samples for flow cytometry analysis were prepared as stated in the general protocol (3.2.4.1).

3.2.4.4.2 Flow cytometry analysis

The samples were transferred to 5 mL polystyrene round-bottom tubes and at least 10 000 events were analyzed with LSR II flow cytometer at a high flow rate. The settings are displayed in Table 23.

Table 23: Settings for flow cytometry analysis of Dox release and Dox-MSN uptake

	Channel	Laser (nm)	Voltage
Size	FSC	488	250
Granularity	SCC	488	250
Doxorubicin	PE	488	370
FVD780	APC-Cy7	635	480
Cy5-MSNs	APC	635	600

The gating and analysis were performed with cytobank.org. First, the whole cell population was gated in a dot plot (Figure 20A) to remove debris and then single cells were identified by gating the cell population in a dot plot by size (Figure 20B). Next, a histogram of the single cells in the APC-Cy7 channel was used to distinguish between viable (unstained) and dead (stained) cells (Figure 20C). Besides, the single cells were further gated in a dot plot (Figure 20D) to distinguish between cells which were associated with Cy5-MSNs and with Dox (+ Cy5 + Dox) or without Dox signal (+ Cy5 - Dox), and cells without Cy5-MSN association with Dox signal (- Cy5 + Dox) and without Dox signal (- Cy5 - Dox), respectively. The experiment was performed three times.

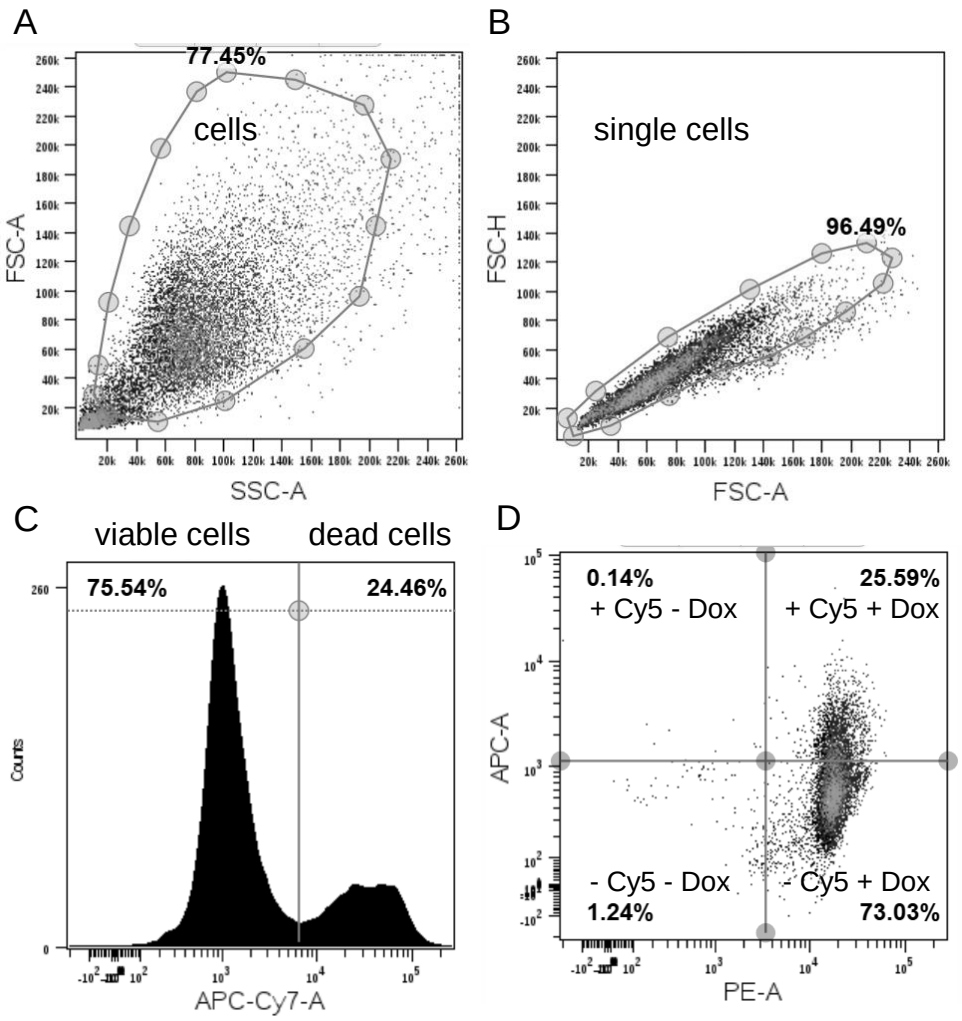

Figure 20: Representative gating of Dox-MSN treated cells (24 hours) to evaluate MSN uptake and Dox release

(A) The cells were identified by gating SSC-A vs FSC-A in a dot plot. (B) The single cells were determined by gating FSC-A vs FSC-H. (C) Single cells were subjected to analysis in a histogram of the APC-Cy7-A channel to identify viable and dead cells. (D) Viable cells were evaluated further in a dot plot of the PE-A (Dox) channel vs. APC-A (Cy5) channel to diagnose MSN uptake and Dox release. Graphics obtained from community.cytobank.org.

3.2.4.5 eGFP expression in HuH7-GFP after eGFP-siRNA-MSN treatment

The efficacy of eGFP-siRNA-MSNs was tested in HuH7-GFP cells. The NPs were prepared according to 3.2.2.4.1 and applied in different concentrations and for different time intervals.

3.2.4.5.1 Sample preparation

The HuH7-GFP and HuH7 cells were seeded at 50 000 cells per well in 12-well cell culture plates and incubated overnight. The next day, the cells were treated with DPEC-H_2O, 10 µg/ mL or 20 µg/ mL Cy5-MSNs, eGFP-siRNA-MSNs, or nsRNA-MSNs in cell culture me-

dium in duplicates for 72 or 144 hours, respectively. A transfection of HuH7-GFP cells with eGFP-siRNA was conducted as described above (3.2.1.7) and cells were incubated for 96 hours. Then, samples for flow cytometry analysis were prepared as mentioned before (3.2.4.1).

3.2.4.5.2 Flow cytometry analysis

The samples were transferred to 5 mL polystyrene round-bottom tubes and at least 10 000 events were analyzed with LSR II flow cytometer at a high flow rate. The settings are shown in Table 24.

Table 24: Flow cytometer settings for analysis of eGFP expression and MSN uptake

	Channel	Laser (nm)	Voltage
Size	FSC	488	250
Granularity	SCC	488	250
GFP	GFP	488	383
FVD780	APC-Cy7	635	480
Cy5-MSNs	APC	635	600

The gating and analysis were performed with cytobank.org according to 3.2.4.3.2. Histograms (viable cells) of the GFP and the APC channel were utilized to evaluate the mean fluorescence intensity of those channels and thereby determine GFP knockdown and NP uptake. The experiment was performed once.

3.2.4.6 eGFP expression in HuH7-GFP after Lipo-eGFP-siRNA-MSN treatment

The efficacy of Lipo-eGFP-siRNA-MSNs was tested in HuH7-GFP cells. The NPs were prepared according to 3.2.2.4.5 and applied in different concentrations. An RNA interference experiment (see 3.2.1.7) was performed in parallel as a positive control in all experiments.

3.2.4.6.1 Sample preparation

The HuH7-GFP cells were seeded at 100 000 cells per well in 12-well cell culture plates and let adhere overnight. In the first experiment, cells were treated with 10 µg/ mL Lipo-eGFP-siRNA-MSNs, Lipo-nsRNA-MSNs, or 10 µL PBS in triplicates, respectively. In a second experiment, cells were treated with 25 µg/ mL Lipo-eGFP-siRNA-MSNs, Lipo-nsRNA-MSNs, Lipo-MSNs, or 25 µL PBS in triplicates, respectively. After 96 hours incubation, the NP treated samples and the transfected samples were prepared for flow cytometry analysis as mentioned before (3.2.4.1).

3.2.4.6.2 Flow cytometry analysis

The samples were transferred to 5 mL polystyrene round-bottom tubes and at least 10 000 events were analyzed with LSR II flow cytometer at a high flow rate. The settings are shown in Table 25.

Table 25: Flow cytometer settings for eGFP expression analysis after Lipo-eGFP-siRNA-MSN treatment

	Channel	Laser (nm)	Voltage
Size	FSC	488	300
Granularity	SCC	488	240
GFP	GFP	488	383
FVD780	APC-Cy7	635	500
Cy5-MSNs	APC	635	650

The gating and analysis were performed with cytobank.org as previously described (3.2.4.3.2). Histograms (viable cells) of the GFP and the APC channel were utilized to evaluate the mean fluorescence intensity of those channels and thereby determine GFP knock-down and NP uptake. Each experiment was performed once.

3.2.4.7 Antibody-coupled nanoparticles

The uptake and binding of EGFR-antibody and IgG2a-antibody-targeted MSNs were evaluated in HNSCCUM-02T cells and RPMI2650 cells. The preparation of antibody-coupled MSNs was performed according to 3.2.2.5.

3.2.4.7.1 Sample preparation

The HNSCCUM-02T cells (100 000 cells per well) and the RPMI2650 cells (200 000 cells per well) were seeded in 12-well cell culture plates and let adhere and proliferate for two days in an incubator. Then, 10 µL of 1 mg/ mL EGFR-MSNs, IgG2a-MSNs, Cy5-MSNs, or PBS were added to the medium in triplicates and cells were incubated further for one hour and 24 hours. Samples for flow cytometry analysis were prepared according to the general protocol (3.2.4.1).

3.2.4.7.2 Flow cytometry analysis

The samples were transferred to 5 mL polystyrene round-bottom tubes and at least 10 000 events were analyzed with LSR II flow cytometer at medium (one hour samples) or low (24 hours samples) flow rates. The settings are shown in Table 26.

Table 26: Flow cytometer settings for analysis of antibody-coupled MSN

	Channel	Laser (nm)	Voltage HNSCCUM-02T	Voltage RPMI2650
Size	FSC	488	280	320
Granularity	SCC	488	240	260
Cy5-MSN	APC	635	550	550
FVD780	APC-Cy7	635	500	500

The gating and analysis were performed with cytobank.org as mentioned before (3.2.4.3.2). The single cells were gated in a dot plot (Figure 21) to distinguish between viable cells which were associated with Cy5-MSNs (viable + Cy5), dead cells associated with Cy5-MSNs (dead + Cy5), viable (viable - Cy5) and dead cells (dead - Cy5) without Cy5-MSN association, respectively. The experiment was performed three times.

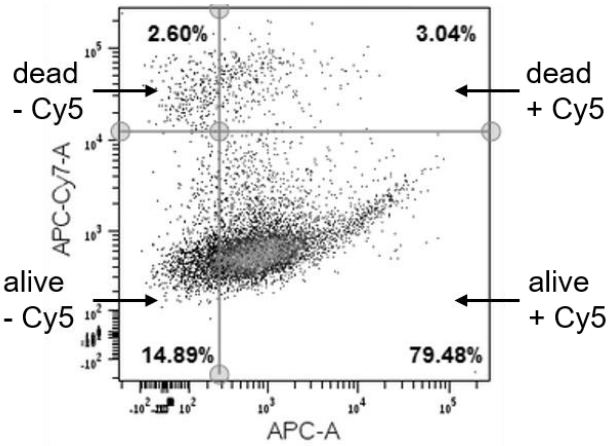

Figure 21: Representative gating of HNSCCUM-02T cells incubated for one hour with EGFR-MSNs

After the population of single cells was identified as described above (3.2.4.3.2), these cells were analyzed in a dot plot with the APC-A (Cy5) channel vs. the APC-Cy7-A (FVD780) to discriminate alive cells with Cy5 association (alive + Cy5), dead cells with Cy5 association (dead + Cy5) and dead and alive cells without Cy5 association (dead - Cy5, alive - Cy5), respectively.

3.2.5 Biocompatibility of MSNs by using the CAM assay

Chicken embryos (CE) were used to simulate an *in vivo* environment and analyze the biocompatibility and the *in vivo* distribution of Cy5-MSNs. All CEs were handled and supervised with the technical assistance of Simone Mendler. An overview of the workflow is presented in Figure 22.

First, the fertilized eggs were carefully cleaned with sterilized water, screened for any damage, and intact eggs were horizontally placed in a freshly cleaned incubator at 37.5 °C. After three days incubation, circa 6 mL albumen were removed from each egg at the side with the air chamber by using a syringe (with a needle), and the hole was sealed with sticky tape. Then, a micropore bandage was attached horizontally to the top of the egg to prevent eggshells falling into the egg while the top was cut out with scissors to generate an oval hole with a longitudinal diameter of 2 cm and a perpendicular diameter of 1.5 cm. The egg was checked for fertilization, sealed with Parafilm “M”™, and further incubated for four days. The CEs were monitored daily for viability and dead embryos were removed. The viability was characterized by steady blood flow and visible heartbeat. On the seventh day of incubation, the hole was increased to 3.5 x 2 cm, a blood vessel was carefully cut with a scalpel, and a 3D-culture of HuH7 or HuH7-GFP cells (preparation described in 3.2.1.6) was directly placed on the wound, and 20 µL Matrigel were added to the cells. Subsequently, the CEs were incubated further with minimal movement to enhance tumor growth, which was monitored regularly. After the tumor could grow for five days, 50 µL 0.9 % (m/V) sodium chloride solution, 0.5 mg/ mL Cy5-MSNs, or 1.0 mg/ mL Cy5-MSNs were injected into a blood vessel. Beforehand, the NPs (SK-275; 750 µg and 1500 µg) were sealed according to the standard protocol (2.2.2.2), but before usage, the dispersion medium was changed to 0.9 % (m/V) sodium chloride. In brief, the MSNs were centrifuged (10 000 g, 5 min, 20 °C), the PBS was removed, the appropriate volume of 0.9 % sodium chloride solution was added, and the Cy5-MSNs were sonicated and vortexed. The CEs were incubated for 24 hours after the injection of Cy5-MSNs or control solution and the viability was evaluated. Furthermore, the CAM with tumor, heart, liver, brain, and kidneys were removed from three embryos of each treatment group, transferred to immunohistochemistry cassettes, and fixed in 4 % PFA overnight. Tissue samples were stored in 1 % PFA until further processing as described in 3.2.6.5.

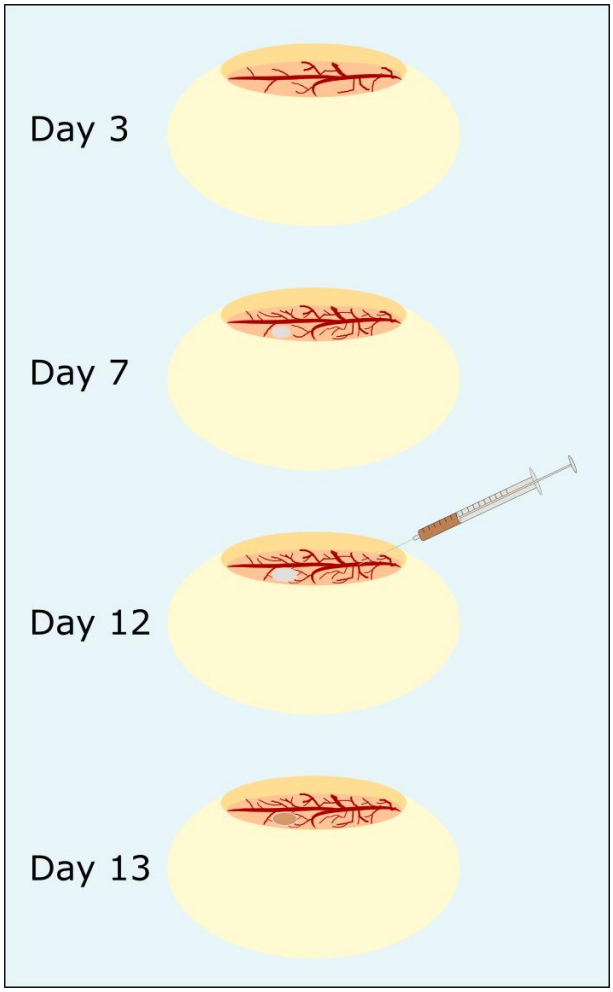

Figure 22: An *in vivo* biocompatibility test by means of the chorioallantoic membrane assay

Fertilized chicken eggs were cut open on the third day of incubation and checked for viability. On the seventh day of incubation, a 3D-cell culture model was placed on the CAM. Cy5-MSNs or 0.9 % sodium chloride solution were injected after the tumor grew for five days. The next day, viability was assessed, and tissue samples were removed for biodistribution studies.

3.2.6 Confocal laser scanning microscopy (CLSM)

If not otherwise stated, the images were taken with a 630-fold magnification (HC PL APO CS2 63x/ 1.40 Oil objective) in the sequential scan mode, with two frames average and a 2048^2 resolution at a DMi8 confocal laser scanning microscope (Leica Microsystems). The pinhole was set at 1.0 airy units and the zoom was set to 1.0. The captured section was 184.52^2 µm² and the pixel size was 90.14^2 nm². The used solutions for staining are depicted in Table 7.

3.2.6.1 Nanoparticle uptake

The MSN uptake was studied in HNSCCUM-02T cells for 24 and 48 hours.

3.2.6.1.1 Sample preparation

The HNSCCUM-02T cells were seeded at 15 000 cells per well in µ-slide 8 well and let adhere overnight. The experiment was performed in parallel to 3.2.4.2 and the same prepared Cy5-MSNs were utilized. The cells were treated with 10 µg/ mL Cap1-Cy5-MSNs or PBS, respectively, and incubated for 24 and 48 hours. Then, the medium was removed, cells were washed with PBS (3 times, 5 min, RT), and the cells were fixed with 4 % PFA (15 min, RT). Next, the cells were washed again with PBS (3 times, 5 min, RT) and stored until staining under light protection at 4 °C. Right before staining, the cells were fixed with ice-cold acetone (4 min, RT), washed with PBS (3 times, 5 min, RT), and blocked with 1 % bovine serum albumin Fraction V (BSA) in PBS at RT. Subsequently, samples were stained with AlexaFluor® 555-Phalloidin (1:40) in 1 % BSA in PBS for 20 minutes while gently shaking. The cells were washed with PBS (3 times, 5 min, RT) and were embedded in Vectashield® Hardset™ Antifade Mounting Medium with DAPI and sealed with a glass coverslip. The samples were stored protected from light at 4 °C.

3.2.6.1.2 Microscopy

Ten microscopic images were obtained per treatment with the standard settings (3.2.6) and the settings stated in Table 27. Images were exported with Fiji [151].

Table 27: Settings for MSN uptake analysis

Target	Color	Laser (nm)	Laser intensity (%)	Gain (V)	PMT detection area (nm)
Nuclei	blue	405	3.70	714.8	408-479
F-Actin	red	552	4.51	646.3	555-638
Cy5-MSNs	green	638	8.04	822.1	640-737

3.2.6.2 Nanoparticle uptake and trafficking

The NP uptake and trafficking were examined in HNSCCUM-02T cells by co-localization staining of Cy5-MSNs with early endosomal marker EEA1 and endosomal and lysosomal marker Lamp1.

3.2.6.2.1 Sample preparation

The HNSCCUM-02T cells were seeded at 10 000 cells per well in µ-slide 8 well and let adhere overnight. For each experiment 100 µg Cy5-labeled MSNs (SK-267 SK2) were sealed

according to the standard protocol (3.2.2.2). The cells were treated with 10 µg/ mL Cy5-MSNs for two, six, 24, 30, and 48 hours while PBS was used as control (zero hours). Then, the medium was removed, the cells were washed with PBS (3 times, 5 min, RT), and the cells were fixed with 4 % PFA (15 min, RT). Next, the cells were washed again with PBS (3 times, 5 min, RT) and stored until staining under light protection at 4 °C. Right before staining, the cells were fixed with ice-cold acetone (4 min, RT), washed with PBS (3 times, 5 min, RT), and blocked with 5 % BSA in PBS + 0.3 % TritonX-100 (1 h, RT). The samples were stained with anti-LAMP1 (D2D11) XP® rabbit antibody (1:100 in PBS + 0.3 % TritonX-100, 1 h, RT) or EEA1 antibody (1:200 in PBS + 0.3 % TritonX-100, 1 h, RT), respectively, and washed twice with PBS (5 min, RT), once with TBST 400 mM NaCl (2 min, RT), and once with PBS (5 min, RT). Subsequently, the samples were stained with secondary goat anti-rabbit AlexaFluor® 488 antibody (1:500), AlexaFluor® 555-Phalloidin (1:40) and DAPI (300 nM) in one dilution in 0.5 % BSA in PBS + 0.3 % TritonX-100 for one hour at RT. After the samples were washed (twice PBS 5 min, once TBST 400 mM NaCl 2 min, PBS 5 min, H_2O 2 min), they were embedded in Vectashield® Antifade Mounting Medium and sealed with a glass coverslip. The samples were stored protected from light at 4 °C.

3.2.6.2.2 Microscopy

Ten microscopic images per time point and marker staining were taken at 4096^2 resolution. Microscope settings are depicted in Table 28 and Table 29.

Table 28: Imaging settings for EEA1 staining

Target	Color	Laser (nm)	Laser intensity (%)	Gain (V)	PMT detection area (nm)
Nuclei	blue	405	2.79	743.7	408-479
EEA-1	green	488	8.11	580	503-548
F-Actin	white	552	7.17	698.7	555-638
Cy5-MSNs	red	638	8.04	650	640-737

Table 29: Imaging settings for Lamp1 staining

Target	Color	Laser (nm)	Laser intensity (%)	Gain (V)	PMT detection area (nm)
Nuclei	blue	405	3.70	780	408-479
Lamp1	green	488	2.68	632.7	503-548
F-Actin	white	552	8.08	700	555-638
Cy5-MSNs	red	638	9.83	700	640-737

3.2.6.2.3 Uptake analysis

All images were analyzed with Fiji (ImageJ). The nuclei per image were counted with the 'Multipoint' tool manually. The channel displaying Cy5-MSNs was converted into a greyscale image to count Cy5-MSNs and the unspecific background was removed by setting the threshold to 0-12 (EEA1 images) or 0-23 (Lamp1 images), respectively. Then, the Cy5-MSNs were counted automatically with the 'Analyze Particles' tool while the size was limited to 15-∞ pixels and the circularity was set to 0.00-1.00. The number of Cy5-MSNs was divided by the nuclei number to determine Cy5-MSNs per cell (n=20 per time point). The experiment was repeated three times.

3.2.6.2.4 Co-localization analysis

The co-localization analysis of Cy5-MSNs with the respective marker was conducted with 'JACoP' plugin in ImageJ [160]. First, the images were split in green (EEA1 or Lamp1) and red (Cy5-MSNs) channels and the thresholds for each channel were set according to Table 30. For some images the chosen threshold could not be set, in that case, the threshold was set one unit higher. Then, the Manders' coefficients *M*1 and *M*2 were determined for each image (Equation 5 and Equation 6) to evaluate the ratio of Cy5-MSN signal with marker signal overlap to total Cy5-MSN signal (*M*1) [161]. The average of each Cy5-MSN and marker co-localization in each experiment was calculated for each time point.

Table 30: Threshold settings for co-localization analysis

Experiment	EEA1		Lamp1	
	red	green	red	green
1	35	21	35	41
2	32/33	20/21	43/44	43/44
3	34/35	30	34/35	50

Equation 5

$$M1 = \frac{\sum_i \text{red and green pixels}}{\sum_i \text{red pixels}}$$

Equation 6

$$M2 = \frac{\sum_i \text{green and red pixels}}{\sum_i \text{green pixels}}$$

3.2.6.3 Detection of DNA damage

The DNA damage after free Dox, Dox-MSN, and Cy5-MSN treatment was evaluated in HNSCCUM-02T and RPMI2650 cells by means of γH2AX foci staining. γH2AX foci are in-

duced upon DNA damage and correlate to the severity of DNA damage by DNA-damaging agents (see 1.4.1).

3.2.6.3.1 Sample preparation

The HNSCCUM-02T cells (5 000 cells per well) and RPMI2650 cells (10 000 cells per well) were seeded each in two µ-slides 8 well and let adhere for two days. One µ-slide was treated for two hours, the other slide for 24 hours with 1 µM Dox, 10 µg/ mL Dox-MSNs, or Cy5-MSNs in the respective cell culture medium, respectively, while PBS was used as control. The preparation of Dox-MSNs and Cy5-MSNs was conducted according to 3.2.2.3 and the same NPs as described in 3.2.4.4.1 were used. In the next step, the treatment solutions were removed, samples were washed with PBS (3 times, 5 min, RT), and cells were fixed with 4 % PFA (15 min, RT). The cells were washed again with PBS (3 times, 5 min, RT) and stored until staining under light protection at 4 °C. Right before staining, cells were fixed with ice-cold methanol (10 min, RT), washed with PBS (3 times, 4 min, RT), and blocked with 5 % BSA in PBS + 0.3 % TritonX-100 (45 min, RT, gentle shaking). Then, the samples were stained with phospho-Histone H2A.X (Ser139) antibody (mouse), Clone JBW301 (1:500 in PBS + 0.3 % TritonX-100, 1 h, RT, gentle shaking) and washed twice with PBS (4 min, RT), once with TBST 400 mM NaCl (2 min, RT) and once with PBS (4 min, RT). The samples were stained with secondary goat anti-mouse AlexaFluor® 488 antibody (1:500) and DAPI (450 nM) in one dilution in 0.5 % BSA in PBS + 0.3 % TritonX-100 for 45 minutes at RT under gentle agitation. After the samples were washed (twice PBS 5 min, once TBST 400 mM NaCl 2 min, PBS 5 min, H_2O 2 min), they were embedded in Vectashield® Antifade Mounting Medium and sealed with a glass coverslip. The samples were stored protected from light at 4 °C.

3.2.6.3.2 Microscopy

At least three images were taken per treatment and time point for each experiment with the standard settings (3.2.6) and the settings presented in Table 31.

Table 31: Imaging settings for γH2AX foci staining

Target	Color	Laser (nm)	Laser intensity (%)	Gain (V) HNSCCUM-02T	Gain (V) RPMI2650	PMT detection area (nm)
Nuclei	blue	405	5.52	700	677.4	408-496
Doxorubicin	white	488	8.12	650	650	581-623
γH2AX foci	green	488	8.12	720	720	505-535
Cy5-MSNs	red	638	7.13	600	600	640-737

3.2.6.3.3 Analysis

The images were handled with Fiji and opened in multichannel mode. The color balance was adjusted for each channel to reduce unspecific background staining. The scale was set to 11.0979 pixels per µm and nuclei were encircled manually as the region of interest (ROI). This ROI was added in the γH2AX foci channel to the ROI manager. In that way, every nucleus could be analyzed separately for the ratio of γH2AX foci area per nucleus. At least 50 nuclei were evaluated per treatment and time point. The γH2AX foci channel was transformed to greyscale and the threshold was set to 80-255 to remove the unspecific background signal. Next, the ratio of γH2AX foci area per nucleus was determined with the 'Analyze Particles' tool. The particle size was set to 0.12-∞ µm² for HNSSCUM-02T and 0.08-∞ for RPMI2650 samples, respectively, while the circularity was set to 0.00-1.00 and a mean was generated for each experiment. Finally, the mean and standard deviation of three independent experiments were determined.

3.2.6.4 Antibody-coupled nanoparticles

The uptake and association of antibody-coupled NPs were examined by confocal laser scanning microscopy. The experiment was performed in parallel with flow cytometry analysis (3.2.4.7) and antibody-coupled NPs were prepared according to 3.2.2.5.

3.2.6.4.1 Sample preparation

The HNSCCUM-02T cells (5000 cells per well) and RPMI2650 cells (20000 cells per well) were seeded in 200 µL per well µ-slides 8 well and let adhere for two days. Then, 2 µL of 1 mg/ mL EGFR-MSNs, IgG2a-MSNs, Cy5-MSNs, or PBS were added to one well per cell line. After one hour or 24 hours incubation, respectively, the supernatants were removed and the samples were washed with PBS (3 times, 5 min, RT). Next, the cells were fixed with 4% PFA (15 min, RT), the samples were washed again with PBS (3 times, 5 min, RT), and stored under light protection at 4 °C. Right before staining, cells were fixed with ice-cold acetone (4 min, RT), washed with PBS (3 times, 5 min, RT), and blocked with 1% BSA in PBS (30 min, RT, gentle shaking, light protection). Samples were incubated with AlexaFluor® 555-Phalloidin (1:40) and DAPI (450 nM) in one dilution in 1% BSA in PBS (45 min, RT, gentle shaking, light protection), washed with PBS (3 times, 5 min, RT), and washed once with H_2O for two minutes. Finally, samples were embedded in Vectashield® Antifade Mounting Medium and sealed with a glass coverslip. The samples were stored protected from light at 4 °C.

3.2.6.4.2 Microscopy

At least five images were taken per treatment and time point for each experiment with the standard settings (3.2.6) and the settings presented in Table 32.

Table 32: Imaging settings for targeted MSNs

Target	Color	Laser (nm)	Laser intensity (%)	Gain (V) HNSCCUM-02T	Gain (V) RPMI2650	PMT detection area (nm)
Nuclei	blue	405	5.51	721.2	671.7	408-479
F-Actin	red	552	7.17	637.4	637.4	555-638
Cy5-MSNs	green	638	8.95	508.8	508.8	640-737

3.2.6.5 Biodistribution of Cy5-MSNs in chicken embryonic organs

Several organs from chicken embryos (see 3.2.5) including the CAM with tumor were examined with confocal laser scanning microscopy to evaluate the *in vivo* distribution of Cy5-MSNs. The preparation of paraffin sections and the DAPI staining were conducted with the technical assistance of [redacted].

3.2.6.5.1 Preparation of paraffin sections and DAPI staining

The washing and dehydration of the tissues were performed at RT and under light protection. First, the fixed tissues were washed thrice with deionized water for 20 minutes each and then were incubated in 70 % (V/V) isopropanol in deionized water for one hour. Next, the samples were incubated in 80 % (V/V) and then 90 % (V/V) isopropanol in deionized water for one hour each and in 100 % isopropanol for one and a half hours. Afterward, the tissues were incubated for two hours in xylene and overnight in fresh xylene. The cassettes were transferred to liquid paraffin, incubated for four hours at 60 °C, transferred to fresh liquid paraffin, and incubated overnight at 60 °C. The embedding of the tissues was conducted with a Leica EG 1140H tissue embedding center. The organs were placed in a small form, liquid paraffin was added, and the form was placed on a cooling plate. The paraffin tissue sections were cut with a Leica RM2165 rotary microtome to 3-5 µm sections and placed on microscope slides. Subsequently, the tissue sections were deparaffinated with the following protocol: incubation in xylene for five minutes twice, incubation in 100 %, 90 %, 80 %, 70 % (V/V) isopropanol in deionized water for five minutes each, and five minutes incubation in deionized water. Finally, the samples were embedded in Vectashield® Hardset™ Antifade Mounting Medium with DAPI and solidified for at least 24 hours before microscopic analysis.

3.2.6.5.2 Microscopy

The analysis of the paraffin sections was performed based on the above-mentioned standard protocol (3.2.6), however, a 40x objective and 1x zoom was used resulting in an image size of 290.62^2 µm^2 and a pixel size of 141.98^2 nm^2. At least five images were recorded per organ and Cy5-MSN concentration with the settings displayed in Table 33.

Table 33: Imaging settings for *in vivo* distribution analysis

Target	Color	Laser (nm)	Laser intensity (%)	Gain (V)	PMT detection area (nm)
Nuclei	blue	405	3.70	678.3	408-479
Autofluorescence	green	488	8.13	628.9	503-548
Cy5-MSNs	red	638	8.17	542.6	640-720

The images were exported with Fiji and the color balance was adjusted to 2- 255 for each channel. A scale bar was added representing 10 µm.

3.2.7 mRNA expression analysis

The mRNA expression was analyzed to determine a change in mRNA expression after RNA interference experiments and siRNA-loaded NP treatment.

3.2.7.1 Sample preparation

The cells were seeded in 6-well plates at 100 000 cells or according to 3.2.1.7. Then, the cells were incubated with different NP dispersions in different concentrations (10 µg/ mL, 25 µg/ mL, 50 µg/ mL) for various time points (24, 72 and 96 hours) and PBS was applied as control (the applied NPs, concentrations and incubation times are stated in the respective results chapter). The media were discarded, the cells were briefly washed with PBS, and detached with Accutase® solution. The medium was added to disperse the cells and the samples were transferred to centrifuge tubes. After centrifugation (1 500 rpm, 5 min, RT), the supernatants were discarded, the samples were washed with PBS, and centrifuged again. The PBS was carefully removed with a pipette and the RNA was isolated.

3.2.7.2 RNA isolation

The RNA isolation was conducted with innuPREPRNA Mini kit according to the manufacturer's protocol. First, 400 µL Lysis solution RL were added to the cell pellet and the sample was incubated at RT for two minutes. Next, the sample was dissolved by pipetting and incubated further for three minutes. The lysed sample was added to a Spin filter D and centrifuged

(12 000 rpm, 2 min, RT, Biofuge fresco). Afterward, the sample was mixed with 400 µL 70 % (V/V) ethanol in water until the solution was clear again, transferred to a Spin filter R, and centrifuged (12 000 rpm, 2 min, RT). The RNA remained on the filter and first was washed with 500 µL washing solution high-salt by centrifugation (12 000 rpm, 1 min, RT) and second, was washed with 700 µL washing solution low salt by centrifugation (12 000 rpm, 1 min, RT). The Spin filter R was centrifuged for three minutes (12 000 rpm, RT) to remove any remaining ethanol. Finally, 40 µL RNAse-free water were added to the middle of the filter, the sample was incubated for one minute, and centrifuged (8 000 rpm, 1 min, RT) in a 1.5 mL centrifuge tube. The RNA concentration was measured with NanoDrop 2000 Spectrophotometer and the isolated RNA was stored at -80 °C.

3.2.7.3 cDNA transcription

Aliquots containing 1 µg isolated RNA were diluted to 50 ng/ µL with DPEC-H_2O in a final volume of 20 µL in 0.2 mL tubes on ice. Then, the diluted RNA was incubated at 65 °C for ten minutes in a Biometra® T personal 48 Thermocycler. Meanwhile, an adequate volume of the master mix for cDNA transcription was prepared on ice according to Table 34. 30 µL of cDNA transcription master mix were added per sample and the cDNA was transcribed with the following program in the Biometra® T personal 48 Thermocycler: Two minutes incubation at 25 °C, 30 minutes incubation at 48 °C, and five minutes incubation at 95 °C. Finally, the samples were kept at 4 °C until storing at -20 °C.

Table 34: Master mix for cDNA transcription

Reagent	1x master mix
Random Primer	1 µL
25 mM $MgCl_2$	8 µL
10 mM nucleotide mix	5 µL
10x buffer Applied Biosystems with 15 mM $MgCl_2$	5 µL
RNasin	0.5 µL
M-MLV	0.5 µL
DPEC-treated water	10 µL
Total volume	30 µL

3.2.7.4 Real-time polymerase chain reaction (qPCR)

A real-time polymerase chain reaction assay was performed to determine the mRNA expression of the desired targets. The instructions by Applied Biosystems™ for TaqMan™ Gene Expression Analysis were adapted to generate the following protocol: The appropriate primers were thawed on ice under light protection and spun down before use. The cDNA was

either directly used after transcription or thawed on ice and was mixed before use. Each sample was analyzed in duplicate and a calibrator cDNA generated from untreated HNSCCUM-02T cells or HuH7-GFP cells was utilized, respectively. First, 5 µL (100 ng) per sample or calibrator sample were pipetted into a MicroAmp® Fast optical 96-well Reaction Plate per required well while DPEC-H_2O was used as the negative control. The master-mixes for the target gene and the reference gene, namely large ribosomal protein (RPLPO), were prepared on ice and contained 10 µL TaqMan™ Universal PCR Master Mix, 1 µL 20x Primer and 4 µL DPEC-H_2O per unit. In the next step, the reaction mixture was added to each well (15 µL), air bubbles were removed with a needle, the plate was tightly sealed with Micro-Amp™ Optical Adhesive Film and briefly centrifuged to collect the samples in the bottom. A StepOnePlus™ was used to perform real-time polymerase chain reaction with the following incubation parameters: two minutes at 50 °C, ten minutes at 95 °C, and 40 cycles with 95 °C for 15 seconds and 60 °C for one minute. The fluorescence probe was measured at the 60 °C incubation step once per cycle. For analysis, the threshold was adjusted to 0.135233 for hnRNP K, to 0.074879 for GAPDH, to 0.149301 for eGFP, and to 0.137207 for RLPLO. The resulting threshold cycle C_T was used to evaluate gene expression with the comparative $\Delta\Delta C_T$ method. Untreated HNSCCUM-02T samples or HuH7-GFP samples were utilized as calibrator samples and RLPLO was employed as the reference gene, respectively [162]. The used equations are stated in Equation 7, Equation 8 and Equation 9.

Equation 7

$$\Delta C_T = \text{average } C_T(\text{Target}) - \text{average } C_T\ (\text{RPLPO})$$

Equation 8

$$\Delta\Delta C_T = \Delta C_T(\text{Sample}) - \Delta C_T(\text{Calibrator})$$

Equation 9

$$r\text{elative mRNA expression} = 2^{-\Delta\Delta C_T}$$

3.2.8 EGFR protein expression analysis

The protein expression of EGFR was analyzed in different cell lines by immunoblot analysis. All used solutions are stated in Table 12.

3.2.8.1 Cell lysis

The HNSCCUM-02T cells and HuH7 cells (400 000 cells per flask) were seeded in small cell culture flasks and incubated for three days. The RPMI2650 cells (500 000 cells per flask)

were also seeded in a small cell culture flask and incubated for four days. Then, the cells were washed once with cold PBS, 600 µL lysis buffer were added, and the cells were lysed for five minutes while incubated on ice. The cells were removed with a cell scraper and transferred to 1.5 mL centrifuge tubes. Next, the samples were sonicated for 30 seconds each (50 %, 0.5-second pulse), centrifuged (12 000 rpm, 10 min, 12 °C), and the supernatants were transferred to fresh 1.5 mL centrifuge tubes. The samples were stored at -20 °C.

3.2.8.2 Protein quantitation

The protein content in each sample was determined with DC™ Protein Assay according to the standard protocol. A standard curve from 0 to 4 µg/ mL BSA in lysis buffer was generated. First, 5 µL of protein standards (0, 0.25, 0.5, 1.0, 2.0 and 4.0 µg/ mL) in quadruplicates and 5 µL per sample in triplicates were pipetted into a clear 96-well plate (flat bottom). Second, 25 µL of freshly prepared reagent A' (1 mL reagent A + 20 µL reagent S) were added to each well. Third, 200 µL of reagent B were added to each well and the plate was incubated in Multiskan Ascent Microplate Reader for ten minutes, shaken for ten seconds and the absorbance was measured at 750 nm. The protein content was quantified by means of the standard curve.

3.2.8.3 Immunoblot sample preparation

40 µg proteins were used per sample and diluted to 42 µL with lysis buffer. Subsequently, 0.5 µL 5 % bromophenol blue and 100 mM dithiothreitol (DTT) were added to each sample. Then, the samples were boiled at 95 °C for ten minutes at 500 rpm in Thermomixer comfort, put on ice, briefly spun down, vortexed, spun down, and vortexed again.

3.2.8.4 SDS-polyacrylamide gel electrophoresis

A small discontinuous SDS-polyacrylamide gel was prepared with TGX Stain-Free™ Fast Cast™ Acrylamide Solutions 12 % kit according to the manufacturers' instructions. The gel was placed in an electrophoresis chamber and electrophoresis buffer was added. The first lane was loaded with Thermo Scientific PageRuler Prestained Protein Ladder and 20 µg protein of each sample were carefully pipetted into the gel pockets. The electrophoresis ran at 10 mA until all samples entered the separating gel, the protein separation was conducted with 20 mA until the bromophenol blue left the gel. Then, the gel was removed from the chamber, placed in transfer buffer, and the protein bands were recorded with ChemiDoc™ MP Imaging System in the Stain-free gel modus for two and a half minutes.

3.2.8.5 Protein transfer

The separated proteins were transferred to a polyvinylidene fluoride (PVDF) membrane via a semi-dry blot in a Trans-Blot® Turbo™ Transfer System. The PVDF membrane was shortly activated in methanol and incubated in the transfer buffer. The blotting papers were cut into appropriate pieces and were also incubated in the transfer buffer for 35 minutes at RT. First, two blotting papers were placed in the transfer chamber, then the PVDF membrane, the gel, and again two blotting papers. A hand drum was used to remove any air bubbles. The protein transfer was performed at 0.06 A for 90 minutes. Finally, the membrane was transferred to TBS-T_{20} recorded at ChemiDoc™ MP Imaging System in the stain-free blot modus and shortly incubated in TBS-T_{20}.

3.2.8.6 Protein detection

3.2.8.6.1 EGFR

First, the membrane was incubated in 5 % (m/V) non-fat dry milk in TBS-T_{20} (1 h, gentle shaking, RT) to block unspecific binding. The membrane was washed with TBS-T_{20} three times for five minutes at RT while shaking. Then, the membrane was incubated with Anti-EGF Receptor (D38B1) XP® mAb (1:1 000) in 5 % (m/V) BSA in TBS-T_{20} overnight at 4 °C under gentle agitation. The next day, the membrane was washed again with TBS-T_{20} three times for five minutes at RT while shaking. The membrane was incubated with an anti-rabbit IgG, HRP-linked antibody (1:3 000) in 5 % (m/V) non-fat dry milk in TBS-T_{20} (1 h, gentle shaking, RT) and washed again three times for five minutes with TBS-T_{20}. Then, a freshly prepared 1:1 mixture of Western Lightning™ Plus enhanced luminol reagent and Western Lightning™ Plus oxidizing reagent was pipetted onto the membrane and incubated for two minutes in the dark. Visualization was performed with ChemiDoc™ MP Imaging System.

3.2.8.6.2 β-Actin

After membrane stripping (see 3.2.8.7), the membrane was blocked with 5 % (m/V) non-fat dry-milk in TBS-T_{20} for one hour at RT and washed three times for five minutes with TBS-T_{20}. Then, the membrane was incubated with an anti-β-Actin monoclonal antibody overnight at 4 °C under gentle agitation. The next day, the membrane was washed with TBS-T_{20} (3 times, 5 min, RT) and the membrane was incubated with an anti-mouse IgG, HRP-linked antibody (1:3 000) in 5 % (m/V) non-fat dry milk in TBS-T_{20} (1 h, gentle shaking, RT) and washed again three times for five minutes with TBS-T_{20}. Then, a freshly prepared 1:1 mixture of Western Lightning™ Plus enhanced luminol reagent and Western Lightning™ Plus oxidizing reagent

was pipetted onto the membrane and incubated for two minutes in the dark. Visualization was performed with ChemiDoc™ MP Imaging System.

3.2.8.7 Membrane stripping

The membrane was stripped between the detection of different proteins at RT. First, the membrane was incubated for 30 minutes in 25 mM Glycine pH 2.0 and second, the membrane was incubated for 30 minutes with 1 % (m/V) SDS in desalted water. Finally, the membrane was washed three times for ten minutes with TBS-T_{20}.

3.2.9 Statistical analysis

All statistical evaluations were conducted with GraphPad Prism Software (Prism 5 for Windows, version 5.04). The amount of independently performed experiments (N) was stated in the respective method description and the respective figure caption. All the data were analyzed with explorative and descriptive statistical methods. Usually, the arithmetic mean + standard deviation (S.D.) or the arithmetic mean ± S.D. were calculated and expressed in the figure caption, respectively. The exceptions were indicated there, too. However, it was not possible to test for normal distribution due to small sample sizes. Generally, the data were analyzed with a one-way analysis of variance (ANOVA) and Dunnett's multiple comparison test or a two-way ANOVA and Bonferroni multiple comparisons test when applicable, respectively. The performed tests and results were mentioned in the figure caption and tabular results are presented in the appendix (8.1).

4 Results

In this chapter, the results of this project are presented in the following order: First, the characteristics of the Cy5-MSNs were evaluated without loaded drugs (4.1 and 4.2) and second, Dox was loaded to Cy5-MSNs to study drug loading and release (4.3). Third, siRNA was incorporated into Cy5-MSNs with different loading protocols (4.4) and finally, targeting of the Cy5-MSNs was performed (4.5).

4.1 Characteristics of Cy5-MSNs

The MSNs were synthesized and characterized by [redacted], member of the group of [redacted]. Spherical NPs with different sizes and pore sizes were utilized depending on the purpose, i.e. MSNs with smaller pores were used for loading of the small molecule drug Dox and MSNs with larger pores were used for siRNA loading (see Table 35).

Table 35: Nanoparticle characteristics

MSNs	Diameter (nm)	Pore size (nm)	Pore volume ($cm^3 \cdot g^{-1}$)	Specific surface area ($m^2 \cdot g^{-1}$)
SK-214	205 ± 21	10.0	0.989	503
SK-267	130 ± 10	8.2	1.02	522
SK-268	180 ± 18	5.7	0.8859	622
SK-275	164 ± 14	11.7	0.7925	448

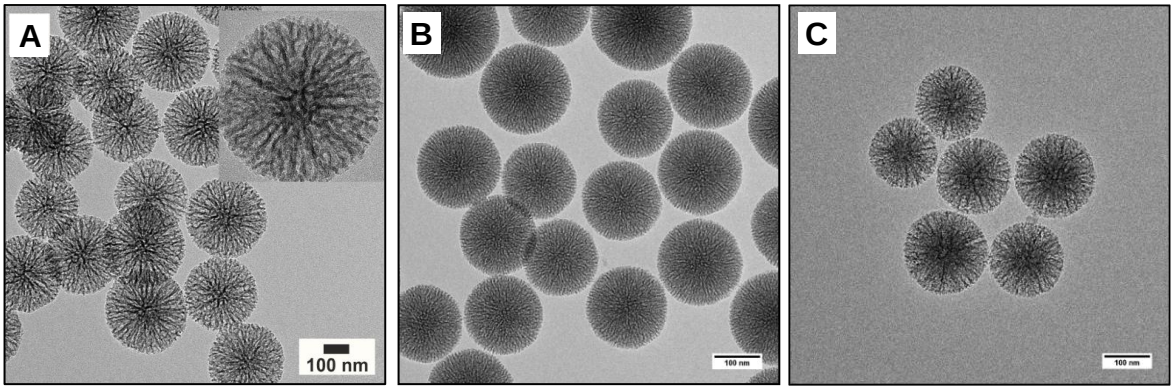

Figure 23: TEM images of predominantly used mesoporous silica nanoparticles
(A) SK-267 with a magnification of a single particle in the right corner. (B) SK-268 and (C) SK-275. Scale: 100 nm. Images provided by [redacted].

The porous structure, spherical shape and even size distribution of the MSNs were observed in TEM images (Figure 23). The respective MSN diameter was determined by dynamic light scattering (DLS) and ranged from 130 ± 10 nm (SK-267) to 205 ± 21 nm (SK-214). Besides, the pore diameter and volume were determined by nitrogen sorption analysis and calculated using the Barrett, Joyner und Halenda (BJH) formula [163]. The MSNs SK-268 had the smallest pores, and the SK-214 had the greatest diameter but both were only used for experiments with unloaded MSNs. The pore size of the MSNs SK-267 was about 8 nm, and these MSNs were used for drug loading and release experiments with Dox. However, MSNs with larger pores (SK-275) were synthesized to enable loading with siRNA. Moreover, the specific surface area was determined according to the Brunauer Emmett-Teller (BET) formula [163] and is depicted in Table 35. The specific surface area is dependent on the adsorbed nitrogen and the applied particle mass and provides an indication for possible loading efficiency in case of drug adsorption to the MSNs' porous structure. The MSNs SK-267 had a greater specific surface area than the MSNs SK-275. All MSNs except SK-214 were labeled with the fluorescent dye Cy5 which allowed monitoring of the NPs via flow cytometry and confocal laser scanning microscopy.

Furthermore, the sealing of the MSNs with ferrocene and β-CD was validated by several examinations: After MSNs (SK-267) were incubated with the gatekeeper solution, the ζ-potential changed from -19 mV to +12 mV, suggesting successful binding of the ferrocene and β-CD (data obtained by Sven Kurch). The application of the gatekeeper system was further examined with DLS, thermogravimetric analysis (TGA) and nitrogen sorption analysis (conducted by Sven Kuch, Figure 24). The diameter of the MSNs slightly increased after ferrocene and β-CD addition (Figure 24A) and loss of organic mass was observed in TGA for ferrocene conju-

gated MSNs (DMSN-AF) and fully sealed MSNs (DMSN-AFC, Figure 24B). Moreover, the pore size and pore volume were evaluated with nitrogen absorption (Figure 24C) after MSN sealing. The pore size of unfunctionalized and unsealed MSNs was about 8 nm on average and the hysteresis regions of the sorption isotherm were shifted to lower relative pressure after addition of the ferrocene and the ferrocene and β-CD, respectively. Also, a decrease in pore volume was noticed upon ferrocene conjugation and adding β-CD further decreased the pore volume. Taken together, conjugation of ferrocene and β-CD sealed the MSNs' pores successfully.

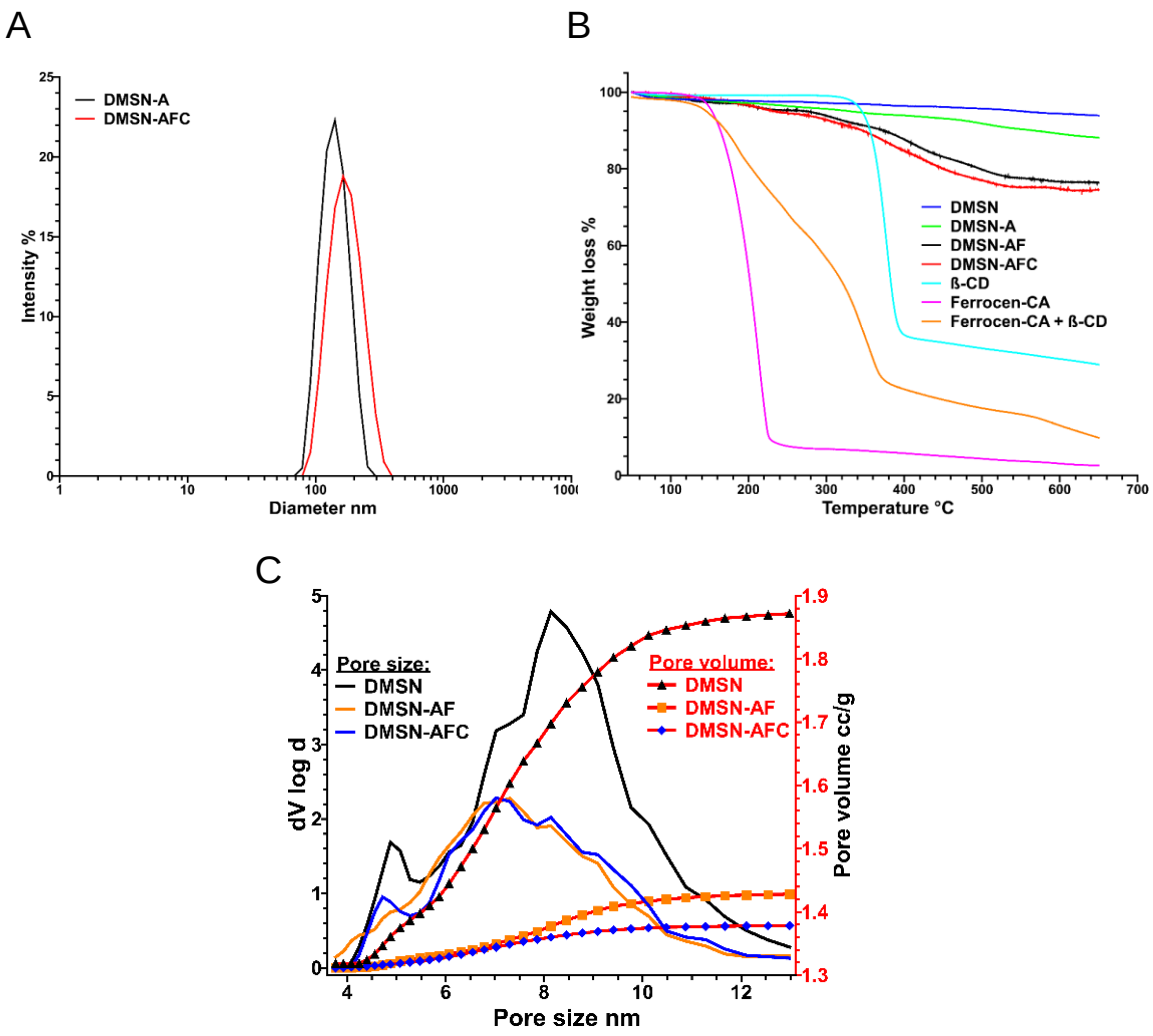

Figure 24: (A) Dynamic light scattering, (B) thermogravimetric analysis, (C) pore size and pore volume of MSNs (SK-267) before and after addition of ferrocene and β-CD

(A) A small increase in particle diameter was observed after incubation of the amino-functionalized MSNs (DMSN-A) with ferrocene and β-CD (DMSN-AFC). (B) The mass loss for each functionalization step of the MSNs (DMSN) was analyzed by thermogravimetric analysis. With an increasing amount of organic coverage by ferrocene (ferrocene-CA) and β-CD, the mass loss increased. The decomposition of the separate components (β-CD, ferrocene-CA) and their inclusion complex (ferrocene-CA + β-CD) is presented, too. DMSN-AF = ferrocene-conjugated and amino-functionalized MSNs. Both decomposition steps were visible, with inflection points at 210 °C and 400 °C. (C) The pore size distribution (x-axis) and pore volume (right y-axis) of the MSNs (DMSN), DMSN-AF, and DMSN-AFC, respectively. After the MSNs were functionalized with the gatekeeper, a shift in the hysteresis region of the sorption isotherm to lower relative pressure was observed. The gatekeeper's attachment diminishes pore size and pore volume slightly. Data obtained and graphics provided by [redacted].

4.2 Properties of unloaded Cy5-MSNs *in vitro* and *in vivo*

Unloaded Cy5-MSNs were first tested for biocompatibility and cellular uptake *in vitro*. Second, Cy5-MSNs were tested *in vivo* by means of the CAM assay and biodistribution was analyzed.

4.2.1 MSNs are highly biocompatible *in vitro*

The biocompatibility of unloaded NPs was examined in several human squamous cell carcinoma cell lines of the head and neck, a hepatocellular carcinoma cell line, and in mouse embryonic fibroblasts. The adherent cell lines were incubated with increasing concentrations of Cy5-MSNs (sealed with ferrocene and β-CD) up to 100 µg/ mL for 24 hours and the metabolic activity was analyzed. For all malignant cell lines, no substantial decrease in metabolic activity was observed. Yet, mouse embryonic fibroblasts exhibited a decreased metabolic activity when incubated with 5 µg/ mL Cy5-MSNs but the metabolic activity increased with higher NP concentrations and was not significantly different from controls. The hepatocellular carcinoma cell line HuH7 showed increased metabolic activity especially for high (50 and 100 µg/ mL) NP concentrations. Overall, Cy5-MSNs exhibited good biocompatibility *in vitro* and for most experiments, only 10 µg/ mL Cy5-MSNs were used.

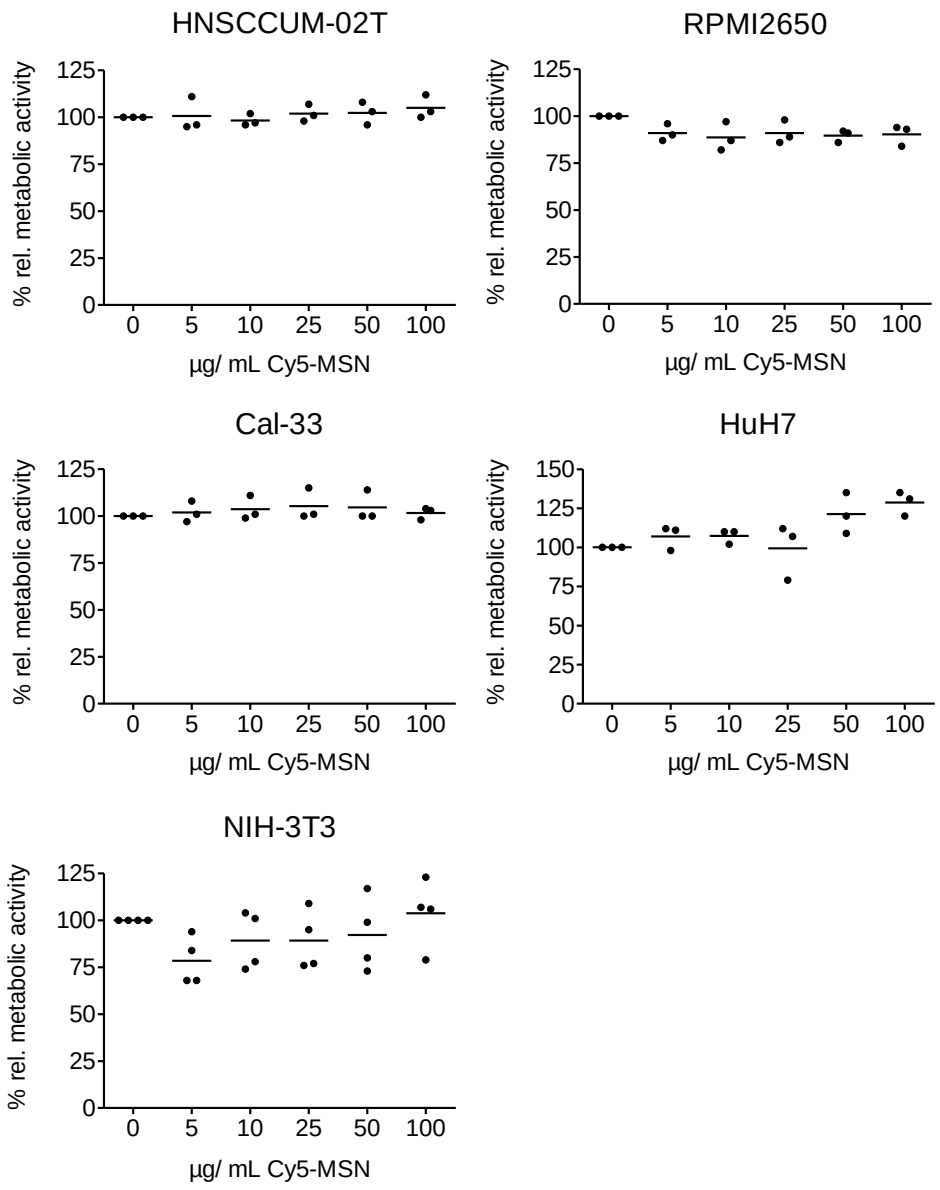

Figure 25: Biocompatibility of Cy5-MSNs in different cell lines after 24 hours incubation

The cell lines were incubated with Cy5-MSNs in increasing concentrations and metabolic activity was measured after 24 hours incubation. No difference in metabolic activity was observed in HNSCCUM-02T, RPMI2650 and Cal-33 cells. N=3, one-way ANOVA, P>0.05. HuH7 cells displayed increased metabolic activity for higher particle concentrations. N=3, one-way ANOVA, P=0.0223, Dunnett's Multiple Comparison Test: 0 µg/ mL vs. 100 µg/ mL $P < 0.05$. Mouse embryonic fibroblasts (NIH-3T3) showed decreased metabolic activity for 5 µg/ mL of Cy5-MSNs, but an insignificant increase in metabolic activity with increasing NP concentrations. N=4, one-way ANOVA, P=0.2741.

4.2.2 MSN are taken up by cancer cells and occur in the endolysosomal system

Next, the uptake of Cy5-MSNs (SK-268) was studied by flow cytometry and microscopic analysis. MSNs were sealed with two different caps, differing in the methyl-β-CD and NH_2-β-CD composition. Cap1 contained only methyl-β-CD, and Cap 2 contained NH_2-β-CD:methyl-β-CD 1:5 while the amount of ferrocene was consistent. HNSCCUM-02T cells were incubated with 10 µg/ mL Cap1-Cy5-MSNs and Cap2-Cy5-MSNs for 24 and 48 hours and then were analyzed by flow cytometry (Figure 26).

The viability was assessed by FVD506 staining (Figure 26A) and no effect of the Cy5-MSNs on viability was observed (Figure 26B). Then, only viable cells were analyzed for NP association by histograms of the APC channel representing the Cy5-signal (Figure 26C) and a time-dependent uptake or binding was noticed, respectively. Yet, the different β-CD compositions did not influence the Cy5-MSN association as depicted in Figure 26D.

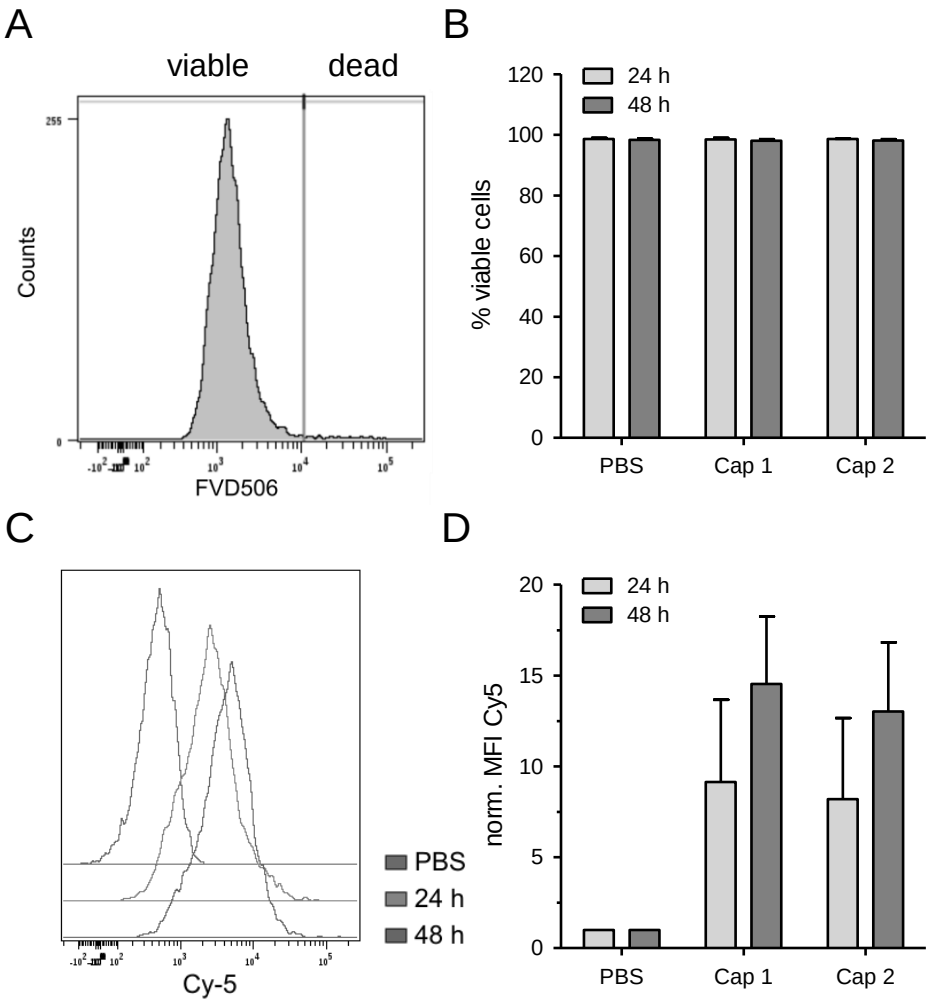

Figure 26: Cy5-MSN uptake in HNSCCUM-02T cells after 24 and 48 hours incubation

(A) Exemplary histogram of FVD506 staining of Cap1-Cy5-MSN treated cells after 24 hours incubation. Viable cells were not stained by FVD506 and occur on the left in the histogram. (B) Cap1-Cy5-MSNs (Cap1) and Cap2-Cy5-MSNs (Cap2) do not reduce the viability of HNSCCUM-02T cells after 24 and 48 hours incubation measured by flow cytometry. N=3, two-way ANOVA: time: n.s., treatment: n.s. (C) Representative overlaid histogram of the Cy5-signal of Cap1-Cy5-MSN treated HNSCCUM-02T cells. A time-dependent shift of the histogram to the right is noted. (D) Normalized mean fluorescence intensity (MFI) of the Cy5-signal to PBS controls. No difference between Cap1 and Cap2 sealed Cy5-MSN association is seen in HNSCCUM-02T cells after 24 and 48 hours. Yet, the Cy5-signal increased with time, suggesting a time-dependent association or uptake of the NPs. N=3, mean + S.D., two-way ANOVA: interaction: P=0.3471 (n.s.), time: P=0.0535 (n.s.), treatment: P=0.0002 (significant).

If the NPs were bound to the cells or incorporated could not be distinguished by flow cytometry. For that reason, NP uptake was also analyzed by confocal laser scanning microscopy, and representative images are shown in Figure 27. Most Cy5-MSNs (green) were observed around the nuclei, hence NPs were rather taken up by the cells than bound to the cellular

membrane after 24 and 48 hours incubation. Besides, z-stacks confirmed NP localization inside the cells (Data not shown).

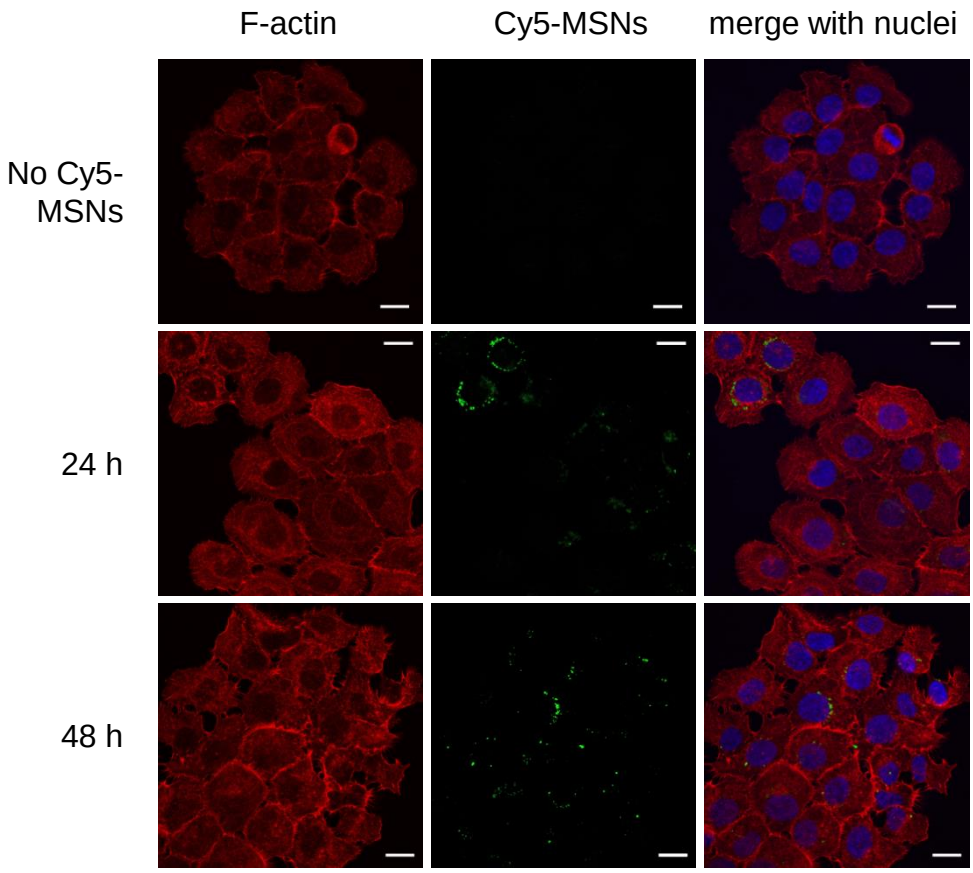

Figure 27: Uptake of Cap1-Cy5-MSNs after incubation in HNSCCUM-02T cells

F-actin (red) represents the cellular structure, Cy5-MSNs are depicted in green, and the nuclei in blue. After 24 and 48 hours, most Cy5-MSNs were observed inside the cells around the nuclei. The number of detected NPs increased over time. Representative images are shown. Scale: 20 µm.

Furthermore, the kinetics of Cy5-MSN uptake and the intracellular localization were analyzed in more detail. HNSCCUM-02T cells were incubated with 10 µg/ mL Cy5-MSNs (Cap1 sealed) for increasing time intervals and co-stained with the early endosome marker EEA1 and the endosome and lysosome marker Lamp1. Overall, 20 images were analyzed per time point per experiment for Cy5-positive vesicles per cell. As shown in Figure 28, after two and six hours, only a few NPs were associated with the cells, but after 24 and 30 hours circa two Cy5-positive vesicles per cell were detected. Moreover, after 48 hours incubation, more than three Cy5-positive vesicles per cell were found on average. A linear regression of the data was performed and suggested a linear NP uptake in HNSCCUM-02T cells which was in accordance with flow cytometry analysis.

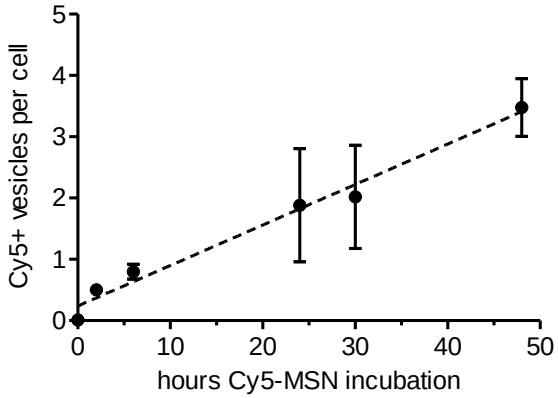

Figure 28: Cy5-MSN uptake in HNSCCUM-02T cells analyzed by CLSM imaging
The number of Cy5-positive (Cy5+) vesicles per cell was determined for 20 images per time point and experiment. Linear regression analysis was performed and proposed a linear increase in Cy5-MSN uptake over time. N=3, mean ± S.D., R^2=0.8542.

Representative images of the co-localization staining of Cy5-MSNs with EEA1 (Figure 29) and Lamp1 (Figure 30) are shown. After two hours incubation, NPs were present at the cellular membrane, but no signal overlap with EEA1 was noticed. Commencing from six hours incubation time, Cy5-MSNs were primarily detected inside the cells and co-localized with Lamp1. This observation is supported by co-localization analysis: The signal overlap of Cy5-MSNs with the respective marker was analyzed and the Manders coefficient M1 (Equation 5) was determined (Figure 31). The values for no Cy5-MSN incubation (zero hours) represent background staining. Only about 30 % of Cy5-MSNs co-localized with EEA1 after six hours incubation, hence, were associated with early endosomes. However, at the same time about 60 % of Cy5-MSNs co-localized with Lamp1 and starting at 24 hours incubation time, almost all Cy5-MSNs exhibited a Lamp1 signal overlap. Therefore, Cy5-MSNs were most likely present in endosomes and lysosomes after 24 hours incubation. Taken together, Cy5-MSNs were taken up by squamous cell carcinoma cells in a time-dependent manner, were found in endosomes and lysosomes, but did not reduce metabolic activity and therefore, were highly biocompatible *in vitro*.

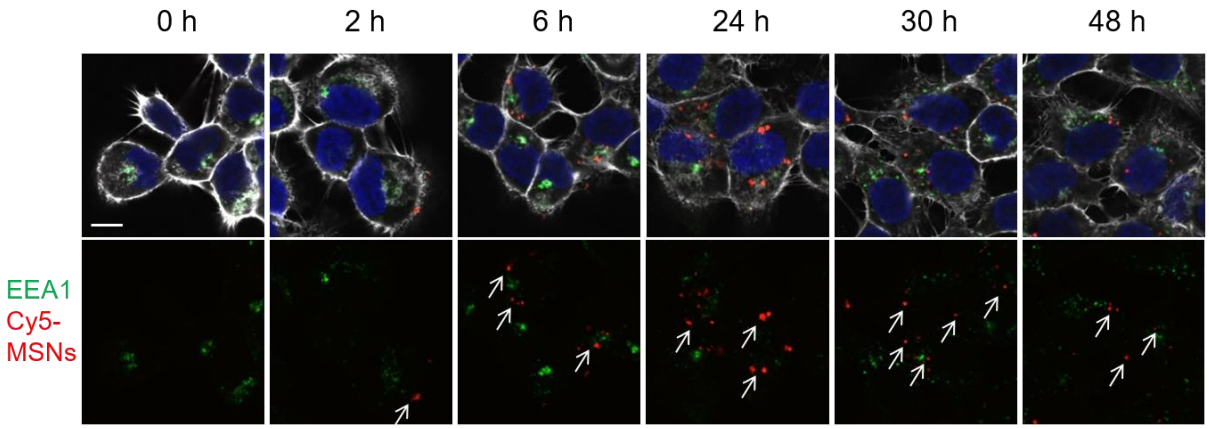

Figure 29: Co-localization staining of Cy5-MSNs and early endosome marker EEA1

HNSCCUM-02T cells were incubated with 10 µg/ mL Cy5-MSNs for the indicated time points, fixed, and stained with EEA1. In the top row, merged images (F-actin: white, nuclei: blue, EEA1: green and Cy5-MSNs: red) are shown. In the bottom row, merged images of EEA1 and Cy5-MSNs (marked with arrows) are depicted. After two hours incubation, single Cy5-MSNs were observed at the cellular membrane but without visible co-localization with EEA1. A time-dependent NP internalization was also seen. Sections of representative images of three independent experiments. Scale: 10 µm.

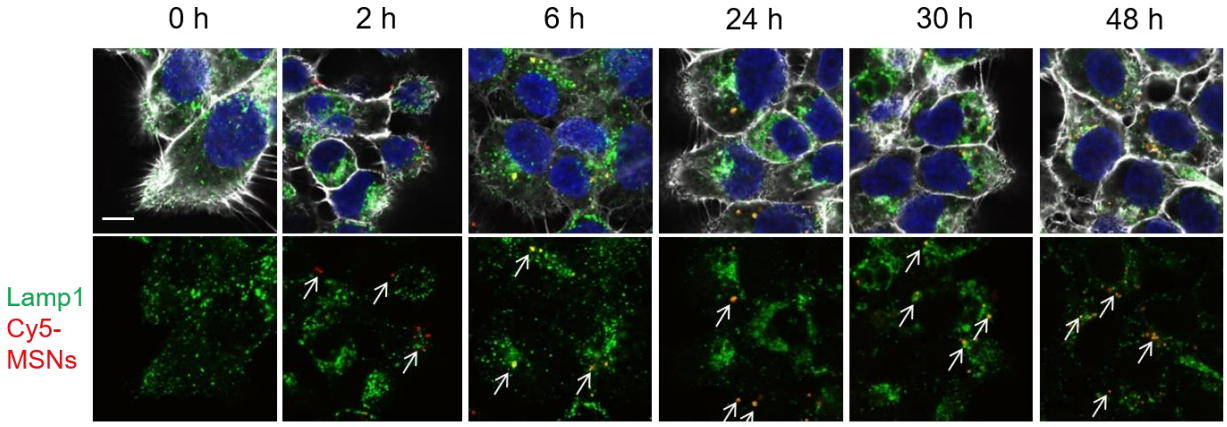

Figure 30: Co-localization staining of Cy5-MSNs and endosome and lysosome marker Lamp1

After HNSCCUM-02T cells were incubated with 10 µg/ mL for the indicated time points, staining of Lamp1 was conducted. Merged images (F-actin: white, nuclei: blue, EEA1: green and Cy5-MSNs: red) are presented in the top row. Below, merged images of Lamp1 and Cy5-MSNs (marked with arrows) are shown. Single Cy5-MSNs occurred at the cellular membrane after 2 hours incubation. Starting at 6 hours, NPs mainly co-localized with Lamp1 (signal overlap in yellow) and a time-dependent uptake was observed. Sections of representative images of three independent experiments. Scale: 10 µm.

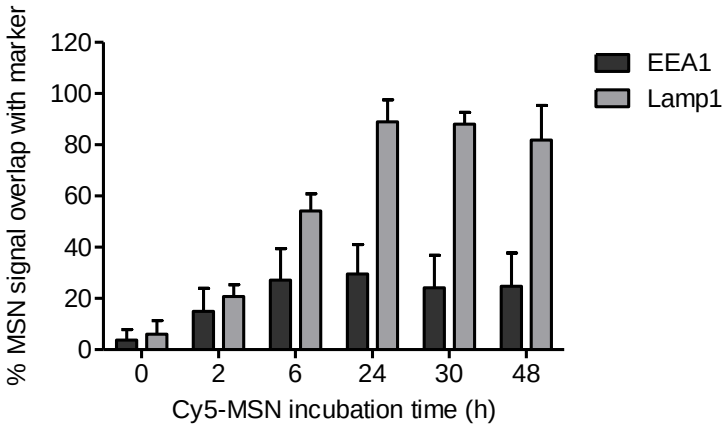

Figure 31: Analysis of Cy5-MSN signal overlap with EEA1 and Lamp1

A time-dependent increase in signal overlap was observed for both markers but overlap with EEA1 remained stable after 6 hours. After 24 hours, almost all Cy5-MSNs co-localized with Lamp1. Hence, Cy5-MSNs were present in endosomes and lysosomes after 6 hours of incubation. Per experiment, 10 images were analyzed per time point and marker. N=3, mean + S.D. Two-way ANOVA: Interaction: P<0.0001; Time: P<0.0001; Marker: P<0.0001

4.2.3 MSNs are biocompatible *in vivo*

Next, the biocompatibility was assessed *in vivo* by means of the CAM-model. Chicken embryos with tumors on their CAM were injected with two different doses of Cy5-MSNs, and the survival rate was determined after 24 hours incubation. No significant difference between the control group and the Cy5-MSNs injected groups was recognized as shown in Figure 32. On average, 70-80% of chicken embryos survived the injection of NPs or sodium chloride solution, respectively. So, Cy5-MSNs also showed great biocompatibility *in vivo*.

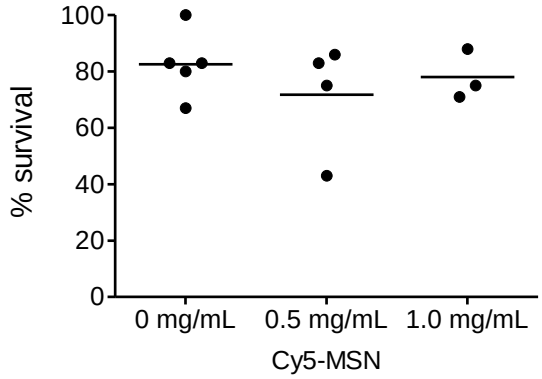

Figure 32: Survival analysis of chicken embryos after Cy5-MSN treatment

Cy5-MSNs were injected into the CAM of chicken embryos with tumors and survival was observed after 24 hours. The survival of the control group (0.9 % NaCl) and the Cy5-MSN injected group was not significantly different. Hence, Cy5-MSNs exhibited good *in vivo* biocompatibility. N=3- 5, one-way ANOVA: P=0.5559.

4.2.4 MSNs are retrieved in different chicken embryonic tissues

The biodistribution of Cy5-MSNs was also examined *in vivo* by means of the CAM assay. The chicken embryos were sacrificed 24 hours after NP injection and several organs and the CAM with tumor were removed, fixed, and processed for paraffin sectioning. Nuclei were stained with DAPI and the tissue sections were analyzed by CLSM (Figure 33). No NPs were observed in control tissues (data not shown). The most Cy5-MSNs were noticed in the liver, the organ with the highest blood flow. Also, many Cy5-MSNs were detected in the glomeruli of the kidneys. Some NPs were found in the blood vessels of the CAM and even in the tumor. Rarely, Cy5-MSNs were seen in capillaries of the heart, but no particles were observed in the brain. So, the injected NPs were retrieved in different organs and the tumor.

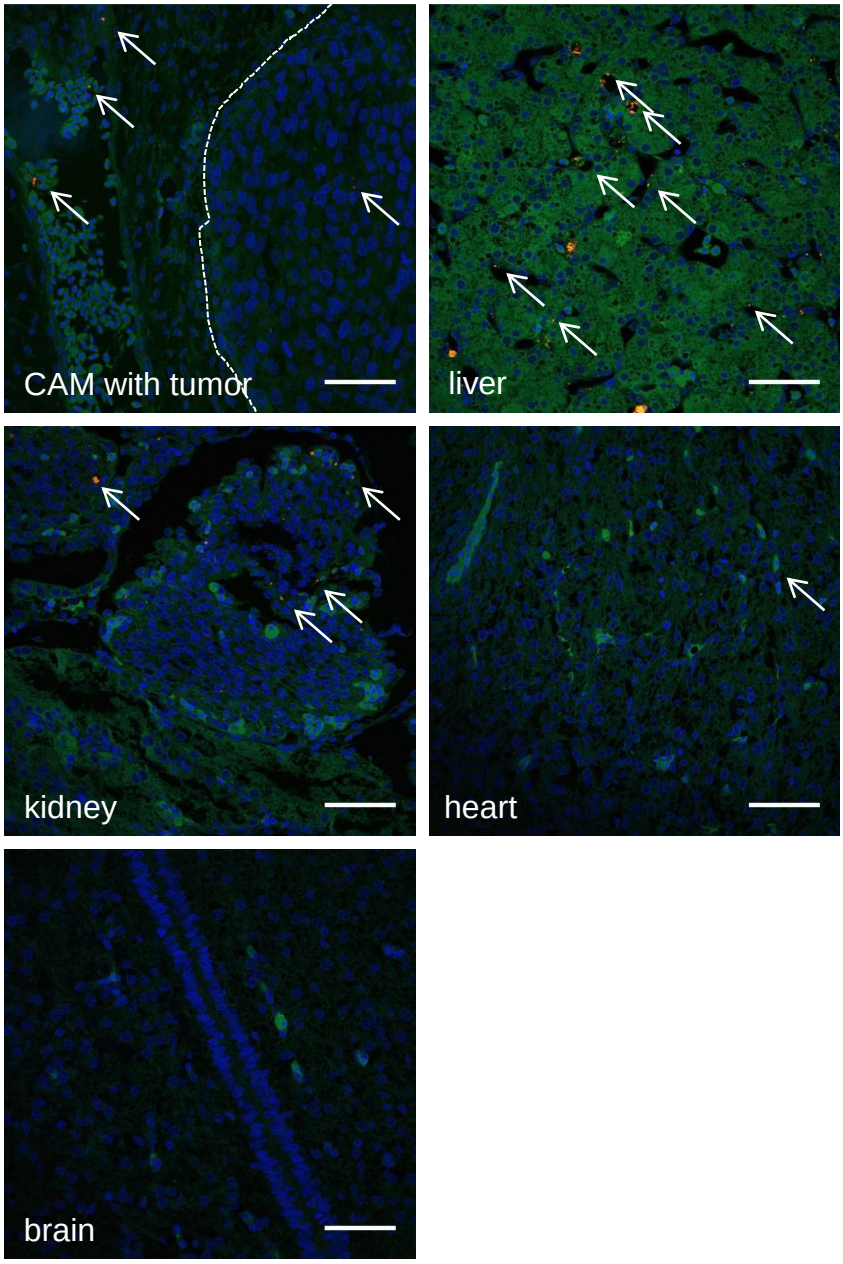

Figure 33: Biodistribution of Cy5-MSNs *in vivo*

1 mg/ mL Cy5-MSNs were injected into the CAM of chicken embryos and after 24 hours incubation, tissues were removed and processed for CLSM. The nuclei are depicted in blue, the tissue autofluorescence in green, and the NPs in red (also marked with arrows). The CAM/ tumor border is indicated by the dotted line. Representative images are shown. Some Cy5-MSNs were detected in the CAM and occasionally in the tumor. The most Cy5-MSNs occurred in the liver and the glomeruli of the kidney. Rarely NPs were noticed in capillaries of the heart and no particles were found in the brain. Scale: 50 µm.

4.3 Drug loading and release of Cy5-MSN

After good biocompatibility and uptake by cells of Cy5-MSNs were confirmed, the drug loading and release of Cy5-MSNs were tested with the model chemotherapeutic drug Dox in HNSCCUM-02T and RPMI2650 cells.

4.3.1 HNSCC cells are sensitive to doxorubicin

First, the sensitivity of HNSCCUM-02T and RPMI2650 cells to Dox after 24 and 48 hours was analyzed and the respective half-maximal reduction in metabolic activity (IC50) was determined (Figure 34, Appendix: Table 48, Table 49). A time- and concentration-dependent effect was observed in both cell lines. With 24 hours incubation time, the IC50 for HNSCCUM-02T cells was 1.57 µM and for RPMI2650 cells 0.75 µM, respectively. So, both cell lines exhibited high sensitivity to Dox, yet RPMI2650 cells were more sensitive than HNSCCUM-02T cells. Taken together, Dox was suited as a model drug and release from NPs could be studied by toxicity analysis in both cell lines.

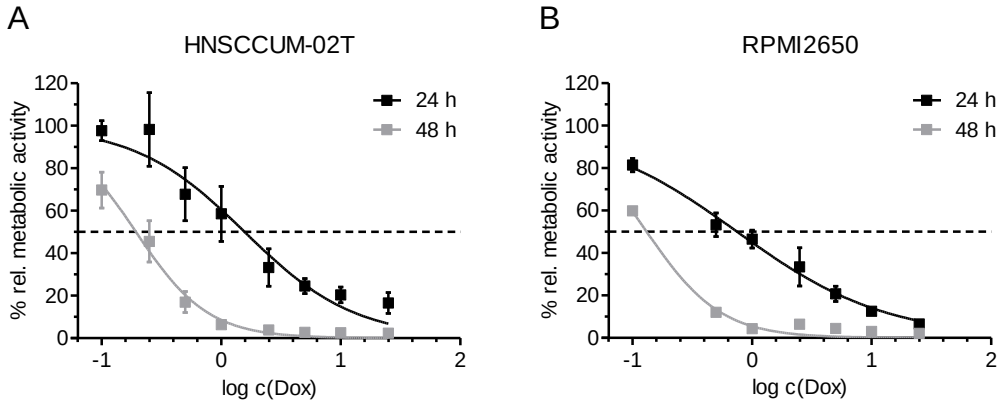

Figure 34: Determination of half maximal reduction in metabolic activity of doxorubicin in (A) HNSCCUM-02T and (B) RPMI2650 cells

The dotted line indicates a 50 % reduction in metabolic activity. A time- and concentration-dependent effect was observed in both cell lines. RPMI2650 cells were more sensitive to Dox than HNSCCUM-02T cells. N=3, mean ± S.D. IC50 (HNSCCUM-02T, 24 h)= 1.569 µM, R^2=0.8899, IC50 (HNSCCUM-02T, 48 h)= 0.1935 µM, R^2=0.9588, IC50 (RPMI2650, 24 h)= 0.7496 µM, R^2=0.9672, IC50 (RPMI2650, 48 h)= 0.1314 µM, R^2=0.9772.

4.3.2 Doxorubicin is successfully loaded to Cy5-MSNs

Dox was loaded to Cy5-MSNs by incubation of naked MSNs with Dox solution overnight and then the Dox-MSNs were sealed with ferrocene and NH_2-β-CD. Unloaded Cy5-MSNs were used as control. The amount of loaded Dox was calculated by adding the remaining Dox in

the supernatants and subtracting it from the initially applied Dox. However, the Dox loading efficiency ranged widely from 6 % to 69 % (SK-267, 5 mg/ mL Dox loading solution). The successful loading was also confirmed visually because the NP pellet was stained red by Dox as depicted in Figure 35.

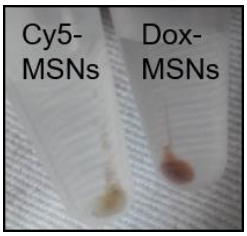

Figure 35: Representative image of control Cy5-MSNs (left) and Dox-MSNs (right)
The NPs were centrifuged to obtain pellets. Cy5-MSNs appeared light brown due to ferrocene/ NH_2-β-CD capping while Dox stained Dox-MSNs in red and the capped particles appeared dark brown.

4.3.3 Dox-MSNs remain stable over at least four days in different media

The Cy5-MSNs were loaded with Dox and incubated in different media at cell culture conditions for 24 and 96 hours. Then, the supernatants were analyzed for Dox with fluorescence measurements and compared to a standard curve generated in the respective medium. No release of Dox from Dox-MSNs was observed in PBS, H_2O, and DMEM after 24 and 96 hours compared to controls (Figure 36). However, less than 6 % of loaded Dox seemed to have been released from Dox-MSNs in DMEM + 5 % FCS after 96 hours incubation but unloaded control NPs also falsely showed Dox release of about 3 %. So, Dox-MSNs remained stable over four days in different media and only negligible Dox release was observed.

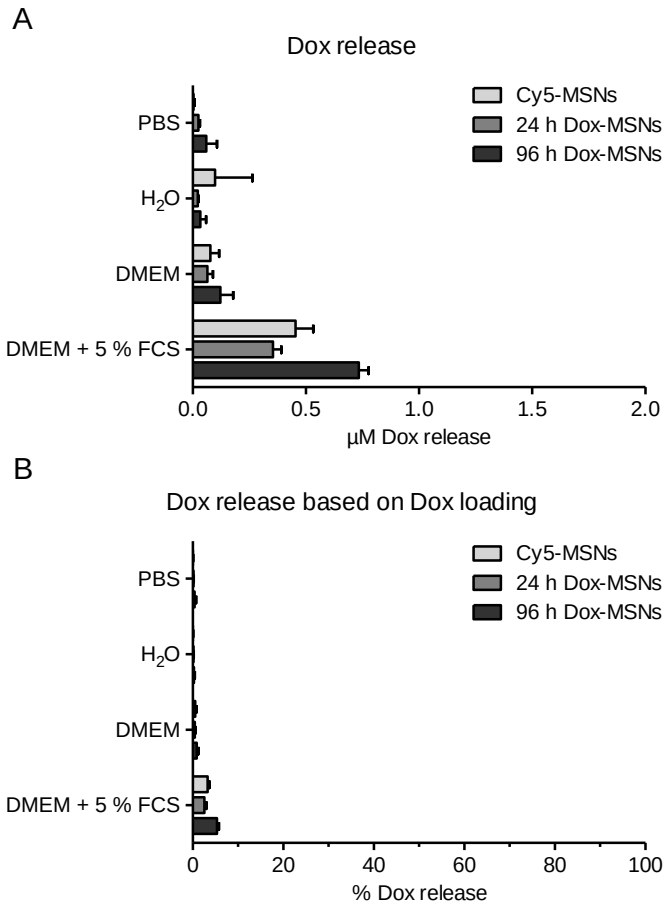

Figure 36: Doxorubicin release from Dox-MSNs in different media after one day and four days incubation at cell culture conditions

(A) The released concentration of Dox determined by fluorescence and (B) Dox release relative to loaded Dox in Dox-MSNs are shown. Cy5-MSNs were used as controls. No substantial release of Dox in the different media was observed. However, DMEM + 5 % FCS also showed increased Dox signal in controls. N=3, mean + S.D.

4.3.4 Dox-MSNs exhibit a retarded drug release in HNSCC cells

After Dox-MSNs did not release Dox in different media, HNSCCUM-02T and RPMI2650 cells were treated with Dox-MSNs to evaluate drug release *in vitro*. The drug release was measured by Dox signal and viability staining in flow cytometry analysis, reduction in metabolic activity due to toxic effects of Dox, and DNA damage as shown by γH2AX foci staining.

4.3.4.1 Dox-MSNs reduce the metabolic activity of HNSCC cells

In the beginning, Cy5-MSNs were loaded with a 2 mg/ mL Dox solution, but even though 5 nmol Dox per µg Cy5-MSN were used, only a small amount of Dox was loaded to the NPs. Unfortunately, the total of the loaded drug could not be determined because the whole

amount of used Dox was retrieved in the supernatants. Still, a retarded drug release was noticed in HNSCCUM-02T and RPMI2650 cells by means of a reduction in metabolic activity as shown in Figure 37. Free Dox (2 µM) induced a time-dependent decrease in relative metabolic activity compared to PBS treated controls. The cells were either treated with Dox-MSNs or Cy5-MSNs for 24, 48, or 96 hours, respectively, or the treatment solutions were removed after 24 or 48 hours and the cells were incubated further without NPs. In HNSCCUM-02T cells (Figure 37A), Dox-MSNs began to reduce the relative metabolic activity after 48 hours incubation. Incubation for 96 hours reduced the metabolic activity to about 30 % independent of NP removal in between. In RPMI2650 cells (Figure 37B), free Dox had the same effect as in HNSCCUM-02T cells. However, Dox-MSNs reduced the metabolic activity already after 24 hours incubation, but a retarded release was still noticed compared to free Dox. Removal of NPs also had no effect on the efficacy of Dox-MSNs. Hence, the Dox-MSNs which were taken up by the cells, released the Dox inside the cells and a decrease in metabolic activity was observed.

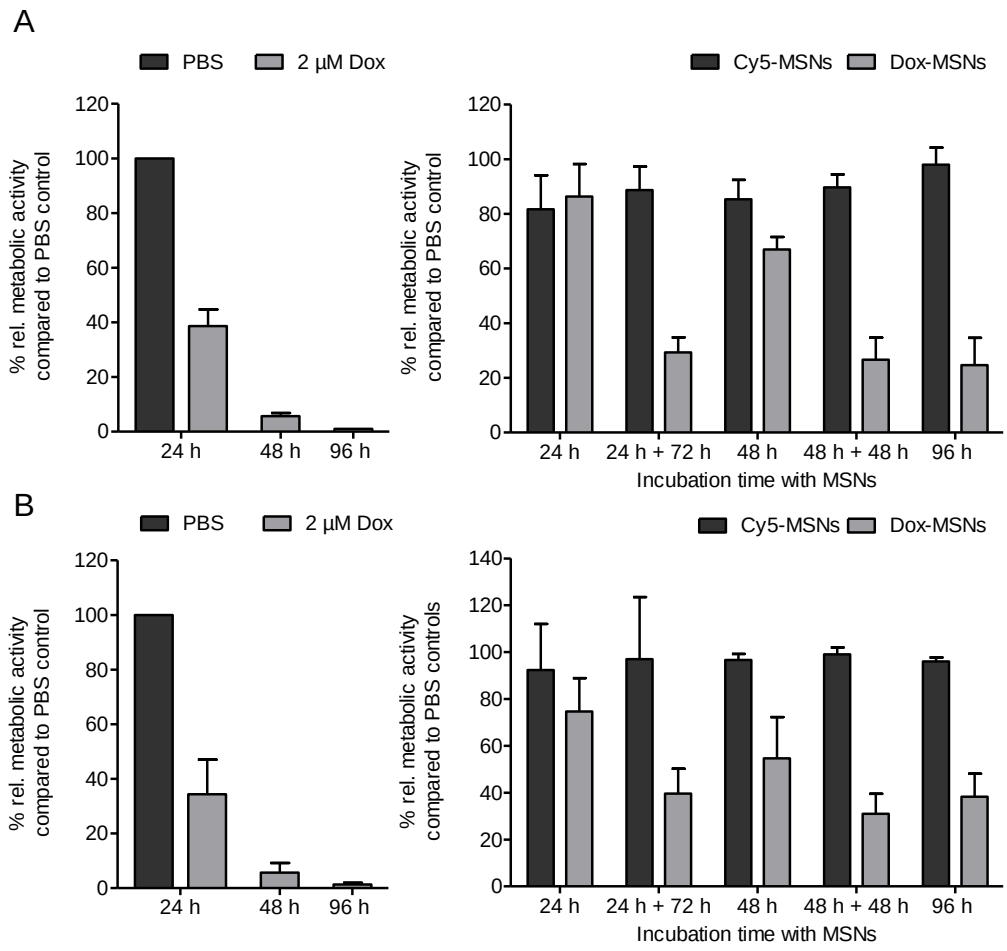

Figure 37: Effect of 2 µM Dox and 10 µg/ mL Dox-MSNs (loaded with 5 nmol Dox per µg Cy5-MSN) on (A) HNSCCUM-02T and (B) RPMI2650 cells

The cell lines were incubated with 2 µM Dox, 10 µg/ mL Dox-MSNs, or Cy5-MSNs for the indicated times, respectively, and PBS was applied as a control. After 24 and 48 hours, the media with NPs were removed and cells were incubated further for 72 or 48 hours (until 96 hours total incubation time). The metabolic activity was normalized to PBS controls. Free Dox reduced the metabolic activity more than half after 24 hours incubation. A retarded drug release was noticed in both cell lines, beginning after 24 hours incubation time. After 96 hours, no difference in metabolic activity was observed between the cells which were incubated the whole time with MSNs and the cells which had the NPs removed in the meantime. N=3, mean + S.D., (A) two-way ANOVA: interaction: $P<0.0001$; treatment: $P<0.0001$, time: $P<0.0001$; Bonferroni multiple comparisons Cy5-MSNs vs. Dox-MSNs: 24 h and 48 h: $P>0.05$; 24 h +72 h, 48 h + 48 h and 96 h: $P<0.0001$. (B) Two-way ANOVA: interaction: $P=0.0415$; treatment: $P<0.0001$; time: $P=0.1622$: Bonferroni multiple comparisons Cy5-MSNs vs. Dox-MSNs: 24 h: $P>0.05$; 48 h: $P<0.01$; 24 h + 72 h and 96 h: $P<0.001$; 48 h + 48 h: $P<0.0001$.

4.3.4.2 Successful Dox-MSN uptake and Dox release in HNSCC cells

Next, the loading protocol for Dox-MSNs was adjusted to increase Dox loading and to enable the analysis of the loading efficiency. A higher concentrated Dox solution (5 mg/ mL) was

used, but less total Dox (2.15 nmol per µg Cy5-MSN) was applied for loading. The capping protocol remained the same while more washing steps were necessary to remove excess Dox. The loading efficiency ranged from 6-31 %, resulting in 4.2 ± 2.2 µM Dox when 10 µg/ mL Dox-MSNs were used. To further examine the uptake and release of Dox-MSNs, HNSCCUM-02T cells were treated with 10 µg/ mL Dox-MSNs or Cy5-MSNs and incubated for 24 or 96 hours. Then, cells were analyzed by flow cytometry for viability, Cy5-MSN uptake, and Dox signal as depicted in Figure 38. Cells were stained with a viability dye (FVD780) before analysis.

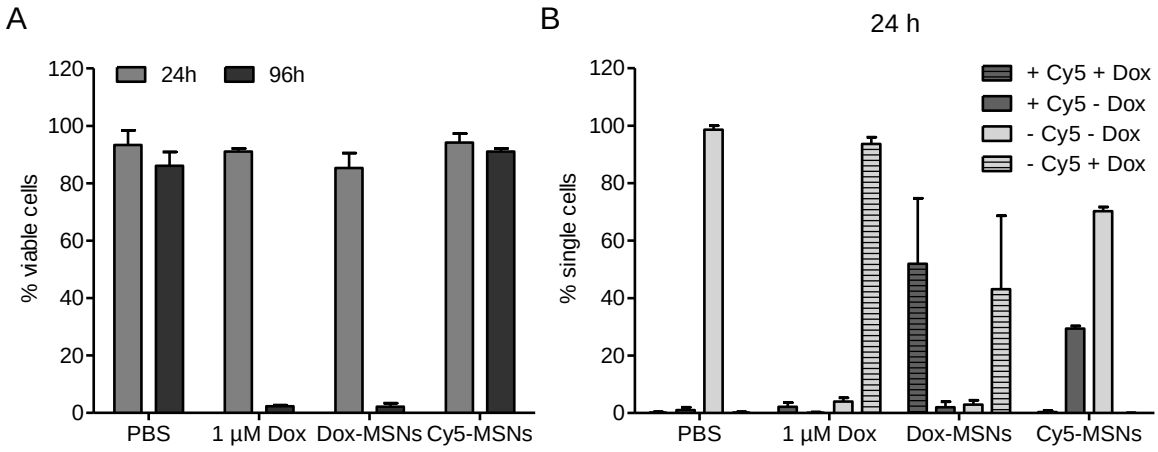

Figure 38: (A) Viability, (B) nanoparticle uptake and doxorubicin signal of HNSCCUM-02T cells after 1 µM Dox, 10 µg/ mL Dox-MSN (loaded with 2.15 nmol Dox per µg Cy5-MSN), and Cy5-MSN treatment for 24 and 96 hours

(A) The viability of HNSCCUM-02T cells was assessed with FVD780. After 24 hours, no substantial cytotoxic effects of Dox and Dox-MSNs were observed. After 96 hours incubation, Dox and Dox-MSNs had killed almost all cells, while Cy5-MSNs did not reduce the viability. N=3, mean + S.D, two-way ANOVA: interaction: P<0.0001, time: P<0.0001, treatment: P<0.0001. (B) Single cells in the stated gate (dead and viable cells) after 24 hours incubation. About 90 % of all free Dox treated cells exhibited a Dox-signal. More than 50 % of Dox-MSN treated cells were positive for Cy5 and Dox, but also about 40 % of the cells contained free Dox. Fewer Cy5-MSNs were taken up than Dox-MSNs by HNSCCUM-02T cells after 24 hours incubation. N=3, mean + S.D, two-way ANOVA: interaction: P<0.0001, population: P<0.0001, treatment: P=1.0000 (n.s.).

After 24 hours incubation, no significant reduction in viability was observed for 1 µM Dox and Dox-MSN treated cells compared to controls (Figure 38A). Incubation for 96 hours reduced viability drastically after Dox and Dox-MSN treatment, while controls showed negligible decrease in viability. Since the number of dead cells was comparable and small after 24 hours of treatment, single cells (viable and dead) were analyzed for Cy5 (MSN) and Dox signal (Figure 38B). A dot plot was used to characterize the cells. As expected, PBS treated control cells were Cy5 and Dox negative and more than 90 % of 1 µM Dox treated cells exhibited a

Dox signal. So, Dox was already inside the cells but had not killed the cells yet. When cells were treated with Dox-MSNs, two major populations were observed: About 50 % of all single cells were positive for Cy5 and Dox, but almost the same number of cells was Cy5 negative and Dox positive. There was great variability between experiments (Appendix: Figure 56), so both populations had a large standard deviation. Only about 30 % of cells treated with Cy5-MSNs showed a Cy5 signal. Hence, Dox-MSN uptake was better than Cy5-MSN uptake in HNSCCUM-02T cells. As expected, no Dox signal was detected in Cy5-MSN treated cells. Overall, Dox-MSNs were detected in HNSCCUM-02T cells after 24 hours incubation while cells were still alive and after longer incubation time Dox caused cell death.

4.3.4.3 Dox-MSNs induce DNA damage in HNSCC cells

In parallel, the release of Dox was further studied by means of γH2AX foci which indicate DNA damage repair sites in the nucleus. HNSCCUM-02T (Figure 39) and RPMI2650 (Figure 40) cells were treated with 1 µM Dox, 10 µg/ mL Dox-MSNs or Cy5-MSNs for two and 24 hours, respectively. Then, cells were fixed and immunofluorescence staining for γH2AX foci was performed. Representative images are shown below. PBS treated control cells and Cy5-MSN treated cells exhibited only a small number of γH2AX foci after both treatment times. When cells were treated with Dox, already after two hours many γH2AX foci were observed in the nuclei, but less γH2AX foci were seen in cells treated with Dox-MSNs at the same time point. After 24 hours incubation, the number of γH2AX foci increased in Dox treated cells and greatly increased in Dox-MSN treated cells. The γH2AX foci area per nucleus was analyzed for all treatment groups (at least 50 nuclei per treatment and experiment) and the results are presented in Figure 41. The analysis confirmed the visual observations: After 24 hours of Dox-MSN treatment increased the amount of γH2AX foci significantly in both cell lines. So, a retarded release of Dox from Dox-MSNs was observed.

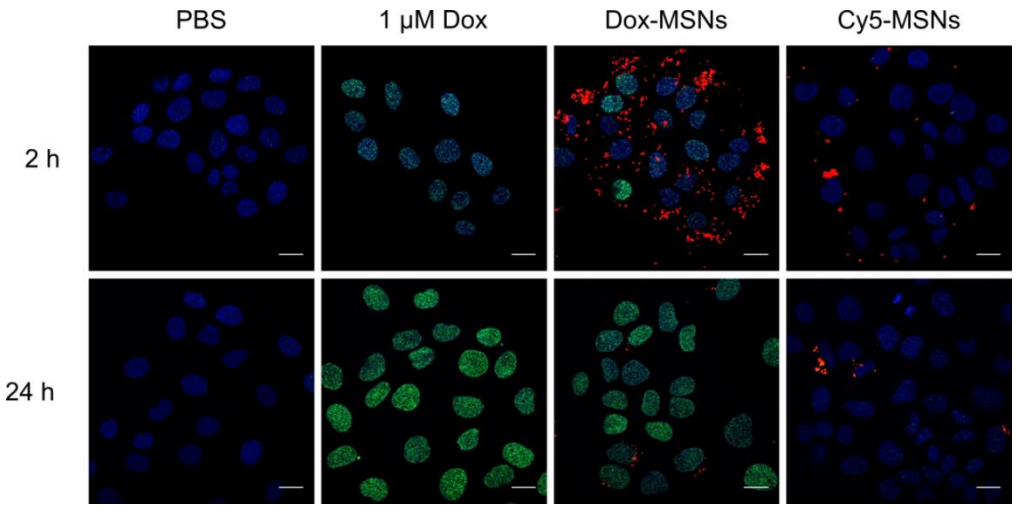

Figure 39: Detection of DNA damage by γH2AX foci staining in HNSCCUM-02T cells after 1 µM Dox, 10 µg/ mL Dox-MSN (loaded with 2.15 nmol Dox per µg Cy5-MSN), or Cy5-MSN treatment, respectively

Nuclei are depicted in blue, Cy5-MSNs in red and γH2AX foci in green. Free Dox induced DNA damage after 2 hours incubation while Dox-MSNs did induce less DNA damage. After 24 hours, the DNA damage strongly increased in these treatment groups. No DNA damage was seen in PBS and Cy5-MSN treated cells after 2 and 24 hours incubation. Representative images out of three independent experiments are shown. Scale: 20 µm.

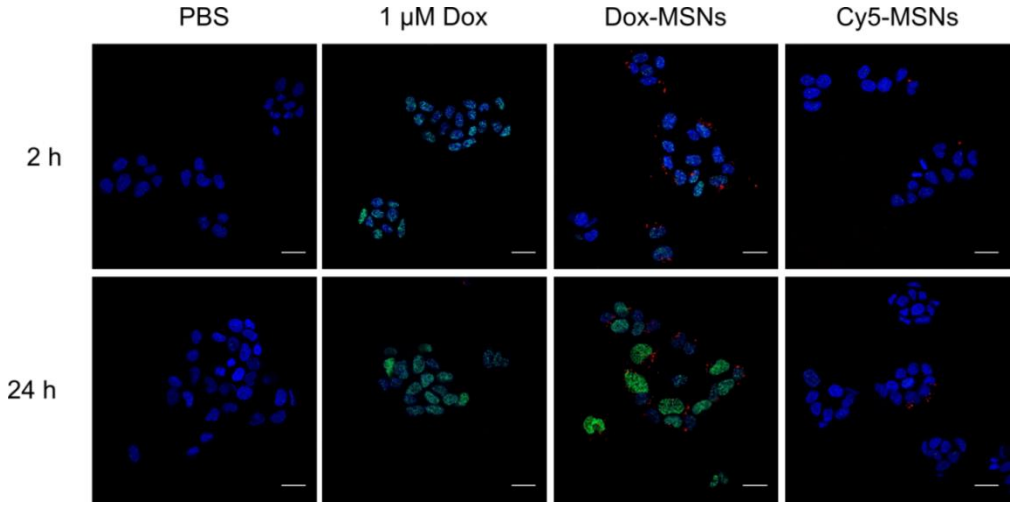

Figure 40: Detection of DNA damage by γH2AX foci staining in RPMI2650 cells after 1 µM Dox, 10 µg/ mL Dox-MSN (loaded with 2.15 nmol Dox per µg Cy5-MSN) or Cy5-MSN treatment, respectively

Merged images are shown with nuclei in blue, Cy5-MSNs in red and γH2AX foci in green. Some DNA damage was induced by 1 µM Dox after 2 hours incubation, Dox-MSNs did induce less DNA damage. After 24 hours the DNA damage increased in these treatment groups. PBS and Cy5-MSN treated cells exhibited no DNA damage after 2 and 24 hours incubation. Representative images out of three independent experiments are shown. Scale: 20 µm.

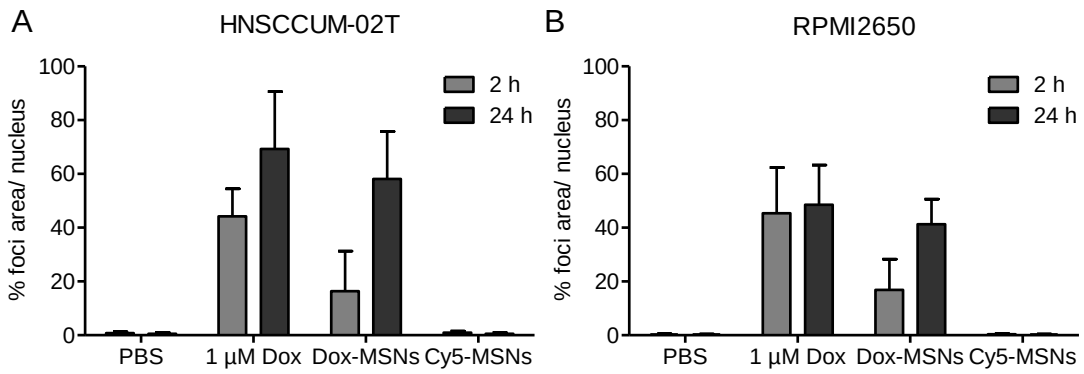

Figure 41: Analysis of foci area per nucleus in (A) HNSCCUM-02T and (B) RPMI2650 cells after 2 and 24 hours incubation with 1 µM Dox, 10 µg/ mL Dox-MSNs, or Cy5-MSNs, respectively

After 2 hours incubation with Dox about 45 % of the nucleus area contained γH2AX foci, whereas in Dox-MSN treated cells only 20 % of the nuclei were covered by γH2AX foci. After 24 hours incubation, the foci area per nucleus increased significantly for both cell lines. Also, γH2AX foci were barely detected in PBS and Cy5-MSN treated controls. Two-way ANOVA, Bonferroni multiple comparisons: Dox-MSNs 2 h vs. 24 h: (A) $P<0.01$; (B) $P<0.05$; n=3, mean + S.D.

4.3.4.4 Proteins in the medium do not influence the effect of Dox-MSNs

Also, the effect of FCS on Dox-MSN efficacy was analyzed in HNSCCUM-02T cells. Dox-MSNs and Cy5-MSNs prepared for analysis of release in different media (see 4.3.3) were applied in DMEM/F12 with FCS (DMEM/F12 + FCS) or DMEM/F12 without FCS (DMEM/F12) for 24 and 96 hours (Figure 42), respectively. The metabolic activity was measured and normalized to PBS treated cells in DMEM/F12 + FCS. Cells treated with Dox and Dox-MSNs exhibited a time-dependent decrease in metabolic activity independent from incubation with or without FCS. Yet, an overall decrease in metabolic activity was observed in cells incubated without FCS and after 24 hours Dox-MSN exposition, a greater reduction of metabolic activity was noticed compared to cells incubated with FCS. After 96 hours of incubation, Dox-MSNs exhibited the same effect on metabolic activity in both incubation media. Still, the difference in the reduction of metabolic activity by Dox-MSN treatment after 24 hours must be evaluated carefully due to the general influence of missing FCS on metabolic activity. Taken together, a retarded Dox release from Dox-MSN was observed independently from the incubation medium.

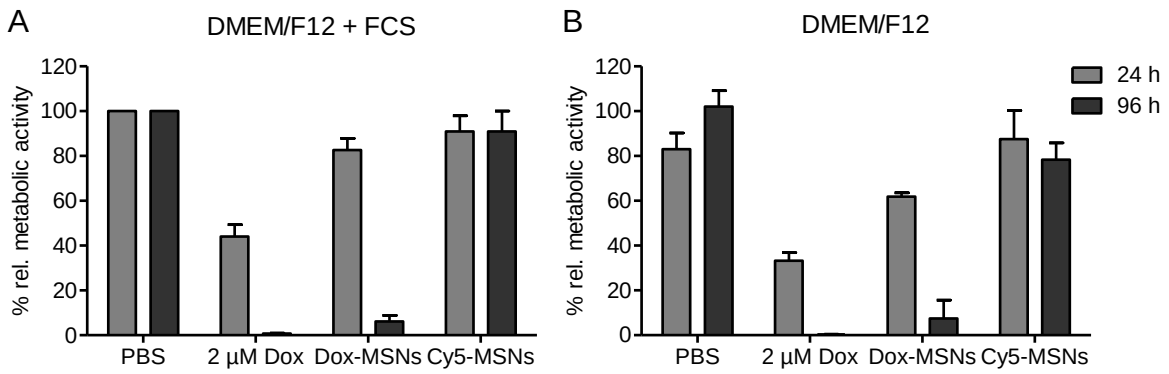

Figure 42: Treatment of HNSCCUM-02T cells with 2 µM Dox, 10 µg/ mL Dox-MSNs or Cy5-MSNs in (A) medium with (DMEM/F12 + FCS) or (B) without (DMEM/F12) FCS for 24 or 96 hours, respectively

The metabolic activity was normalized to PBS controls incubated with FCS. A time-dependent decrease in metabolic activity was noticed after 2 µM Dox and Dox-MSN treatment. Cells incubated without FCS for 24 hours had an overall slightly decreased metabolic activity compared to cells incubated with FCS. So, the reduced metabolic activity after 24 hours of Dox-MSN treatment in DMEM/F12 needs to be evaluated carefully. N=3, mean + S.D.

Overall, the obtained data indicated that the model drug Dox was released in a retarded manner and intracellularly from Dox-MSNs at an effective dose. So, Cy5-MSNs were suited as drug carriers for small molecule drugs.

4.4 Cy5-MSNs as siRNA nanocarriers

After the small molecule drug Dox was successfully loaded into and released from Cy5-MSNs, siRNA loading and release were examined. Different NPs and loading protocols were tested and modified. Since it is more difficult to study siRNA efficiency, distinctive model systems were used. On one side, a stable enhanced green fluorescent protein (eGFP) expressing hepatocarcinoma cell line, namely HuH7-GFP, was exploited as a model system to test siRNA-MSN efficiency, and on the other side, FAM™-labeled siRNA was used to evaluate different loading protocols. Also, the nucleic-acid binding protein and p53 cofactor heterogeneous nuclear ribonucleoprotein K (hnRNP K) was utilized as an example target for RNA interference experiments. It was previously shown, that a reduction of hnRNP K expression sensitized HNSCC cells to irradiation, and inhibited cellular migration [164,165]. Therefore, hnRNP K is an interesting target for siRNA induced protein expression regulation.

4.4.1 Reduction of eGFP expression in stable eGFP expressing cell line

First, the stable eGFP expressing cell line (HuH7-GFP, Figure 43A) was used as a model system to test eGFP knockdown by Silencer® GFP (eGFP) siRNA (eGFP-siRNA) executed with Lipofectamine™ RNAiMAX transfection reagent (Lipo). This eGFP knockdown by regular transfection was examined as a positive control (Figure 43B, C and D). HuH7-GFP cells were transfected with eGFP-siRNA and Silencer® Select Negative Control siRNA #2 (nsRNA) for 24 hours, then the transfection reagents were removed, and the cells were further incubated for 48 (total incubation time 72 hours) or 72 hours (total incubation time 96 hours), respectively. The cells were harvested, stained for viability, and analyzed by flow cytometry for viability and eGFP content. The transfection did not reduce the viability of the cells, only the viability of eGFP-siRNA treated cells was reduced by less than 20 % (controls 10 %) after 72 hours incubation (Figure 43B). Moreover, cells transfected with eGFP-siRNA showed a reduced eGFP signal compared to Lipo and nsRNA treated cells depicted by an exemplary overlaid histogram (Figure 43C). Two populations of HuH7-GFP cells were noticed in the histogram by the means of two peaks, one small population with a high eGFP expression (peak on the right), and one large population with a medium eGFP expression (peak in the middle). After eGFP knockdown by eGFP-siRNA, the peaks were shifted to the left, corresponding to decreased eGFP expression and the peak associated with high eGFP expression was greatly reduced. Overall, eGFP expression decreased by 70 % (72 hours) or 75 % (96 hours) compared to untreated control cells while nsRNA did not reduce eGFP expression.

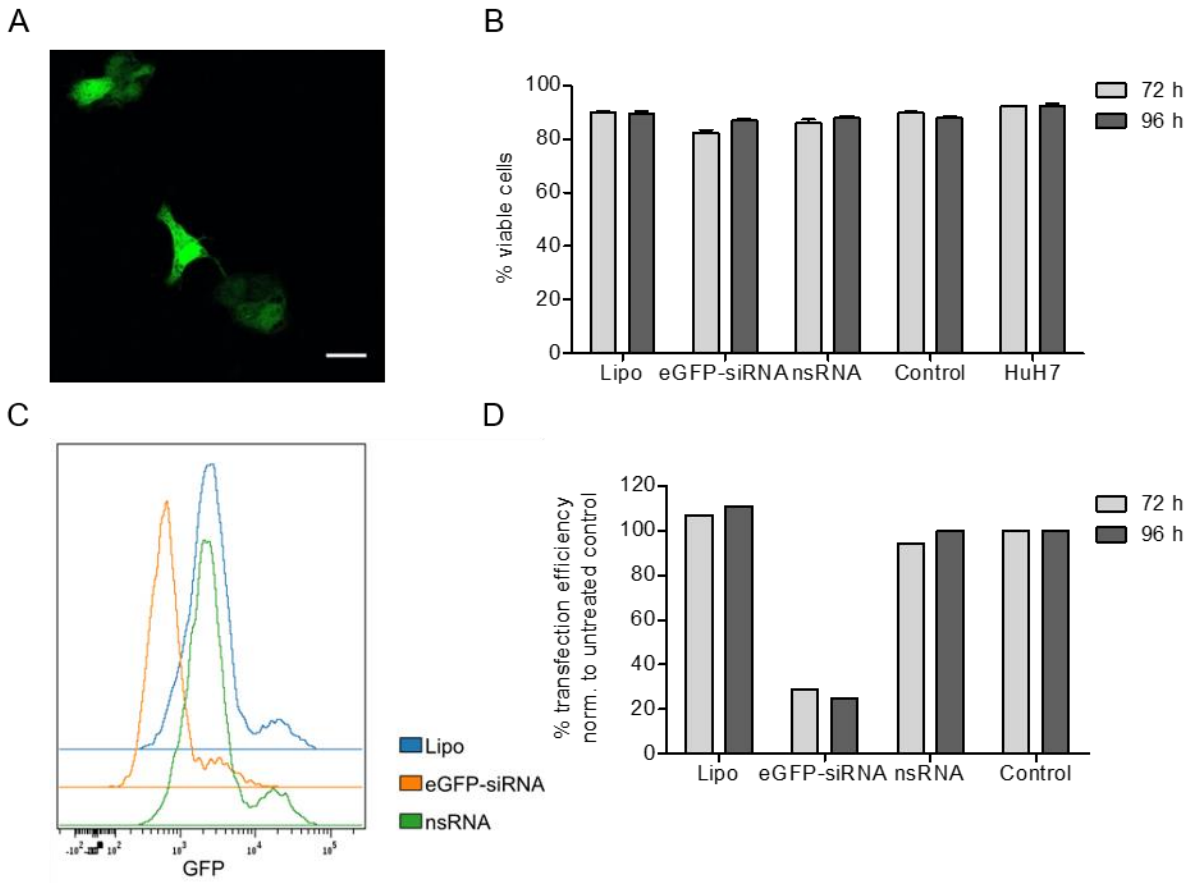

Figure 43: HuH7-GFP cells as a model system

(A) Exemplary image of HuH7-GFP cells. Scale: 20 µm. (B) Viability of HuH7-GFP cells after eGFP-siRNA transfection measured by flow cytometry. After incubation for 72 and 96 hours after transfection, cells were stained with FVD780 for dead cells. Transfection with eGFP-siRNA or nsRNA did not reduce the viability. Mean + S.D., triplicates. (C) Exemplary overlaid histogram (with a logarithmic scale) of viable cells in the GFP channel 72 hours after transfection. Lipofectamine™ RNAiMAX (Lipo) treated cells and nsRNA transfected cells were used as controls. Two peaks corresponding to two populations were observed. A small peak on the right indicating high rates of eGFP expression and a large peak in the middle indicating medium rates of eGFP expression. The eGFP signal of eGFP-siRNA transfected cells was shifted to the left indicating a reduction in eGFP expression. (D) Transfection efficiency normalized to untreated control HuH7-GFP cells. EGFP-siRNA reduced the eGFP expression by about 70 % after 72 hours and 75 % after 96 hours incubation time. NsRNA transfection did not reduce the eGFP expression. N=1.

4.4.2 No eGFP knockdown is observed after eGFP-siRNA-MSN treatment in HuH7-GFP cells

The MSNs (SK-267) were loaded with eGFP-siRNA or nsRNA, respectively, and sealed with ferrocene and NH_2-β-CD. Unloaded Cy5-MSNs were used as controls. Adherent HuH7-GFP cells were treated with 10 or 20 µg/ mL eGFP-siRNA-MSNs, nsRNA-MSNs, or Cy5-MSNs for 72 or 144 hours, respectively. Then, cells were harvested, stained for viability, and analyzed

by flow cytometry. Treatment with eGFP-siRNA-MSNs and nsRNA-MSNs did not affect the viability independent of incubation time and NP concentration (Figure 44A, B), respectively. The NP uptake was observed by the Cy5-signal and an improved uptake by eGFP-siRNA-MSNs and nsRNA-MSNs was noticed also dependent on the applied concentration, especially after 72 hours incubation (Figure 44C, D). Moreover, the Cy5-signal of eGFP-siRNA-MSNs and nsRNA-MSNs decreased over time while the signal of Cy5-MSNs remained relatively stable. However, eGFP expression was not reduced by eGFP-siRNA-MSNs after 72 hours incubation (Figure 44E), while after 144 hours, 20 µg/ mL eGFP-siRNA-MSNs slightly reduced eGFP expression compared to nsRNA-MSNs and Cy5-MSNs (Figure 44F). So, either the eGFP-siRNA amount loaded to the Cy5-MSNs or the NP amount was not enough for a significant knockdown of eGFP or the eGFP-siRNA was not released in time to reduce eGFP protein expression.

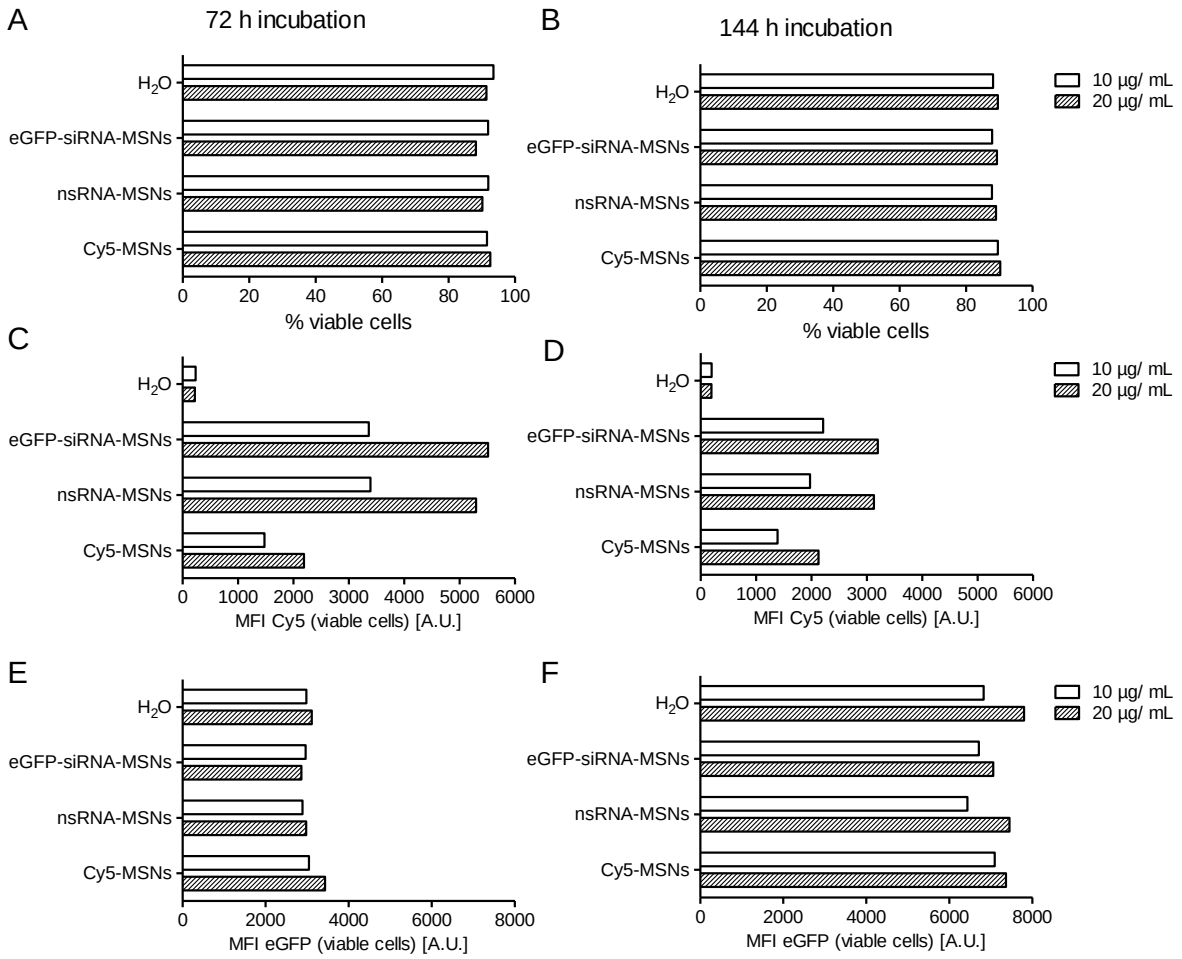

Figure 44: Treatment of HuH7-GFP cells with 10 and 20 µg/ mL eGFP-siRNA-MSNs, nsRNA-MSNs and Cy5-MSNs for (A, C, E) 72 and (B, D, F) 144 hours, respectively

Treatment with eGFP-siRNA-MSNs, nsRNA-MSNs, and Cy5-MSNs did not affect the viability at (A) 72 hours and (B) 144 hours after treatment. The NP uptake was measured by Cy5-signal and a higher Cy5-signal for eGFP-siRNA-MSNs and nsRNA-MSNs was observed (C, D). After (C) 72 hours a greater difference between 10 and 20 µg/ mL MSNs was seen than after (D) 144 hours. The Cy5-signal of eGFP-siRNA-MSNs and nsRNA-MSNs decreased over time while the signal of Cy5-MSNs remained relatively stable. (E) Even though eGFP-siRNA-MSNs were taken up, they did not reduce the mean fluorescence intensity of the eGFP signal independent of the applied concentrations after 72 hours. (F) After 144 hours, 20 µg/ mL eGFP-siRNA-MSNs slightly reduced the eGFP expression compared to controls (nsRNA-MSNs, Cy5-MSNs). An overall increase of eGFP expression from 72 to 144 hours after treatment was noticed. N=1.

4.4.3 siRNA-MSNs do not reduce mRNA expression after 96 hours incubation

As no reduction in eGFP protein expression could be detected in HuH7-GFP cells, it was speculated that the siRNA loading efficiency was too small because the siRNA would barely fit in the pores of SK-267 (pore size: 8.2 nm, siRNA: ~7 nm × 2 nm [6]). For this reason, different MSNs with larger pores (SK-275,11.7 nm pores) were used for siRNA loading. Moreo-

ver, the uncapped MSNs were functionalized by amino groups and therefore were positively charged while the siRNA was negatively charged. Strong electrostatic binding was expected to lead to impaired siRNA release thus, the amino groups were saturated by ferrocene before siRNA loading. Higher NP concentrations were applied to compensate for the expected decrease in loading efficiency. Also, mRNA expression was analyzed instead of protein expression, because mRNA reduction occurs and is detectable earlier than a reduction in protein expression, respectively. In line with this, two different siRNA-MSNs were studied in HNSCCUM-02T and RPMI2650 cells. One part of MSNs was loaded with FAM™-siRNA targeting GAPDH (FAM™-siRNA-MSNs) and another part of MSNs was loaded with Silencer® Select siRNA hnRNP K (hnRNP K-siRNA-MSNs). Besides, nsRNA-MSNs were used as control. The HNSCCUM-02T and RPMI2650 cells were treated with 50 µg/ mL FAM™-siRNA-MSNs, hnRNP K-siRNA-MSNs, nsRNA-MSNs, and PBS for 24 or 96 hours, respectively. A transfection with Lipo was performed as a positive control, mRNA expression was normalized to calibrator samples, and analyzed with the comparative $\Delta\Delta C_T$ method (see 3.2.7.4). In both cell lines, FAM™-siRNA transfection greatly reduced the GAPDH mRNA expression (Figure 45A, B) but not the hnRNP K mRNA expression. Yet, hnRNP K-siRNA transfection decreased hnRNP K and GAPDH mRNA expression 96 hours after transfection in both cell lines. So, the positive controls confirmed that GAPDH and hnRNP K mRNA expression could be detected by quantitative real-time PCR and were still reduced 96 hours after transfection. When HNSCCUM-02T cells were treated with FAM™-siRNA-MSNs, no reduction in GAPDH mRNA expression was observed after 24 and 96 hours (Figure 45C). In RPMI2650 cells, the GAPDH mRNA expression was also not affected by FAM™-siRNA-MSNs (Figure 45D). HnRNP K-siRNA-MSNs did slightly reduce the hnRNP K mRNA expression in HNSCCUM-02T cells after 24 hours compared to nsRNA-MSNs (Figure 45E), however, no difference in hnRNP K expression to PBS treated controls was seen. After 96 hours incubation, the hnRNP K mRNA expression did not differ between hnRNP K-siRNA-MSN and nsRNA-MSN treated cells. Also, in RPMI2650 cells was observed no effect of hnRNP K-siRNA-MSNs on hnRNP K mRNA expression after both incubation times (Figure 45F). The experiment was only performed once, so results must be evaluated carefully. Nevertheless, 50 µg/ mL siRNA-MSNs did not reduce mRNA expression in HNSCCUM-02T and RPMI2650 cells after 24 and 96 hours incubation, respectively.

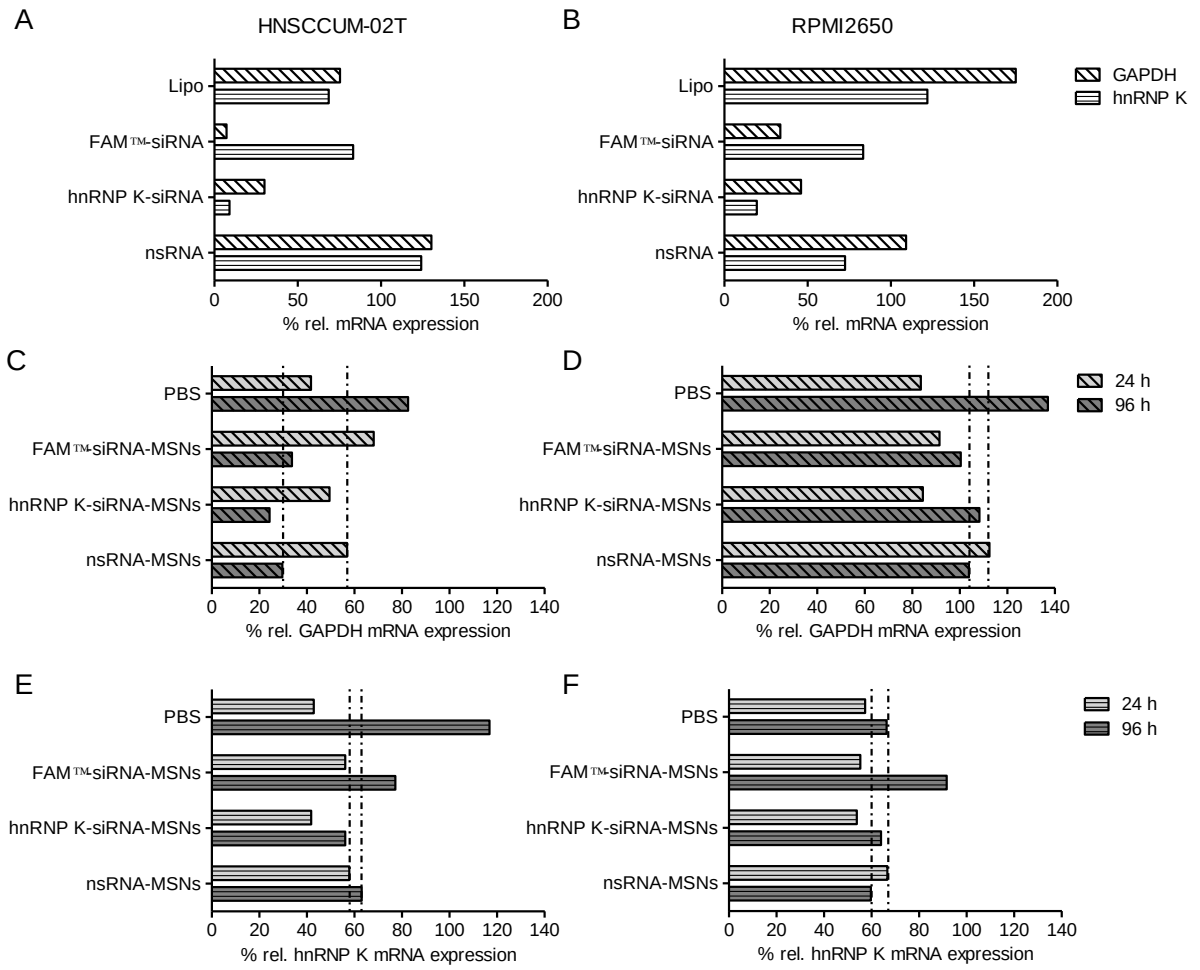

Figure 45: Analysis of hnRNP K and GAPDH mRNA expression after incubation with 50 µg/ mL FAM™-siNRA-MSNs and hnRNP K-siRNA-MSNs in (A, C, E) HNSCCUM-02T and (B, D, F) RPMI2650 cells, respectively

Transfection with Lipo and FAM™-siRNA, Lipo and hnRNP K siRNA, or Lipo and nsRNA in (A) HNSCCUM-02T cells and (B) RPMI2650 cells was performed as a positive control, respectively. A great reduction in GAPDH mRNA expression was observed for FAM™-siRNA transfected cells compared to nsRNA transfected controls after 96 hours. Yet, GAPDH mRNA expression was also reduced in hnRNP K siRNA transfected cells. Transfection with hnRNP K siRNA led to a decrease in hnRNP K mRNA expression compared to nsRNA transfected controls. The (C, D) GAPDH mRNA expression of FAM™-siRNA-MSN treated cells was not reduced after 24 and 96 hours incubation compared to nsRNA-MSN treated cells (dotted lines) in (C) HNSCCUM-02T cells and (D) RPMI2650 cells, respectively. Moreover, (E, F) hnRNP K mRNA expression did not decrease after hnRNP K-siRNA-MSN treatment in (E) HNSCCUM-02T cells and (F) RPMI2650 cells compared to PBS or nsRNA-MSN treated cells (dotted lines). N=1.

4.4.4 Less siRNA loading after MSNs are preincubated with ferrocene

So far, siRNA loading and release could not be proven. For that reason, siRNA loading to Cy5-MSNs (SK-275) was examined in more detail by using FAM™-siRNA and applying dif-

ferent protocols for sealing. It was speculated that the ferrocene preincubation might impair siRNA loading, thus it was examined if siRNA loading is still possible when amino groups were partly saturated by ferrocene (Table 36). In the next step, the FAM™-siRNA was loaded to the NPs overnight and NH_2-β-CD was added.

Table 36: Preincubation with ferrocene before FAM™-siRNA loading to MSNs

Label	c(ferrocene) in µg/ mL	n(FAM™-siRNA) in pmol
A	0	500
B	54.1	500
C	89.6	500
Control (Co)	133.2	500
Standard	493.5	0

The FAM™-siRNA-MSNs were centrifuged, the pellets were observed at Darkreader™ 195 M Transilluminator, and photographically documented as shown in Figure 46. Only MSNs which were not preincubated with ferrocene exhibited a strong fluorescence corresponding to successful FAM™-siRNA loading. When MSNs were preincubated with ferrocene, only weak FAM™-siRNA fluorescence was observed. So, preincubation with ferrocene did reduce the siRNA loading too much as that a facilitated release would compensate for the missing amount of siRNA.

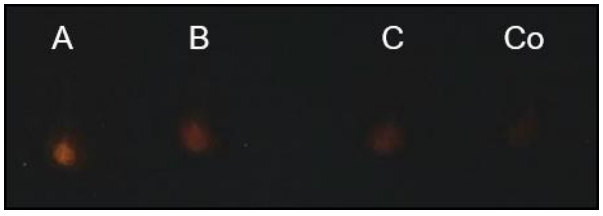

Figure 46: FAM™-siRNA loading to MSNs preincubated with ferrocene
MSNs were first incubated with different amounts of ferrocene as depicted in Table 36, then FAM™-siRNA was added overnight, and particles were capped with the same amount of NH_2-β-CD. After centrifugation, the pellets were examined at Darkreader™ 195 M Transilluminator and documented. Only MSNs without ferrocene preincubation (A) showed a strong fluorescence signal representing FAM™-siRNA loading.

4.4.5 Encapsulation of MSNs with Lipofectamine™ RNAiMAX improves cellular uptake

Because siRNA loading and release could not be proven so far, a new method for siRNA-MSN preparation had to be developed. Moreover, it was speculated that the siRNA-MSNs

were taken up by the endolysosomal system (data shown in 4.2.2) so, the siRNA could have been degraded before it could exhibit its effects. For this reason, NPs were incubated with Lipofectamine™ RNAiMAX instead of ferrocene and NH_2-β-CD after siRNA loading to improve cellular uptake and siRNA release independent of the endolysosomal system.

First, an encapsulation protocol with Lipo for siRNA-MSNs was developed. The MSNs (SK-275, pore size 11.7 nm) were loaded with FAM™-siRNA or nsRNA as control and encapsulated with different amounts of Lipo for different times and at different temperatures according to Table 37, respectively.

Table 37: Lipo encapsulation parameters for Lipo-FAM™-siRNA-MSNs

Label	RNA	Incubation parameters	µL Lipofectamine™ RNAiMAX per µg MSN
A1	FAM™-siRNA	1 h (RT)	0.3
B1	FAM™-siRNA	1 h (RT)	0.4
A3	FAM™-siRNA	3 h (4 °C)	0.3
B3	FAM™-siRNA	3 h (4 °C)	0.4
ACo	nsRNA	1 h (RT)	0.3
BCo	nsRNA	3 h (4 °C)	0.4

The Lipo-FAM™-siRNA-MSNs and Lipo-nsRNA-MSNs were centrifuged and the pellets were illuminated with Darkreader™ 195 M Transilluminator as shown in Figure 47. Lipo-FAM™-siRNA-MSNs exhibited a high brightness while no difference in brightness was observed between the differently encapsulated Lipo-FAM™-siRNA-MSNs. Besides, Lipo-nsRNA-MSNs showed a reduced brightness compared to Lipo-FAM™-siRNA-MSNs. So, FAM™-siRNA was successfully loaded to MSNs independent of the Lipo incubation protocol and the siRNA loading was remarkably higher than after ferrocene preincubation (Figure 46).

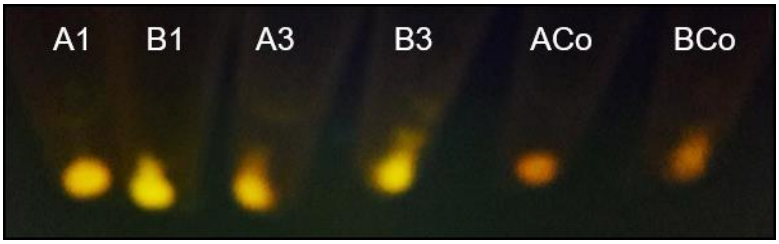

Figure 47: Lipo-FAM™-siRNA-MSN pellets after different loading protocols

Different Lipo-FAM™-siRNA-MSNs were prepared according to Table 37, centrifuged, and illuminated with Darkreader™ 195 M Transilluminator. The labels correspond to the labels in Table 37. Lipo-FAM™-siRNA-MSNs exhibited a high brightness while control Lipo-nsRNA-MSNs showed a reduced brightness. No difference in brightness was observed for different Lipo-FAM™-siRNA-MSNs.

Moreover, the toxicity of Lipo incubated MSNs was studied in HNSCCUM-02T cells. The cells were treated with 10 µg/ mL Lipo-FAM™-siRNA-MSNs or Lipo-nsRNA-MSNs for 24 hours, respectively, and the metabolic activity was assessed. All Lipo-FAM™-siRNA-MSNs decreased the metabolic activity by about 40 % compared to H_2O treated controls. The Lipo-nsRNA-MSNs reduced metabolic activity less. The experiment was only performed once, so the results must be evaluated carefully. Still, it was most likely that Lipo was in fact bound to the NPs because transfection with Lipo also induces (minor) toxicity (data not shown). For most further experiments, less Lipo was used for encapsulation (0.1 µL/ µg MSN) to keep the toxicity as low as possible and siRNA-MSNs were incubated for three hours at 4 °C with Lipo to protect the siRNA.

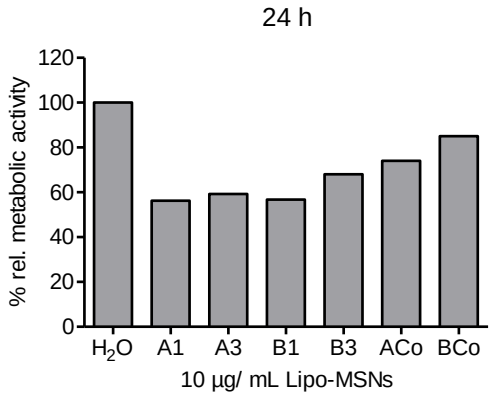

Figure 48: Toxicity of differently encapsulated Lipo-siRNA/ nsRNA-MSNs in HNSCCUM-02T cells after 24 hours incubation

The cells were treated with 10 mg/ mL Lipo-FAM™-siRNA-MSNs or Lipo-nsRNA-MSNs for 24 hours and the metabolic activity was measured. The Lipo-FAM™-siRNA-MSNs reduced the metabolic activity by 40 % compared to H_2O treated controls, independent from the encapsulation parameters. The Lipo-nsRNA-MSNs decreased metabolic activity less. N=1, mean of triplicates.

Furthermore, the influence of the Lipo encapsulation of siRNA-MSNs on cellular uptake was studied. HNSCCUM-02T cells were incubated with 10 µg/ mL Cy5-MSNs (ferrocene and NH_2-β-CD sealed MSNs according to the standard protocol), Lipo-FAM™-siRNA-MSNs, or Lipo-MSNs for 24 and 96 hours, respectively. Then, the cells were stained for viability and were analyzed by flow cytometry. The incubation of MSNs with Lipo decreased the viability of Lipo-FAM™-siRNA-MSN and Lipo-MSN treated cells after 24 hours by about 10 % compared to Cy5-MSN treated cells (Figure 49A). After 96 hours incubation, no difference in viability was observed between the different capped MSNs. The Cy5 signal of Lipo-FAM™-siRNA-MSNs and Lipo-MSNs was remarkably increased compared to Cy5-MSNs after 24 hours incubation (Figure 49B), so Lipo encapsulation enhanced the NP uptake tremendously. After 96 hours incubation, the Cy5-signal differed only a bit, but it was still better for Lipo-FAM™-siRNA-MSNs and Lipo-MSNs. So, Lipo encapsulation greatly improved the NP uptake. However, the FAM™ signal was about the same for Lipo-FAM™-siRNA-MSNs and Lipo-MSNs after 24 hours incubation (Figure 49C) probably caused by Lipo autofluorescence in the detection range. After 96 hours, the FAM™ signal was almost completely reduced to the level of the control cells (Cy5-MSNs, PBS). The experiment was only performed once (with triplicates), for that reason, the results must be evaluated with care. Taken together, the Lipo encapsulation of MSNs decreased the viability only minimally while increasing the NP uptake massively. The FAM™ signal of Lipo-FAM™-siRNA-MSNs could not be distinguished from Lipo-MSNs, so no FAM™-siRNA presence in the cells could be proven.

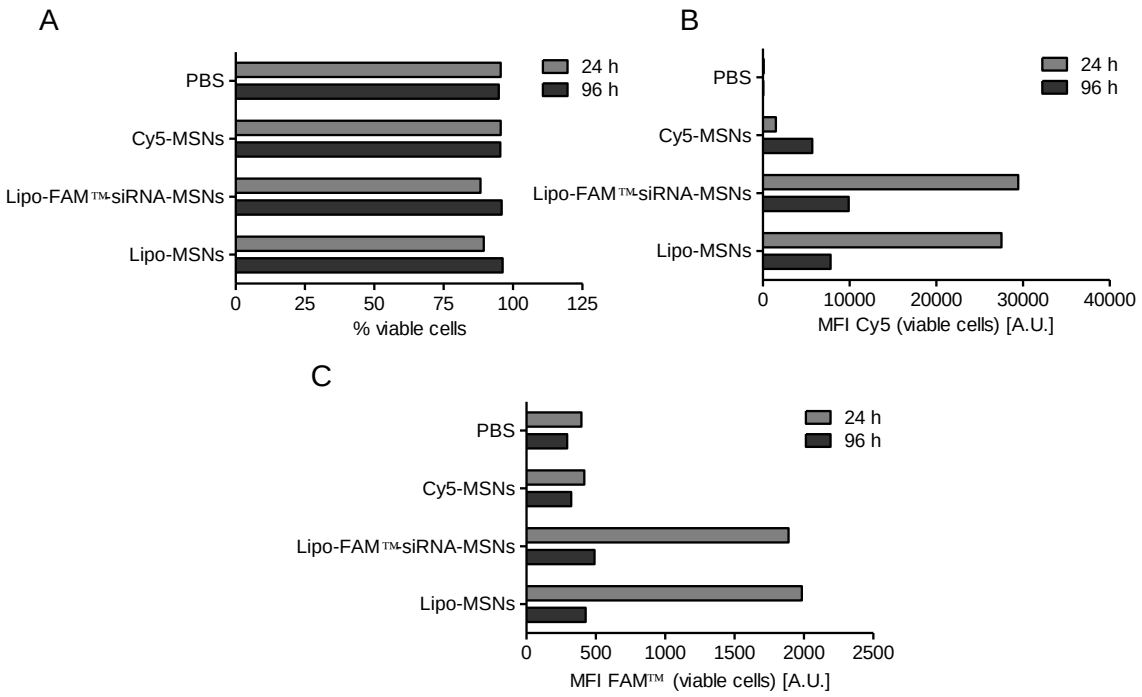

Figure 49: Comparison of nanoparticle uptake in HNSCCUM-02T cells after 24 and 96 hours incubation

MSNs (SK-275) were sealed with ferrocene and NH_2-β-CD (Cy5-MSNs) or Lipo (Lipo-MSNs). Also, MSNs were loaded with FAM™-siRNA and encapsulated with Lipo (Lipo-FAM™-siRNA-MSNs). HNSCCUM-02T cells were incubated with 10 µg/ mL MSNs and analyzed by flow cytometry after 24 and 96 hours. The (A) viability was assessed by FVD780 staining. After 24 hours, the viability of Lipo-sealed MSN treated cells was marginally decreased compared to PBS controls and Cy5-MSN treated cells, respectively. (B) Lipo sealing remarkably increased the Cy5 signal after 24 hours compared to Cy-MSNs. The difference was less after 96 hours of incubation. (C) The FAM™ signal of FAM™-siRNA was also analyzed. After 24 hours incubation, the same FAM™ signal was detected in Lipo-FAM™-siRNA-MSN and Lipo-MSN treated cells. So, Lipo might exhibit autofluorescence in that range. The FAM™ signal was diminished after 96 hours of incubation. N=1, mean of triplicates.

4.4.6 Higher concentrations of Lipo-eGFP-siRNA-MSNs do not reduce eGFP expression in HuH7-GFP cells

Since a better uptake of Lipo-MSNs compared to Cy5-MSNs was observed, it was examined if higher concentrations of Lipo-eGFP-siRNA-MSNs could reduce eGFP expression in HuH7-GFP cells. If more NPs were applied, more eGFP-siRNA should have been transported into HuH7-GFP cells. In one experiment, HuH7-GFP cells were incubated with 10 µg/ mL Lipo-eGFP-siRNA-MSNs or Lipo-nsRNA-MSNs for 96 hours, respectively, and in a second experiment, 25 µg/ mL Lipo-MSNs, Lipo-eGFP-siRNA-MSNs or Lipo-nsRNA-MSNs were applied for 96 hours. Also, the cells were transfected with eGFP-siRNA as a positive control and nsRNA as a negative control. The dead cells were stained, and the samples were analyzed

by flow cytometry for viability, Cy5-signal, and eGFP signal. When HuH7-cells were incubated with 10 µg/ mL Lipo-eGFP-siRNA-MSNs or Lipo-nsRNA-MSNs, respectively, no substantial reduction in viability was observed (Figure 50A). However, 25 µg/ mL Lipo-MSNs, Lipo-nsRNA-MSNs, and Lipo-eGFP-siRNA-MSNs reduced the viability of HuH7-GFP cells by about 10 % compared to PBS treated controls (Figure 50B). The control transfections with eGFP-siRNA did not affect the cellular viability in both experiments. Besides, NP uptake was examined by means of the Cy5 mean fluorescence intensity (MFI) and a great difference between 10 µg/ mL (Figure 50C) and 25 µg/ mL (Figure 50D) Lipo-eGFP-siRNA-MSNs was observed. Although only 2.5 times more NPs were applied, the Cy5 signal for 25 µg/ mL Lipo-eGFP-siRNA-MSNs was about 5.5 times higher than for 10 µg/ mL Lipo-eGFP-siRNA-MSNs. Still, the NPs were prepared for each experiment separately and the experiments were only performed once (with triplicates per treatment), so results must be evaluated carefully. Moreover, the eGFP MFI was determined to examine eGFP expression (Figure 50E and F). Both eGFP-siRNA control transfections reduced the eGFP expression of HuH7-GFP cells by about 80 %. 10 µg/ mL Lipo-eGFP-siRNA-MSNs did not decrease the eGFP expression. Unfortunately, no effect on eGFP expression was seen for 25 µg/ mL Lipo-eGFP-siRNA-MSNs compared to Lipo-nsRNA-MSNs.

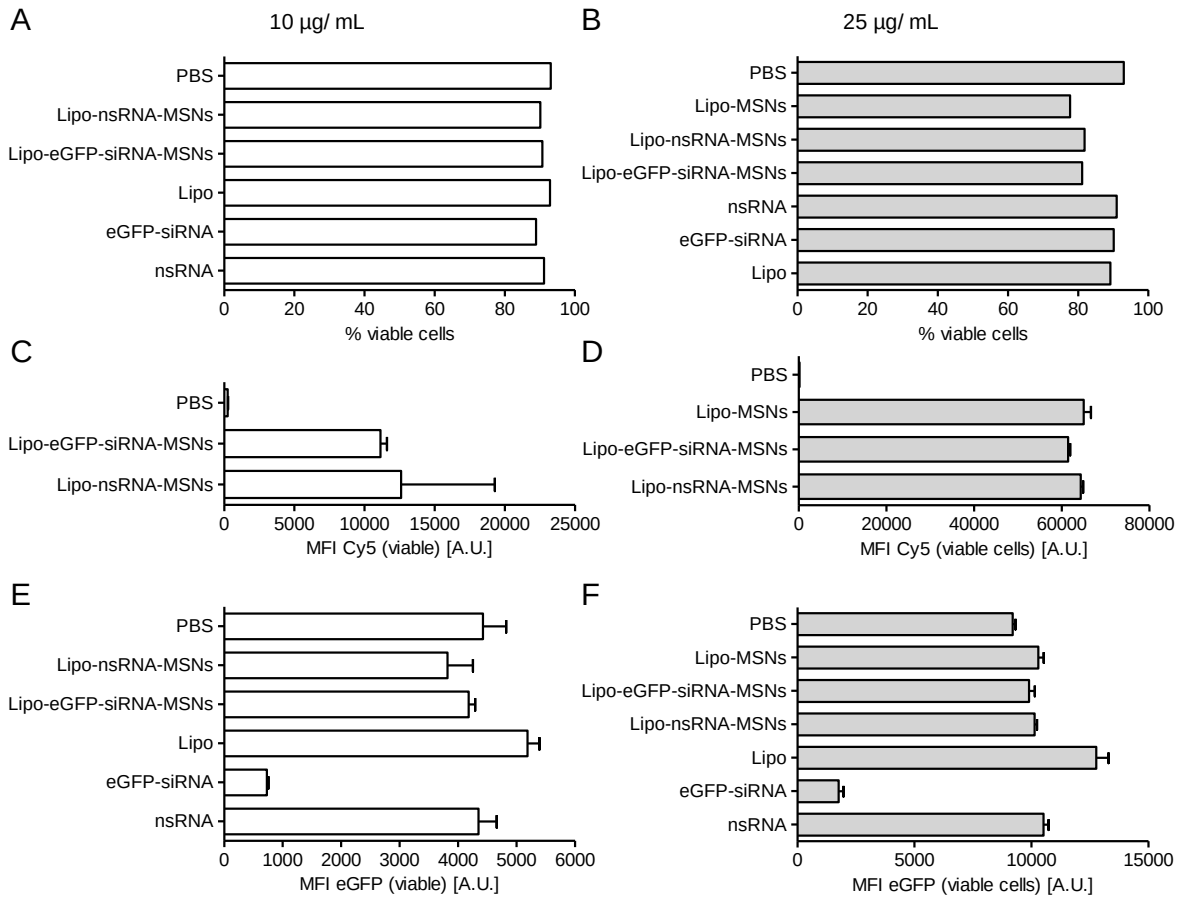

Figure 50: Treatment of HuH7-GFP cells with (A, C, E) 10 and (B, D, F) 25 µg/ mL Lipo-eGFP-siRNA-MSNs for 96 hours analyzed by flow cytometry

(A) 10 µg/ mL Lipo-eGFP-siRNA-MSNs and Lipo-nsRNA-MSNs did not reduce the viability compared to PBS treatment. (B) 25 µg/ mL Lipo-eGFP-siRNA-MSNs and Lipo-nsRNA-MSNs decreased the cellular viability by circa 15 % compared to PBS. (C) The Cy5-signal was comparable for 10 µg/ mL Lipo-eGFP-siRNA-MSNs and Lipo-nsRNA-MSNs. (D) When HuH7-GFP cells were treated with 25 µg/ mL MSNs, the signal was greater than after 10 µg/ mL treatment but did not differ between Lipo-MSNs, Lipo-eGFP-siRNA-MSNs, and Lipo-nsRNA-MSNs, respectively. (E) Cells transfected with eGFP-siRNA exhibited a reduction of the eGFP signal of about 80 % compared to nsRNA transfected cells. 10 µg/ mL Lipo-eGFP-siRNA-MSNs did not decrease the eGFP signal. (F) The positive control (eGFP-siRNA transfection) showed a reduced eGFP signal, while 25 µg/ mL Lipo-eGFP-siRNA-MSNs did not diminish the eGFP signal. N=1, mean of triplicates.

Furthermore, the eGFP mRNA expression was studied after treatment of HuH7-GFP cells with 10 µg/ mL and 25 µg/ mL Lipo-eGFP-siRNA-MSNs, respectively. A protocol for eGFP mRNA expression detection was established and relative eGFP mRNA expression (normalized to calibrator) was greatly reduced after eGFP-siRNA transfection for 72 hours compared to nsRNA transfection (Figure 51A). Although 10 µg/ mL Lipo-eGFP-siRNA-MSNs decreased relative eGFP mRNA expression compared to Lipo-nsRNA-MSN treated cells (Figure 51B), the relative eGFP mRNA expression did not differ from PBS treated HuH7-GFP cells. When

25 µg/ mL Lipo-eGFP-siRNA-MSNs were applied, also no reduction in relative eGFP mRNA expression compared to PBS, Lipo-nsRNA-MSNs, and Lipo-MSNs was noticed.

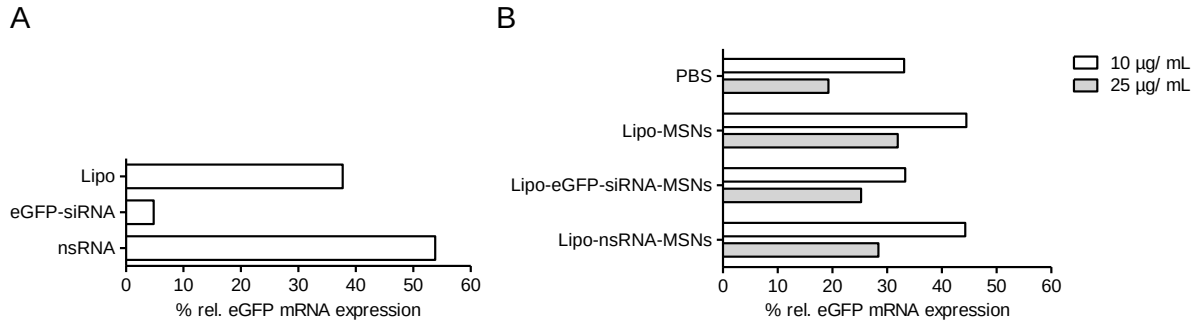

Figure 51: EGFP mRNA expression in HuH7-GFP cells after (A) eGFP transfection and (B) Lipo-eGFP-siRNA-MSN treatment for 72 hours

(A) HuH7-GFP cells transfected with eGFP-siRNA had a greatly reduced eGFP mRNA expression compared to nsRNA transfection. (B) 10 µg/ mL Lipo-eGFP-siRNA-MSNs reduced the eGFP mRNA expression compared to Lipo-nsRNA-MSNs but not compared to PBS. The same effect was observed for 25 µg/ mL Lipo-eGFP-siRNA-MSNs. N=1.

Overall, Lipo-eGFP-siRNA-MSNs neither decreased eGFP expression nor eGFP mRNA expression in HuH7-GFP cells independent from the applied concentration and incubation times.

4.5 Active targeting of Cy5-MSNs *in vitro*

Another approach to enhance NP uptake uses active targeting moieties that target cell surface structures dominantly expressed on malignant cells. About 90 % of HNSCC cells highly express EGFR. Therefore, a monoclonal EGFR-antibody that binds the extracellular domain of the EGFR was utilized for targeting. First, EGFR expression in two different HNSCC cell lines, namely HNSCCUM-02T and RPMI2650, was analyzed. As depicted in Figure 52 by immunoblot analysis and immunofluorescence staining, HNSCCUM-02T cells highly expressed EGFR while RPMI2650 barely express EGFR. For this reason, both cell lines were used to validate EGFR-targeting success by EGFR-antibody conjugated MSNs.

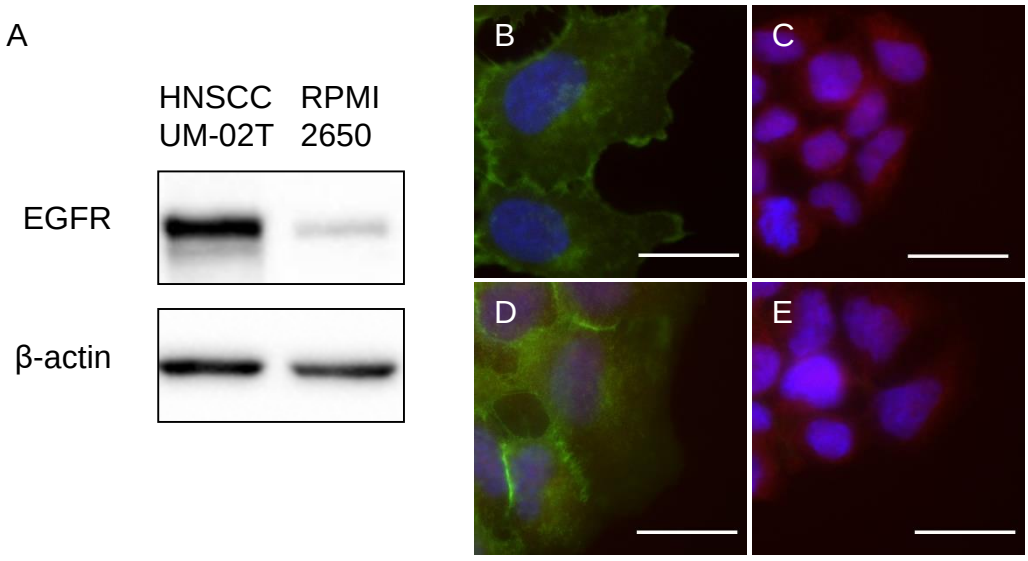

Figure 52: EGFR expression in HNSCCUM-02T and RPMI2650 cells

(A) Immunoblot analysis of EGFR expression in HNSCCUM-2T and RPMI2650 cells. HNSCCUM-02T cells highly express EGFR while RPMI2650 cells barely express EGFR. Immunofluorescence staining of EGFR with (B, C) anti-EGFR antibody (Thermo Fisher Scientific) or (D, E) anti-EGFR antibody (CST). Merged images with EGF receptors depicted in green, nuclei in blue and F-actin in red are presented. High EGFR expression of HNSCCUM-02T cells (B, D) was demonstrated with both antibodies. In accordance with immunoblot analysis was no EGFR expression identified in RPMI2650 cells (C, E). Representative images are shown. Scale bar: 10 µm.

4.5.1 Antibodies are successfully conjugated to MSNs

The antibody conjugation to the MSNs was performed with a linker molecule. The linker contained polyethylene glycol moieties for spacing and an *N*-hydroxysuccinimide ester for coupling the amino groups of the NH_2-β-CD with an amide bond. After antibodies were sulfhydrated with Traut's reagent, $(SH)_x$-antibodies were conjugated by a disulfide bond replacing a 2-pyridyldithio group. As mentioned above, a monoclonal anti-EGFR mouse IgG2a antibody was used, so as unspecific control a mouse IgG2a control antibody was utilized. The Coupling Factor (CF, see 3.2.2.5.1) was determined for each experiment to evaluate the coupling success. As presented in Figure 53A, the CF for EGFR-MSNs and IgG2a-MSNs was significantly greater than for Cy5-MSNs. However, when the CF was normalized to Cy5-MSNs in the respective experiment, one experiment showed a greater coupling success than the other experiments (Figure 53B). Still, successful antibody conjugation was proven for each experiment.

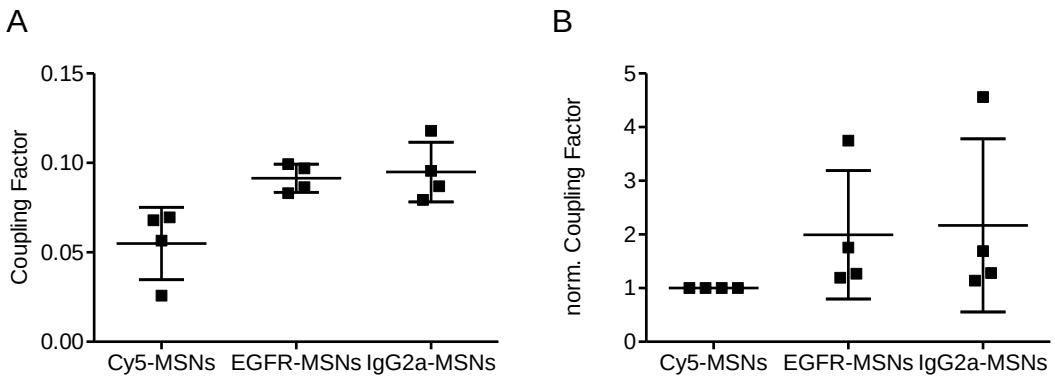

Figure 53: Coupling Factor and normalized Coupling Factor of antibody conjugation to MSNs

The determination of the CF is described in detail in 3.2.2.5.1. (A) The CF is significantly higher for EGFR-MSNs and IgG2a-MSNs compared to Cy5-MSNs. N=4, mean ± S.D., one-way ANOVA: P=0.0107; Dunnett's Multiple Comparison Test: Cy5-MSNs vs. EGFR-MSNs: P<0.05, Cy5-MSNs vs. IgG2a-MSNs: P<0.05. (B) When data were normalized to Cy5-MSNs, only one experiment showed a great coupling efficiency while the other experiments had similar coupling efficiencies.

4.5.2 EGFR-MSNs are faster taken up by high EGFR expressing cells than IgG2a-MSNs

As mentioned above, active targeting should improve cellular NP uptake. This hypothesis was tested by comparing the MSN association between a high EGFR expressing cell line, HNSCCUM-02T, and a low EGFR expressing cell line, RPMI2650, respectively. Moreover, different incubation times were analyzed, and the results are presented in Figure 54. Single cells were plotted in a dot plot dependent on viability and Cy5 signal, then were gated in four populations.

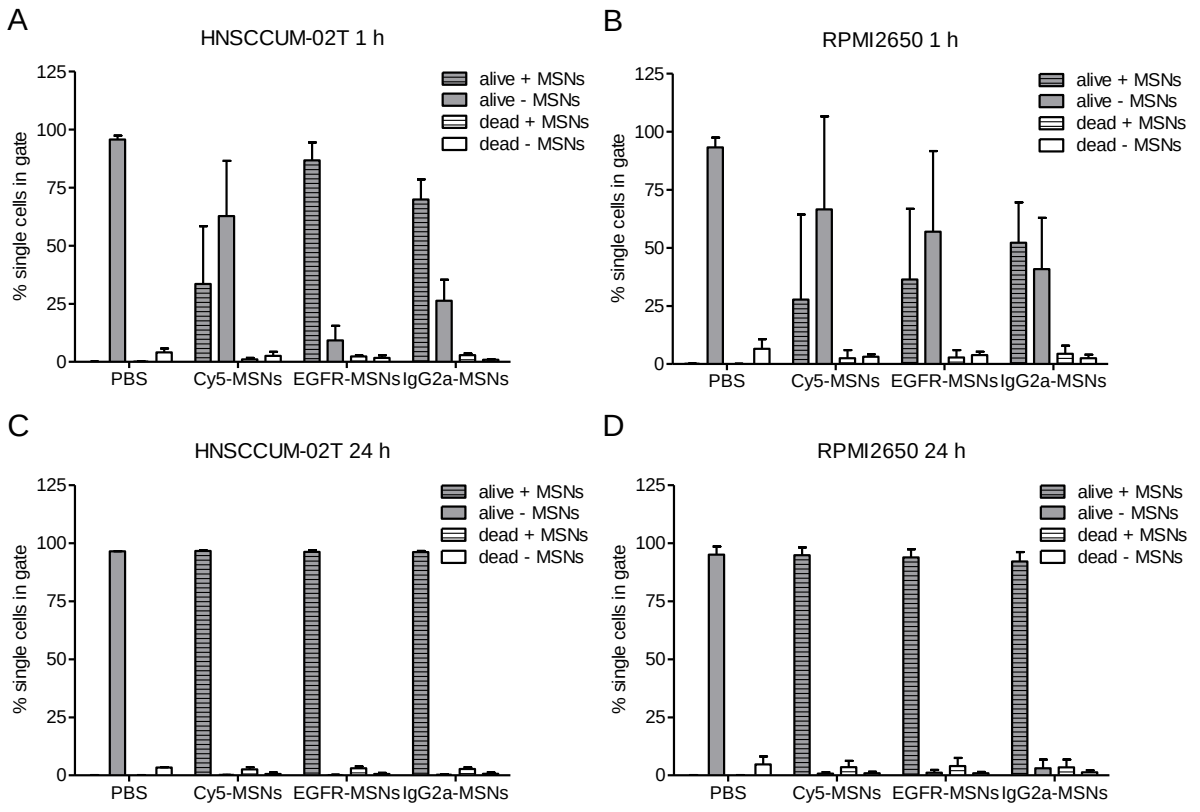

Figure 54: Uptake of 10 µg/ mL Cy5-MSNs, EGFR-MSNs and IgG2a-MSNs in (A, C) HNSCCUM-02T and (B, D) RPMI2650 cells after (A, B) 1 hour and (C, D) 24 hours incubation analyzed by flow cytometry

Single cells were gated for alive + Cy5, alive - Cy5, dead + Cy5, and dead - Cy5. Overall, no effect on viability was seen. (A) About 90 % of high EGFR expressing HNSCCUM-02T cells were alive with Cy5 signal after 1 hour incubation after EGFR-MSN treatment while IgG2a-MSN treatment led to less MSN association. The lowest uptake was observed for Cy5-MSN treatment and no NPs were detected in PBS treated cells. (B) In low EGFR expressing RPMI2650 cells, the MSN association was not enhanced by EGFR-targeting after 1 hour incubation, but high standard deviations between experiments occurred. After 24 hours incubation no difference between Cy5-MSN, EGFR-MSN and IgG2a-MSN treatment was noticed in (C) HNSCCUM-02T and (D) RPMI2650 cells. Almost all single and alive cells of both cell lines had taken up the MSNs and antibody-conjugated MSNs. N=3, mean + S.D.

Overall, the viability was not affected by Cy5-MSN, EGFR-MSN and IgG2a-MSN treatment after one hour and 24 hours incubation in both cell lines, respectively. Also, no Cy5 positive population was identified after PBS treatment in both cell lines and after both time points. After one hour EGFR-MSN incubation in HNSCCUM-02T cells (Figure 54A), about 85 % of the single cells were positive for Cy5 whereas about 70 % of all cells were positive for Cy5 after IgG2a-MSN treatment. Yet, incubation with Cy5-MSNs for one hour only led to 33 % Cy5 positive cells on average but with a high standard deviation. In contrast, no difference in the Cy5 signal was observed after 24 hours incubation of the different NPs in HNSCCUM-02T cells

(Figure 54C). In RPMI2650 cells, great differences in the Cy5 signal between experiments were noticed in all MSN treatment groups after one hour incubation (Figure 54B). Besides, no substantial differences of alive and Cy5 positive cells were detected between Cy5-MSN and antibody-conjugated MSN treated cells. The amount of alive and Cy5 positive RPMI2650 cells was smaller than the amount of corresponding HNSCCUM-02T cells one hour after treatment, and after 24 hours incubation time, all MSN treated RPMI2650 cells were Cy5 positive (Figure 54D). In conclusion, EGFR-targeting accelerated MSN uptake in high EGFR expressing HNSCCUM-02T cells compared to low EGFR expressing RPMI2650 cells while viability was not impaired.

4.5.3 Active targeting of eGFP-siRNA-MSNs does not reduce eGFP mRNA expression

Active targeting against EGFR revealed an accelerated uptake of EGFR-MSNs. So, eGFP-siRNA-MSNs were also conjugated with the EGFR-antibody and eGFP mRNA expression was analyzed in HuH7-GFP cells. HuH7 cells exhibit less EGFR expression than HNSCCUM-02T cells, nevertheless, EGFR protein expression was still detectable (Figure 55A). First, MSNs were loaded with eGFP or nsRNA overnight, respectively, second, MSNs were sealed with ferrocene and NH_2-β-CD, and third, EGFR-antibodies or IgG2a-antibodies were conjugated to the eGFP-siRNA-MSNs and nsRNA-MSNs, respectively. PBS treatment was used as a control. After 72 hours incubation with 10 µg/ mL of various MSNs, the RNA was isolated, transcribed to cDNA and a qPCR was conducted with eGFP as the target gene and RPLPO as the reference gene. The eGFP mRNA expression was normalized to untreated HuH7-GFP cells (calibrator samples) as presented in Figure 55B. No reduction in relative eGFP mRNA expression was observed for eGFP-siRNA-MSNs, EGFR-eGFP-siRNA-MSNs, and IgG2a-eGFP-siRNA-MSNs compared to the PBS control, indicated by the dotted line. At the same time, neither nsRNA-MSNs nor EGFR-nsRNA-MSNs nor IgG2a-nsRNA-MSNs decreased the relative eGFP mRNA expression. However, the experiment was only performed once, so results must be evaluated carefully. Taken together, active targeting did not facilitate eGFP-siRNA-MSN efficacy in HuH7-GFP cells.

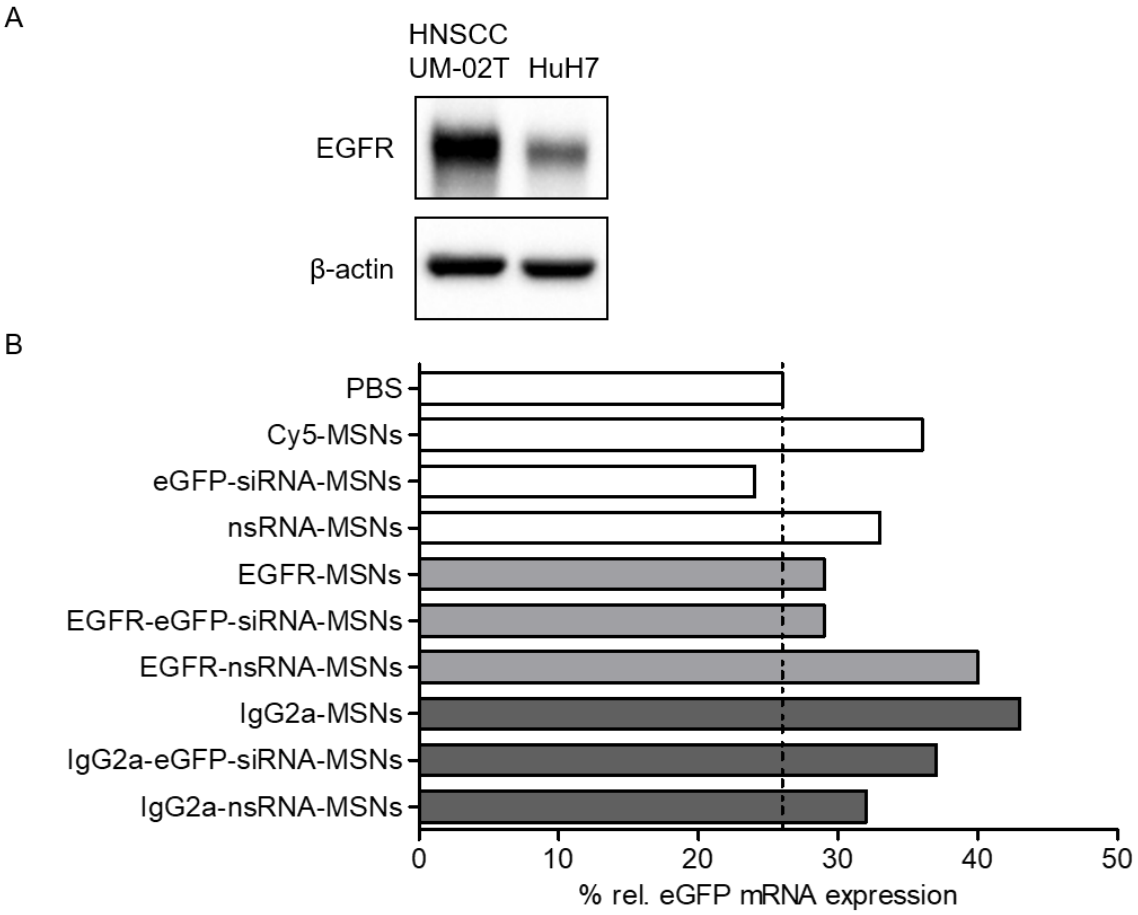

Figure 55: (A) EGFR expression in HNSCCUM-02T and HuH7 cells and (B) relative eGFP mRNA expression in HuH7-GFP after 10 µg/ mL EGFR-eGFP-siRNA-MSN treatment for 72 hours

(A) Immunoblot analysis was performed with the assistance of Simone Mendler. HuH7 cells expressed less EGFR than HNSCCUM-02T but an EGFR expression was still detectable. β-actin was used as control. (B) MSNs were first loaded with eGFP-siRNA or nsRNA, sealed with ferrocene and NH_2-β-CD, and conjugated to EGFR or IgG2a antibodies, respectively. HuH7-GFP cells were treated with 10 µg/ mL of the stated MSN variants for 72 hours and then the RNA was isolated, transcribed to cDNA, and qPCR was performed. The dotted line indicates relative eGFP mRNA expression for PBS controls. Neither eGFP-siRNA-MSNs nor EGFR-eGFP-siRNA-MSNs nor IgG2a-eGFP-siRNA-MSNs reduced the relative eGFP mRNA expression in HuH7-GFP cells. All nsRNA-MSN controls also not affected relative eGFP mRNA expression. N=1.

5 Discussion

The aim of this work was to evaluate MSNs as drug carriers for head and neck squamous cell carcinoma therapy *in vitro*. In general, drug carriers should meet certain criteria that qualify them for the use as drug delivery vehicles. First, the system must be classified as safe. Second, efficient drug loading and release must be ensured and third, the delivery and efficacy of the loaded drug must be proven at the target site. The evaluation of these parameters regarding the examined MSN drug carrier system will be discussed in the following subchapters.

5.1 Characteristics and safety of the drug delivery system

One major advantage of MSNs is the possibility to generate various shapes, particle and pore sizes dependent on the synthesis parameters such as time, stirring velocity, and the used surfactant. The here applied MSNs had a spherical shape and a hydrodynamic diameter between 140 and 200 nm after conjugation of the gatekeeper system dependent on the particle batch. In general, the MSNs exhibited a uniform size distribution and shape observed in TEM images and with DLS measurements. Gratton et al. discovered that the NP shape and size influence the cellular uptake of MSNs: On the one side, MSN rods are taken up the best compared to spheres, cylinders, and cubes for particle sizes greater than 100 nm [72]. On the other side, the smaller the NP size the higher the possibility that the NPs are taken up by chance by caveolae-dependent endocytosis or macropinocytosis, respectively [166]. In contrast, larger NPs (> 50 nm) must be usually incorporated by receptor-mediated endocytosis, so the uptake efficiency of untargeted NPs is also dependent on surface modifications. In this work, it was shown that the spherical MSNs with the gatekeeper system were present in endosomes and lysosomes after six hours incubation time, so a general uptake occurred. However, incubation of the MSNs with Lipofectamine RNAiMAX, a cationic lipid formulation for experimental siRNA transfection, tremendously increased cellular uptake. Presumably, this effect was dependent on the membrane penetration capability of cationic lipids and the positive surface charge [69,100]. The cellular membrane is negatively charged and could interact with the positively charged Lipo-MSNs [69], hence the Lipo encapsulated MSNs could be taken up passively in a high number. Still, it is not known, and was not examined if the cellular uptake was mediated passively by electrostatic interaction or actively by endocytosis. Slowing et al. found that positively charged NPs are taken up faster by human cancer cells than neutral or negatively charged NPs [70]. Hence, not only the application of the cationic lipids but also the ferrocene/ β-CD gatekeeper system enhanced the uptake probability be-

cause a positive charge was detected for the sealed MSNs. Still, the ζ-potential measurements were not conducted in a physiological milieu, so the Cy5-MSNs did not have a protein corona during measurements. When NPs are incubated in a serum enriched medium, a protein corona develops and the characteristics of the NPs change. For example, the uptake of MSNs without a protein corona is better than the uptake of MSNs with a protein corona [167]. Yet, the extent of the protein corona of the here applied Cy5-MSNs was not analyzed, therefore, it can only be speculated that the positive surface charge enhanced NP uptake. *In vivo*, the nanoparticle uptake is also dependent on the evasion of the mononuclear phagocytic system (MPS). On the one side, an MSN size of 100- 200 nm is favorable for MPS evasion [80] and on the other side, coating with PEG enhances blood circulation times [58,75]. For this reason, a modification of the NH_2-β-CD with PEG should be considered to improve the *in vivo* compatibility.

A major characteristic of the MSNs is their dendritic structure which generates pores that can be loaded with drugs. These pores must be sealed with a gatekeeper system to prevent uncontrolled drug release and a plethora of gatekeeper systems for MSNs are described in the literature (see 1.3.2.2). Usually, the pores should be opened inside the cancer cells or the extracellular environment of the tumor. Thus, these systems should react to internal or external stimuli, e.g. acidic pH, reducing or oxidizing agents, light. Here, the examined drug delivery system had a capping system that reacted to intracellular stimuli. The redox- and pH-sensitive gatekeeper system was constructed as follows: Ferrocenecarboxaldehyde was conjugated to the amino-functionalized MSNs via an imine bond that is cleaved by protonation in an acidic environment. So, when the MSNs were taken up by endocytosis, the imine bond could be cleaved in the endosomes and lysosomes (pH gradient from 6.2 to 4.6) [168]. Besides, the ferrocene stalk is encircled by β-cyclodextrin via so-called host-guest interactions i.e. through hydrophobic interactions which are weakened upon oxidation of the iron [169]. Then, the pores are opened, and the cargo can be released. The functionality of this system was described by Xiao et al. and Khashab et al. who studied controlled release of Rhodamine B but did not examine the system *in vitro* and *in vivo* [64,170]. Intracellularly, oxidizing agents such as ROS, which are byproducts of the cellular oxidative metabolism and also include hydrogen peroxide [171], can oxidize the iron and thereby decrease the hydrophobic interaction with the β-CD [170]. However, no experiments were conducted to examine the ROS levels in the used cell lines in this work, and the effect of ROS on the Cy5-MSNs.

In this work, the MSNs with the ferrocene/ β-CD gatekeeper system were analyzed for the first time *in vitro* and *in vivo*. The unloaded and sealed Cy5-MSNs exhibited good biocompat-

ibility in various cancer cell lines, a mouse embryonic fibroblast cell line and in chicken embryos. This is not surprising, considering that two of the main components, silica and β-CD, are recognized as safe by the FDA [53,172], and ferrocenecarboxaldehyde is categorized as not harmful by REACH [173]. In many cell culture studies MSNs did not exhibit toxicity up to 100 µg/ mL [90,100,105,135], too, and sometimes even higher concentrations of 500 µg/ mL did not reduce the viability of the cells [91]. It should be noted that the *in vitro* and *in vivo* biocompatibility of the MSNs is dependent on the modifications of the MSNs, e.g. PEI coating reduced the metabolic activity after 100 µg/ mL MSN treatment [134]. Interestingly, the mouse embryonic fibroblast cell line NIH-3T3 exhibited reduced metabolic activity for 5 µg/ mL of Cy5-MSNs while concentrations from 10 µg/ mL to 50 µg/ mL showed stable metabolic activity. This effect was also observed by Salis et al. after 24 hours of MSN incubation but no explanation was given [174]. In contrast, higher concentrations (≥ 50 µg/ mL) of Cy5-MSNs even increased the metabolic activity of a hepatocarcinoma cell line (HuH7). This phenomenon was also observed in a human melanoma cell line for even higher concentrations of MSNs in the MTT assay, an assay which also evaluates the metabolic activity. Huang et al. even found increased tumor growth caused by MSNs in a nude mice xenograft model when tumor cells were pretreated with 0.2 mg/ mL MSNs before subcutaneous injection and claim that the effects are mediated by a decrease in endogenous ROS [175]. However, this was one murine study of many and in most *in vivo* studies no increased tumor growth by unloaded MSNs compared to the saline-treated controls was detected [88,114] which was also the case for the evaluated HNSCC cell lines (HNSCCUM-02T, RPMI2650, and Cal-33) in this work. Nonetheless, the promising biocompatibility data were reassessed *in vivo*, e.g. by Tamanoi et al. who determined a maximally tolerated dose of 50 mg/ kg spherical MSNs when the particles were applied intravenously in nude mice. Moreover, a long-term toxicity study revealed no unusual response after injection of 18 doses (50 mg/ kg) within two months [82]. Yet, the absence of an immune response is not surprising considering that the nude mice lacked a T-cell response and the MSNs were degraded to silicic acid or smaller particles and excreted via the kidneys [135]. It might seem contradictory that in this work, the biodistribution analysis in the CAM model revealed an accumulation of the MSNs in the glomeruli of the kidneys and the liver but the incubation time of 24 hours was too short for the NPs to degrade to smaller particles that could be excreted during that short time. Also, from an experimental point of view, degraded Cy5-MSNs could not be detected by CLSM because the degraded NPs would also dissociate from the fluorescent dye. Furthermore, the Cy5-MSN concentration in the chicken embryos blood circulation can only be estimated according to the data by C. Kind, who determined that the blood volume on day 12, the day the Cy5-MSNs were in-

jected into the CAM, was 1.15 mL [176]. So, the initial concentration would have been 43 µg/ mL or 21.5 µg/ mL of Cy5-MSNs in the embryo's blood circulation, respectively, which was 4-fold or 2-fold higher than the concentration applied in most cell culture experiments (10 µg/ mL), respectively. Another characteristic of the CAM model is the immunodeficiency of the chicken embryo [177]. On the one side, this allows to establish xenograft tumor models on the CAM, on the other side, it cannot be evaluated if MSNs cause inflammatory effects at high accumulation sites such as the liver. Altogether, Cy5-MSNs were detected mainly in the blood vessels of the examined organs and no NPs were detected in the brain. Hence, the blood-brain-barrier retained the NPs. When the organs were removed, an increase of the kidney size was noticed which could have been caused by an accumulation of the Cy5-MSNs in the glomeruli. The higher the particle concentration, the more pronounced was this effect. Of course, this is unfavorable and could cause an increase in blood pressure and organ failure if the MSNs are not degraded in time. Still, the chicken embryos survived the Cy5-MSN treatment for 24 hours, but longer incubation times would be necessary to examine the NP accumulation in more detail.

A 3D tumor model consisting of hepatocarcinoma cells (HuH7 cell line) was established on the CAM to study whether Cy5-MSNs can extravasate the blood vessels. The EPR effect should enhance NP accumulation in the tumor but only a few Cy5-MSNs were detected in the tumor on the CAM. Yet, this is not surprising since the EPR effect only causes a 2-fold increase in NP accumulation compared to critical normal organs (liver, spleen, kidneys) [32,178]. Furthermore, the Cy5-MSN uptake was examined by flow cytometry and CLSM to confirm that the NPs can be internalized by the cells, the pores can be opened, and the cargo released. It was noticed that the unloaded and sealed NPs were taken up time-dependently by endocytosis because after six hours incubation, more than half of the Cy5-MSNs, and after 24 hours, almost all Cy5-MSNs were present in endosomes and lysosomes as shown by co-localization analysis. Along the endolysosomal system, the pH decreases which facilitates pore opening by cleavage of the imine bond between ferrocene and the MSNs. Then, the cargo would be released but would also have to escape the endosomes and lysosomes before degradation. The endosomal escape could be modulated by the proton sponge effect which could be induced by the then free amino groups of the MSNs. Still, co-localization analysis by CLSM is not completely accurate and the analysis method can also influence the results [160]. A more accurate method to analyze the NP localization would have been TEM, e.g. J. Liu et all showed their hollow MSNs in endosomes and the cytoplasm of hepatocarcinoma cells (HepG2 cell line) [114]. Moreover, no differences in NP uptake were observed

between methylated β-CD and amino-functionalized β-CD/ methylated β-CD capped MSNs. In later experiments, when MSNs were sealed only with NH_2-β-CD, the Cy5-MSNs were still taken up comparably. The amino-functionalization of the β-CD enabled further modifications of the drug delivery system, e.g. with a targeting moiety or cell-penetrating peptides. Also, the NH_2-β-CD could facilitate endosomal release, and targeting can improve cellular uptake and will be discussed later. After good biocompatibility and efficient Cy5-MSN uptake were established in cancer cells, drug loading and release were studied, which will be discussed next.

5.2 Drug loading and release of MSNs

The aim of this work was to use MSNs for drug delivery. Especially, the transport of siRNA as therapeutic agent for protein expression regulation is challenging and requires modified nanocarriers. For this reason, it was examined if the MSNs with the ferrocene/ β-CD gatekeeper are suited as siRNA delivery system. It was found that detecting the loading and release of siRNA is complex, and therefore, different model systems were exploited. On the one side, the small molecule drug Dox was used because of its characteristics, namely toxicity in small concentrations and fluorescence, and on the other side, fluorescent dye-labeled siRNA was utilized. Also, a stable eGFP-expressing cell line (HuH7-GFP) was employed to test siRNA efficiency.

The chemotherapeutic drug Dox is widely used as a model drug for testing innovative drug delivery systems and was also employed in this work. Dox exhibits fluorescence and therefore, the drug loading and efficiency of the gatekeeper could be observed. The MSNs which were used for Dox loading had an average pore size of 8.2 nm, which is relatively large compared to other MSN systems. The most published MSNs with a similar diameter had pore sizes between 2 and 4 nm for loading of small molecule drugs [114,119,179]. After the Dox-MSNs were loaded with Dox and sealed with the gatekeeper system, washing up to eight times to remove excess Dox was necessary. Then, the drug loading was determined by measuring the absorption and fluorescence of Dox in the supernatants. Mostly, the loading efficiency was between 20-30 % of the initially loaded Dox amount and could be visually observed by red staining of the NP pellet. The loading efficiency was higher than most described by others (11 %) but mostly MSNs with smaller pores were used for Dox loading [91,114]. Of course, MSNs with larger pore sizes also have a higher drug loading capacity, e.g. Chen et al. synthesized MSNs (diameter 130 nm) with 4.7 nm pores and achieved a Dox loading efficiency of 58.3 % [180] with a different loading protocol and different protocol to determine the loading efficiency. Here, the MSNs had a greater pore size (8.2 nm) and it was

found that the loading efficiency was dependent on the used Dox concentration and not the total Dox mass. The Dox concentration was limited by the Dox solubility and 5 mg/ mL Dox in H_2O was the highest possible concentration observed. Moreover, the incubation of Dox-MSNs in different media for 24 and 96 hours revealed a Dox release of only small fractions of the loaded drug. Consequently, the gatekeeper system efficiently retained the drug under the examined conditions. In PBS, H_2O, and DMEM less than 1 % of the loaded drug (equals less than 0.15 µM) were retrieved after four days incubation at 37 °C. Yet, DMEM with FCS exhibited an increased Dox signal in the supernatants but also in the Cy5-MSN incubated control, even though the standard curve was prepared in the same medium. It was speculated that the present proteins might disturb the fluorescence measurement because the fluorescence value for the control was above the Dox-MSN value after 24 hours incubation. After four days of incubation, about 2.5 % of the Dox were retrieved in the supernatant of Dox-MSNs when the control value was deducted. Thus, FCS might facilitate a minimal Dox release in the medium, but only low effects of Dox were expected by the released Dox. The toxic effect of Dox is time- and concentration-dependent as shown by the determination of the IC50 in two different HNSCC cell lines which also exhibited different sensitivity. When the base of tongue squamous cell carcinoma cells were incubated with 1 µM Dox, 10 µg/ mL Dox-MSNs, and control Cy5-MSNs in medium with and without FCS, the metabolic activity was decreased for cells incubated in medium without FCS after 24 hours. Still, the reduction of metabolic activity was also observed for the control groups, so the decrease was rather caused by the missing nutrients and growth factors. At the same time, a retarded release of Dox from Dox-MSNs was noticed. In the beginning, Dox-MSNs were loaded with a lower concentrated Dox solution, but the loading efficiency could not be determined because the whole Dox was detected in the supernatants. Yet, Dox-MSNs decreased the metabolic activity of two cell lines after incubation for 24 or 48 hours with the NPs and 72 or 48 hours without the NPs, respectively. Hence, it was assumed that the gatekeeper system dissociated inside the cells and released the Dox in a retarded manner. Then, the loading protocol was changed, and Dox-MSNs were loaded with a 2.5-fold higher concentrated Dox solution, but less total Dox which allowed quantification of the loading efficiency. Cancer cells were incubated with these Dox-MSNs and were analyzed by flow cytometry for viability, NP uptake, and Dox signal. The efficacy on the viability of Dox-MSNs corresponded to more than 1 µM Dox after 24 and 96 hours incubation. Still, after 24 hours of 1 µM Dox and Dox-MSN treatment, the viability was only slightly reduced compared to controls. On average, only half of all viable cells showed a Cy5 and Dox signal after 24 hours treatment with Dox-MSNs but almost all the rest of the viable cells were positive for Dox. So, Dox was released into the cells but probably also in the medium.

Yet, the concentration was too low to kill the cells within 24 hours. Almost all cells treated with 1 µM Dox exhibited a Dox signal while the controls (PBS and Cy5-MSNs) were negative for Dox. Only 30 % of all viable cells were positive for Cy5, so the uptake of unloaded NPs was lower than the uptake of Dox-MSNs. After 96 hours of treatment with free Dox or Dox-MSNs, only a few cells survived while the controls consisted of more than 90 % viable cells. Higher concentrations of Dox-MSNs could have been applied to enhance the toxicity, but experiments were performed with 10 µg/ mL NPs to be able to study the release kinetics in more detail. The retarded release of Dox was further analyzed in two cell lines by staining of γH2AX foci which indicate DNA damage. It was detected in both cell lines, that the γH2AX foci per nucleus increased from two to 24 hours incubation with Dox-MSNs. Also, after two hours incubation, MSNs were probably associated with the cellular membranes but only the nuclei were stained and not the cellular membranes for verification. Yet, experiments with unloaded MSNs revealed that the particles already associated with the cellular membrane after two hours incubation and were internalized and distributed around the nuclei after 24 hours incubation. As expected, control NPs did not induce DNA damage. Overall, a retarded release of Dox from Dox-MSNs was observed in two cancer cell lines, hence drug loading and release of a small molecule drug were possible in general.

Next, siRNA loading and release in MSNs were tested using the MSN batch which was previously utilized for Dox loading and release. In the first experiment, MSNs were loaded with eGFP-targeting siRNA and stable eGFP-expressing cells (HuH7-GFP) were incubated with different particle concentrations and for different incubation times. The particle concentrations were even doubled compared to the experiments with Dox. Still, no reduction in eGFP expression was observed by flow cytometric analysis after eGFP-siRNA-MSN incubation. At the same time, transfection with Lipofectamine™ RNAiMAX transfection reagent and eGFP siRNA reduced the eGFP expression decently. Thus, the incorporated siRNA did not exhibit its effect on protein expression. Possible explanations were that the siRNA was degraded during loading and sealing (total preparation time 25 hours, incubated at 4 °C) or the NP concentration was too small, respectively. Yet, Hickerson et al. showed that siRNA could even be incubated at 37 °C for 24 hours without degradation [181]. For that reason, the siRNA should be stable at the chosen incubation conditions. It was assumed that the pore size of the MSNs (8.2 nm) was too small for the siRNA which has a diameter of circa 2 nm and is about 7 nm long and therefore no adequate loading could be achieved. For this reason, a new batch of MSNs (SK275) with larger pores (11.7 nm diameter on average) was utilized for siRNA loading. Another possibility for absent siRNA efficacy could have been, that the electrostatic inter-

action between the negatively charged siRNA and the positively charged amino-functionalized MSNs was too strong and the siRNA did not dissociate from the NPs inside the cells [182]. Thus, the MSNs were also pre-incubated with ferrocene before siRNA loading and afterward sealed with NH_2-β-CD. These NPs were tested in HNSCCUM-02T cells and mRNA expression analysis after incubation with FAM™-siRNA-MSNs and hnRNP K-siRNA-MSNs. Also, the applied NP concentration was increased to 50 µg/ mL and the incubation time was reduced to 24 and 96 hours because a reduction in mRNA expression is detectable earlier than a reduction in protein expression. However, no decrease in mRNA expression was noticed after NP treatment independent of the incubation time and target compared to nsRNA-MSNs and PBS. This could have been provoked by different causes, namely, the loaded amount of siRNA was insufficient or was degraded in the endolysosomal system before it could exhibit its effect. On this account, the loading of siRNA to MSNs was examined more detailed and MSNs were pre-incubated with various smaller amounts of ferrocene compared to regular sealing before FAM™-siRNA loading. Yet, the ferrocene pre-incubation decreased the FAM™-siRNA loading, in other words, only minimal amounts of siRNA were loaded to the MSNs. Thus, it is not surprising that the mRNA expression was not reduced even by a high concentration of siRNA-MSNs. The siRNA loading efficiency could not be determined, although RNA can be detected by UV/Vis measurement. The supernatants which were retrieved directly after loading were measured with a spectrophotometer, but the ferrocene and NH_2-β-CD interfered with the measurement. Thus, siRNA loading could only be evaluated qualitatively and not quantitatively.

Another strategy for siRNA delivery via MSNs was applied by Durfee et al. who loaded siRNA and other drugs into MSNs and sealed the pores with a lipid bilayer mainly consisting of different lipids (e.g. DOPC, DPPC, DOPE, DPPE). Also, cholesterol and PEG were added for stabilization and shielding, respectively, and linker molecules were conjugated for further modifications [100]. Based on this approach, a new encapsulation strategy was examined to enable efficient siRNA transport and improve cellular NP uptake by using positively charged lipids [69]. After FAM™-siRNA loading, the MSNs were encapsulated by the common transfection reagent Lipofectamine™ RNAiMax which also consists of different lipids (exact composition is not known), instead of the ferrocene/ NH_2-β-CD system. Various incubation protocols were tested, and FAM™-siRNA was successfully loaded to the MSNs independent of the incubation protocol. However, a disadvantage of the Lipo encapsulation was the cytotoxicity, thus the applied concentration must be carefully chosen. The Lipo encapsulation increased the MSN uptake tremendously compared to the ferrocene/ NH_2-β-CD gatekeeper system.

Yet, FAM™-siRNA which was loaded to the MSNs could not be identified by flow cytometry because of Lipo autofluorescence. Still, this fluorescence vanished after 96 hours incubation (compared to 24 hours incubation), so the pores of the MSNs should have been opened by then and the siRNA was released. It can be assumed that the improved uptake is caused by the fact that the lipid shell (formed by Lipo) enables uptake via different routes of endocytosis e.g. macropinocytosis, caveolae- and clathrin-mediated endocytosis [183]. Next, Lipo-eGFP-siRNA-MSNs were evaluated for eGFP-siRNA delivery to HuH7-GFP cells and eGFP protein and mRNA expression were analyzed. Only 25 µg/ mL NPs reduced the viability as observed by flow cytometry after four days of incubation. Still, no decrease in eGFP expression was noted although Lipo-eGFP-siRNA-MSNs were vastly taken up by the cells. Moreover, eGFP mRNA expression was also not affected by 25 µg/ mL Lipo-eGFP-siRNA-MSNs after three days of incubation.

Taken together, siRNA could be loaded to the MSNs, but no siRNA release could be proven. The lack of siRNA release can be caused by several factors: First, only insufficient amounts of siRNA could be loaded to the MSNs, second, the electrostatic binding of the siRNA to the MSNs was too strong for a timely release, and third, the siRNA was degraded before it could reach the cytoplasm. This issue could be further addressed, e.g. by modifications of the drug delivery system with endosome bursting peptides or other reagents that can induce the proton sponge effect [129]. For example, Li et al. loaded magnetic MSNs with siRNA, sealed them with PEI, and added an endosome bursting peptide (KALA) via an SPDP linker to the drug delivery system. They showed that the NPs were taken up by the cells and the siRNA escaped the endolysosomal system. Also, they found a significant reduction in A549 tumor volume after five injections of their drug delivery system within 18 days *in vivo* [134]. The here evaluated siRNA delivery system was also modified to enhance cellular uptake by EGFR targeting which will be discussed next.

5.3 Further modifications of the MSNs

For efficient drug delivery *in vivo,* the drug much reach the target site at high concentrations. This can be achieved by passive targeting based on the EPR effect, but angiogenesis is mostly slower than tumor growth, so active targeting is favorable. A site-directed delivery can be realized by conjugation of ligands that target especially receptors which are abnormally high expressed in malignant tissue. The EGFR receptor expression is upregulated in 70- 90 % of HNSCC and therefore suited as target structure [102,103]. Other prominent targets are the folate receptor by folic acid [61,90,184], CD20 by Rituximab [105], integrin αvβ3 by the RGD

motif [95]. In this work, an EGFR-antibody was chosen that bound the extracellular domain of EGFR, but would not inhibit EGF binding, and an antibody of the same subtype (mouse IgG2a) was used as control. The antibody was first tested in immunofluorescence staining and exhibited good specificity, but could not be applied in immunoblot analysis. So, the immunoblot analysis was conducted with a different EGFR-antibody that exhibited similar results in immunofluorescence staining: The cell line HNSSCUM-02T highly expressed EGFR while the cell line RPMI2650 weakly expressed EGFR and was used as control. The conjugation protocol was developed based on different protocols from Thermo Fisher Scientific and a linker with PEG-spacer was chosen to reduce steric hindrance and optimize the coupling efficiency. For antibody conjugation, first, sulfhydryl groups were added to primary amines of the antibodies ($(SH)_x$-Ab), e.g. on lysine side chains. Yet, it could not be controlled whether the sulfhydryl groups were added in the constant or the variable regions of the antibodies. Therefore, conjugation within the variable regions was possible and could impair the binding to the EGFR. The applied reagent for sulfhydration was photosensitive and might have caused that the coupling efficiency decreased gradually during the experiments, but antibodies were still conjugated to the Cy5-MSNs. In the second step, MSNs were sealed with ferrocene and NH_2-β-CD and the linker was conjugated to the amino group. However, the number of attached linker molecules was not determined. Third, the $(SH)_x$-antibodies were added to the linker-modified Cy5-MSNs and incubated overnight at almost neutral (pH 7.2) conditions to ensure the stability of the antibodies and the NPs. Also, a protocol to verify successful antibody conjugation was developed, and the coupling efficiency was determined for every performed experiment with a fluorescently labeled anti-mouse antibody. The fluorescence of the secondary antibody was normalized to the Cy5-signal of the NPs to compensate differences in MSN mass. A fluorescence background signal of unconjugated Cy5-MSNs was detected but was a lot smaller in one experiment than in the other experiments. Therefore, a great standard deviation occurred for the normalized Coupling Factor.

The cellular uptake of EGFR-MSNs, IgG2a-MSNs, and Cy5-MSNs was compared in two cancer cell lines with different EGFR expression, as mentioned above. In HNSCCUM-02T cells a higher EGFR-MSN association than IgG2a-MSN association with the cells was observed after one hour incubation, but no differences in NP uptake were noticed after 24 hours. The control cell line showed a great variance between experiments for NP association after one hour incubation, but overall the fraction of Cy5-positive cells was the same for all applied MSNs. So, the EGFR-targeting only accelerated MSN uptake but did not enhance overall MSN uptake. The uptake of EGFR-Ab conjugated MSNs is in accordance with a study per-

formed by Durfee et al. who also found a fast uptake of the targeted MSNs within one hour [100]. The IgG2a-MSNs were also taken up better than the Cy5-MSNs. Thus, it can be speculated that the addition of proteins alone could improve NP uptake. In a final experiment, MSNs were loaded with eGFP-siRNA or nsRNA, sealed with ferrocene and NH_2-β-CD, and EGFR-antibodies or IgG2a-antibodies were conjugated to the particles, respectively. Then, HuH7-GFP cells were incubated with the different NPs for 72 hours, and the eGFP mRNA expression was analyzed because the detection of mRNA expression is more sensitive than the detection of protein expression. Still, eGFP mRNA expression was only slightly reduced by eGFP-siRNA-MSNs but not by EGFR-eGFP-siRNA-MSNs compared to PBS treatment. Previous experiments detecting eGFP expression regulation by using Lipo as transfection reagent revealed a knockdown of about 90 % by eGFP siRNA compared to nsRNA. For this reason, great downregulation of eGFP by the eGFP-siRNA would be possible. On that account, siRNA release from untargeted and targeted siRNA-MSNs could not be proven.

Overall, an EGFR-antibody was successfully conjugated to the Cy5-MSNs and accelerated NP uptake by high EGFR expressing cancer cells. Still, the experiments were performed *in vitro* under controlled settings, and further experiments *in vivo* would be necessary to confirm the targeting capability of the EGFR-MSNs. Also, active targeting did not induce the efficacy of siRNA-MSNs, and further improvement of the drug delivery system is necessary to achieve RNA interference.

6 Conclusion

In this work, MSNs were evaluated as drug delivery vehicles for drug delivery to head and neck cancer cells. The MSNs were sealed with a pH- and redox-sensitive gatekeeper system and showed good biocompatibility *in vitro* and *in vivo*. Moreover, the Cy5-MSNs were injected in the CAM of chick embryos, and the NPs could be detected mainly in the liver and kidney but were also found in a tumor within the CAM. *In vitro*, MSNs were retrieved in the endolysosomal system and uptake could be accelerated by EGFR-targeting. Furthermore, drug loading and release were examined by the incorporation of the drug doxorubicin. Effective Dox loading and retarded intracellular release were shown in two cancer cell lines by several assays. Furthermore, a larger drug for protein expression regulation, namely siRNA, was incorporated in MSNs. However, efficient siRNA loading was challenging, and several loading protocols were tested: The pore size of the MSNs was increased, and the MSNs were preincubated with ferrocene to reduce electrostatic interactions. It was determined that siRNA could be loaded to the MSNs, but no effects on mRNA and protein expression were noticed although the applied NP concentrations were increased. Moreover, the gatekeeper system was replaced by the common transfection agent Lipofectamine RNAiMAX, which increased cellular NP uptake tremendously while exhibiting toxic effects. Still, no siRNA release was detected through a reduction in protein and mRNA expression. The siRNA-loaded MSNs were also targeted with an EGFR-antibody, which also did not induce a decrease in mRNA expression. Overall, the evaluated system exhibited promising characteristics in the beginning, but a siRNA transport could not be achieved because either the siRNA was not released, or the siRNA was degraded before it could reach the cytoplasm and induce RNA interference. For this reason, the here evaluated drug delivery system is not suited for large and charged molecules such as siRNA and further modifications are necessary to enable siRNA transport. Nonetheless, MSNs exhibited promising characteristics as drug carriers for small molecule drugs in head and neck cancer therapy.

7 References

1. Watermann, A.; Brieger, J. Mesoporous silica nanoparticles as drug delivery vehicles in cancer. *Nanomaterials* **2017**, *7*, doi:10.3390/nano7070189.

2. *Bericht zum Krebsgeschehen in Deutschland 2016*; Zentrum für Krebsregisterdaten im Robert Koch-Institut: Berlin, 2016;

3. Fire, A.; Xu, S.; Montgomery, M. K.; Kostas, S. A.; Driver, S. E.; Mello, C. C. Potent and specific genetic interference by double-stranded RNA in Caenorhabditis elegans. *Nature* **1998**, *391*, 806–811, doi:10.1038/35888.

4. Elbashir, S. M.; Harborth, J.; Lendeckel, W.; Yalcin, A.; Weber, K.; Tuschl, T. Duplexes of 21-nucleotide RNAs mediate RNA interference in cultured mammalian cells. *Nature* **2001**, *411*, 494–498, doi:10.1038/35078107.

5. Singh, A.; Trivedi, P.; Jain, N. K. Advances in siRNA delivery in cancer therapy. *Artif. Cells, Nanomedicine, Biotechnol.* **2018**, *46*, 274–283, doi:10.1080/21691401.2017.1307210.

6. Schroeder, A.; Levins, C. G.; Cortez, C.; Langer, R.; Anderson, D. G. Lipid-based nanotherapeutics for siRNA delivery. *J. Intern. Med.* **2010**, *267*, 9–21, doi:10.1111/j.1365-2796.2009.02189.x.

7. Elbashir, S. M.; Lendeckel, W.; Tuschl, T. RNA interference is mediated by 21- and 22-nucleotide RNAs. *Genes Dev.* **2001**, *15*, 188–200, doi:10.1101/gad.862301.

8. Resnier, P.; Montier, T.; Mathieu, V.; Benoit, J. P.; Passirani, C. A review of the current status of siRNA nanomedicines in the treatment of cancer. *Biomaterials* 2013, *34*, 6429–6443.

9. Mocellin, S.; Provenzano, M. RNA interference: Learning gene knock-down from cell physiology. *J. Transl. Med.* 2004, *2*, 39.

10. Dykxhoorn, D. M.; Novina, C. D.; Sharp, P. A. Killing the messenger: short RNAs that silence gene expression. *Nat. Rev. Mol. Cell Biol.* **2003**, *4*, 457–67, doi:10.1038/nrm1129.

11. Chernikov, I. V.; Vlassov, V. V.; Chernolovskaya, E. L. Current Development of siRNA Bioconjugates: From Research to the Clinic. *Front. Pharmacol.* **2019**, *10*, 444, doi:10.3389/fphar.2019.00444.

12. Volkov, A. A.; Kruglova, N. S.; Meschaninova, M. I.; Venyaminova, A. G.; Zenkova, M. A.; Vlassov, V. V.; Chernolovskaya, E. L. Selective Protection of Nuclease-Sensitive Sites in siRNA Prolongs Silencing Effect. *Oligonucleotides* **2009**, *19*, 191–202, doi:10.1089/oli.2008.0162.

13. Liu, X.; Wang, W.; Samarsky, D.; Liu, L.; Xu, Q.; Zhang, W.; Zhu, G.; Wu, P.; Zuo, X.; Deng, H.; Zhang, J.; Wu, Z.; Chen, X.; Zhao, L.; Qiu, Z.; Zhang, Z.; Zeng, Q.; Yang, W.; Zhang, B.; Ji, A. Tumor-targeted in vivo gene silencing via systemic delivery of cRGD-conjugated siRNA. *Nucleic Acids Res.* **2014**, *42*, 11805–11817, doi:10.1093/nar/gku831.

14. Czauderna, F.; Fechtner, M.; Dames, S.; Aygün, H.; Klippel, A.; Pronk, G. J.; Giese, K.; Kaufmann, J. Structural variations and stabilising modifications of synthetic siRNAs in mammalian cells. *Nucleic Acids Res.* **2003**, *31*, 2705–2716, doi:10.1093/nar/gkg393.

15. Viel, T.; Boisgard, R.; Kuhnast, B.; Jego, B.; Siquier-Pernet, K.; Hinnen, F.; Dolle, F.; Tavitian, B. Molecular Imaging Study on *In Vivo* Distribution and Pharmacokinetics of Modified Small Interfering RNAs (siRNAs). *Oligonucleotides* **2008**, *18*, 201–212, doi:10.1089/oli.2008.0133.

16. Deleavey, G. F.; Watts, J. K.; Alain, T.; Robert, F.; Kalota, A.; Aishwarya, V.; Pelletier, J.; Gewirtz, A. M.; Sonenberg, N.; Damha, M. J. Synergistic effects between analogs of DNA and RNA improve the potency of siRNA-mediated gene silencing. *Nucleic Acids Res.* **2010**, *38*, 4547–4557, doi:10.1093/nar/gkq181.

17. Xia, C.-F.; Zhang, Y.; Zhang, Y.; Boado, R. J.; Pardridge, W. M. Intravenous siRNA of Brain Cancer with Receptor Targeting and Avidin–Biotin Technology. *Pharm. Res.* **2007**, *24*, 2309–

2316, doi:10.1007/s11095-007-9460-8.

18. McNamara, J. O.; Andrechek, E. R.; Wang, Y.; Viles, K. D.; Rempel, R. E.; Gilboa, E.; Sullenger, B. A.; Giangrande, P. H. Cell type–specific delivery of siRNAs with aptamer-siRNA chimeras. *Nat. Biotechnol.* **2006**, *24*, 1005–1015, doi:10.1038/nbt1223.

19. Lau, S.; Graham, B.; Cao, N.; Boyd, B. J.; Pouton, C. W.; White, P. J. Enhanced Extravasation, Stability and in Vivo Cardiac Gene Silencing via in Situ siRNA–Albumin Conjugation. *Mol. Pharm.* **2012**, *9*, 71–80, doi:10.1021/mp2002522.

20. Thomas, M.; Kularatne, S. A.; Qi, L.; Kleindl, P.; Leamon, C. P.; Hansen, M. J.; Low, P. S. Ligand-Targeted Delivery of Small Interfering RNAs to Malignant Cells and Tissues. *Ann. N. Y. Acad. Sci.* **2009**, *1175*, 32–39, doi:10.1111/j.1749-6632.2009.04977.x.

21. Nair, J. K.; Willoughby, J. L. S.; Chan, A.; Charisse, K.; Alam, M. R.; Wang, Q.; Hoekstra, M.; Kandasamy, P.; Kel'in, A. V.; Milstein, S.; Taneja, N.; O'Shea, J.; Shaikh, S.; Zhang, L.; van der Sluis, R. J.; Jung, M. E.; Akinc, A.; Hutabarat, R.; Kuchimanchi, S.; Fitzgerald, K.; Zimmermann, T.; van Berkel, T. J. C.; Maier, M. A.; Rajeev, K. G.; Manoharan, M. Multivalent N -Acetylgalactosamine-Conjugated siRNA Localizes in Hepatocytes and Elicits Robust RNAi-Mediated Gene Silencing. *J. Am. Chem. Soc.* **2014**, *136*, 16958–16961, doi:10.1021/ja505986a.

22. Lorenz, C.; Hadwiger, P.; John, M.; Vornlocher, H.-P.; Unverzagt, C. Steroid and lipid conjugates of siRNAs to enhance cellular uptake and gene silencing in liver cells. *Bioorg. Med. Chem. Lett.* **2004**, *14*, 4975–4977, doi:10.1016/j.bmcl.2004.07.018.

23. Meade, B. R.; Gogoi, K.; Hamil, A. S.; Palm-Apergi, C.; Berg, A. van den; Hagopian, J. C.; Springer, A. D.; Eguchi, A.; Kacsinta, A. D.; Dowdy, C. F.; Presente, A.; Lönn, P.; Kaulich, M.; Yoshioka, N.; Gros, E.; Cui, X.-S.; Dowdy, S. F. Efficient delivery of RNAi prodrugs containing reversible charge-neutralizing phosphotriester backbone modifications. *Nat. Biotechnol.* **2014**, *32*, 1256–1261, doi:10.1038/nbt.3078.

24. Rozema, D. B.; Lewis, D. L.; Wakefield, D. H.; Wong, S. C.; Klein, J. J.; Roesch, P. L.; Bertin, S. L.; Reppen, T. W.; Chu, Q.; Blokhin, A. V; Hagstrom, J. E.; Wolff, J. A. Dynamic PolyConjugates for targeted in vivo delivery of siRNA to hepatocytes. *Proc. Natl. Acad. Sci. U. S. A.* **2007**, *104*, 12982–7, doi:10.1073/pnas.0703778104.

25. Yang, J.; Chen, C.; Tang, X. Cholesterol-Modified Caged siRNAs for Photoregulating Exogenous and Endogenous Gene Expression. *Bioconjug. Chem.* **2018**, *29*, 1010–1015, doi:10.1021/acs.bioconjchem.8b00080.

26. Turner, J. J.; Ivanova, G. D.; Verbeure, B.; Williams, D.; Arzumanov, A. A.; Abes, S.; Lebleu, B.; Gait, M. J. Cell-penetrating peptide conjugates of peptide nucleic acids (PNA) as inhibitors of HIV-1 Tat-dependent trans-activation in cells. *Nucleic Acids Res.* **2005**, *33*, 6837–6849, doi:10.1093/nar/gki991.

27. Chen, X.; Bai, Y.; Zaro, J. L.; Shen, W.-C. Design of an in vivo cleavable disulfide linker in recombinant fusion proteins. *Biotechniques* **2010**, *49*, 513–8, doi:10.2144/000113450.

28. Mullard, A. 2018 FDA drug approvals. *Nat. Rev. Drug Discov.* **2019**, *18*, 85–89, doi:10.1038/d41573-019-00014-x.

29. Adams, D.; Gonzalez-Duarte, A.; O'Riordan, W. D.; Yang, C.-C.; Ueda, M.; Kristen, A. V.; Tournev, I.; Schmidt, H. H.; Coelho, T.; Berk, J. L.; Lin, K.-P.; Vita, G.; Attarian, S.; Planté-Bordeneuve, V.; Mezei, M. M.; Campistol, J. M.; Buades, J.; Brannagan, T. H.; Kim, B. J.; Oh, J.; Parman, Y.; Sekijima, Y.; Hawkins, P. N.; Solomon, S. D.; Polydefkis, M.; Dyck, P. J.; Gandhi, P. J.; Goyal, S.; Chen, J.; Strahs, A. L.; Nochur, S. V.; Sweetser, M. T.; Garg, P. P.; Vaishnaw, A. K.; Gollob, J. A.; Suhr, O. B. Patisiran, an RNAi Therapeutic, for Hereditary Transthyretin Amyloidosis. *N. Engl. J. Med.* **2018**, *379*, 11–21, doi:10.1056/NEJMoa1716153.

30. Solomon, S. D.; Adams, D.; Kristen, A.; Grogan, M.; González-Duarte, A.; Maurer, M. S.; Merlini, G.; Damy, T.; Slama, M. S.; Brannagan, T. H.; Dispenzieri, A.; Berk, J. L.; Shah, A. M.; Garg, P.; Vaishnaw, A.; Karsten, V.; Chen, J.; Gollob, J.; Vest, J.; Suhr, O. Effects of Patisiran,

an RNA Interference Therapeutic, on Cardiac Parameters in Patients With Hereditary Transthyretin-Mediated Amyloidosis. *Circulation* **2019**, *139*, 431–443, doi:10.1161/CIRCULATIONAHA.118.035831.

31. Search of: siRNA - List Results - ClinicalTrials.gov Available online: https://clinicaltrials.gov/ct2/results?cond=&term=siRNA&cntry=&state=&city=&dist= (accessed on Jun 22, 2019).

32. Matsumura, Y.; Maeda, H. A New Concept for Macromolecular Therapeutics in Cancer Chemotherapy: Mechanism of Tumoritropic Accumulation of Proteins and the Antitumor Agent Smancs. *Cancer Res.* **1986**, *46*, 6387–6392, doi:10.1021/bc100070g.

33. Titze-de-Almeida, R.; David, C.; Titze-de-Almeida, S. S. The Race of 10 Synthetic RNAi-Based Drugs to the Pharmaceutical Market. *Pharm. Res.* **2017**, *34*, 1339–1363, doi:10.1007/s11095-017-2134-2.

34. Ramanathan, R. K.; Hamburg, S. I.; Borad, M. J.; Seetharam, M.; Kundranda, M. N.; Lee, P.; Fredlund, P.; Gilbert, M.; Mast, C.; Semple, S. C.; Judge, A. D.; Crowell, B.; Vocila, L.; MacLachlan, I.; Northfelt, D. W. Abstract LB-289: A phase I dose escalation study of TKM-080301, a RNAi therapeutic directed against PLK1, in patients with advanced solid tumors. In *Clinical Research*; American Association for Cancer Research, 2013; Vol. 73, p. LB-289-LB-289.

35. NCT02191878 Safety, Pharmacokinetics and Preliminary Anti-Tumor Activity of Intravenous TKM-080301 in Subjects With Advanced Hepatocellular Carcinoma - Full Text View - ClinicalTrials.gov Available online: https://clinicaltrials.gov/ct2/show/NCT02191878 (accessed on Jun 23, 2019).

36. NCT01262235 A Dose Finding Study of TKM-080301 Infusion in Neuroendocrine Tumors (NET) and Adrenocortical Carcinoma (ACC) Patients - Full Text View - ClinicalTrials.gov Available online: https://clinicaltrials.gov/ct2/show/NCT01262235 (accessed on Jun 23, 2019).

37. Demeure, M. J.; Armaghany, T.; Ejadi, S.; Ramanathan, R. K.; Elfiky, A.; Strosberg, J. R.; Smith, D. C.; Whitsett, T.; Liang, W. S.; Sekar, S.; Carpten, J. D.; Fredlund, P.; Niforos, D.; Dye, A.; Gahir, S.; Semple, S. C.; Kowalski, M. M. A phase I/II study of TKM-080301, a *PLK1* -targeted RNAi in patients with adrenocortical cancer (ACC). *J. Clin. Oncol.* **2016**, *34*, 2547–2547, doi:10.1200/JCO.2016.34.15_suppl.2547.

38. NCT01188785 Phase I - Escalating Dose Study of siG12D LODER (Local Drug EluteR) in Patients With Locally Advanced Adenocarcinoma of the Pancreas, and a Single Dose Study of siG12D LODER (Local Drug EluteR) in Patients With Non-operable Adenocarcinoma of the Pancreas - Full Text View - ClinicalTrials.gov Available online: https://clinicaltrials.gov/ct2/show/NCT01188785?term=siRNA&draw=9&rank=22 (accessed on Jun 23, 2019).

39. Golan, T.; Khvalevsky, E. Z.; Hubert, A.; Gabai, R. M.; Hen, N.; Segal, A.; Domb, A.; Harari, G.; David, E. Ben; Raskin, S.; Goldes, Y.; Goldin, E.; Eliakim, R.; Lahav, M.; Kopleman, Y.; Dancour, A.; Shemi, A.; Galun, E. RNAi therapy targeting KRAS in combination with chemotherapy for locally advanced pancreatic cancer patients. *Oncotarget* **2015**, *6*, 24560–70, doi:10.18632/oncotarget.4183.

40. NCT01676259 A Phase 2 Study of siG12D LODER in Combination With Chemotherapy in Patients With Locally Advanced Pancreatic Cancer - Full Text View - ClinicalTrials.gov Available online: https://clinicaltrials.gov/ct2/show/NCT01676259?term=siRNA&draw=6&rank=57 (accessed on Jun 23, 2019).

41. Santel, A.; Aleku, M.; Roder, N.; Mopert, K.; Durieux, B.; Janke, O.; Keil, O.; Endruschat, J.; Dames, S.; Lange, C.; Eisermann, M.; Loffler, K.; Fechtner, M.; Fisch, G.; Vank, C.; Schaeper, U.; Giese, K.; Kaufmann, J. Atu027 Prevents Pulmonary Metastasis in Experimental and Spontaneous Mouse Metastasis Models. *Clin. Cancer Res.* **2010**, *16*, 5469–5480, doi:10.1158/1078-0432.CCR-10-1994.

42. Santel, A.; Aleku, M.; Keil, O.; Endruschat, J.; Esche, V.; Fisch, G.; Dames, S.; Löffler, K.; Fechtner, M.; Arnold, W.; Giese, K.; Klippel, A.; Kaufmann, J. A novel siRNA-lipoplex technology for RNA interference in the mouse vascular endothelium. *Gene Ther.* **2006**, *13*, 1222–1234, doi:10.1038/sj.gt.3302777.

43. Schultheis, B.; Strumberg, D.; Santel, A.; Vank, C.; Gebhardt, F.; Keil, O.; Lange, C.; Giese, K.; Kaufmann, J.; Khan, M.; Drevs, J. First-in-Human Phase I Study of the Liposomal RNA Interference Therapeutic Atu027 in Patients With Advanced Solid Tumors. *J. Clin. Oncol.* **2014**, *32*, 4141–4148, doi:10.1200/JCO.2013.55.0376.

44. Zhao, M.-X.; Zeng, E.-Z.; Zhu, B.-J. The Biological Applications of Inorganic Nanoparticle Drug Carriers. *ChemNanoMat* **2015**, *1*, n/a-n/a, doi:10.1002/cnma.201500036.

45. Bobo, D.; Robinson, K. J.; Islam, J.; Thurecht, K. J.; Corrie, S. R. Nanoparticle-Based Medicines: A Review of FDA-Approved Materials and Clinical Trials to Date. *Pharm. Res.* **2016**, *33*, 2373–2387, doi:10.1007/s11095-016-1958-5.

46. Allen, T. M.; Martin, F. J. Advantages of liposomal delivery systems for anthracyclines. *Semin. Oncol.* **2004**, *31*, 5–15, doi:10.1053/j.seminoncol.2004.08.001.

47. Susewind, M.; Schilmann, A.-M.; Heim, J.; Henkel, A.; Link, T.; Fischer, K.; Strand, D.; Kolb, U.; Tahir, M. N.; Brieger, J.; Tremel, W. Silica-coated Au@ZnO Janus particles and their stability in epithelial cells. *J. Mater. Chem. B* **2015**, *3*, 1813–1822, doi:10.1039/C4TB02017K.

48. Wang, Y. X. J.; Hussain, S. M.; Krestin, G. P. Superparamagnetic iron oxide contrast agents: Physicochemical characteristics and applications in MR imaging. *Eur. Radiol.* **2001**, *11*, 2319–2331, doi:10.1007/s003300100908.

49. Bianco, A.; Kostarelos, K.; Prato, M. Applications of carbon nanotubes in drug delivery. *Curr. Opin. Chem. Biol.* **2005**, *9*, 674–679, doi:10.1016/j.cbpa.2005.10.005.

50. Bruchez Jr., M.; Moronne, M.; Gin, P.; Weiss, S.; Alivisatos, A. P. Semiconductor Nanocrystals as Fluorescent Biological Labels. *Science (80-.).* **1998**, *281*, 2013–2016, doi:10.1126/science.281.5385.2013.

51. Lu, J.; Liong, M.; Zink, J. I.; Tamanoi, F. Mesoporous Silica Nanoparticles as a Delivery System for Hydrophobic Anticancer Drugs. *Small* **2007**, *3*, 1341–1346, doi:10.1002/smll.200700005.

52. Targeted Silica Nanoparticles for Image-Guided Intraoperative Sentinel Lymph Node Mapping in Head and Neck Melanoma, Breast and Gynecologic Malignancies Available online: https://clinicaltrials.gov/ct2/show/NCT02106598 (accessed on Jun 17, 2019).

53. US Food and Drug Administration GRAS Substances (SCOGS) Database - Select Committee on GRAS Substances (SCOGS) Opinion: Silicates Available online: https://www.fda.gov/food/ingredientspackaginglabeling/gras/scogs/ucm260849.htm (accessed on Apr 7, 2017).

54. Liberman, A.; Mendez, N.; Trogler, W. C.; Kummel, A. C. Synthesis and surface functionalization of silica nanoparticles for nanomedicine. *Surf. Sci. Rep.* **2014**, *69*, 132–158, doi:10.1016/j.surfrep.2014.07.001.

55. Kresge, C. T.; Leonowicz, M. E.; Roth, W. J.; Vartuli, J. C.; Beck, J. S. Ordered mesoporous molecular sieves synthesized by a liquid-crystal template mechanism. *Nature* **1992**, *359*, 710–712, doi:10.1038/359710a0.

56. Tang, F.; Li, L.; Chen, D. Mesoporous silica nanoparticles: Synthesis, biocompatibility and drug delivery. *Adv. Mater.* **2012**, *24*, 1504–1534, doi:10.1002/adma.201104763.

57. Zhao, D.; Feng, J.; Huo, Q.; Melosh, N.; Fredrickson, G.; Chmelka, B.; Stucky, G. Triblock copolymer syntheses of mesoporous silica with periodic 50 to 300 angstrom pores. *Science (80-.).* **1998**, *279*, 548–52, doi:10.1126/science.279.5350.548.

58. Na, H.-K.; Kim, M.-H.; Park, K.; Ryoo, S.-R.; Lee, K. E.; Jeon, H.; Ryoo, R.; Hyeon, C.; Min, D.-H. Efficient functional delivery of siRNA using mesoporous silica nanoparticles with ultralarge pores. *Small* **2012**, *8*, 1752–1761, doi:10.1002/smll.201200028.

59. Wu, M.; Meng, Q.; Chen, Y.; Zhang, L.; Li, M.; Cai, X.; Li, Y.; Yu, P.; Zhang, L.; Shi, J. Large Pore-Sized Hollow Mesoporous Organosilica for Redox-Responsive Gene Delivery and Synergistic Cancer Chemotherapy. *Adv. Mater.* **2016**, *28*, 1963–1969, doi:10.1002/adma.201505524.

60. Roberts, C. M.; Shahin, S. A.; Wen, W.; Finlay, J. B.; Dong, J.; Wang, R.; Dellinger, T. H.; Zink, J. I.; Tamanoi, F.; Glackin, C. A. Nanoparticle delivery of siRNA against TWIST to reduce drug resistance and tumor growth in ovarian cancer models. *Nanomedicine Nanotechnology, Biol. Med.* **2016**, doi:10.1016/j.nano.2016.11.010.

61. Liu, X.; Yu, D.; Jin, C.; Song, X.; Cheng, J.; Zhao, X.; Qi, X.; Zhang, G. A dual responsive targeted drug delivery system based on smart polymer coated mesoporous silica for laryngeal carcinoma treatment. *New J. Chem.* **2014**, *38*, 4830–4836, doi:10.1039/C4NJ00579A.

62. Ebabe Elle, R.; Rahmani, S.; Lauret, C.; Morena, M.; Bidel, L. P. R.; Boulahtouf, A.; Balaguer, P.; Cristol, J. P.; Durand, J. O.; Charnay, C.; Badia, E. Functionalized Mesoporous Silica Nanoparticle with Antioxidants as a New Carrier That Generates Lower Oxidative Stress Impact on Cells. *Mol. Pharm.* **2016**, *13*, 2647–2660, doi:10.1021/acs.molpharmaceut.6b00190.

63. Albanese, A.; Tang, P. S.; Chan, W. C. W. The Effect of Nanoparticle Size, Shape, and Surface Chemistry on Biological Systems. *Annu. Rev. Biomed. Eng.* **2012**, *14*, 1–16, doi:10.1146/annurev-bioeng-071811-150124.

64. Xiao, Y.; Wang, T.; Cao, Y.; Wang, X.; Zhang, Y.; Liu, Y.; Huo, Q. Enzyme and voltage stimuli-responsive controlled release system based on β-cyclodextrin-capped mesoporous silica nanoparticles. *Dalton Trans.* **2015**, *44*, 4355–61, doi:10.1039/c4dt03758h.

65. Lin, D.; Cheng, Q.; Jiang, Q.; Huang, Y.; Yang, Z.; Han, S.; Zhao, Y.; Guo, S.; Liang, Z.; Dong, A. Intracellular cleavable poly(2-dimethylaminoethyl methacrylate) functionalized mesoporous silica nanoparticles for efficient siRNA delivery in vitro and in vivo. *Nanoscale* **2013**, *5*, 4291–4301, doi:10.1039/C3NR00294B.

66. Möller, K.; Müller, K.; Engelke, H.; Bräuchle, C.; Wagner, E.; Bein, T. Highly efficient siRNA delivery from core-shell mesoporous silica nanoparticles with multifunctional polymer caps. *Nanoscale* **2016**, *8*, 4007–4019, doi:10.1039/c5nr06246b.

67. Ashley, C. E.; Carnes, E. C.; Phillips, G. K.; Padilla, D.; Durfee, P. N.; Brown, P. A.; Hanna, T. N.; Liu, J.; Phillips, B.; Carter, M. B.; Carroll, N. J.; Jiang, X.; Dunphy, D. R.; Willman, C. L.; Petsev, D. N.; Evans, D. G.; Parikh, A. N.; Chackerian, B.; Wharton, W.; Peabody, D. S.; Brinker, C. J. The targeted delivery of multicomponent cargos to cancer cells by nanoporous particle-supported lipid bilayers. *Nat. Mater.* **2011**, *10*, 389–397, doi:10.1038/nmat3042.

68. Kaszuba, M.; McKnight, D.; Connah, M. T.; McNeil-Watson, F. K.; Nobbmann, U. Measuring sub nanometre sizes using dynamic light scattering. *J. Nanoparticle Res.* **2008**, *10*, 823–829, doi:10.1007/s11051-007-9317-4.

69. Fröhlich, E. The role of surface charge in cellular uptake and cytotoxicity of medical nanoparticles. *Int. J. Nanomedicine* **2012**, *7*, 5577–5591, doi:10.2147/IJN.S36111.

70. Slowing, I.; Trewyn, B. G.; Lin, V. S.-Y. Effect of surface functionalization of MCM-41-type mesoporous silica nanoparticles on the endocytosis by human cancer cells. *J Am Chem Soc* **2006**, *128*, 14792–14793, doi:10.1021/ja0645943.

71. Nel, A. E.; Mädler, L.; Velegol, D.; Xia, T.; Hoek, E. M. V.; Somasundaran, P.; Klaessig, F.; Castranova, V.; Thompson, M. Understanding biophysicochemical interactions at the nano-bio interface. *Nat. Mater.* **2009**, *8*, 543–557, doi:10.1038/nmat2442.

72. Gratton, S. E. A.; Ropp, P. A.; Pohlhaus, P. D.; Luft, J. C.; Madden, V. J.; Napier, M. E.; DeSimone, J. M. The effect of particle design on cellular internalization pathways. *Proc. Natl. Acad. Sci.* **2008**, *105*, 11613–11618, doi:10.1073/pnas.0801763105.

73. Lu, F.; Wu, S. H.; Hung, Y.; Mou, C. Y. Size effect on cell uptake in well-suspended, uniform mesoporous silica nanoparticles. *Small* **2009**, *5*, 1408–1413, doi:10.1002/smll.200900005.

74. Sorkin, A.; Von Zastrow, M. Signal transduction and endocytosis: close encounters of many kinds. *Nat. Rev. Mol. Cell Biol.* **2002**, *3*, 600–614, doi:10.1038/nrm883.

75. He, Q.; Zhang, J.; Shi, J.; Zhu, Z.; Zhang, L.; Bu, W.; Guo, L.; Chen, Y. The effect of PEGylation of mesoporous silica nanoparticles on nonspecific binding of serum proteins and cellular responses. *Biomaterials* **2010**, *31*, 1085–1092, doi:10.1016/j.biomaterials.2009.10.046.

76. Folkman, J.; Hanahan, D. Switch to the angiogenic phenotype during tumorigenesis. *Princess Takamatsu Symp.* **1991**, *22*, 339–47.

77. Wilhelm, S.; Tavares, A. J.; Dai, Q.; Ohta, S.; Audet, J.; Dvorak, H. F.; Chan, W. C. W. Analysis of nanoparticle delivery to tumours. *Nat. Rev. Mater.* **2016**, *1*, 1–12, doi:10.1038/natrevmats.2016.14.

78. Fang, J.; Nakamura, H.; Maeda, H. The EPR effect: Unique features of tumor blood vessels for drug delivery, factors involved, and limitations and augmentation of the effect. *Adv. Drug Deliv. Rev.* **2011**, *63*, 136–151, doi:10.1016/j.addr.2010.04.009.

79. van Furth, R.; Cohn, Z. A.; Hirsch, J. G.; Humphrey, J. H.; Spector, W. G.; Langevoort, H. L. The mononuclear phagocyte system: a new classification of macrophages, monocytes, and their precursor cells. *Bull. World Health Organ.* **1972**, *46*, 845–852.

80. Yang, Y.; Yu, C. Advances in silica based nanoparticles for targeted cancer therapy. *Nanomedicine Nanotechnology, Biol. Med.* **2016**, *12*, 317–332, doi:10.1016/j.nano.2015.10.018.

81. Huang, X.; Li, L.; Liu, T.; Hao, N.; Liu, H.; Chen, D.; Tang, F. The shape effect of mesoporous silica nanoparticles on biodistribution, clearance, and biocompatibility in vivo. *ACS Nano* **2011**, *5*, 5390–5399, doi:10.1021/nn200365a.

82. Lu, J.; Liong, M.; Li, Z.; Zink, J. I.; Tamanoi, F. Biocompatibility, biodistribution, and drug-delivery efficiency of mesoporous silica nanoparticles for cancer therapy in animals. *Small* **2010**, *6*, 1794–805, doi:10.1002/smll.201000538.

83. Arnida; Malugin, A.; Ghandehari, H. Cellular uptake and toxicity of gold nanoparticles in prostate cancer cells: A comparative study of rods and spheres. *J. Appl. Toxicol.* **2010**, *30*, 212–217, doi:10.1002/jat.1486.

84. Mishra, S.; Webster, P.; Davis, M. E. PEGylation significantly affects cellular uptake and intracellular trafficking of non-viral gene delivery particles. *Eur. J. Cell Biol.* **2004**, *83*, 97–111, doi:10.1078/0171-9335-00363.

85. Zhu, Y.; Fang, Y.; Borchardt, L.; Kaskel, S. PEGylated hollow mesoporous silica nanoparticles as potential drug delivery vehicles. *Microporous Mesoporous Mater.* **2011**, *141*, 199–206, doi:10.1016/j.micromeso.2010.11.013.

86. Heldin, C.-H.; Rubin, K.; Pietras, K.; Östman, A. High interstitial fluid pressure — an obstacle in cancer therapy. *Nat. Rev. Cancer* **2004**, *4*, 806–813, doi:10.1038/nrc1456.

87. Parker, N.; Turk, M. J.; Westrick, E.; Lewis, J. D.; Low, P. S.; Leamon, C. P. Folate receptor expression in carcinomas and normal tissues determined by a quantitative radioligand binding assay. *Anal. Biochem.* **2005**, *338*, 284–293, doi:10.1016/j.ab.2004.12.026.

88. Qi, X.; Yu, D.; Jia, B.; Jin, C.; Liu, X.; Zhao, X.; Zhang, G. Targeting CD133+ laryngeal carcinoma cells with chemotherapeutic drugs and siRNA against ABCG2 mediated by thermo/pH-sensitive mesoporous silica nanoparticles. *Tumor Biol.* **2016**, *37*, 2209–2217, doi:10.1007/s13277-015-4007-9.

89. Zhang, H.; Zhang, W.; Zhou, Y.; Jiang, Y.; Li, S. Dual Functional Mesoporous Silicon Nanoparticles Enhance the Radiosensitivity of VPA in Glioblastoma. *Transl. Oncol.* **2017**, *10*, 229–240, doi:10.1016/j.tranon.2016.12.011.

90. Cheng, W.; Nie, J.; Xu, L.; Liang, C.; Peng, Y.; Liu, G.; Wang, T.; Mei, L.; Huang, L.; Zeng, X. A pH-sensitive delivery vehicle based on folic acid-conjugated polydopamine-modified mesoporous silica nanoparticles for targeted cancer therapy. *ACS Appl. Mater. Interfaces* **2017**,

acsami.7b02457, doi:10.1021/acsami.7b02457.

91. Chen, X.; Sun, H.; Hu, J.; Han, X.; Liu, H.; Hu, Y. Transferrin gated mesoporous silica nanoparticles for redox-responsive and targeted drug delivery. *Colloids Surfaces B Biointerfaces* **2017**, *152*, 77–84, doi:10.1016/j.colsurfb.2017.01.010.

92. Chen, N. T.; Souris, J. S.; Cheng, S. H.; Chu, C. H.; Wang, Y. C.; Konda, V.; Dougherty, U.; Bissonnette, M.; Mou, C. Y.; Chen, C. T.; Lo, L. W. Lectin-functionalized mesoporous silica nanoparticles for endoscopic detection of premalignant colonic lesions. *Nanomedicine Nanotechnology, Biol. Med.* **2017**, *13*, 1941–1952, doi:10.1016/j.nano.2017.03.014.

93. Sweeney, S. K.; Luo, Y.; O'Donnell, M. A.; Assouline, J. G. Peptide-Mediated Targeting Mesoporous Silica Nanoparticles: A Novel Tool for Fighting Bladder Cancer. *J. Biomed. Nanotechnol.* **2017**, *13*, 232–242, doi:10.1166/jbn.2017.2339.

94. Hirano, Y.; Kando, Y.; Hayashi, T.; Goto, K.; Nakajima, A. Synthesis and cell attachment activity of bioactive oligopeptides: RGD, RGDS, RGDV, and RGDT. *J. Biomed. Mater. Res.* **1991**, *25*, 1523–1534, doi:10.1002/jbm.820251209.

95. Wang, F.; Li, Y.; Shen, Y.; Wang, A.; Wang, S.; Xie, T. The functions and applications of RGD in tumor therapy and tissue engineering. *Int. J. Mol. Sci.* **2013**, *14*, 13447–13462, doi:10.3390/ijms140713447.

96. Pan, L.; Liu, J.; He, Q.; Shi, J. MSN-mediated sequential vascular-to-cell nuclear-targeted drug delivery for efficient tumor regression. *Adv. Mater.* **2014**, *26*, 6742–6748, doi:10.1002/adma.201402752.

97. Hicke, B. J.; Stephens, A. W.; Gould, T.; Chang, Y.-F.; Lynott, C. K.; Heil, J.; Borkowski, S.; Hilger, C.-S.; Cook, G.; Warren, S.; Schmidt, P. G. Tumor targeting by an aptamer. *J. Nucl. Med.* **2006**, *47*, 668–78, doi:47/4/668 [pii].

98. Babaei, M.; Abnous, K.; Taghdisi, S. M.; Amel Farzad, S.; Peivandi, M. T.; Ramezani, M.; Alibolandi, M. Synthesis of theranostic epithelial cell adhesion molecule targeted mesoporous silica nanoparticle with gold gatekeeper for hepatocellular carcinoma. *Nanomedicine* **2017**, nnm-2017-0028, doi:10.2217/nnm-2017-0028.

99. Tang, Y.; Hu, H.; Zhang, M. G.; Song, J.; Nie, L.; Wang, S.; Niu, G.; Huang, P.; Lu, G.; Chen, X. An aptamer-targeting photoresponsive drug delivery system using "off–on" graphene oxide wrapped mesoporous silica nanoparticles. *Nanoscale* **2015**, *7*, 6304–6310, doi:10.1039/C4NR07493A.

100. Durfee, P. N.; Lin, Y. S.; Dunphy, D. R.; Muñiz, A. J.; Butler, K. S.; Humphrey, K. R.; Lokke, A. J.; Agola, J. O.; Chou, S. S.; Chen, I. M.; Wharton, W.; Townson, J. L.; Willman, C. L.; Brinker, C. J. Mesoporous Silica Nanoparticle-Supported Lipid Bilayers (Protocells) for Active Targeting and Delivery to Individual Leukemia Cells. *ACS Nano* **2016**, *10*, 8325–8345, doi:10.1021/acsnano.6b02819.

101. Dokala, A.; Thakur, S. S. Extracellular region of epidermal growth factor receptor: a potential target for anti-EGFR drug discovery. *Oncogene* **2017**, *36*, 2337–2344, doi:10.1038/onc.2016.393.

102. Chung, C. H.; Ely, K.; McGavran, L.; Varella-Garcia, M.; Parker, J.; Parker, N.; Jarrett, C.; Carter, J.; Murphy, B. A.; Netterville, J.; Burkey, B. B.; Sinard, R.; Cmelak, A.; Levy, S.; Yarbrough, W. G.; Slebos, R. J. C.; Hirsch, F. R. Increased epidermal growth factor receptor gene copy number is associated with poor prognosis in head and neck squamous cell carcinomas. *J. Clin. Oncol.* **2006**, *24*, 4170–6, doi:10.1200/JCO.2006.07.2587.

103. Dassonville, O.; Formento, J. L.; Francoual, M.; Ramaioli, A.; Santini, J.; Schneider, M.; Demard, F.; Milano, G. Expression of epidermal growth factor receptor and survival in upper aerodigestive tract cancer. *J. Clin. Oncol.* **1993**, *11*, 1873–1878, doi:10.1200/JCO.1993.11.10.1873.

104. Specenier, P.; Vermorken, J. B. Cetuximab in the treatment of squamous cell carcinoma of the head and neck. *Expert Rev. Anticancer Ther.* **2011**, *11*, 511–524, doi:10.1586/era.11.20.

105. Zhou, S.; Wu, D.; Yin, X.; Jin, X.; Zhang, X.; Zheng, S.; Wang, C.; Liu, Y. Intracellular pH-responsive and rituximab-conjugated mesoporous silica nanoparticles for targeted drug delivery to lymphoma B cells. *J. Exp. Clin. Cancer Res.* **2017**, *36*, 24, doi:10.1186/s13046-017-0492-6.

106. Maloney, D. G.; Grillo-López, A. J.; White, C. A.; Bodkin, D.; Schilder, R. J.; Neidhart, J. A.; Janakiraman, N.; Foon, K. A.; Liles, T.-M.; Dallaire, B. K.; Wey, K.; Royston, I.; Davis, T.; Levy, R. IDEC-C2B8 (Rituximab) Anti-CD20 Monoclonal Antibody Therapy in Patients With Relapsed Low-Grade Non-Hodgkin's Lymphoma. *Blood* **1997**, *9*, 2188–2195, doi:Blood. 1997 Sep 15;90(6):2188-95.

107. Chen, F.; Hong, H.; Shi, S.; Goel, S.; Valdovinos, H. F.; Hernandez, R.; Theuer, C. P.; Barnhart, T. E.; Cai, W. Engineering of Hollow Mesoporous Silica Nanoparticles for Remarkably Enhanced Tumor Active Targeting Efficacy. *Sci. Rep.* **2014**, *4*, 5080, doi:10.1038/srep05080.

108. Chen, F.; Nayak, T. R.; Goel, S.; Valdovinos, H. F.; Hong, H.; Theuer, C. P.; Barnhart, T. E.; Cai, W. In vivo tumor vasculature targeted PET/NIRF Imaging with TRC105(Fab)-conjugated, dual-labeled mesoporous silica nanoparticles. *Mol. Pharm.* **2014**, *11*, 4007–4014, doi:10.1021/mp500306k.

109. Mekaru, H.; Lu, J.; Tamanoi, F. Development of mesoporous silica-based nanoparticles with controlled release capability for cancer therapy. *Adv. Drug Deliv. Rev.* **2015**, *95*, 40–49, doi:10.1016/j.addr.2015.09.009.

110. Gatenby, R. A.; Gillies, R. J. Why do cancers have high aerobic glycolysis? *Nat. Rev. Cancer* **2004**, *4*, 891–899, doi:10.1038/nrc1478.

111. Meng, H.; Xue, M.; Xia, T.; Zhao, Y. L.; Tamanoi, F.; Stoddart, J. F.; Zink, J. I.; Nel, A. E. Autonomous in vitro anticancer drug release from mesoporous silica nanoparticles by pH-sensitive nanovalves. *J. Am. Chem. Soc.* **2010**, *132*, 12690–12697, doi:10.1021/ja104501a.

112. Xiong, L.; Bi, J.; Tang, Y.; Qiao, S. Z. Magnetic Core-Shell Silica Nanoparticles with Large Radial Mesopores for siRNA Delivery. *Small* **2016**, *12*, 4735–4742, doi:10.1002/smll.201600531.

113. Popat, A.; Liu, J.; Lu, G. Q. (Max); Qiao, S. Z. A pH-responsive drug delivery system based on chitosan coated mesoporous silica nanoparticles. *J. Mater. Chem.* **2012**, *22*, 11173–11178, doi:10.1039/c2jm30501a.

114. Liu, J.; Luo, Z.; Zhang, J.; Luo, T.; Zhou, J.; Zhao, X.; Cai, K. Hollow mesoporous silica nanoparticles facilitated drug delivery via cascade pH stimuli in tumor microenvironment for tumor therapy. *Biomaterials* **2016**, *83*, 51–65, doi:10.1016/j.biomaterials.2016.01.008.

115. Estrela, J. M.; Ortega, A.; Obrador, E. Glutathione in Cancer Biology and Therapy. *Crit. Rev. Clin. Lab. Sci.* **2006**, *43*, 143–181, doi:10.1080/10408360500523878.

116. Kim, H.; Kim, S.; Park, C.; Lee, H.; Park, H. J.; Kim, C. Glutathione-induced intracellular release of guests from mesoporous silica nanocontainers with cyclodextrin gatekeepers. *Adv. Mater.* **2010**, *22*, 4280–4283, doi:10.1002/adma.201001417.

117. Liu, R.; Zhao, X.; Wu, T.; Feng, P. Tunable Redox-Responsive Hybrid Nanogated Ensembles. *J. Am. Chem. Soc.* **2008**, *130*, 14418–14419, doi:10.1021/ja8060886.

118. Li, Y.; Hei, M.; Xu, Y.; Qian, X.; Zhu, W. Ammonium salt modified mesoporous silica nanoparticles for dual intracellular-responsive gene delivery. *Int. J. Pharm.* **2016**, *511*, 689–702, doi:10.1016/j.ijpharm.2016.07.029.

119. Mondragón, L.; Mas, N.; Ferragud, V.; de la Torre, C.; Agostini, A.; Martínez-Máñez, R.; Sancenón, F.; Amorós, P.; Pérez-Payá, E.; Orzáez, M. Enzyme-responsive intracellular-controlled release using silica mesoporous nanoparticles capped with ε-poly-L-lysine. *Chemistry* **2014**, *20*, 5271–5281, doi:10.1002/chem.201400148.

120. Bernardos, A.; Mondragón, L.; Aznar, E.; Marcos, M. D.; Martínez-Mánez, R.; Sancenón, F.; Soto, J.; Barat, J. M.; Pérez-Payá, E.; Guillem, C.; Amorós, P. Enzyme-responsive intracellular controlled release using nanometric silica mesoporous supports capped with "saccharides."

ACS Nano **2010**, *4*, 6353–6368, doi:10.1021/nn101499d.

121. Guardado-Alvarez, T. M.; Sudha Devi, L.; Russell, M. M.; Schwartz, B. J.; Zink, J. I. Activation of snap-top capped mesoporous silica nanocontainers using two near-infrared photons. *J. Am. Chem. Soc.* **2013**, *135*, 14000–14003, doi:10.1021/ja407331n.

122. Croissant, J.; Maynadier, M.; Gallud, A.; Peindy N'Dongo, H.; Nyalosaso, J. L.; Derrien, G.; Charnay, C.; Durand, J. O.; Raehm, L.; Serein-Spirau, F.; Cheminet, N.; Jarrosson, T.; Mongin, O.; Blanchard-Desce, M.; Gary-Bobo, M.; Garcia, M.; Lu, J.; Tamanoi, F.; Tarn, D.; Guardado-Alvarez, T. M.; Zink, J. I. Two-photon-triggered drug delivery in cancer cells using nanoimpellers. *Angew. Chemie - Int. Ed.* **2013**, *52*, 13813–13817, doi:10.1002/anie.201308647.

123. Chen, P.-J.; Hu, S.-H.; Hsiao, C.-S.; Chen, Y.-Y.; Liu, D.-M.; Chen, S.-Y. Multifunctional magnetically removable nanogated lids of Fe3O4–capped mesoporous silica nanoparticles for intracellular controlled release and MR imaging. *J. Mater. Chem.* **2011**, *21*, 2535, doi:10.1039/c0jm02590a.

124. Thomas, C. R.; Ferris, D. P.; Lee, J. H.; Choi, E.; Cho, M. H.; Kim, E. S.; Stoddart, J. F.; Shin, J. S.; Cheon, J.; Zink, J. I. Noninvasive remote-controlled release of drug molecules in vitro using magnetic actuation of mechanized nanoparticles. *J. Am. Chem. Soc.* **2010**, *132*, 10623–10625, doi:10.1021/ja1022267.

125. Saokham, P.; Muankaew, C.; Jansook, P.; Loftsson, T. Solubility of Cyclodextrins and Drug/Cyclodextrin Complexes. *Molecules* **2018**, *23*, doi:10.3390/molecules23051161.

126. Davis, M. E.; Brewster, M. E. Cyclodextrin-based pharmaceutics: past, present and future. *Nat. Rev. Drug Discov.* **2004**, *3*, 1023–1035, doi:10.1038/nrd1576.

127. Matsue, T.; Evans, D. H.; Osa, T.; Kobayashi, N. Electron-transfer reactions associated with host-guest complexation. Oxidation of ferrocenecarboxylic acid in the presence of .beta.-cyclodextrin. *J. Am. Chem. Soc.* **1985**, *107*, 3411–3417, doi:10.1021/ja00298a003.

128. Dash, A. C.; Dash, B.; Praharaj, S. Hydrolysis of imines: kinetics and mechanism of spontaneous acid-, base-, and metal ion-induced hydrolysis of N-salicylidene-2-aminothiazole. *J. Chem. Soc. Dalt. Trans.* **1981**, 2063, doi:10.1039/dt9810002063.

129. Freeman, E. C.; Weiland, L. M.; Meng, W. S. Modeling the proton sponge hypothesis: examining proton sponge effectiveness for enhancing intracellular gene delivery through multiscale modeling. *J. Biomater. Sci. Polym. Ed.* **2013**, *24*, 398–416, doi:10.1080/09205063.2012.690282.

130. Finlay, J.; Roberts, C. M.; Dong, J.; Zink, J. I.; Tamanoi, F.; Glackin, C. A. Mesoporous silica nanoparticle delivery of chemically modified siRNA against TWIST1 leads to reduced tumor burden. *Nanomedicine* **2015**, *11*, 1657–1666, doi:10.1016/j.nano.2015.05.011.

131. Ma, D. Enhancing endosomal escape for nanoparticle mediated siRNA delivery. *Nanoscale* **2014**, *6*, 6415–25, doi:10.1039/c4nr00018h.

132. Hoekstra, D.; Martin, O. C. Transbilayer redistribution of phosphatidylethanolamine during fusion of phospholipid vesicles. Dependence on fusion rate, lipid phase separation, and formation of nonbilayer structures. *Biochemistry* **1982**, *21*, 6097–6103, doi:10.1021/bi00267a011.

133. Zhang, X.; Li, F.; Guo, S.; Chen, X.; Wang, X.; Li, J.; Gan, Y. Biofunctionalized polymer-lipid supported mesoporous silica nanoparticles for release of chemotherapeutics in multidrug resistant cancer cells. *Biomaterials* **2014**, *35*, 3650–3665, doi:10.1016/j.biomaterials.2014.01.013.

134. Li, X.; Chen, Y.; Wang, M.; Ma, Y.; Xia, W.; Gu, H. A mesoporous silica nanoparticle – PEI – Fusogenic peptide system for siRNA delivery in cancer therapy. *Biomaterials* **2013**, *34*, 1391–1401, doi:10.1016/j.biomaterials.2012.10.072.

135. Park, J.-H.; Gu, L.; von Maltzahn, G.; Ruoslahti, E.; Bhatia, S. N.; Sailor, M. J. Biodegradable luminescent porous silicon nanoparticles for in vivo applications. *Nat. Mater.* **2009**, *8*, 331–6,

doi:10.1038/nmat2398.

136. Wu, M.; Meng, Q.; Chen, Y.; Du, Y.; Zhang, L.; Li, Y.; Zhang, L.; Shi, J. Large-pore ultrasmall mesoporous organosilica nanoparticles: Micelle/precursor co-templating assembly and nuclear-targeted gene delivery. *Adv. Mater.* **2015**, *27*, 215–222, doi:10.1002/adma.201404256.

137. Duan, J.; Yu, Y.; Li, Y.; Yu, Y.; Li, Y.; Zhou, X.; Huang, P.; Sun, Z. Toxic effect of silica nanoparticles on endothelial cells through DNA damage response via Chk1-dependent G2/M checkpoint. *PLoS One* **2013**, *8*, e62087, doi:10.1371/journal.pone.0062087.

138. Heikkilä, T.; Santos, H. A.; Kumar, N.; Murzin, D. Y.; Salonen, J.; Laaksonen, T.; Peltonen, L.; Hirvonen, J.; Lehto, V. P. Cytotoxicity study of ordered mesoporous silica MCM-41 and SBA-15 microparticles on Caco-2 cells. *Eur. J. Pharm. Biopharm.* **2010**, *74*, 483–494, doi:10.1016/j.ejpb.2009.12.006.

139. Tarn, D.; Ashley, C. E.; Xue, M.; Carnes, E. C.; Zink, J. I.; Brinker, C. J. Mesoporous silica nanoparticle nanocarriers: biofunctionality and biocompatibility. *Acc. Chem. Res.* **2013**, *46*, 792–801, doi:10.1021/ar3000986.

140. He, Q.; Zhang, Z.; Gao, F.; Li, Y.; Shi, J. In vivo biodistribution and urinary excretion of mesoporous silica nanoparticles: Effects of particle size and PEGylation. *Small* **2011**, *7*, 271–280, doi:10.1002/smll.201001459.

141. Mobaraki, M.; Faraji, A.; Zare, M.; Manshadi, H. R. D.; Ataei, M.; Manshadi, H. R. D. Molecular Mechanisms of Cardiotoxicity: A Review on Major Side-effect of Doxorubicin. *Indian J. Pharm. Sci.* **2017**, *79*, 335–344, doi:10.4172/pharmaceutical-sciences.1000235.

142. Yang, F.; Teves, S. S.; Kemp, C. J.; Henikoff, S. Doxorubicin, DNA torsion, and chromatin dynamics. *Biochim. Biophys. Acta - Rev. Cancer* **2014**, *1845*, 84–89, doi:10.1016/J.BBCAN.2013.12.002.

143. Working, P. K.; Newman, M. S.; Huang, S. K.; Mayhew, E.; Vaage, J.; Lasic, D. D. Pharmacokinetics, Biodistribution and Therapeutic Efficacy of Doxorubicin Encapsulated in Stealth® Liposomes (Doxil®). *J. Liposome Res.* **1994**, *4*, 667–687, doi:10.3109/08982109409037065.

144. Zeman, S. M.; Phillips, D. R.; Crothers, D. M. Characterization of covalent adriamycin-DNA adducts. *Proc. Natl. Acad. Sci. U. S. A.* **1998**, *95*, 11561–5, doi:10.1073/pnas.95.20.11561.

145. Luger, K.; Mäder, A. W.; Richmond, R. K.; Sargent, D. F.; Richmond, T. J. Crystal structure of the nucleosome core particle at 2.8 Å resolution. *Nature* **1997**, *389*, 251–260, doi:10.1038/38444.

146. Fernandez-Capetillo, O.; Lee, A.; Nussenzweig, M.; Nussenzweig, A. H2AX: the histone guardian of the genome. *DNA Repair (Amst).* **2004**, *3*, 959–67, doi:10.1016/j.dnarep.2004.03.024.

147. Rogakou, E. P.; Pilch, D. R.; Orr, A. H.; Ivanova, V. S.; Bonner, W. M. DNA double-stranded breaks induce histone H2AX phosphorylation on serine 139. *J. Biol. Chem.* **1998**, *273*, 5858–68, doi:10.1074/JBC.273.10.5858.

148. Shiloh, Y. ATM and related protein kinases: safeguarding genome integrity. *Nat. Rev. Cancer* **2003**, *3*, 155–168, doi:10.1038/nrc1011.

149. Ribatti, D. The chick embryo chorioallantoic membrane (CAM). A multifaceted experimental model. *Mech. Dev.* **2016**, *141*, 70–77, doi:10.1016/j.mod.2016.05.003.

150. National Institute of Health; Office of Laboratory Animal Welfare The Public Health Service Responds to Commonly Asked Questions Available online: https://grants.nih.gov/grants/olaw/references/ilar91.htm (accessed on Jun 25, 2019).

151. Schindelin, J.; Arganda-Carreras, I.; Frise, E.; Kaynig, V.; Longair, M.; Pietzsch, T.; Preibisch, S.; Rueden, C.; Saalfeld, S.; Schmid, B.; Tinevez, J.-Y.; White, D. J.; Hartenstein, V.; Eliceiri, K.; Tomancak, P.; Cardona, A. Fiji: an open-source platform for biological-image analysis. *Nat. Methods* **2012**, *9*, 676–682, doi:10.1038/nmeth.2019.

152. Gioanni, J.; Fischel, J. L.; Lambert, J. C.; Demard, F.; Mazeau, C.; Zanghellini, E.; Ettore, F.; Formento, P.; Chauvel, P.; Lalanne, C. M. Two new human tumor cell lines derived from squamous cell carcinomas of the tongue: establishment, characterization and response to cytotoxic treatment. *Eur. J. Cancer Clin. Oncol.* **1988**, *24*, 1445–55.

153. Welkoborsky, H. J.; Jacob, R.; Riazimand, S. H.; Bernauer, H. S.; Mann, W. J. Molecular biologic characteristics of seven new cell lines of squamous cell carcinomas of the head and neck and comparison to fresh tumor tissue. *Oncology* **2003**, *65*, 60–71, doi:10.1159/000071206.

154. Nakabayashi, H.; Taketa, K.; Yamane, T.; Miyazaki, M.; Miyano, K.; Sato, J. Phenotypical Stability of a Human Hepatoma Cell Line, HuH-7, in Long-Term Culture with Chemically Defined Medium. *GANN Japanese J. Cancer Res.* **1984**, *75*, 151–158, doi:10.20772/cancersci1959.75.2_151.

155. Kowarz, E.; Löscher, D.; Marschalek, R. Optimized Sleeping Beauty transposons rapidly generate stable transgenic cell lines. *Biotechnol. J.* **2015**, *10*, 647–653, doi:10.1002/biot.201400821.

156. Raptis, L.; Bolen, J. B. Polyomavirus transforms rat F111 and mouse NIH 3T3 cells by different mechanisms. *J. Virol.* **1989**, *63*, 753–8.

157. Moorhead, P. S. Human tumor cell line with a quasi-diploid karyotype (RPMI 2650). *Exp. Cell Res.* **1965**, *39*, 190–196, doi:10.1016/0014-4827(65)90022-4.

158. Kurch, S. Mesoporous Silica Nanoparticle for Drug Delivery of Cancer Therapeutics, Johannes Gutenberg University, 2018.

159. Ahmed, S. A.; Gogal, R. M.; Walsh, J. E. A new rapid and simple non-radioactive assay to monitor and determine the proliferation of lymphocytes: an alternative to [3H]thymidine incorporation assay. *J. Immunol. Methods* **1994**, *170*, 211–24.

160. Bolte, S.; Cordelières, F. P. A guided tour into subcellular colocalization analysis in light microscopy. *J. Microsc.* **2006**, *224*, 213–32, doi:10.1111/j.1365-2818.2006.01706.x.

161. Manders, E. M. M.; Verbeek, F. J.; Aten, J. A. Measurement of co-localization of objects in dual-colour confocal images. *J. Microsc.* **1993**, *169*, 375–382, doi:10.1111/j.1365-2818.1993.tb03313.x.

162. Livak, K. J.; Schmittgen, T. D. Analysis of Relative Gene Expression Data Using Real-Time Quantitative PCR and the 2−ΔΔCT Method. *Methods* **2001**, *25*, 402–408, doi:10.1006/meth.2001.1262.

163. Clemments, A. M.; Botella, P.; Landry, C. C. Protein Adsorption From Biofluids on Silica Nanoparticles: Corona Analysis as a Function of Particle Diameter and Porosity. *ACS Appl. Mater. Interfaces* **2015**, *7*, 21682–21689, doi:10.1021/acsami.5b07631.

164. Strozynski, J.; Heim, J.; Bunbanjerdsuk, S.; Wiesmann, N.; Zografidou, L.; Becker, S. K.; Meierl, A. M.; Gouveris, H.; Lüddens, H.; Grus, F.; Brieger, J. Proteomic identification of the heterogeneous nuclear ribonucleoprotein K as irradiation responsive protein related to migration. *J. Proteomics* **2015**, *113*, 154–161, doi:10.1016/j.jprot.2014.09.017.

165. Wiesmann, N.; Strozynski, J.; Beck, C.; Zimmermann, N.; Mendler, S.; Gieringer, R.; Schmidtmann, I.; Brieger, J. Knockdown of hnRNPK leads to increased DNA damage after irradiation and reduces survival of tumor cells. *Carcinogenesis* **2017**, *38*, 321–328, doi:10.1093/carcin/bgx006.

166. Zhang, S.; Gao, H.; Bao, G. Physical Principles of Nanoparticle Cellular Endocytosis. *ACS Nano* 2015, *9*, 8655–8671.

167. Lesniak, A.; Fenaroli, F.; Monopoli, M. P.; Åberg, C.; Dawson, K. A.; Salvati, A. Effects of the Presence or Absence of a Protein Corona on Silica Nanoparticle Uptake and Impact on Cells. *ACS Nano* **2012**, *6*, 5845–5857, doi:10.1021/nn300223w.

168. Scott, C. C.; Gruenberg, J. Ion flux and the function of endosomes and lysosomes: pH is just

the start. *BioEssays* **2011**, *33*, 103–110, doi:10.1002/bies.201000108.

169. Yi, S.; Zheng, J.; Lv, P.; Zhang, D.; Zheng, X.; Zhang, Y.; Liao, R. Controlled Drug Release from Cyclodextrin-Gated Mesoporous Silica Nanoparticles Based on Switchable Host–Guest Interactions. *Bioconjug. Chem.* **2018**, *29*, 2884–2891, doi:10.1021/acs.bioconjchem.8b00416.

170. Khashab, N. M.; Trabolsi, A.; Lau, Y. A.; Ambrogio, M. W.; Friedman, D. C.; Khatib, H. A.; Zink, J. I.; Stoddart, J. F. Redox- and pH-controlled mechanized nanoparticles. *European J. Org. Chem.* **2009**, *2009*, 1669–1673, doi:10.1002/ejoc.200801197.

171. Xia, Q.; Hwang, H.-M.; Ray, P. C.; Yu, H. Mechanisms of nanotoxicity: Generation of reactive oxygen species. *J. Food Drug Anal.* **2014**, *22*, 64–75, doi:10.1016/J.JFDA.2014.01.005.

172. U.S. Food and Drug Administration GRAS Notices GRN No. 74 Available online: https://www.accessdata.fda.gov/scripts/fdcc/?set=GRASNotices&id=74&sort=GRN_No&order=DESC&startrow=1&type=column&search=GRN No.¤DECIMAL¤74 (accessed on Jul 4, 2019).

173. Sigma-Aldrich Chemie GmbH *MSDS - Ferrocenaldehyd (German)*; 2019;

174. Salis, A.; Fanti, M.; Medda, L.; Nairi, V.; Cugia, F.; Piludu, M.; Sogos, V.; Monduzzi, M. Mesoporous Silica Nanoparticles Functionalized with Hyaluronic Acid and Chitosan Biopolymers. Effect of Functionalization on Cell Internalization. *ACS Biomater. Sci. Eng.* **2016**, *2*, 741–751, doi:10.1021/acsbiomaterials.5b00502.

175. Huang, X.; Zhuang, J.; Teng, X.; Li, L.; Chen, D.; Yan, X.; Tang, F. The promotion of human malignant melanoma growth by mesoporous silica nanoparticles through decreased reactive oxygen species. *Biomaterials* **2010**, *31*, 6142–6153, doi:10.1016/j.biomaterials.2010.04.055.

176. Kind, C. The development of the circulating blood volume of the chick embryo. *Anat. Embryol. (Berl).* **1975**, *147*, 127–132, doi:10.1007/BF00306727.

177. Ribatti, D. The chick embryo chorioallantoic membrane as a model for tumor biology. *Exp. Cell Res.* **2014**, *328*, 314–324, doi:10.1016/j.yexcr.2014.06.010.

178. Nakamura, Y.; Mochida, A.; Choyke, P. L.; Kobayashi, H. Nanodrug Delivery: Is the Enhanced Permeability and Retention Effect Sufficient for Curing Cancer? *Bioconjug. Chem.* **2016**, *27*, 2225–2238, doi:10.1021/acs.bioconjchem.6b00437.

179. Freitas, L. B. de O.; Corgosinho, L. de M.; Faria, J. A. Q. A.; dos Santos, V. M.; Resende, J. M.; Leal, A. S.; Gomes, D. A.; Sousa, E. M. B. de Multifunctional mesoporous silica nanoparticles for cancer-targeted, controlled drug delivery and imaging. *Microporous Mesoporous Mater.* **2017**, *242*, 271–283, doi:10.1016/j.micromeso.2017.01.036.

180. Chen, Z.; Zhu, P.; Zhang, Y.; Liu, Y.; He, Y.; Zhang, L.; Gao, Y. Enhanced Sensitivity of Cancer Stem Cells to Chemotherapy Using Functionalized Mesoporous Silica Nanoparticles. *Mol. Pharm.* **2016**, *13*, 2749–2759, doi:10.1021/acs.molpharmaceut.6b00352.

181. Hickerson, R. P.; Vlassov, A. V; Wang, Q.; Leake, D.; Ilves, H.; Gonzalez-Gonzalez, E.; Contag, C. H.; Johnston, B. H.; Kaspar, R. L. Stability study of unmodified siRNA and relevance to clinical use. *Oligonucleotides* **2008**, *18*, 345–54, doi:10.1089/oli.2008.0149.

182. Steinbacher, J. L.; Landry, C. C. Adsorption and release of siRNA from porous silica. *Langmuir* **2014**, *30*, 4396–4405, doi:10.1021/la402850m.

183. Kang, J. H.; Jang, W. Y.; Ko, Y. T. The Effect of Surface Charges on the Cellular Uptake of Liposomes Investigated by Live Cell Imaging. *Pharm. Res.* **2017**, *34*, 704–717, doi:10.1007/s11095-017-2097-3.

184. Niedermayer, S.; Weiss, V.; Herrmann, A.; Schmidt, A.; Datz, S.; Müller, K.; Wagner, E.; Bein, T.; Bräuchle, C. Multifunctional polymer-capped mesoporous silica nanoparticles for pH-responsive targeted drug delivery. *Nanoscale* **2015**, *7*, 7953–64, doi:10.1039/c4nr07245f.

8 Appendix

8.1 Supplementary Results

Table 38: Results of one-way ANOVA corresponding to Figure 25, HNSCCUM-02T

One-way analysis of variance (HNSCCUM-02T)					
P value	0.7691				
P value summary	ns				
Are means signif. different? (P < 0.05)	No				
Number of groups	6				
F	0.5023				
R square	0.1731				
ANOVA Table	**SS**	**df**	**MS**		
Treatment (between columns)	78.28	5	15.66		
Residual (within columns)	374.0	12	31.17		
Total	452.3	17			
Dunnett's Multiple Comparison Test	**Mean Diff.**	**q**	**Significant? P < 0.05?**	**Summary**	**95 % CI of diff.**
0 vs 5	-0.6667	0.1463	No	ns	-13.89 to 12.56
0 vs 10	1.667	0.3656	No	ns	-11.56 to 14.89
0 vs 25	-2.000	0.4388	No	ns	-15.22 to 11.22
0 vs 50	-2.333	0.5119	No	ns	-15.56 to 10.89
0 vs 100	-5.000	1.097	No	ns	-18.22 to 8.23

Table 39: Results of one-way ANOVA corresponding to Figure 25, RPMI2650

One-way analysis of variance (RPMI2650)					
P value	0.1635				
P value summary	ns				
Are means signif. different? (P < 0.05)	No				
Number of groups	6				
F	1.925				
R square	0.4451				
ANOVA Table	**SS**	**df**	**MS**		
Treatment (between columns)	255.1	5	51.02		
Residual (within columns)	318.0	12	26.50		
Total	573.1	17			
Dunnett's Multiple Comparison Test	**Mean Diff.**	**q**	**Significant? P < 0.05?**	**Summary**	**95 % CI of diff.**
0 vs 5	9.000	2.141	No	ns	-3.20 to 21.20
0 vs 10	11.33	2.696	No	ns	-0.86 to 23.53
0 vs 25	9.000	2.141	No	ns	-3.20 to 21.19
0 vs 50	10.33	2.458	No	ns	-1.86 to 22.53
0 vs 100	9.667	2.300	No	ns	-2.53 to 21.86

Table 40: Results of one-way ANOVA corresponding to Figure 25, Cal-33

One-way analysis of variance (Cal-33)					
P value	0.8816				
P value summary	ns				
Are means signif. different? (P < 0.05)	No				
Number of groups	6				
F	0.3359				
R square	0.1228				
ANOVA Table	**SS**	**df**	**MS**		
Treatment (between columns)	61.11	5	12.22		
Residual (within columns)	436.7	12	36.39		
Total	497.8	17			
Dunnett's Multiple Comparison Test	**Mean Diff.**	**q**	**Significant? P < 0.05?**	**Summary**	**95% CI of diff.**
0 vs 5	-2.000	0.4061	No	ns	-16.29 to 12.29
0 vs 10	-3.667	0.7444	No	ns	-17.96 to 10.62
0 vs 25	-5.333	1.083	No	ns	-19.62 to 8.96
0 vs 50	-4.667	0.9475	No	ns	-18.96 to 9.62
0 vs 100	-1.667	0.3384	No	ns	-15.96 to 12.62

Table 41: Results of one-way ANOVA corresponding to Figure 25, HuH7

One-way analysis of variance (HuH7)					
P value	0.0223				
P value summary	*				
Are means signif. different? (P < 0.05)	Yes				
Number of groups	6				
F	4.030				
R square	0.6268				
ANOVA Table	**SS**	**df**	**MS**		
Treatment (between columns)	2114	5	422.7		
Residual (within columns)	1259	12	104.9		
Total	3372	17			
Dunnett's Multiple Comparison Test	**Mean Diff.**	**q**	**Significant? P < 0.05?**	**Summary**	**95 % CI of diff.**
0 vs 5	-7.000	0.8371	No	ns	-31.26 to 17.26
0 vs 10	-7.333	0.8770	No	ns	-31.59 to 16.93
0 vs 25	0.6667	0.07972	No	ns	-23.59 to 24.93
0 vs 50	-21.33	2.551	No	ns	-45.59 to 2.93
0 vs 100	-28.67	3.428	Yes	*	-52.93 to -4.41

Table 42: Results of one-way ANOVA corresponding to Figure 25, NIH-3T3

One-way analysis of variance (NIH-3T3)					
P value	0.2741				
P value summary	ns				
Are means signif. different? (P < 0.05)	No				
Number of groups	6				
F	1.392				
R square	0.2788				
ANOVA Table	**SS**	**df**	**MS**		
Treatment (between columns)	1597	5	319,5		
Residual (within columns)	4132	18	229,6		
Total	5729	23			
Dunnett's Multiple Comparison Test	**Mean Diff.**	**q**	**Significant? P < 0.05?**	**Summary**	**95 % CI of diff.**
0 vs 5	21.50	2.007	No	ns	-8.09 to 51.09
0 vs 10	10.75	1.003	No	ns	-18.84 to 40.34
0 vs 25	10.75	1.003	No	ns	-18.84 to 40.34
0 vs 50	7.750	0.7234	No	ns	-21.84 to 37.34
0 vs 100	-3.750	0.3500	No	ns	-33.34 to 25.84

Table 43: Results of two-way ANOVA corresponding to Figure 26B

Two-way ANOVA				
Source of Variation	**% of total variation**	**P value**		
Interaction	1.01	0.9148		
Time	23.94	0.0617		
Treatment	7.42	0.5357		
Source of Variation	**P value summary**	**Significant?**		
Interaction	ns	No		
Time	ns	No		
Treatment	ns	No		
Source of Variation	**Df**	**Sum-of-squares**	**Mean square**	**F**
Interaction	2	0.02874	0.01437	0.08970
Time	1	0.6806	0.6806	4.248
Treatment	2	0.2108	0.1054	0.6579
Residual	12	1.923	0.1602	

Table 44: Results of two-way ANOVA corresponding to Figure 26D

Two-way ANOVA				
Source of Variation	**% of total variation**	**P value**		
Interaction	4.14	0.3471		
Time	8.21	0.0535		
Treatment	66.17	0.0002		
Source of Variation	**P value summary**	**Significant?**		
Interaction	ns	No		
Time	ns	No		
Treatment	***	Yes		
Source of Variation	**Df**	**Sum-of-squares**	**Mean square**	**F**
Interaction	2	26.46	13.23	1.157
Time	1	52.43	52.43	4.586
Treatment	2	422.7	211.4	18.49
Residual	12	137.2	11.43	

Table 45: Linear regression analysis corresponding to Figure 28

Best-fit values	
Slope	0.06607 ± 0.006825
Y-intercept when X=0.0	0.2370 ± 0.1722
X-intercept when Y=0.0	-3.587
1/slope	15.13
95 % Confidence Intervals	
Slope	0.05160 to 0.08054
Y-intercept when X=0.0	-0.1281 to 0.6021
X-intercept when Y=0.0	-11.06 to 1.678
Goodness of Fit	
R square	0.8542
Sy.x	0.5020
Is slope significantly non-zero?	
F	93.72
DFn, DFd	1.000, 16.00
P value	< 0.0001
Deviation from zero?	Significant
Data	
Number of X values	6
Maximum number of Y replicates	3
Total number of values	18
Number of missing values	0

Table 46: Results of two-way ANOVA corresponding to Figure 31

Two-way ANOVA				
Source of Variation	**% of total variation**	**P value**		
Interaction	16,84	< 0,0001		
Marker	33,44	< 0,0001		
Time	43,49	< 0,0001		
Source of Variation	**P value summary**	**Significant?**		
Interaction	****	Yes		
Marker	****	Yes		
Time	****	Yes		
Source of Variation	**Df**	**Sum-of-squares**	**Mean square**	**F**
Interaction	5	5851	1170	13,00
Marker	1	11619	11619	129,1
Time	5	15110	3022	33,58
Residual	24	2160	90,00	

Table 47: Results of one-way ANOVA corresponding to Figure 32

One-way analysis of variance					
P value	0.5559				
P value summary	ns				
Are means signif. different? (P < 0.05)	No				
Number of groups	3				
F	0.6271				
R square	0.1223				
ANOVA Table	**SS**	**df**	**MS**		
Treatment (between columns)	261.7	2	130.9		
Residual (within columns)	1878	9	208.7		
Total	2140	11			
Dunnett's Multiple Comparison Test	**Mean Diff.**	**q**	**Significant? P < 0.05?**	**Summary**	**95 % CI of diff.**
0 mg/mL vs 0.5 mg/mL	10.85	1.120	No	ns	-14.48 to 36.18
0 mg/mL vs 1.0 mg/mL	4.600	0.4361	No	ns	-22.97 to 32.17

Table 48: Results of IC50 analysis of Dox in HNSCCUM-02T corresponding to Figure 34A

log c(Dox) vs. normalized response – Variable slope	24 h	48 h
Best-fit values		
LogIC50	0.1957	-0.7133
HillSlope	-0.9437	-1.442
IC50	**1.569**	**0.1935**
Std. Error		
LogIC50	0.06282	0.02531
HillSlope	0.1203	0.1184
95% Confidence Intervals		
LogIC50	0.06545 to 0.3260	-0.7658 to -0.6608
HillSlope	-1.193 to -0.6942	-1.687 to -1.196
IC50	1.163 to 2.119	0.1715 to 0.2184
Goodness of Fit		
Degrees of Freedom	22	22
R square	**0.8899**	**0.9588**
Absolute Sum of Squares	2774	570,2
Sy.x	11.23	5.091
Number of points analyzed	24	24

Table 49: Results of IC50 analysis of Dox in RPMI2650 corresponding to Figure 34B

log c(Dox) vs. normalized response – Variable slope	24 h	48 h
Best-fit values		
LogIC50	-0.1252	-0.8816
Hill Slope	-0.6971	-1.399
IC50	**0.7496**	**0.1314**
Std. Error		
LogIC50	0.03646	0.02035
Hill Slope	0.04282	0.08719
95% Confidence Intervals		
LogIC50	-0.2015 to -0.04886	-0.9242 to -0.8390
Hill Slope	-0.7867 to -0.6075	-1.582 to -1.217
IC50	0.6288 to 0.8936	0.1191 to 0.1449
Goodness of Fit		
Degrees of Freedom	19	19
R square	**0.9672**	**0.9772**
Absolute Sum of Squares	416.5	178.6
Sy.x	4.682	3.066
Number of points analyzed	21	21

Table 50: Results of two-way ANOVA corresponding to Figure 36A

Two-way ANOVA				
Source of Variation	**% of total variation**	**P value**		
Interaction	9.17	0.0002		
Time	5.07	0.0002		
Medium	80.70	< 0.0001		
Source of Variation	**P value summary**	**Significant?**		
Interaction	***	Yes		
Time	***	Yes		
Medium	****	Yes		
Source of Variation	**Df**	**Sum-of-squares**	**Mean square**	**F**
Interaction	6	0.1624	0.02707	7.264
Time	2	0.08983	0.04492	12.05
Medium	3	1.429	0.4763	127.8
Residual	24	0.08944	0.003727	
Number of missing values		1		
Bonferroni multiple comparisons: Number of comparisons 8				
96 h Dox-MSNs vs 24 h Dox-MSNs				
Medium	**96 h Dox-MSNs**	**24 h Dox-MSNs**	**Difference**	**95 % CI of diff.**
DMEM + 5 % FCS	0.7333	0.3543	-0.3790	-0.53 to -0.23
DMEM	0.1217	0.06467	-0.0570	-0.21 to 0.092
H_2O	0.0330	0.0220	-0.0110	-0.16 to 0.14
PBS	0.0600	0.0250	-0.0350	-0.18 to 0.11
Medium	**Difference**	**t**	**P value**	**Summary**
DMEM + 5 % FCS	-0.3790	7.604	P < 0.0001	****
DMEM	-0.0570	1.144	P > 0.05	ns
H_2O	-0.0110	0.2207	P > 0.05	ns
PBS	-0.0350	0.7022	P > 0.05	ns
96 h Dox-MSNs vs Cy5-MSNs				
Medium	**96 h Dox-MSNs**	**Cy5-MSNs**	**Difference**	**95 % CI of diff.**
DMEM + 5 % FCS	0.7333	0.4537	-0.2797	-0.43 to -0.13
DMEM	0.1217	0.07733	-0.04433	-0.19 to 0.11
H_2O	0.0330	0.09867	0.06567	-0.084 to 0.22
PBS	0.0600	0.003667	-0.05633	-0.21 to 0.093
Medium	**Difference**	**t**	**P value**	**Summary**
DMEM + 5 % FCS	-0.2797	5.611	P < 0.0001	****
DMEM	-0.04433	0.8894	P > 0.05	ns
H_2O	0.06567	1.317	P > 0.05	ns
PBS	-0.05633	1.130	P > 0.05	ns

Table 51: Results of two-way ANOVA corresponding to Figure 36B

Two-way ANOVA				
Source of Variation	**% of total variation**	**P value**		
Interaction	8.12	< 0.0001		
Time	5.71	< 0.0001		
Medium	84.28	< 0.0001		
Source of Variation	**P value summary**	**Significant?**		
Interaction	****	Yes		
Time	****	Yes		
Medium	****	Yes		
Source of Variation	**Df**	**Sum-of-squares**	**Mean square**	**F**
Interaction	6	7.536	1.256	17.74
Time	2	5.296	2.648	37.41
Medium	3	78.20	26.07	368.2
Residual	23	1.628	0.07079	
Number of missing values		1		
Bonferroni multiple comparisons: Number of comparisons 5				
Cy5-MSNs vs 24 h Dox-MSNs				
Medium	**Cy5-MSNs**	**24 h Dox-MSNs**	**Difference**	**95 % CI of diff.**
DMEM + 5 % FCS	3.280	2.587	-0.6933	-1.35 to -0.04
DMEM	0.5533	0.4633	-0.0900	-0.74 to 0.56
H_2O	0.0250	0.1633	0.1383	-0.59 to 0.87
PBS	0.02333	0.1800	0.1567	-0.50 to 0.81
Medium	**Difference**	**t**	**P value**	**Summary**
DMEM + 5 % FCS	-0.6933	3.192	P < 0.05	*
DMEM	-0.0900	0.4143	P > 0.05	ns
H_2O	0.1383	0.5695	P > 0.05	ns
PBS	0.1567	0.7212	P > 0.05	ns
Cy5-MSNs vs 96 h Dox-MSNs				
Medium	**Cy5-MSNs**	**96 h Dox-MSNs**	**Difference**	**95 % CI of diff.**
DMEM + 5 % FCS	3.280	5.340	2.060	1.41 to 2.71
DMEM	0.5533	0.8733	0.3200	-0.33 to 0.97
H_2O	0.0250	0.2467	0.2217	-0.51 to 0.95
PBS	0.02333	0.4233	0.4000	-0.25 to 1.05
Medium	**Difference**	**t**	**P value**	**Summary**
DMEM + 5 % FCS	2.060	9.483	P < 0.0001	****
DMEM	0.3200	1.473	P > 0.05	ns
H_2O	0.2217	0.9126	P > 0.05	ns
PBS	0.4000	1.841	P > 0.05	ns

Table 52: Results of two-way ANOVA corresponding to Figure 37A (right)

Two-way ANOVA				
Source of Variation	**% of total variation**	**P value**		
Interaction	27.31	< 0.0001		
Treatment	53.65	< 0.0001		
Time	13.33	< 0.0001		
Source of Variation	**P value summary**	**Significant?**		
Interaction	****	Yes		
Treatment	****	Yes		
Time	****	Yes		
Source of Variation	**Df**	**Sum-of-squares**	**Mean square**	**F**
Interaction	4	6692	1673	23.91
Treatment	1	13146	13146	187.9
Time	4	3267	816.7	11.67
Residual	20	1399	69.97	
Bonferroni multiple comparisons: Number of comparisons 5				
Cy5-MSNs vs Dox-MSNs				
Time	**Cy5-MSNs**	**Dox-MSNs**	**Difference**	**95 % CI of diff.**
24 h	81.67	86.33	4.667	-14.77 to 24.10
24 h + 72 h	88.67	29.33	-59.33	-78.77 to -39.90
48 h	85.33	67.00	-18.33	-37.77 to 1.100
48 h + 48 h	89.67	26.67	-63.00	-82.43 to -43.57
96 h	98.00	24.67	-73.33	-92.77 to -53.90
Time	**Difference**	**t**	**P value**	**Summary**
24 h	4.667	0.6833	P > 0.05	ns
24 h + 72 h	-59.33	8.688	P < 0.0001	****
48 h	-18.33	2.684	P > 0.05	ns
48 h + 48 h	-63.00	9.224	P < 0.0001	****
96 h	-73.33	10.74	P < 0.0001	****

Table 53: Results of two-way ANOVA corresponding to Figure 37B (right)

Two-way ANOVA				
Source of Variation	**% of total variation**	**P value**		
Interaction	9.16	0.0415		
Treatment	70.25	< 0.0001		
Time	5.52	0.1622		
Source of Variation	**P value summary**	**Significant?**		
Interaction	*	Yes		
Treatment	****	Yes		
Time	ns	No		
Source of Variation	**Df**	**Sum-of-squares**	**Mean square**	**F**
Interaction	4	2303	575.7	3.038
Treatment	1	17666	17666	93.22
Time	4	1389	347.2	1.832
Residual	20	3790	189.5	
Bonferroni multiple comparisons: Number of comparisons 5				
Cy5-MSNs vs Dox-MSNs				
Time	**Cy5-MSNs**	**Dox-MSNs**	**Difference**	**95 % CI of diff.**
24 h	92.33	74.67	-17.67	-49.65 to 14.31
24 h + 72 h	97.00	39.67	-57.33	-89.31 to -25.35
48 h	96.67	54.67	-42.00	-73.98 to -10.02
48 h + 48 h	99.00	31.00	-68.00	-99.98 to -36.02
96 h	96.00	38.33	-57.67	-89.65 to -25.69
Time	**Difference**	**t**	**P value**	**Summary**
24 h	-17.67	1.572	P > 0.05	ns
24 h + 72 h	-57.33	5.101	P < 0.001	***
48 h	-42.00	3.737	P < 0.01	**
48 h + 48 h	-68.00	6.050	P < 0.0001	****
96 h	-57.67	5.131	P < 0.001	***

Table 54: Results of two-way ANOVA corresponding to Figure 38A

Two-way ANOVA				
Source of Variation	**% of total variation**	**P value**		
Interaction	27.88	< 0.0001		
Time	35.44	< 0.0001		
Treatment	36.16	< 0.0001		
Source of Variation	**P value summary**	**Significant?**		
Interaction	****	Yes		
Time	****	Yes		
Treatment	****	Yes		
Source of Variation	**Df**	**Sum-of-squares**	**Mean square**	**F**
Interaction	3	9809	3270	290.7
Time	1	12467	12467	1109
Treatment	3	12721	4240	377.0
Residual	16	179.9	11.25	

Table 55: Results of two-way ANOVA corresponding to Figure 38B

Two-way ANOVA				
Source of Variation	**% of total variation**	**P value**		
Interaction	78.54	< 0.0001		
Population	17.42	< 0.0001		
Treatment	0.00	1.0000		
Source of Variation	**P value summary**	**Significant?**		
Interaction	****	Yes		
Population	****	Yes		
Treatment	ns	No		
Source of Variation	**Df**	**Sum-of-squares**	**Mean square**	**F**
Interaction	9	46392	5155	69.13
Population	3	10288	3429	45.99
Treatment	3	$1.676*10^{-7}$	$5.585*10^{-8}$	$7.490*10^{-10}$
Residual	32	2386	74.57	

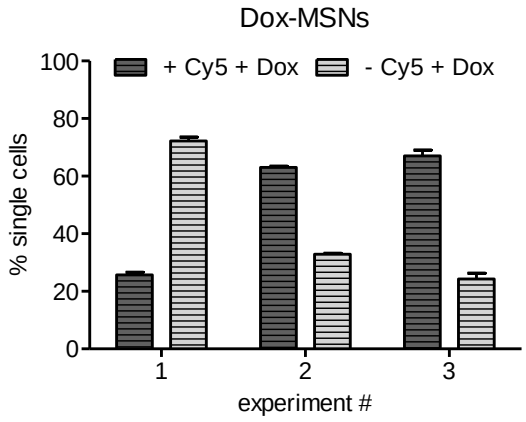

Figure 56: Single experiments corresponding to data in Figure 38B

Cy5 positive and Dox positive (+Cy5 + Dox) and Cy5 negative and Dox positive (-Cy5 + Dox) populations of HNSCCUM-02T cells treated with Dox-MSNs for 24 hours are depicted, respectively. In the first experiment, just about 20 % of all single cells were positive for Cy5 and Dox, in the second and third experiment more than 60 % were positive for Cy5 and Dox. 1: n=3; 2,3: n= 2, mean + S.D.

Table 56: Results of two-way ANOVA corresponding to Figure 41A

Two-way ANOVA				
Source of Variation	**% of total variation**	**P value**		
Interaction	9.71	0.0160		
Time	8.31	0.0033		
Treatment	70.85	< 0.0001		
Source of Variation	**P value summary**	**Significant?**		
Interaction	*	Yes		
Time	**	Yes		
Treatment	****	Yes		
Source of Variation	**Df**	**Sum-of-squares**	**Mean square**	**F**
Interaction	3	1917	639,0	4.654
Time	1	1640	1640	11.95
Treatment	3	13985	4662	33.95
Residual	16	2197	137.3	
Bonferroni multiple comparisons: Number of comparisons 4				
2 h vs 24 h				
Treatment	**2 h**	**24 h**	**Difference**	**95 % CI of diff.**
PBS	0.7967	0.5633	-0.2333	-27.15 to 26.68
1 µM Dox	44.21	69.25	25.04	-1.87 to 51.95
Dox-MSNs	16.36	58.13	41.76	14.85 to 68.68
Cy5-MSNs	0.9767	0.5400	-0.4367	-27.35 to 26.48
Treatment	**Difference**	**t**	**P value**	**Summary**
PBS	-0.2333	0.02439	P > 0.05	ns
1 µM Dox	25.04	2.617	P > 0.05	ns
Dox-MSNs	41.76	4.365	P < 0.01	**
Cy5-MSNs	-0.4367	0.04564	P > 0.05	ns

Table 57: Results of two-way ANOVA corresponding to Figure 41B

Two-way ANOVA				
Source of Variation	**% of total variation**	**P value**		
Interaction	5.28	0.1162		
Time	2.40	0.0952		
Treatment	80.09	< 0.0001		
Source of Variation	**P value summary**	**Significant?**		
Interaction	ns	No		
Time	ns	No		
Treatment	****	Yes		
Source of Variation	**Df**	**Sum-of-squares**	**Mean square**	**F**
Interaction	3	624.8	208.3	2.301
Time	1	284.7	284.7	3.145
Treatment	3	9483	3161	34.92
Residual	16	1448	90.53	
Bonferroni multiple comparisons: Number of comparisons 4				
2 h vs 24 h				
Treatment	**2 h**	**24 h**	**Difference**	**95 % CI of diff.**
PBS	0.2633	0.3000	0.03667	-21.82 to 21.89
1 µM Dox	45.37	48.51	3.137	-18.72 to 24.99
Dox-MSNs	16.85	41.27	24.42	2.57 to 46.28
Cy5-MSNs	0.3600	0.3167	-0.04333	-21.90 to 21.81
Treatment	**Difference**	**t**	**P value**	**Summary**
PBS	0.03667	0.004720	P > 0.05	ns
1 µM Dox	3.137	0.4038	P > 0.05	ns
Dox-MSNs	24.42	3.144	P < 0.05	*
Cy5-MSNs	-0.04333	0.005578	P > 0.05	ns

Table 58: Results of two-way ANOVA corresponding to Figure 42A

Two-way ANOVA				
Source of Variation	**% of total variation**	**P value**		
Interaction	16.85	< 0.0001		
Time	14.65	< 0.0001		
Treatment	67.44	< 0.0001		
Source of Variation	**P value summary**	**Significant?**		
Interaction	****	Yes		
Time	****	Yes		
Treatment	****	Yes		
Source of Variation	**Df**	**Sum-of-squares**	**Mean square**	**F**
Interaction	3	6199	2066	84.69
Time	1	5388	5388	220.8
Treatment	3	24812	8271	339.0
Residual	16	390.4	24.40	
Bonferroni multiple comparisons: Number of comparisons 4				
24 h vs 96 h				
Treatment	**24 h**	**96 h**	**Difference**	**95 % CI of diff.**
PBS	100.0	100.0	0,0	-11.35 to 11.35
2 µM Dox	44.07	0.7333	-43.33	-54.68 to -31.99
Dox-MSNs	82.63	6.167	-76.47	-87.81 to -65.12
Cy5-MSNs	90.97	90.90	-0.06667	-11.41 to 11.28
Treatment	**Difference**	**t**	**P value**	**Summary**
PBS	0,0	0.0	P > 0.05	ns
2 µM Dox	-43.33	10.74	P < 0.0001	****
Dox-MSNs	-76.47	18.96	P < 0.0001	****
Cy5-MSNs	-0.06667	0.01653	P > 0.05	ns

Table 59: Results of two-way ANOVA corresponding to Figure 42B

Two-way ANOVA				
Source of Variation	**% of total variation**	**P value**		
Interaction	14.06	< 0.0001		
Time	7.07	< 0.0001		
Treatment	76.34	< 0.0001		
Source of Variation	**P value summary**	**Significant?**		
Interaction	****	Yes		
Time	****	Yes		
Treatment	****	Yes		
Source of Variation	**Df**	**Sum-of-squares**	**Mean square**	**F**
Interaction	3	4480	1493	29.63
Time	1	2252	2252	44.68
Treatment	3	24332	8111	160.9
Residual	16	806,5	50.41	
Bonferroni multiple comparisons: Number of comparisons 4				
24 h vs 96 h				
Treatment	**24 h**	**96 h**	**Difference**	**95 % CI of diff.**
PBS	83.10	102.1	18.97	2.66 to 35.27
2 µM Dox	33.23	0.3333	-32.90	-49.21 to -16.59
Dox-MSNs	61.87	7.433	-54.43	-70.74 to -38.13
Cy5-MSNs	87.50	78.37	-9.133	-25.44 to 7.17
Treatment	**Difference**	**t**	**P value**	**Summary**
PBS	18.97	3.272	P < 0.05	*
2 µM Dox	-32.90	5.675	P < 0.001	***
Dox-MSNs	-54.43	9.390	P < 0.0001	****
Cy5-MSNs	-9.133	1.576	P > 0.05	ns

Table 60: Results of one-way ANOVA corresponding to Figure 53A

One-way analysis of variance					
P value	0.0107				
P value summary	*				
Are means signif. different? (P < 0.05)	Yes				
Number of groups	3				
F	7.826				
R square	0.6349				
ANOVA Table	**SS**	**df**	**MS**		
Treatment (between columns)	0.003919	2	0.001959		
Residual (within columns)	0.002253	9	0.0002503		
Total	0.006172	11			
Dunnett's Multiple Comparison Test	**Mean Diff.**	**q**	**Significant? P < 0.05?**	**Summary**	**95% CI of diff.**
Cy5-MSNs vs EGFR-MSNs	-0.03646	3.259	Yes	*	-0.06571 to -0.007218
Cy5-MSNs vs IgG2a-MSNs	-0.03996	3.572	Yes	*	-0.06921 to -0.01072

Table 61: Results of two-way ANOVA corresponding to Figure 54A

Two-way ANOVA (only alive cells)				
Source of Variation	**% of total variation**	**P value**		
Interaction	90.28	< 0.0001		
Population	0.02	0.8668		
Treatment	0.00	1.0000		
Source of Variation	**P value summary**	**Significant?**		
Interaction	****	Yes		
Population	ns	No		
Treatment	ns	No		
Source of Variation	**Df**	**Sum-of-squares**	**Mean square**	**F**
Interaction	3	26878	8959	49.65
Population	1	5.241	5.241	0.02904
Treatment	3	0.2315	0.07718	0.0004277
Residual	16	2887	180.5	
Bonferroni multiple comparisons: Number of comparisons 4				
alive - MSNs vs alive + MSNs				
Treatment	**alive - MSNs**	**alive + MSNs**	**Difference**	**95 % CI of diff.**
PBS	95.72	0.07108	-95.65	-126.5 to -64.79
Cy5-MSNs	62.78	33.52	-29.26	-60.12 to 1.593
EGFR-MSNs	9.214	86.77	77.55	46.70 to 108.4
IgG2a-MSNs	26.29	69.91	43.62	12.77 to 74.48
Treatment	**Difference**	**t**	**P value**	**Summary**
PBS	-95.65	8.720	P < 0.0001	****
Cy5-MSNs	-29.26	2.668	P > 0.05	ns
EGFR-MSNs	77.55	7.070	P < 0.0001	****
IgG2a-MSNs	43.62	3.977	P < 0.01	**

Table 62: Results of two-way ANOVA corresponding to Figure 54B

Two-way ANOVA				
Source of Variation	**% of total variation**	**P value**		
Interaction	30.97	0.0285		
Population	26.80	0.0057		
Treatment	0.01	1.0000		
Source of Variation	**P value summary**	**Significant?**		
Interaction	*	Yes		
Population	**	Yes		
Treatment	ns	No		
Source of Variation	**Df**	**Sum-of-squares**	**Mean square**	**F**
Interaction	3	8640	2880	3.911
Population	1	7478	7478	10.16
Treatment	3	1,453	0.4844	0.0006578
Residual	16	11782	736.4	
Bonferroni multiple comparisons: Number of comparisons 4				
alive - MSNs vs alive + MSNs				
Treatment	**alive - MSNs**	**alive + MSNs**	**Difference**	**95 % CI of diff.**
PBS	93.29	0.1178	-93.17	-155.5 to -30.84
Cy5-MSNs	66.62	27.74	-38.88	-101.2 to 23.45
EGFR-MSNs	56.95	36.37	-20.58	-82.90 to 41.75
IgG2a-MSNs	40.83	52.24	11.41	-50.92 to 73.74
Treatment	**Difference**	**t**	**P value**	**Summary**
PBS	-93.17	4.205	P < 0.01	**
Cy5-MSNs	-38.88	1.755	P > 0.05	ns
EGFR-MSNs	-20.58	0.9287	P > 0.05	ns
IgG2a-MSNs	11.41	0.5150	P > 0.05	ns

8.2 Acknowledgements

First of all, I express my deepest gratitude to my supervisor [redacted] who welcomed me to his working group three and a half years ago and supported, challenged, and guided me during this time. I thank him for his trust and his professional and personal guidance at the right times, the fruitful discussions and the space he gave me to conduct this doctoral work. Moreover, I thank him for structuring and editing my publications, and letting me present my results at conferences.

Moreover, I sincerely thank my second supervisor [redacted] who made this collaborative project possible and supported me through the chemical parts of this work. He was always available when needed and promoted this project with his expertise.

Furthermore, I express my gratitude to [redacted] who was a supportive cooperation partner in this interdisciplinary project and would always provide me with new MSN batches when needed. Also, I thank him for explaining me everything I wanted to know about MSN synthesis and characterization and for our fruitful discussions.

Also, I express my deepest gratitude to the members of our working group who all welcomed me from my first day of work and let me fit in easily. I thank [redacted] who supported and helped me with every issue that was cell culture related or molecular biology related, and I am especially grateful for her technical assistance with the CAM-assay. Moreover, I thank [redacted] for her advice on everything related to microscopy and her technical assistance with the chicken embryo immunofluorescence staining. I [redacted] who always answered my questions, discussed my experiments with me when I was at a dead end and gave me new ideas. Also, we had a great time at the conferences (and cities ;-)) we visited together. I will miss our daily lunch breaks together! Especially, I thank [redacted] who was always available for discussions and support, professionally and personally and [redacted] who always spread a positive vibe in the lab and always tried to find the answers to my questions (scientific and medical).

This work would not have been possible without the Max Planck Graduate Center with the Johannes Gutenberg University Mainz. I am thankful for their financial and personal support, for giving me the possibility to present my work at conferences and to enjoy two retreats with other international PhD candidates in Berlin and Dresden. The student seminars gave me the opportunity to openly discuss my work and to get new ideas from other interdisciplinary projects and drove this project forward.

Moreover, I thank the focus program BiomaTiCS of the University Medical Center Mainz and the “Stiftung Tumorforschung Kopf-Hals” for financial support of this project.

I thank [redacted] for her support and guidance as my mentor during the past years.

I had the opportunity to use some equipment of other institutes and working groups. First, I thank [redacted] (Hautklinik) who gave me valuable advices on drug delivery systems and gave me access to the LSR II flow cytometer and the HIDEX. He was not only a great colleague but also became great friend!

Second, I thank [redacted] (Cell Biology Unit, UMC Mainz) for letting me use their CLSM and always quickly fulfilling my appointment wishes.

During the time of this doctoral thesis I had the pleasure to supervise [redacted] in her own thesis. She let me practice my managing and leading skills and would always have time for a quick chat. Also, the medical doctorate candidates were and are a great addition to our lab: Thanks to [redacted]. It was a pleasure to work with you.

I thank all current and former members of the group of [redacted] for the good cooperation.

I also thank my supervisor of my Master thesis from the LMU Munich, [redacted], and my supervisor in the lab during that time, [redacted], who encouraged me to conduct a doctoral thesis.

Finally, I express my deepest gratitude to my family who always believed in me and supported me whatever I wanted to do. I am especially thankful and grateful to my grandfather Helmuth who enabled me to study in Munich and to my mother who let me explore the world and is always available when needed. Moreover, I thank my friends ([redacted]) for always being there for me even though they have not heard from me much the past years. I am sincerely grateful to [redacted] for proof-reading my thesis and finding inconsistencies I never would have found.

All the mentioned above contributed something to this thesis and I am thankful to all of you!

8.3 Conference Contributions (Poster)

Transmed Science Day, September 19th 2016, University Medical Center Mainz:

"Nanoparticles as drug carriers in HNSCC"

Retreat of Max Planck Graduate Center, May 15th 2017, Mainz:

"Mesoporous silica nanoparticles as drug carriers in head and neck cancer therapy"

2nd International Conference on 3D Printing in Medicine, May 19th- 20th 2017, Mainz:

"Nanoparticulate drug depots for modulation of specific material-tissue interaction"

88th Annual Meeting of the German Society of Oto-Rhino-Laryngology, Head and Neck Surgery, May 24th-27th 2017, Erfurt:

"SiRNA delivery to HNSCC cells via mesoporous silica nanoparticles"

Annual Meeting of the German Society for Biomaterials 2017, November 9th- 11th 2017, Würzburg:

"Mesoporous silica nanoparticles for drug delivery in head and neck cancer therapy"

3rd International Conference on 3D Printing in Medicine, May 4th- 5th 2018, Mainz:

"Implant coating with antibiotic active mesoporous nano-depots for prevention of post-implantation infection"

Annual Meeting of German Society for Biomaterials, November 8th- 10th 2018, Braun-schweig:

"Mesoporous silica nanocarrier with a pH-responsive gatekeeper system for drug delivery"

BiomaTiCS-Symposium "Advances in 3D-Printing", May 10th 2019, Mainz:

"Mesoporous nano-depots for modulation of specific material-tissue interaction"

8.4 Publications

“Two-pore channel function is crucial for migration of invasive cancer cells”
Ong Nam Phuong Nguyen, Christian Grimm, Lina S. Schneider, Yu-Kai Chao, Carina Atzberger, Karin Bartel, **Anna Watermann,** Melanie Ulrich, Doris Mayr, Christian Wahl-Schott, Martin Biel, and Angelika Vollmar, *published* in Cancer Research, 2017, 77, 1427-1438

“Mesoporous Silica Nanoparticles as Drug Delivery Vehicles in Cancer”
Anna Watermann, Juergen Brieger, *published* in Nanomaterials, 2017, 7, 189

“Fluorescein- and EGFR-antibody conjugated silica nanoparticles for enhancement of real-time tumor border definition using confocal laser endomicroscopy in squamous cell carcinoma of the head and neck”
Anna Watermann, Rita Gieringer, Anna-Maria Bauer, Sven Kurch, Ralf Kiesslich, Wolfgang Tremel, Jan Gosepath and Juergen Brieger, *submitted*

8.5 Curriculum Vitae